Optimisation of Macroscale Functional Surfaces Through Numerical Investigation of Naturally Occurring Bedforms

A thesis submitted in partial fulfilment of the requirements of Liverpool John Moores University for the degree of Doctor of Philosophy

Phillip Stephen Taylor

June 2020

Contents

List of Figures

List of Tables

List of Symbols

Latin Alphabet

$a_i, b_i,\ s_i$ Geomtric properties of segmented surface profiles

C Log-law intercept constant

C_f Coefficient of friction in a spatially developing boundary layer

C_p Pressure component of the coefficient of friction

C_v Viscous component of the coefficient of friction

C_{sgs} Dimensionless constant for sub-grid scale turbulence models

Co Courant number

$d^{[PE]}$ Cell-to-cell vector

f Channel friction factor

f_p Sum of f_{p1} and f_{p2}

f_v Sum of f_{v1} and f_{v2}

S_{ij} Symmetric strain-rate tensor

t Instantaneous physical time

T_{av} Temporal averaging period

u Instantaneous streamwise component of velocity

u_∞ Instantaneous streamwise component veloctiy in the free-stream flow

u_τ Friction velocity

U_{av} Bulk average velocity of an internal channel flow

V Cell volume

v Wall-normal component of velocity

v'_{ref} Reference velocity fluctuation value for the numerical trip

v_{ref} Reference velocity value for the numerical trip

w Spanwise component of flow velocity

x Streamwise coordinate axis

y Wall-normal coordinate axis

z Spanwise coordinate axis

Greek Alphabet

α_t Weighting factor for the numerical trip

β Clauser pressure gradient parameter

ΔN_x Number of cells in the streamwise direction

ΔN_y Number of cells in the wall-normal direction

ΔN_z Number of cells in the spanwise direction

Δt Time step size

Δx Streamwise cell width

Δy Wall-normal cell width

Δz Spanwise cell width

δ^* Boundary layer displacement thickness

δ_{99} Boundary layer velocity thickness

δ_{ij} Kronecker delta

γ_1 Limiting factor for the numerical gradient scheme

γ_2 Limiting factor for the numerical Laplacian scheme

γ_{cn} Weighting factor for the Crank-Nicolson numerical scheme

γ_p Relaxation factor for the pressure field

γ_u Relaxation factor for the velocity field

κ Von-Karman constant

Λ Turbulence cut-off length

λ Axis-aligned wavelength of a periodic profile

λ_g Crest-to-crest wavelength of a periodic profile

λ_x Streamwise wavelength of a periodic profile

λ_z Spanwise wavelength of a periodic profile

μ Dynamic viscosity

ν Kinematic viscosity

ν_t Kinematic turbulent viscosity

ω Vorticity

Ω_{ij} Asymmetric vorticity tensor

ϕ Arbitrary vector or scalar property

$\psi_{ij}, \xi_{ij}, \zeta_{ij}$ Secondary sub-grid stress tensors

ρ Density

τ_0 Wall shear stress at a fluid-solid boudnary

τ_t Turbulent shear stress

τ_{ij} Turbulent stress tensor

θ Boundary layer momentum thickness

φ Orientation of a geometric surface profile, repective to the streamwise axis

Subscripts

∞ Located at at the furthest point from the wall, i.e. the free-stream

i, j, k Vector index

in Located at the inlet of the flow domain

l Laminar

max Maximum value

min Minimum value

ref User-specified reference value

rms Root mean square value

t Turbulent

x Parallel alignment to the streawise axis

y Parallel alignment to wall-normal axis

z Parallel alignment to the spanwise axis

Superscripts

$'$ Instantaneous fluctuation of a time-dependant component

$*$ Normalised property

$+$ Inner-scaled property

$[]$ Index from a tensor property or numerical matrix

Overbars & Brackets

$\bar{\cdot}$ Temporal averaging

$\langle\rangle$ Spatial averaging

$\tilde{\cdot}$ Spatial filtering

$\vec{\cdot}$ Vector property

Acronyms

CAD   Computer Aided Design

CPU   Central Processing Unit

DNS   Direct Numerical Simulation

DR   Drag Reduction

GUI   Graphical User Interface

LES   Large-Eddy Simulation

LHS   Left Hand Side

RANS Reynolds-Averaged Navier Stokes model

RHS   Right Hand Side

RMS   Root Mean Square

WALE Wall-Adapting Local Eddy-Viscosity model

Abstract

This thesis presents a detailed investigation into the potential of optimising the geometric profiles of macroscale grooves, to improve their drag reducing performance in internal laminar flow and spatially developing turbulent flow. The investigation explored whether the asymmetric profiles of naturally occurring sand ripples constitute an optimisation over the simple, symmetrical geometric profiles which have formed the typical focus for past investigations of macroscale grooves. In order to enable this analysis, the thesis developed and validated methodologies within the open source code OpenFOAM, which can overcome the bottlenecks associated with both modelling complex geometries in large-scale parametric studies, and implementing surface geometries into spatially developing turbulent flows.

The first stage of the investigation developed a methodology for resolving laminar-turbulent transition in OpenFOAM using large-eddy simulation. To the authors knowledge, this work represents the first systematic validation and verification of resolved laminar-turbulent transition in OpenFOAM to investigate the combined effect of large-eddy simulation and controlled tripping. The results identify that a purely laminar boundary layer can be destabilised through imposing a period of psuedo-random, time-dependant fluctuations in the wall-normal velocity field at the wall. If the magnitude of these fluctuations match the maximum wall-normal velocity fluctuations in an equivalent boundary layer of equal thickness, then the initially period of two-dimensional instabilities is bypassed, and transition can be induced almost instantaneously downstream of the trip. Under these tripping conditions, the results expand the typical design criteria for large-eddy simulation spatial resolution, and show that typical design recommendations can sufficiently converge the flow resistance and shape factor by the start of the fully turbulent regime. Increasing this resolution by a factor of 2

achieve this convergence early on in the laminar-turbulent transitional regime.

The second stage of the investigation involved an extensive parametric study of highly detailed sand ripple profiles within a periodic laminar channel flow. In all cases, the presence of both ripples and sinusoidal grooves had a negative impact on the flow resistance, typically due to a reduction in viscous forces being balanced out by the creation of a larger pressure force. The higher order details of the geometric profiles did not have a significant impact on the flow resistance, even when such details had a significant impact on promoting or delaying flow separation. The details of the geometric profile only became significant for three-dimensional ripples, when applied with a sufficient depth and and Reynolds number to manipulate the bulk flow field towards the centre of the channel, and direct high velocity flow from the centre towards the crests of the ripple profiles.

The final stage of the investigation applied simplified sand ripple profiles into a wall-resolved spatially developing turbulent boundary layer, through the novel incorporation of a split-hexahedral mesh, through OpenFOAM's snappyHexMesh utility. Whilst ripples with a depth of 5% of their wavelength had a negligible impact on flow resistance, deeper ripples (15%) produced an increase in flow resistance which was independent of the growing ratio between boundary layer thickness and ripple depth. The local distribution of turbulent velocity fluctuations was consistent with known drag reducing phenomenon, with amplified spanwise velocity fluctuations over the shear stress spike approaching the crest, and amplified streamwise velocity fluctuations accompanying the free-shear region of flow separation downstream of the crest. It was in this free-shear region, that the streamwise resolution had the greatest impact on the accuracy of the local wall shear stress. The present approach confirms the capabilities of split-hexahedral meshes to efficiently balance the varying requirements of spatial resolution in near-wall and free-stream regions, regardless of the geometric surface profile.

Thesis Declaration

I declare that no portion of the work referred to in the thesis has been submitted in support of an application for another degree or qualification of this or any other university or other institute of learning.

Acknowledgements

I give my most gracious thank you to Professor Xun Chen for guiding me through this process and granting me the possibilities to carry out this research, and for supporting my development and growth within this field. In addition, I am grateful to Dr Mehdi Seddighi and Dr David Allanson for their guidance and support. Thank you to the UK turbulence consortium, for providing funding and access to the ARCHER supercomputing facility.

I also give thanks to my colleague Dr James Wharton, for our lengthy discussions have only ever served to deepen my passion for fluid mechanics and numerical analysis.

Thank you most of all, to my mum and stepdad whose love and support has been invaluable during these past years. Finally, I would like to acknowledge the contribution of my darling cats Ollie and Rocky, whose quiet and calm company was much appreciated during the many hours of writing this thesis.

CHAPTER 1

Introduction

In the late 20th century, it was observed that shark skin consists of a series of short staggered blades aligned lengthwise on the shark. Subsequent experiments on simplified replica structures, known as riblets, discovered that these micro-geometries can work to reduce the drag force acting on the body of a swimming shark, in relation to smooth skin.

Riblets with drag reducing properties require a height and width which lie on the same order of magnitude as the smallest length scale of a turbulent flow (the inner length scale). In addition to the associated manufacturing difficulties, these small length scales significantly increase the required spatial resolution for numerical analysis. Fully resolving turbulent flows is itself cost intensive in terms of the required computational power. In internal flows, the computational domain, and hence com-

putational workload, can be significantly reduced by assuming streamwise periodicity. For an external flow, the boundary layer grows along the streamwise direction, such that the influence of the upstream conditions cannot be ignored. Hence, the computational workload cannot be reduced in order to accommodate the finer spatial resolutions required for investigating drag reducing riblets. For this reason, an overwhelming majority of numerical investigations into drag reducing surface textures in turbulent flow focuses on the specific application of internal channel flow.

Macroscale geometries possess geometric dimensions which lie on the same order of magnitude as the largest length scale of the flow (the outer length scale). Hence, they may be modelled to a spatial resolution of similar magnitude to a standard smooth wall flow. As discussed in Chapter 2, macroscale grooves, most notably shallow dimples, have been found to produce a drag reduction of less than 4% in turbulent flows (Tay *et al.* 2015). Meanwhile, macroscale grooves have been mostly detrimental in laminar flows (Mohammadi & Floryan 2013b). In each case, the authors propose the possibility of an improved performance through the optimisation of the groove profile, expanding beyond simple geometric shapes. Efficient optimisation of this type requires a means of constructing a numerical mesh around increasingly complex geometries in a way which simultaneously minimises the rise in the computational workload, and minimises the pre-processing time, sufficiently enough to permit cost effective parametric investigations.

The main aim of this thesis is to develop new numerical methodologies for the optimisation of macroscale grooves for drag reduction properties. The thesis focuses on the application of internal laminar flow and external turbulent flow, where drag reducing macroscale grooves stand to provide the greatest benefits and novelties in terms of practical application and fundamental understanding. In diverging from a

focus on simple geometric shapes, this thesis looks to the patterns of naturally occurring sand ripples as a means of anchoring the optimisation procedure. These ripples can form when a bed of loose sediment is submerged in a flow undergoing either uniform or oscillating motion.

1.1 Objectives

1. To reverse engineer profiles from naturally occurring macroscale grooves, through direct replication of naturally occurring sand ripple bedforms on a sand beach. To construct smooth, periodic geometric profiles which capture the geometric features of asymmetric sand ripples to a high detail.

2. To assess the suitability of applying automatically generated split-hexhaedral cells (utilising the snappyHexMesh utility in OpenFOAM) for parametric studies of macroscale grooves with arbitrary geometric profiles.

3. To assess the potential of optimising the drag reducing capabilities of macroscale grooves in laminar flow by incorporating the geometric profiles of naturally occurring sand ripples. To determine the conditions which are required for the finer details of surface geometry to have a significant impact on the flow resistance in internal laminar flow.

4. To develop a methodology in OpenFOAM for modelling the laminar, transitional and fully turbulent regimes of a spatially developing turbulent boundary layer within a single domain. This methodology must be optimised to balance realistic inflow conditions, numerical accuracy and turbulence resolution with practical computational cost.

5. To incorporate periodic grooves into the optimised smooth wall boundary layer,

and assess the suitability of applying local cell refinement and automatically generated split-hexahedral cells for improving spatial resolution over deep periodic grooves in a spatially developing turbulent boundary layer.

1.2 Thesis Structure

The remainder of the introduction presents fundamental theory regarding fluid flow and shear layer growth, in preparation for a critical discussion of published works pertaining to flow control methods, and advances in numerical analysis, in Chapter 2. Chapter 3 then presents theory pertaining to the modelling of fluid flows with the finite volume approach, with a particular emphasis on the open source code OpenFOAM. The contributions of the thesis are divided into four chapters. Chapter 4 presents the design, optimisation and validation of a numerical methodology for utilising OpenFOAM to model spatially developing turbulent boundary layers with an optimal balance between physical representation, numerical accuracy, and economic computational cost. Chapter 5 presents the two-dimensional and three-dimensional profiles which are reverse engineered from naturally occurring sand ripples. The suitability of OpenFoam's automated mesh generating utility (snappyHexMesh) is investigated and validated; firstly for replicating published solutions of simple geometric shapes, and then for modelling highly detailed sand ripple profiles. Chapter 6 provides a detailed parametric study of two-dimensional and three-dimensional sand ripples in controlling flow resistance in laminar flow through an internal channel. Finally, in Chapter 7, simplified two-dimensional profiles, based upon asymmetric sand ripples, are incorporated into the optimised smooth surface boundary layer simulations from Chapter 4, using the automated meshing procedure which was explored in Chapter 5 and Chapter 6. This pre-

liminary investigation assesses the capability of split-hexahedral near-wall cells in capturing laminar-turbulent transition and resolving the geometric profiles of macroscale grooves in turbulent flow. The thesis concludes with a compilation of key findings and their implications for further advancement in numerical analysis and surface optimisation.

1.3 Mechanism of Laminar and turbulent Flow

1.3.1 Laminar Shear Flow

A boundary layer is a region in a flow in which the velocity of the fluid is reduced due to the presence of a solid body. For a solid planar surface in the absence of a non-negligible pressure gradient, the boundary layer lies directly adjacent to the wall. The Reynolds number (Equation 1.1) represents the ratio between the inertial forces and the viscous forces of the fluid in the flow. There are various definitions of the Reynolds Number which vary in their selected reference properties for the length scale $[L]$ and the velocity scale $[U]$. The density and dynamic viscosity of the fluid are represented by ρ and μ respectively.

$$Re = \frac{\rho\,[L]\,[U]}{\mu}, \tag{1.1}$$

The two primary states are referred to as laminar flow and turbulent flow. In laminar flow, the flow can exist in parallel layers, with little to no interaction between adjacent layers. Within a laminar flow at equilibrium, the velocity and pressure at a point in the flow will not vary with time. Stokes flow describes a flow in which the viscous forces dominate to the extent that the influence of inertia is negligible; i.e when $Re << 1$.

1.3.2 Laminar-Turbulent Transition

An initially laminar Poisuille flow between two smooth plates can theoretically remain stable up to the limit $Re_h = 3848.1$, where Re_h takes the bulk velocity and the half-height of the channel as the velocity and length scales respectively (Moradi *et al.* 2017). Surface roughness, Reynolds number and background noise can all influence the susceptibility of a stable flow to destabilising effects.

Orszag & Kells (1980) produced numerical solutions from direct numerical simulation to compare the response of an initially stable, laminar Poisuille flow to two-dimensional and three-dimensional disturbances in the velocity field. Their results found that small-amplitude disturbances significantly constricted the laminar regime ($Re_h < 666$) when acting in three dimensions, compared with larger disturbances which are uniform in the spanwise direction ($Re_h < 2000$). Orszag & Patera (1983) identified a mechanism of transition for which the more unstable three-dimensional instabilities could not grow without a strong enough two-dimensional instability; approximately 1% of the maximum streamwise velocity.

The experiments and theoretical predictions of Floryan (2005) and Asai & Floryan (2006) observed that shallow, large wavelength grooves could reduce the critical Reynolds number by up to 30% and enable two-dimensional instabilities to induce transition below the limit $Re_h \approx 2667$. Saha *et al.* (2015) made similar observations in their direct numerical simulations of corrugated pipes. The initially laminar flow remained stable inside all domains with axisymmetric boundary conditions, despite the presence of asymmetric disturbances.

1.3.3 Fundamental Behaviour of Turbulent Flow

Turbulent motions are three-dimensional, chaotic and time-dependant. For a turbulent flow in equilibrium, a flow property at a given point will randomly fluctuate around a steady, mean value. This behaviour is illustrated in Figure 1.1 for an arbitrary physical property at a single spatial location in a fully turbulent flow.
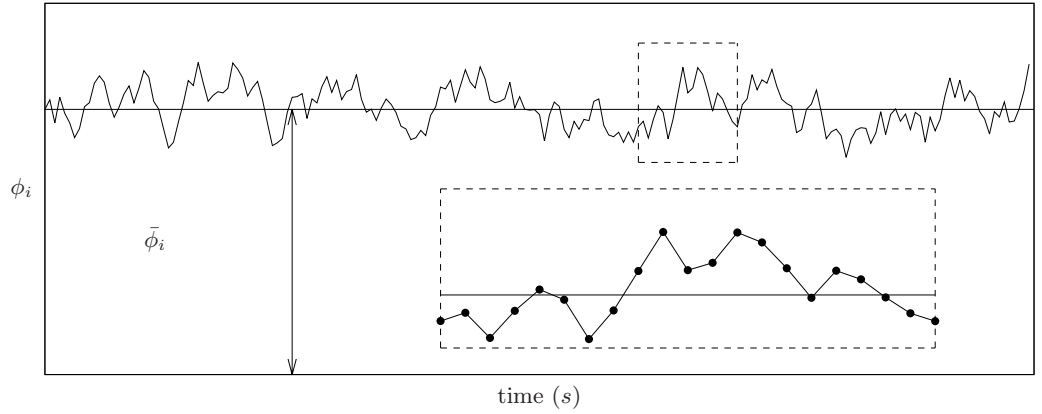
Figure 1.1: *An example of the time dependant behaviour of a property $\phi(t)$ at a point in turbulent fluid flow.*

The time-dependant variable can be decomposed into two components; a time-averaged mean value (Equation 1.3) and a fluctuating, time-dependant value (Equation 1.2).

$$\phi(t) = \bar{\phi} + \phi'(t), \tag{1.2}$$

$$\bar{\phi} = \frac{1}{\Delta t} \int_0^\infty \phi(t) \quad dt, \tag{1.3}$$

If the flow field is averaged over a sufficiently large period of time T_{av}, and the flow exists in an equilibrium state, the temporal average of the fluctuations will return a zero value (Equation 1.4).

$$\bar{\phi}' = \frac{1}{\Delta t} \int_0^\infty \phi'(t) \quad dt = 0, \tag{1.4}$$

The root mean square (Equation 1.5) of a time-dependant variable expresses the

strength of the instantaneous fluctuations relative to the time-averaged mean value.

$$\bar{\phi}'_{rms} = \sqrt{\frac{1}{N_t} \sum_1^{N_t} = \left(\bar{\phi} - \phi(t)\right)}, \tag{1.5}$$

A 'coherent structure' refers to an eddy or vortex which exists for long enough that it can be observed and quantified. These coherent structures can exist over a wide range of length scales. If the largest eddies in a turbulent shear flow have a length scale L_e, and a velocity scale U_e, then the length and velocity scales of the smallest eddies can be predicted by the relations in Equation (1.6) and Equation (1.7) respectively.

$$l_e \approx L_e \left(\frac{L_e U_e}{\nu}\right)^{-0.75}, \tag{1.6}$$

$$u_e \approx U_e \left(\frac{L_e U_e}{\nu}\right)^{-0.25}, \tag{1.7}$$

When an eddy breaks up due to instability, two smaller eddies are formed which contain the energy of the previous eddy. Further instability and break-up causes this energy to be passed down to eddies of increasingly smaller length scales. Once the size of an eddy is sufficiently small, the increased contribution of viscous forces, relative to the previously dominant inertial forces, dissipates the energy of the eddies. A continuous exchange of energy is observed as the random formation of large eddies is followed by their disintegration into smaller and smaller structures. The dissipation of the smallest eddies returns the energy to the flow.

1.3.4 Definition of a Vortex

Connected regions of rotational flow which possess temporal coherence are referred to as either 'coherent structures' or vortices. A flow structure has temporal coherence if

its existence is observable over a time period of at least equal magnitude to the time-averaging periods of the flow. The mathematical definition of a vortex relies on the second order tensor or velocity gradients (Equation 1.8).

$$\nabla u_{ij} = \begin{bmatrix} \frac{\partial u}{\partial x} & \frac{\partial v}{\partial x} & \frac{\partial w}{\partial x} \\[2mm] \frac{\partial u}{\partial y} & \frac{\partial v}{\partial y} & \frac{\partial w}{\partial y} \\[2mm] \frac{\partial u}{\partial z} & \frac{\partial v}{\partial z} & \frac{\partial w}{\partial z} \end{bmatrix}, \tag{1.8}$$

The tensor can be decomposed into two second order tensors (Equation 1.9). The symmetrical tensor S_{ij} (Equation 1.10), corresponds to the rate-of-strain, and the asymmetrical tensor Ω_{ij} (Equation 1.11), corresponds to the rotational motions (vorticity) in the flow.

$$\nabla u_{ij} = S_{ij} + \Omega_{ij}, \tag{1.9}$$

$$S_{ij} = \frac{1}{2} \left(\frac{\partial u_i}{\partial x_j} + \frac{\partial u_j}{\partial x_i} \right), \tag{1.10}$$

$$\Omega_{ij} = \frac{1}{2} \left(\frac{\partial u_i}{\partial x_j} - \frac{\partial u_j}{\partial x_i} \right), \tag{1.11}$$

Vorticity is a vector of three components, which each relate to an axis which is parallel to the Cartesian vectors $\omega = (\omega_x, \omega_y, \omega_z)$. The vorticity of the flow around an axis is determined from the rotational motions in a two-dimensional plane which is normal to that axis. These motions can be obtained from the vorticity tensors, as shown in Equation (1.12).

$$\omega = \begin{bmatrix} \Omega_{32} \\[2mm] \Omega_{13} \\[2mm] \Omega_{12} \end{bmatrix} = \begin{bmatrix} \frac{\partial w}{\partial y} - \frac{\partial v}{\partial z} \\[2mm] \frac{\partial u}{\partial z} - \frac{\partial w}{\partial x} \\[2mm] \frac{\partial u}{\partial y} - \frac{\partial y}{\partial x} \end{bmatrix}, \tag{1.12}$$

1.3.5 Outer Length Scale

For internal flow in a smooth channel, the growth of a shear layer is constrained by the dimensions of the channel. Once the flow is fully developed, the shear layers on opposing walls make contact at the midpoint between them, i.e. the channel half-height, preventing further growth. Hence, the outer length scale of the shear layer, defined by the shear layer width, remains fixed along the streamwise direction as a geometric property of the channel.

For boundary layers which grow along an external boundary, the growth of the boundary layer is not constrained. The boundary layer simply displaces the fluid in the uniform free-stream and continues to do so as its thickness increases, as illustrated in Figure 1.2, where δ_l and δ_t denotes the thickness of the laminar boundary layer and turbulent boundary layer respectively. Hence, even when a boundary layer has developed enough to reach an equilibrium state, the outer length scale continues to vary along the streamwise direction. Furthermore, the outer length scale at a physical geometric location along the streamwise direction is dependant on the behaviour and structure of the boundary layer upstream.
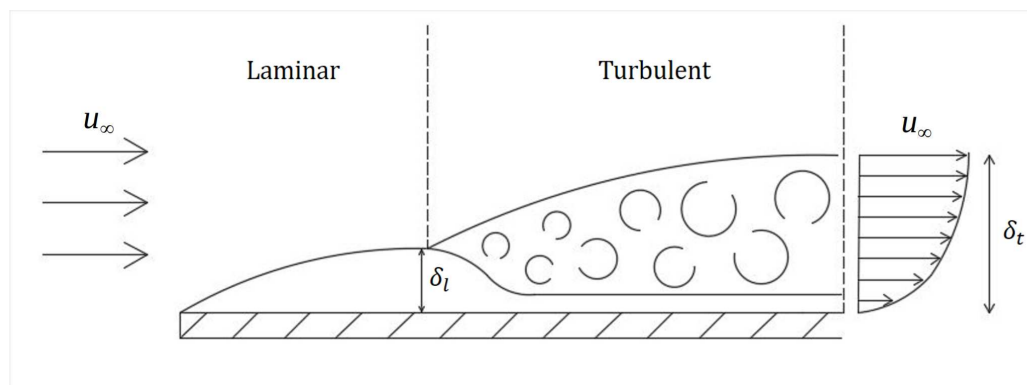
Figure 1.2: *Illustration of a spatially developing boundary layer passing through laminar-turbulent transition.*

Three different definitions of the boundary thickness are given to represent the

outer length scale. The velocity thickness is defined as the height below which the flow velocity is reduced from the initial free-stream velocity by the presence of the solid surface. The exact region in which this occurs is unclear, hence, the velocity thickness is taken as the point at which the streamwise velocity is equal to 99% of the free-stream velocity (Equation 1.13).

$$u\left(y = \delta_{99}\right) = 0.99u_{\infty}, \tag{1.13}$$

As the boundary layer grows, the free-stream flow is deflected away from the wall. The displacement thickness δ^* (Equation 1.14) defines the wall-normal distance by which the streamlines of velocity u_{∞} are shifted away from the wall, due to the presence of the boundary layer.

$$\delta^* = \frac{1}{u_{\infty}} \int_0^{\infty} \left(u_{\infty} - u\right) \quad dy, \tag{1.14}$$

The shear stress at the wall acts against the flow and reduces the momentum within the boundary layer. The momentum thickness θ (Equation 1.15), is defined as the distance that a solid body would have to be moved into the flow to regain this lost momentum.

$$\theta = \frac{1}{u_{\infty}^2} \int_0^{\infty} u\left(u_{\infty} - u\right) \quad dy, \tag{1.15}$$

For laminar and turbulent boundary layers with incompressible flow; Equation (1.16) displays the relation between the wall shear stress, the displacement thickness and the momentum thickness.

$$\tau_0 = \rho \left(\frac{d}{dx} \left(u_{\infty}^2 \theta\right) + \delta^* u_{\infty} \frac{du_{\infty}}{dx} \right), \tag{1.16}$$

The second term on the right-hand side of Equation (1.16) accounts for a change in the free-stream velocity due to the presence of a streamwise pressure gradient.

1.3.6 Inner Length Scale

The shear stress at the local point on the wall is directly related to the wall-normal gradient of streamwise velocity at that point (i.e. as $y \rightarrow 0$), as shown in Equation (1.17).

$$\tau_0 = \mu \left(\frac{\partial u}{\partial y} \right)_{y=0}, \tag{1.17}$$

In turbulent flow, the mixing length l_m, describes the length scale of the displacement with which a body of fluid moves across the wall-normal direction of the boundary layer (Schlichting 1978). Equation (1.18) displays Prandtl's mixing-length hypothesis, where τ_t denotes the turbulent shear stress.

$$\tau_t = \rho l_m^2 |\frac{\partial \bar{u}}{\partial y}| \frac{\partial \bar{u}}{\partial y}, \tag{1.18}$$

Equation (1.19) displays the relation between the mixing length, streamwise velocity fluctuations and wall-normal velocity fluctuations (Schlichting 1978), for which $-\bar{u'}v'$ is referred to as the Reynolds shear stress.

$$-\bar{u'}v' = l_m^2 |\frac{\bar{u}}{\partial y}| \frac{\partial \bar{u}}{\partial y}, \tag{1.19}$$

In a region near to the wall, the sum of the laminar and turbulent components of shear stress is approximately constant along the wall-normal direction (Equation 1.20).

$$\nu \left(\frac{\partial \bar{u}}{\partial y} \right) + l_m^2 |\frac{\partial \bar{u}}{\partial y}| \frac{\partial \bar{u}}{\partial y} = \nu \left(\frac{\partial \bar{u}}{\partial y} \right)_{y=0} \quad for \quad y << \delta_{99}, \tag{1.20}$$

Von Karman defined a velocity scale, known as the friction velocity (Equation 1.21), to represent the magnitude of the turbulent velocity fluctuations.

$$u_\tau = \sqrt{\frac{\tau_t}{\rho}}, \tag{1.21}$$

According to the relation $l_m \propto y$, the mixing length at the solid surface will be zero. If the total shear stress at the wall was assumed to be a turbulent shear stress, then the friction velocity at the wall can be defined by Equation (1.22).

$$u_\tau = \sqrt{\frac{\tau_0}{\rho}} = l_m \frac{\partial \bar{u}}{\partial y}, for \quad \tau_0 \to \tau_t, \tag{1.22}$$

By substituting the velocity gradient based upon the laminar component of shear stress at the wall (Equation 1.17), a hypothetical mixing length scale can be defined based upon the total shear stress in the near-wall region (Equation 1.23). This property defines the inner length scale of a turbulent shear flow, and is referred to referred to as the viscous length l_τ.

$$l_\tau = \frac{\nu}{u_\tau}, \tag{1.23}$$

1.3.7   Boundary Layer Structure

A fully developed turbulent boundary layer can be divided into two regions based on the relevant length scale. Within the inner region of the boundary layer, the flow properties scale with the inner length scale, i.e. the viscous length l_τ. The inner-scaled coordinates for velocity and length are defined in Equation (1.24) and Equation (1.25).

$$y^+ = \frac{y}{l_\tau} = \frac{yu_\tau}{\nu}, \tag{1.24}$$

$$u^+ = \frac{u}{u_\tau}, \quad \bar{u}'^+_{rms} = \frac{\bar{u}'_{rms}}{u_\tau} \quad and \quad \bar{u'v'}^+ = \frac{\bar{u'v'}}{u_\tau^2}, \tag{1.25}$$

The inner region lies adjacent to the wall and usually has a width equal to approximately 20% of the boundary layer velocity thickness δ_{99}. The remainder of the boundary layer makes up the outer region in which the flow properties scale with the outer length scale δ_{99}. Figure 1.3 displays the inner-scaled streamwise velocity profile across the inner region and outer region of a turbulent boundary layer.
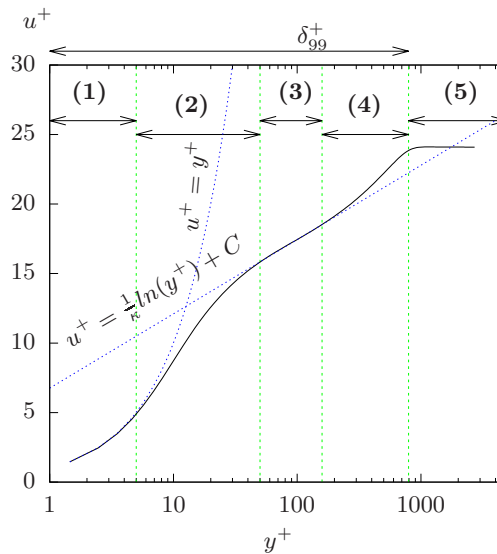
Figure 1.3: *Structure of a fully turbulent boundary layer flow, in terms of the inner-scaled velocity profile.* **(1)** *viscous sub-layer* **(2)** *buffer layer* **(3)** *logarithmic layer* **(4)** *outer layer* **(5)** *free-stream*

The inner region can be further divided into two regions; the viscous sub-layer and the logarithmic region, with a buffer region connecting the two. The viscous sub-layer lies directly adjacent to the wall. In a smooth wall boundary layer, the width of the viscous sub-layer typically extends between the points $y^+ = 0$ and $y^+ = 5$. In this region there is a direct linear relationship between u^+ and y^+ (Equation 1.26). The viscous sub-layer is dominated by high velocity gradients, and hence, high viscous stresses. Turbulence generation is suppressed through rapid dissipation.

$$u^+ = y^+ \quad for \quad y^+ < 5, \tag{1.26}$$

The limits of the logarithmic region are commonly estimated to lie between the points $y^+ > 30 - 50$ and $y/\delta_{99} < 0.2$ (Bradshaw & Huang 1995). The function of y^+ takes the form of the linear relationship in Equation (1.27), known as the 'Log-Law of the Wall'. The validity of this equation relies on an accurate prediction of the Von Karman Constant κ, and the logarithmic constant C.

$$u^+ = \frac{1}{\kappa} ln\left(y^+\right) + C, \qquad (1.27)$$

The logarithmic region contains the strongest instantaneous fluctuations in the wall-normal and spanwise components of the velocity field. The strongest instantaneous fluctuations of the streamwise component of velocity lie closer to the wall, within the buffer region. Within the buffer region, the streamwise velocity flow field is characterised by longitudinal streaks of alternating high and low velocity.

Literature Review

2.1   Introduction

Some of the most successful designs for functional textured surfaces have arisen from

observing the fruits of evolution. The process of natural selection drives animal and

plant life to adapt for its survival. This review considers three main types of naturally

occurring surface patterns. Textures from natural shark skin (Section 2.2.1) and the

lotus leaf (Section 2.2.2) have been found to produce beneficial drag reducing effects,

although their small length scales limit their applicability. In cases where surface tex-

tures with larger length scales have proved successful for drag reduction, the overall

benefits have been modest (Section 2.3 and Section 2.4), with the reoccurring proposal

that greater potential may be unlocked through optimisation of the geometric profile

beyond simple geometric shapes. Hence, Section 2.5 discusses the phenomenon of natural bedform formation and the key mechanisms behind the emergence of asymmetric and three-dimensional patterns. However, the investigation of such surface contains one crucial bottleneck. Current limitations in computational cost and capability typically limit the complexity of both the physical flow scenario and the geometry of the surface profile which can be investigated through numerical methods. For this reason, the majority of the numerical analysis covers periodic channel flows and simple geometric designs. The final section (Section 2.6) of this review critically discusses the ongoing development of numerical methods for modelling spatially developing external flows over both simple smooth surfaces and textured geometries.

2.2 Naturally Occurring Drag Reduction

2.2.1 Shark Skin

The skin of a shark consists of a series of overlapping scales with three-dimensional textures containing ridges which are aligned parallel to the length of the shark, samples of which are shown in Figure 2.1. In 1983, Walsh (1983) performed experiments in which a replica of this shark skin pattern was placed in a fully turbulent boundary layer, and compared its performance against the standard smooth, planar surface. These test surfaces consisted of simplified designs of purely two-dimensional 'riblets' with a triangular cross-section, oriented parallel to the bulk flow direction. When compared to a smooth surface, the presence of these triangular riblets reduced the overall flow resistance by up to 8%. Bechert *et al.* (1997) undertook a comprehensive optimisation study within an experimental oil channel to compare the flow resistance over riblets for a variety of profile shapes and dimensions. Riblets with thin blade profiles, which

contained the smallest crests and the widest troughs out of all profile shapes considered, resulted in the greatest drag reduction. They observed a drag reduction of 10% for thin blade riblets of 16 viscous lengths in width and 8 viscous lengths in height. Garcia-Mayoral & Jimenez (2011a) proposed an alternative optimisation parameter for drag reducing riblets. After observing the experimental data of Walsh (1983) and Bechert *et al.* (1997), they identified that the square root of the cross-sectional area of the riblet groove could provide a more accurate indicator for optimisation, with an accuracy of approximately $\pm 10\%$. For riblets of simple geometric profiles, they proposed an optimal value of 10.7 viscous lengths.

Though successful in turbulent flows, the potential drag reduction for riblets in purely laminar flows is not as clear. In an early investigation of streamwise riblets, Choi *et al.* (1991) considered a laminar channel flow with a fixed pressure gradient in the streamwise direction. Implementing triangular riblets ($\lambda_g/k_g = 0.2$) into the upper and lower surfaces caused a drag increase in both cases. The numerical analysis of Djenidi *et al.* (1994) suggested that shallower riblets ($\lambda_g/k_g = 0.8$) could produce a drag reduction of 2.6% within a spatially developing laminar boundary layer. However, experimental validations could not confirm these observations as the potential experimental error was reported to be 3%.

Attempts to improve the $\approx 10\%$ limit of streamwise riblets and move closer to real shark skin geometries, have shown limited results. Bechert *et al.* (2000) experimented with discontinuous riblet segments, which were geometrically similar to their previous designs (Bechert *et al.* 1997), in a staggered arrangement. These new designs degraded the drag reducing effect by approximately -1.7% of the corresponding smooth surface drag. The numerical analysis of Martin & Bhushan (2016) confirmed these observations for an array of scalloped riblet segments, separated into groups of threes; each
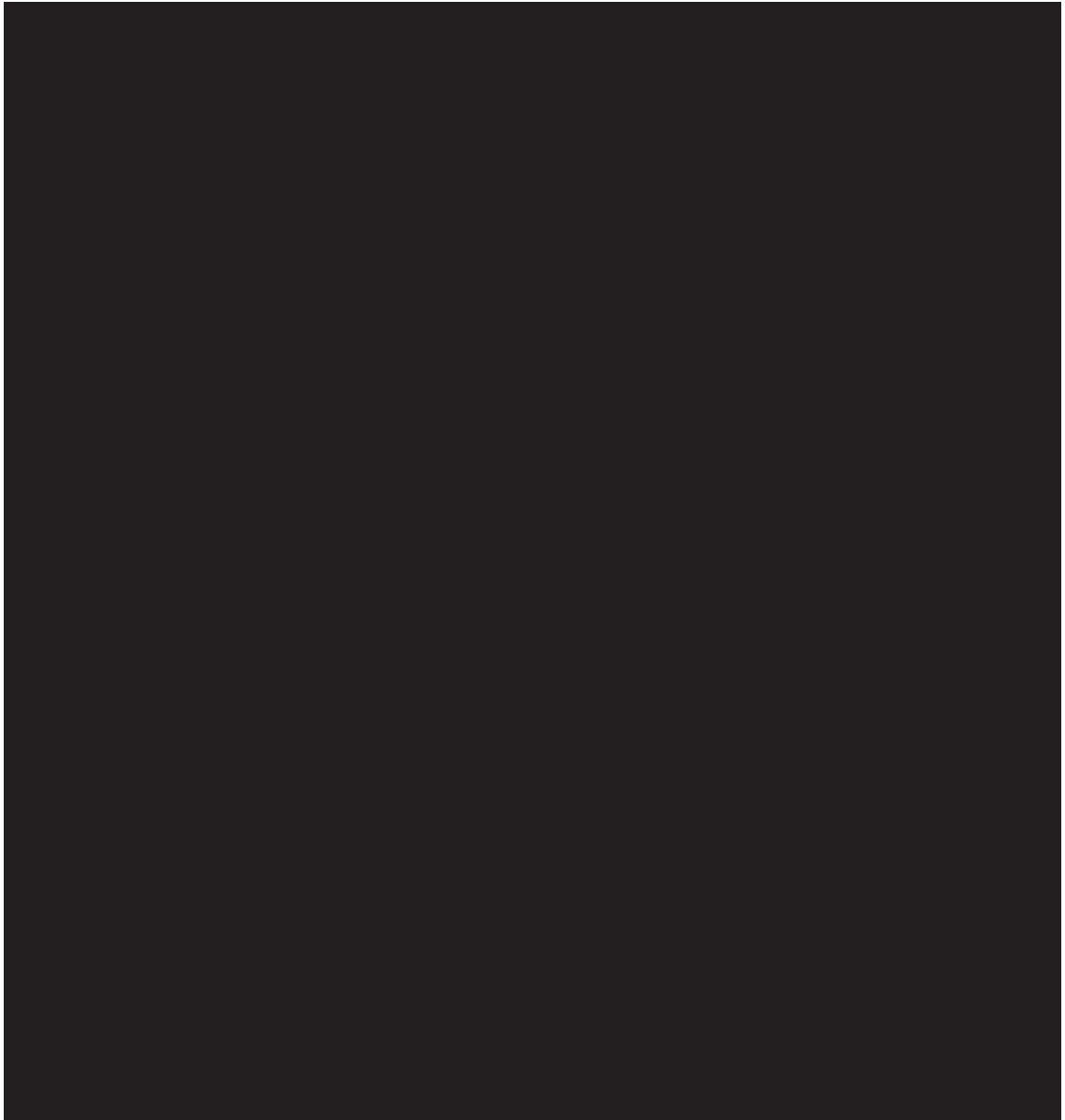
Figure 2.1: *Examples of streamwise aligned ridges over the body of a shark. After Bechert & Bartenwerfer (1989)*

Figure 2.2: *Diagram of the three-dimensional shark skin denticles and flow domain investigated by Boomsma & Sotiropoulus (2016). After Boomsma & Sotiropoulus (2016)*

representing a shark skin scale. The discontinuous riblets produced a similar magnitude change with a -1.2% fall in drag reduction. Boomsma & Sotiropoulus (2016) produced a numerical solution for highly resolved, three-dimensional shark skin denticles, with a natural geometry, as shown in Figure 2.2. For turbulent channel flow, the natural denticles produced a viscous drag increase of up to 25%, with an additional 25% increase caused by the creation of an additional form drag. Benschop & Breugem (2017) investigated surfaces of converging and diverging riblets, as shown in Figure 2.3. Such a texture is known as a 'herringbone' pattern, which can be observed on bird feathers. Although the riblet length scales lay within the optimal drag reduction limits, the resultant spanwise motion of the fluid produced a strong secondary flow in the form of streamwise vortices which could raise the flow resistance by more than 70%.

Prior to their comprehensive optimisation study in Bechert *et al.* (1997), Bechert & Bartenwerfer (1989) had established a theoretical link between the riblet height and the drag reduction. They first defined the protrusion height of riblets as the distance between the crest of the riblets and the virtual origin of an identical boundary layer over a reference smooth wall flow. Luchini *et al.* (1991) later refined this definition as the difference between the virtual origin in the spanwise direction and the virtual

Figure 2.3: *Diagram of blade riblets in a herringbone formation. After Benschop & Breugem (2017).*

origin of the flow in the streamwise direction. By assuming that the riblets are almost entirely submerged within a region that is dominated by viscosity, i.e. the laminar sublayer, Bechert & Bartenwerfer (1989) predicted that the drag reducing riblets require a protrusion height that is less than or equal to 22% of the spanwise spacing.

To identify the flow mechanism behind these drag reducing effects, investigations by Choi & Kim (1993), Goldstein & Tuan (1998) and Chu & Karniadakis (1993), obtained high resolution numerical solutions for turbulent flow through a channel with one wall of triangular riblets. Each study identified a reduction in the viscous flow resistance of approximately $3\% - 6\%$, which occurred when the riblet crests were spaced ≤ 23 viscous lengths apart. Furthermore, Choi & Kim (1993) and Goldstein & Tuan (1998) observed that the drag reducing cases were accompanied by a reduction in the turbulent fluctuations of spanwise velocity in the vicinity of the riblets. Choi & Kim (1993) compared visualisation of the flow field data for cases of drag reducing and drag decreasing riblets. They observed an important correlation between drag reduction and the near-wall behaviour of small-scale turbulent vortices. They theorised that

riblets served to restrict the movement of turbulent vortices in the near-wall region and prevent their penetration into the grooves. This would reduce the percentage of the wetted area which would be exposed to the high velocity fluid which the vortices propel towards the wall. Lee & Lee (2001) performed flow visualisation experiments for a spatially developing turbulent boundary layer over scalloped riblets. Photographs of the instantaneous flow field showed similar behaviour to the numerical solution of Choi & Kim (1993).

The behaviour observed by Choi & Kim (1993) and Lee & Lee (2001) would become more apparent for the optimised thin blade riblets of Bechert *et al.* (1997). El-Sammi *et al.* (2007) and Martin & Bhushan (2014) obtained detailed numerical solutions of the flow fields for turbulent channel flow over thin blade riblets with a range of riblet dimensions spanning the proposed drag reducing regime. Figure 2.4 displays the interaction of streamwise voricies with scalloped ribets observed by Martin & Bhushan (2014) in the drag reducing (Figure 2.4a) and drag increasing (Figure 2.4b) regimes. When the spacing between the riblets was smaller than the vortex diameter, the riblets shifted the vortex away from the trough. The large spikes in shear stress at the crest were overwhelmed by the reduction in shear stress within the trough. If the width was increased beyond the vortex diameter then the vortex descended into the trough and exposed this area to the high turbulent shear stresses normally experienced by the smooth wall. There was some disparity concerning the point at which this occurs, where Martin & Bhushan (2014) conclude a limit of 30 viscous lengths and El-Sammi *et al.* (2007) concluded a limit of 40 viscous lengths. However, this may be attributed to the lower mesh resolution and non-physical representation of the solid boundary in the latter case. These simulations predicted drag reduction values nearly identical to the experimental findings of Bechert *et al.* (1997) and predicted similar values for

(a) $\lambda_g^+ = 16.9$

(b) $\lambda_g^+ = 33.0$
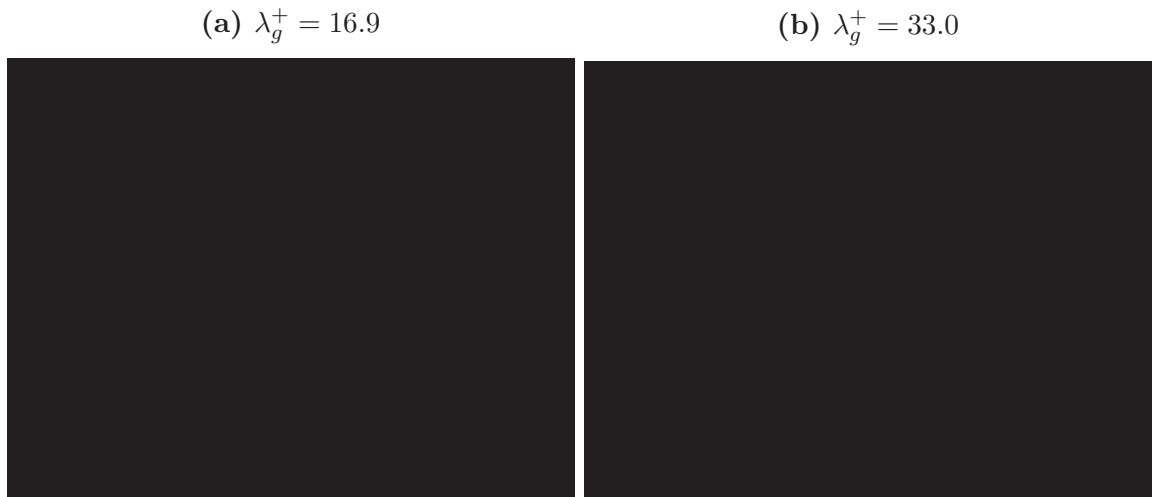
Figure 2.4: *The behaviour of near-wall streamwise vortices over streamwise aligned riblets in (a) the drag reducing regime and (b) the drag increasing regime. After Martin & Bhushan (2016)*

optimal riblet spacing; 18 viscous lengths in width and 8-10 viscous lengths in height.

Garcia-Mayoral & Jimenez (2011b) produced a high resolution numerical analysis to compare the flow field of blade riblets in a turbulent channel flow, for varying values of the groove area. They proposed an alternative mechanism to account for the transition from a drag reducing effect to a drag increasing effect. In the drag reducing regime, they observed a low velocity, recirculating vortex within the riblet groove, with an absence of the restricted small-scale vortices observed in the previous studies of Choi & Kim (1993), Lee & Lee (2001), El-Sammi *et al.* (2007). As the riblet area increased, this vortex became unstable and eventually broke down. Simultaneously, a large, streamwise oriented recirculating region appeared a short distance above the riblet crests, within the region $y^+ \leq 20$, producing a large increase in Reynolds stresses in this region.

Krieger *et al.* (2018) investigated the potential of streamwise riblets for stabilising weakly turbulent flows within the transitional regime. A flow through a plane, periodic channel, with square grooves on one wall, was initiated with a turbulence intensity of 20%. By optimising the initial grooves, they identified a profile of deep triangular

geometries, with a large depth to width ratio of 2.5, which could maintain a steady shear layer along the lower wall, even in the presence of fully turbulent flow across the bulk of the channel. This produced a resultant drag reduction of more than 60% compared to a fully developed turbulent channel flow.

2.2.2 The Lotus Leaf

A second crucial breakthrough lay in the discovery of the lotus leaf and its 'self cleaning' mechanism (Barthlott & Neinhuis 1997). The micro-textures on the leaf of the lotus plant serve to resist the penetration of water into its grooves and keep the liquid mobile whilst in contact with the surface. In addition to the potential for 'self cleaning' surfaces, it was soon realised that similar surfaces which are immersed in a bulk flow could create a continuous region of trapped gas between the fluid and the surface, reducing the flow resistance at this point (Rothstein 2010). The same effect can occur for a secondary liquid state in place of trapped gas (Chen *et al.* 2016), provided that liquid has a higher viscosity than the bulk flow. Further investigations found that for a surface with a periodically occurring free-shear region between the bulk and trapped fluids, the viscous drag forces could be decreased beyond that of a smooth surface (Maynes *et al.* 2007; Ou *et al.* 2004; Davies *et al.* 2006; Ou *et al.* 2004), with a potential reduction to the pressure loss on the order of 50% . A limiting factor of these investigations was the assumption of a flat interface between the liquid and the trapped gas. Curvature of the interface can reduce the drag reduction, and create an overall drag increase if the interface protrudes into the flow (Teo & Khoo 2010). The practical application of these 'superhydrophobic' surfaces with large slip lengths is limited by the instability of large gas pockets (Lee *et al.* 2016), and the required viscosity of the flow.

2.3 Practical Drag Reduction in Turbulent Flow

2.3.1 Fundamental Mechanisms

Many investigations have identified significant drag reduction by introducing spanwise motions into the flow through mechanical surfaces. The introduction of spanwise components into the main flow stream can lead to a drag reduction of up to 40% (Karniadakis & Choi 2003). Du *et al.* (2002) compared numerical data of flow fields for turbulent channel flow subject to a body force at the wall, which oscillated in the form of a spanwise travelling wave. They varied the wavelength between 1.4 and 5.6 times the channel half-height (or $210 - 840$ viscous lengths) and found a drag reduction that increased monotonically with the wavelength. Furthermore, they observed a significant reduction in the intensity of the near-wall velocity streaks. Within a plane channel flow of $Re_\tau = 180$, Canton *et al.* (2016) demonstrated these mechanisms directly by inducing artificial, streamwise vortices into the bulk flow through a numerical volume force. The large-scale structures shifted the distribution of turbulent flow away from the wall and into the bulk flow, reducing the turbulent stresses at the wall. In practical applications, these active methods require an energy input to function. When Quadrio & Ricco (2004) determined the energy requirement to produce a 44.7% drag reduction through spanwise oscillations, the potential drag reduction fell to only 7.3%. Even with a significant drag reduction potential, the costs and complexities of active methods demand an improved benefit over passive methods in order to qualify as practical solutions.

The real potential, and the greatest challenge, for drag reduction through spanwise motions lies, in replicating these motions using passive surfaces which require no energy input. Table 2.1 outlines key numerical and experimental investigations into

the drag reducing potential of passive surface designs through generation of large-scale spanwise motions. Depending on the configuration, each study is summarised by the Reynolds number range (based on either the channel half-height h, or the boundary layer thickness δ_{99}), groove depth (or dimple depth) k_g, groove wavelength (or dimple diameter) λ_g, and the minimum change in the total drag which was achieved.

Table 2.1: Overview of key numerical and experimental investigations of flow over dimples and oblique grooves.

Publication	Scenario,Geometry	Re_h or Re_δ	k_g/λ_g	λ_g/h	$DR_{min}(\%)$
Experimental					
Lienhart *et al.* (2008)	channel flow, dimples	$10,000 \sim$ $65,000$	0.05	$0.53 \sim$ 1.67	$\approx 0\%$
Nesselrooij *et al.* (2016)	spatially developing flow, dimples	$10000 \sim$ 40000	$0.025 \sim$ 0.05	$0.25 \sim$ 1.5	-6%
Tay *et al.* (2015)	channel flow, dimples	$3333 \sim$ 23333	$0.015 \sim$ 0.05	0.2	-3%
Tay & Lim (2017)	channel flow, dimples	$3333 \sim$ 22667	0.05	0.2	-4%
Numerical					
Lienhart *et al.* (2008)	channel flow, dimples	10935	0.05	1.67	2%
Ghebali *et al.* (2017)	channel flow, oblique grooves	6200	$0.024 \sim$ 0.072	$1.7 \sim$ 2.55	$-1.7\% \sim$ 3.1
Tay *et al.* (2017)	channel flow, dimples	$2000 \sim$ 10000	$0.015 \sim$ 0.05	0.2	-1.5%

2.3.2 Experimental Investigations

Initial numerical and experimental investigations by Lienhart *et al.* (2008) proved unsuccessful for turbulent channel flow. Their dimples, with a depth equal to 5% of the diameter, produced a negative effect on the overall flow resistance, which grew with flow strength ($Re_h \geq 1 \times 10^4$). Further experiments by Tay *et al.* (2015) investigated the potential benefits of dimple induced vortices when applied to fully turbulent channel flow. The dimple depth was limited to 5% and 1.25% of the dimple diameter. In each case, one or more pairs of counter-rotating streamwise vortices formed over each dimple. For the deeper dimples, a set of four co-rotating vortices occupied a region with a spanwise width of 2000 viscous lengths. The overall viscous drag fell as turbulent energy was redistributed towards the larger length scales, and their corresponding lower frequencies. The accompanying pressure drag initially offset the viscous drag reduction, but decreased with falling dimple depth or rising Reynolds number. Hence, by $Re_h \geq 2 \times 10^4$, both surfaces provided an overall drag reduction of 1% to 3%. Although the flow scenario was similar to that of Lienhart *et al.* (2008), the surfaces in Tay *et al.* (2015) contained a greater texture density with the crests forming less than 10% of the total surface area, which could account for the improved performance in a similar manner to optimised riblet designs (Bechert *et al.* 1997).

The experimental investigations of Nesselrooij *et al.* (2016) applied the dimple geometries of Tay *et al.* (2015) to a spatially developing turbulent boundary layer with otherwise similar flow conditions. Their results indicated that external flows inverted the optimisation trends, such that the flow resistance fell with increasing crest area, and that a crest area far greater than 10% was necessary for a beneficial drag reduction. However, the relationship between dimple depth and Reynolds number in channel flow was maintained within the low Reynolds number range. Tay & Lim (2017) investigated

the potential of increasing the drag reducing performance of shallow dimples applying asymmetry to the dimple profile. Their results showed that moving the minimum point downstream by a distance equal to 10% of the dimple diameter, could provide a modest improvement to the drag reduction over a wide range of Reynolds numbers. On the other hand, shifting the minimum point upstream reduced the drag reduction, with a severe drag increase of more than 10% occurring for an upstream shift of just 20% of the dimple diameter.

2.3.3 Numerical Investigations

Crucially, the most significant drag reducing mechanism of the flow exists at a length scale which is two orders of magnitude greater than traditional streamwise riblets. The existence of the large-scale drag reducing vortices which were observed by Tay *et al.* (2017) was confirmed from numerical solutions of a replica flow scenario for periodic dimples (Tay *et al.* 2017). Note that the economically efficient detached-eddy simulation approach was sufficient to resolve the large-scale turbulent vortices, but unable to reproduce the small drag reduction benefit to a sufficient accuracy. Figure 2.5 provides an example of a dimple geometry with rounding applied at the edges to limit flow separation, as applied in the numerical investigations of Tay *et al.* (2017).

As an alternative to dimples; recent studies have identified the potential of simple, three-dimensional textures which can recreate the effects of spanwise waves without the required energy input. Ghebali *et al.* (2017) explored the drag reducing potential of misaligned grooves, rotated approximately 70° to the flow direction. They achieved an overall drag reduction of 0.7%. Although minimal, compared to an active surface, this result was achieved without energy input and with a surface wavelength more than 45 times that of an optimised riblet spacing. Over the lee-side, Ghebali *et al.*

Figure 2.5: *Rounded dimple geometry, flow domain and mesh in the numerical investigation of Tay* et al. *(2017). After Tay* et al. *(2017).*

(2017) observed a reduction in the strength of the near-wall velocity streaks below the logarithmic region. Meanwhile the production and dissipation of turbulent kinetic energy was amplified within the logarithmic region.

2.4 Practical Drag Reduction in Laminar Flow

2.4.1 Drag Reduction Potential

The absence of the key turbulent mechanisms related to flow control would seem to remove the benefits of oblique grooves and shallow dimples from laminar flow applications. Figure 2.6 displays a typical configuration of two-dimensional sinusoidal grooves, applied to one or more walls of an infinite channel and orientated obliquely to the flow direction. As observed in the case of riblets, two-dimensional sinusoidal grooves commonly produce a negative impact on the flow resistance for single phase laminar flow (Mohammadi & Floryan 2012) and single phase turbulent flow (Henn & Sykes 1999).

These losses occur due to the resultant pressure drag which exceeds the otherwise beneficial reduction in viscous drag. However, the need for practical drag reducing geometries in laminar flow, drives ongoing research to explore the drag reducing potential of such surfaces through extensive optimisation studies of profile shape, surface orientation and length scale.

(a) *Textured lower wall coupled with a smooth upper wall*

(b) *Textures applied to both walls of the channel*

Figure 2.6: *Typical application of sinusoidal wavy surfaces in an infinite channel with profiles misaligned with the flow direction. After Ghebali* et al. *(2017).*

The spectrally accurate numerical code of Mohammadi & Floryan (2012) has formed the basis for one of the most comprehensive investigations into the drag reducing potential of practical grooves in laminar flow. They first considered a series of shallow, sinusoidal grooves in laminar Poisuille flow (Mohammadi & Floryan 2013b). These grooves covered a wide range of Reynolds numbers, wavelengths and depths, in ad-

dition to varying orientation to the flow. Mohammadi & Floryan (2013b) observed that orientating the grooves to be parallel to the streamwise direction minimised the streamwise flow resistance. This lies in contrast to the behaviour in turbulent flow, in which Ghebali *et al.* (2017) identified both a minimum drag, and an overall drag reduction, corresponding to an oblique angle of orientation.

For streamwise sinusoidal grooves, the results of Mohammadi & Floryan (2013b) suggested that a drag reduction may be achieved if the groove spacing is greater than π times the channel half-height. However, the effect was marginal, with an overall drag reduction of only 0.025%. Mohammadi & Floryan (2013b) aimed to improve the performance of these simple sinusoidal grooves by optimising the geometric profile. They first explored a systematic optimisation of a universal geometric profile (Mohammadi & Floryan 2013a), and then a parametric study of simple, non-sinusoidal shapes (Mohammadi & Floryan 2015). The response was improved by amplifying the groove depth to length scales to be of equal magnitude to the channel half-height. Under these constraints, the optimisation process revealed possible improvements by up to 50% of the drag reduction. Whilst a successful confirmation of drag reduction potential, the large length scales of these surface would in practise require a significant redesign of the overall flow domain application. Raayai-Ardakani & McKinley (2017) reported simular success for streamwise sinusoidal grooves in a spatially developing laminar boundary layer and claimed a drag reduction of up to 20% as the depth ratio approached $k_g/\lambda_g \to 1$. However, this may be the result of the unaccounted modification to the mean flow field, and the shift in the boundary layer origin.

2.4.2 Impact of Flow Separation

In turbulent flows, previous investigations have indicated a correlation between the pressure drag in a separated free-shear region, as in the case of shallow dimples, and the drag reduction or drag increase (Tay *et al.* 2015). In addition, flow separation is a key parameter in classifying and predicting the behaviour of naturally occurring bedforms. However, in the interests of drag reduction for laminar flows, the significance of flow separation remains unclear. The critical limits of flow separation rely on a combination of groove depth, profile shape and the contribution of flow inertia.

Mohammadi & Floryan (2013b) observed full attachment for a depth to wavelength ratio of 0.08 at any laminar Reynolds number in Poisuille flow. However, for deep grooves with a depth to wavelength ratio of 0.39, even stokes flow was sufficient to produce a free-shear region which spanned the majority of the trough. In addition, the shear stress distribution did not change between the two extremes of the laminar regime. Niavarani & Priezjev (2009) concluded a critical depth to wavelength ratio of 0.126 for the onset of flow separation in highly viscous stokes flow.

Saha *et al.* (2015) produced numerical solutions of spanwise sinusoidal grooves around the circumference of a pipe. Both laminar flow and turbulent flow cases displayed identical trends between increasing groove depth and the growth in the significance of the pressure drag. In addition, whilst the overall flow resistance in the laminar regime grew with rising Reynolds number, the influence of the Reynolds number fell with increasing groove depth. However, they observed no behavioural correlation between the weighted contribution of the pressure interaction drag and flow separation. Grooves with a maximum surface angle of 30° could produce a pressure drag which exceeds the viscous drag, whilst maintaining shear layer attachment in the trough.

2.4.3 Impact of Spanwise Motions

Finally, the development and optimisation of passive flow control method needs to consider the potential to induce large-scale motions even in laminar flow fields. Tay *et al.* (2014) carried out flow visualisation investigations of laminar boundary layer flow over a pair of dimples with depths ranging from 5% to 50% of the dimple diameter, which in turn ranged from 10% to 50% of the boundary layer width. For a flow strength within the region of $Re_\theta \approx 105$, a depth to diameter ratio of 10% was sufficient to induce a stable pair of counter-rotating vortices within the dimples, similar to the hairpin vortex observed for turbulence transition. This behaviour was further identified by the steady-state numerical simulations of Xu *et al.* (2016), where a single vortex existed at low Re_h for a dimple depth equal to 25% of the diameter, then split into two co-rotating vortices when this rose to 50%. However, their investigation also indicated that reducing the channel height would produce a similar response to that achieved by varying the dimple depth.

Moradi *et al.* (2017) investigated the potential of transverse sinusoidal grooves to enhance mixing through the creation of streamwise vortices, with a focus on small amplitudes, with a depth to wavelength ratio of ≤ 0.05, for minimal flow resistance. Although successful, the Reynolds numbers required were extreme, many limits lying far within the turbulent regime, and only rising as the depth to wavelength ratio fell. The experimental investigations of Xu *et al.* (2018) demonstrated the capability of a herringbone riblet pattern to produce similar streamwise vortices through the alternating upwash and downwash. Further developments have expanded the spectral code of Mohammadi & Floryan (2012) to deal with three-dimensional surface geometries (Sakib *et al.* 2017), with the persistent limitation on periodic flow conditions.

2.5 Naturally Occurring Bedforms

2.5.1 Overview

The naturally occurring shark skin and lotus leaf patterns have produced positive results in flow control. However, these surfaces exist at small length scales in the flow, thus limiting their application potential and cost effectiveness. As such, ongoing investigations (as discussed in Section 2.4) have explored the potential of producing drag reducing surfaces at larger length scales through exploratory optimisation studies involving profiles of simple geometric shapes. Such efforts have demonstrated either a negative or marginal success, with suggestions of improvement through geometric optimisation (Mohammadi & Floryan 2013b; Tay *et al.* 2015; Ghebali *et al.* 2017). Designs for riblets and superhydrophobic surfaces have demonstrated the benefits of anchoring flow control optimisation on naturally forming patterns and textures.

Consider the view of a sand beach during the receding tide. The once flat sand surface reveals an array of various two-dimensional and three-dimensional periodic forms, as displayed in Figure 2.7. In a more general sense, a surface of loose particles may reform into a pattern of periodic structures when submerged in a moving body of fluid. Such patterns can emerge from an oscillating flow created by waves travelling over a free surface, steady flow created by a current, or a combination of the two (Fredsoe *et al.* 1999).

The classification of bedforms relies on the streamwise pattern wavelength, where dunes have a wavelength on the order of $1m$ or higher, whilst ripples have a wavelength on the order of $1cm$ (Charru *et al.* 2013). For both dunes and ripples, the crest to trough depth is typically one order of magnitude lower than the wavelength. The

(a) (b)

Figure 2.7: *Bedform patterns formed by a) tidal flow over a sand beach and b) steady, shallow flow over coarse sediment.*

early experiments of Bagnold (1946) defined two primary types of transverse ripples; rolling grain ripples, for which sand grains move in contact with the surface, and vortex ripples, for which the flow separates from the crest and carries sediment particles within it. Meanwhile, the wavelength of a dune is influenced by the flow depth. Due to the large length scales of dunes, in relation to the bulk flow, dunes are characterised by a cycle of shear layer detachment from the crest, followed by shear layer growth along the lee-side (Best 2005). The separated free-shear layer moves into the bulk flow away from the surface.

2.5.2   Theoretical Predictions

Early stability analysis, though limited to purely viscous flows, demonstrated a process by which two dimensional ripples, as shown in Figure 2.8a, could grow from a small perturbation in an otherwise flat sand bed (Blondeaux 1990). However, predicting the equilibrium amplitude of developing ripples requires consideration of the non-linear effects. Vittori & Blondeaux (1990) achieved this through an additional assumption that the ripple amplitude is smaller than the near-wall boundary layer, and that the flow does not separate from the crests, thus keeping the non-linear effects weak. As demonstrated by the steady flow model of Charru & Hinch (2006), the inertial effects

of the decelerating flow along the lee-side, which destabilises the flat sand bed, are counteracted by erosion of sand grains around the point of maximum shear stress. In this way, a migrating bedform at equilibrium maintains a balance between the removal of sand grains from the stoss-side and the deposition of sand grains on the lee-side. Despite the observed correlations between grain diameter and ripple size, the validity of discounting the influence of flow depth remains controversial, with alternative theoretical models from Colombini & Stocchino (2011) and Bartholdy *et al.* (2015) implying its relevance for steady current flows.

(a) *Two-dimensional ripples* **(b)** *Asymmetric ripples*

(c) *Sinusoidal ripples* **(d)** *Brick-pattern ripples*
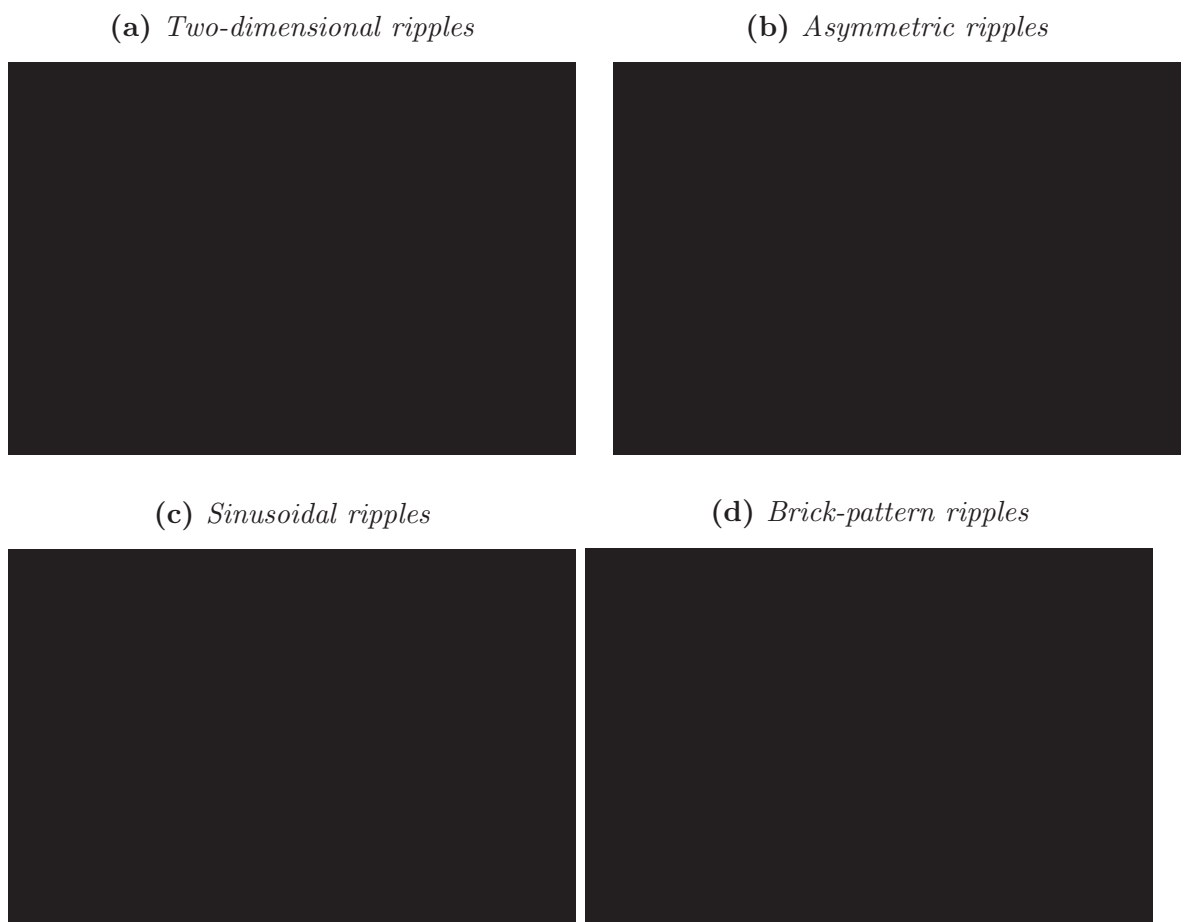
Figure 2.8: *Sand ripples of varying topology as predicted by the application of linear and non-linear stability analysis. After Roos & Blondeaux (2001) (a,b) and Vittori & Blondeaux (1992) (c,d).*

Blondeaux *et al.* (2015) considered the impact of combining an oscillating flow field with a steady current flow. Whereas a purely oscillating flow produced a symmetrical ripple profile, the steady current flow produced an asymmetrical profile, with a single

curved lee-side, and a dual curved stoss-side. At low Reynolds numbers, the asymmetry index, which is defined as the ratio of the streamwise length of the stoss-side divided by that of the lee-side, always exceeded one. The asymmetry index falls with increasing Reynolds number. The trends indicate that as the strength of the steady current velocity grows, relative to the strength of the oscillating flow, the asymmetry index tends towards an asymptotic limit. Whilst these theoretical models provide a direct approach to obtaining exact solutions, and they correlate with the highly scattered experimental observations, the models cannot be expanded to the analysis of vortex ripple behaviour. As stated by Blondeaux *et al.* (2015), a further understanding would require iterative numerical solutions.

Non-linear stability models which consider the simultaneous growth of both two-dimensional and three-dimensional perturbations in an initially flat sediment bed, have predicted the emergence of three-dimensional ripple patterns (Figure 2.8b, Figure 2.8c and Figure 2.8d) in both oscillating (Vittori & Blondeaux 1992) and steady (Langlois & Valance 2005) viscous flows. The sinusoidal ripples in Figure 2.8c form when the strength of the three-dimensional instability exceeds that of the two-dimensional instability. Devauchelle *et al.* (2010b) concluded that, unlike sand ripples, such three-dimensional structures can only form in a highly viscous flow if they lie below a free surface. Their model theorised that these bedforms may form in the absence of a free surface when inertial effects become significant ($Re_h >> 1$).

2.5.3 Experimental Investigations

Table 2.2 provides an overview of key experimental investigations concerning bedform geometries in unidirectional, laminar and turbulent flows. In each case, the range of the flow Reynolds number is provided, along with the geometric pattern of the bedforms.

The range of streamwise wavelength is scaled by either the flow depth or pipe radius, depending on the application.

Table 2.2: Overview of key experimental investigations of bedform geometries in steady, unidirectional laminar and turbulent flows.

Publication	Scenario	Regime	Re_h	Pattern	λ_x/h
Coleman & Eling (2000)	open channel	steady laminar	$155 \sim 440$	2D ripples	$1 \sim 2$
Devauchelle *et al.* (2010a)	open channel	steady laminar	$10 \sim 420$	3D rhomboid	$1 \sim 50$
Rauen *et al.* (2008)	open channel	steady turbulent	10×10^3 $\sim 49 \times 10^3$	2D ripples	0.033 ~ 0.6
Edelin *et al.* (2015)	pipe	steady turbulent	< 7500	2D ripples	13.5 ~ 11.8
Venditti (2007)	open channel	steady turbulent	73×10^3	2D and 3D dunes	3

Though initially believed to be a product of turbulent motions, practical experimental investigations have confirmed the formation of both two-dimensional and three-dimensional bedform patterns in purely laminar flows. The experiments of Coleman & Eling (2000) displayed clear evidence of small-scale two-dimensional bedforms forming within an open channel containing a laminar flow with a unidirectional current. As in turbulent flow, the wavelength was dependant on the size of the sand grains, and was not influenced by the properties of the flow. Devauchelle *et al.* (2010a) observed the growth of three-dimensional rhomboid patterns in laminar channel flow. The angle between the rhomboid edges and the spanwise axis displayed significant scatter in the lower laminar regime but settled towards an asymptomatic limit of $\approx 20°$ for flows of $Re_h > 200$. At this point, the bedform patterns possessed a closer resemblance to a streamwise riblet than to transverse ripples. Similarly, the wavelength of the pattern

showed no clear correlation with Re_h towards the lower end of the laminar regime, but grew to around $10 \sim 40$ times the flow depth by $Re_h > 240$.

The traditional narrative considers the wavelength of a subaqueous ripple to be determined primarily by the grain size, whilst being independent of the flow depth. Rauen *et al.* (2008) used acoustic imaging to investigate the transition of the initial bedforms (referred to as 'wavelets') into vortex ripples on a bed of fine sand grains. The wavelength of the wavelets remained fixed with respect to depth, and was dependant on the grain size. Once the wavelength height exceeded a critical value, the wavelets transitioned into vortex ripples, for which the wavelength varied with grain diameter, such that the ratio between the bedform depth and wavelength remained constant. Edelin *et al.* (2015) studied the development of bedforms in a flow of suspended particles. Two-dimensional ripples were observed to form in laminar flow; however, since the Reynolds number lay close to the limit of transitional flow, the presence of the sand ripples induced laminar-turbulence transition. The density of sediment in the flow had no impact on the bedform geometry, with the wavelength consistently lying between 200 and 300 times the grain diameter. The ripples displayed a depth to wavelength ratio on the order of 0.05, yet in each case the bedforms transitioned into vortex ripples.

Finally, consider the significance of the more complex geometric features of natural bedform patterns with three-dimensional variation. The experimental analysis of Venditti (2007) compared rigid dunes of two-dimensional profiles, sinusoidal three-dimensional variation, and irregular three-dimensional variation, as displayed in Figure 2.9, in a unidirectional turbulent channel flow. Although the three-dimensional dunes suppressed the strength of flow separation compared to the two-dimensional dune, the overall flow resistance was greater. However, when the three-dimensional variation followed an irregular pattern, the flow resistance dropped to 20% below the

two-dimensional dune due to a reduction in turbulence intensity in the region of the dune.

Figure 2.9: *Rigid sand dune geometries which were implemented in the experimental investigations of Venditti (2007). After Venditti (2007).*

2.5.4 Numerical Investigations

Table 2.3 provides an overview of key numerical investigations concerning bedform geometries in unidirectional turbulent flows. In each case, the range of the flow Reynolds number is provided, along with the geometric pattern of the bedforms. The range of streamwise wavelength is scaled by either the flow depth or channel half-height, depending on the application.

Although bedforms can form in the absence of turbulence motions, the near-wall turbulent structures may influence the initial destabilisation of the flow. Furthermore, the bedform structure can exert a strong influence on the distribution of turbulence throughout the shear layer. Khosronejad & Sotiropoulos (2015) applied finite volume analysis to produce detailed flow fields over a moveable flat bed in an open turbulent channel flow. Initially, the near-wall streaks would sweep towards the bed and initiate a series of perturbations which collectively resembled a cross-hatch pattern. These perturbations would grow into transverse ripples which enhanced the formation of spanwise vortices. Finally, the ripples would develop a spanwise geometric variation, for which the detached spanwise vortices would form into horse shoe structures as they

Table 2.3: Overview of key numerical investigations of bedform geometries in steady, unidirectional turbulent flows.

Publication	Scenario	Re_h	Pattern	λ_x/h
Bhaganagar & Hsu (2009)	closed channel	$180 \sim 400$	2D and 3D ripples	2
Grigoriadis *et al.* (2009)	open channel	$17,500 \sim 93,000$	2D dunes	4.2
Lefebvre *et al.* (2016)	open channel	8200	2D bedforms	3.07
Omidyeganeh & Piomelli (2013a),Omidyeganeh & Piomelli (2013b)	open channel	$18,900$	3D dunes	5.71
Khosronejad & Sotiropoulos (2015)	open channel	$75,900$	developing bedforms	$0.26 \sim 3.29$
Omidyeganeh & Piomelli (2011)	open channel	$18,900$	2D dunes	5.71
Kidanemariam & Uhlmann (2017)	open channel	3011	2D ripples	$3.9 \sim 11.8$

detached from the crest.

The numerical analysis of Kidanemariam & Uhlmann (2017) coupled a domain of turbulent channel flow over a sediment bed with resolved particle motion. Bedform growth required a domain to possess a streamwise length greater than 100 times the sand grain diameter. The bedform would only exceed this critical value when the domain was unable to accommodate an integer number of bedforms of this critical wavelength.

From a numerical perspective, accounting for particle motion significantly impacts the computational workload, and can be crippling when applied in turbulence resolving simulations. In the moveable bed simulations of Khosronejad & Sotiropoulos (2015), the average bedform velocity was recorded as being two orders of magnitude lower than

the bulk flow velocity, lending strong support to the assumption of a rigid bedform surface as an accurate simplification of moveable bedform problems. Omidyeganeh & Piomelli (2011) carried out turbulence resolving simulations for a rigid two-dimensional dune in turbulent flow though an open channel. In this case, the groove depth was equal to $\approx 30\%$ of the flow depth, which, for a fully developed shear layer, placed the lee-side length on a greater order of magnitude than the viscous inner region of the boundary layer. Hence, the flow separates as it leaves the crests which forms a spanwise vortex over the lee-side with enhanced energy production and dissipation, whilst a separated shear layer transports turbulent energy away from the surface and into the flow. As the spanwise rollers pass through the accelerating flow over the stoss-side they deform and stretch into structures similar to horse shoe vortices (Grigoriadis *et al.* 2009), as observed in the moveable bed simulations of Khosronejad & Sotiropoulos (2015).

Further analysis explored the influence of incorporating a spanwise variation by extruding this two-dimensional profile sinusoidal profile in the spanwise direction (Omidyeganeh & Piomelli 2013a; Omidyeganeh & Piomelli 2013b). The depth of the spanwise sinusoidal profile varied between 5% and 20% of the streamwise wavelength. Three-dimensional variation had a minimal impact on the pressure drag, whilst simultaneously suppressing the shear layer separation. The redirection of fluid towards the lobe gave rise to a secondary flow of streamwise oriented vortices above the lobes and the saddles. When the wavelength of the spanwise profile was smaller than the flow depth, these spanwise vortices failed to materialise within the confined space. The subsequent redistribution of flow produced stronger eddy separation from the lobe and the saddle. Bhaganagar & Hsu (2009) investigated ripples with a smaller length scale, and simple sinusoidal profiles, for which the streamwise wavelength was equal to 50% of the flow depth (channel half-height). For a friction Reynolds number of $Re_\tau = 180$, the three-

dimensionality of the surface had a negligible impact on the flow resistance, despite producing a non-negligible reduction in the spanwise and wall-normal velocity fluctuations near the ripple and away from the wall. By $Re_\tau = 400$ the three-dimensional ripples reduced the flow rate by as much as 17.5% compared to the two-dimensional case.

Lefebvre *et al.* (2016) investigated the flow resistance over rigid ripple profiles with a lee-side and stoss-side comprised of multiple straight line segments, including the common lee-side slip face. The ripples were shallow with a depth to wavelength ratio of 0.036, lying far below the predicted limit of 0.1 for the onset of vortex ripple growth (Blondeaux *et al.* 2015). In all cases produced by Lefebvre *et al.* (2016), flow separation occurred when the slip face angle exceeded 18°. Note that this angle lies close to the maximum lee-side angle of a sinusoidal wave which lies on the supposed limit of vortex ripple formation (17.4° at a depth to wavelength ratio of 0.1). The flow resistance depended primarily on the angle of the lee-side slip face. Increasing this angle from 6° to 24° raised the flow resistance by up to 73%. Applying a sinusoidal profile to an initially flat stoss-side raised the flow resistance by up to 5%. There was a strong linear relationship between the flow resistance and the mean turbulent kinetic energy; the latter increasing with the former. Reducing the length of the slip face, by installing a shallow 4° segment connecting the crest and the slip face, reduced the flow resistance by 15.8%.

2.6 Computational Limitations and Complexities

2.6.1 Spatially Developing Flows

External flow applications (relevant to an aircraft wing, car body etc.) provide more complex physical scenarios. Unlike in channel flow, the flow develops spatially and exists over length scales that far exceed the small length scales of textures such as riblets. The assumption of streamwise periodicity is typically considered to be valid for fully developed channel flow where the channel is of sufficient length and width. As per its fundamental definition, the flow field of a spatially developing boundary layer will vary along the streamwise direction and the assumption of periodicity is rendered invalid. A steady-state, fully laminar flow field is predictable and easily implemented. A turbulence flow field is random and chaotic, and hence, cannot be exactly reproduced through theoretical calculation or approximation. This problem is negated in periodic channel flow, as the developing instabilities of transitional flows accumulate through successive passes through the periodic domain, until a naturally occurring state of fully developed turbulence is reached. The influence of the upstream laminar and transitional stages are accounted for without directly modelling or approximation. As with channel flow, the simplest case of a spatially developing turbulent flow contains a smooth planar wall within a rectangular domain of fixed dimensions. Whilst simulations can differ in the usual parameters of numerical design, the physical flow scenario can vary depending on the behaviour of the upstream flow.

In a turbulent boundary layer, the coherent structures which lie in the near-wall region scale against a viscous length derived from the shear stress at the wall ($l_v = \nu/u_\tau$), whilst the structures away from the wall scale with the shear layer thickness. Computational advancements continually increase the feasibility of direct numerical simulation

for internal flows with an assumed streamwise periodicity, and its associated reduction in computational cost. Computing a time-dependant flow field under direct numerical simulation can produce a crippling cost, when combined with the large streamwise length of spatially developing flow, as the difference between the two scales grows with Reynolds number. Furthermore, high accuracy, computationally efficient spectral codes, which pioneered fundamental advancements for internal flows (Moser *et al.* 1999) and passive flow control (Chu & Karniadakis 1993; Garcia-Mayoral & Jimenez 2011b), typically require a periodic flow domain to function. One solution for a zero-pressure gradient boundary layer, shown in Figure 2.10, adapts the periodic domain of a spectral code to a spatially developing turbulent boundary layer by artificially forcing the flow into the steady-state laminar regime in a region leading up to the outlet. This approach has produced highly detailed solutions of continuous laminar-turbulent boundary layer development up to Reynolds numbers as large as $Re_\theta \approx 8300$ (Schlatter *et al.* 2009; Schlatter *et al.* 2010; Eitel-Amor *et al.* 2014; Matai & Durbin 2019).
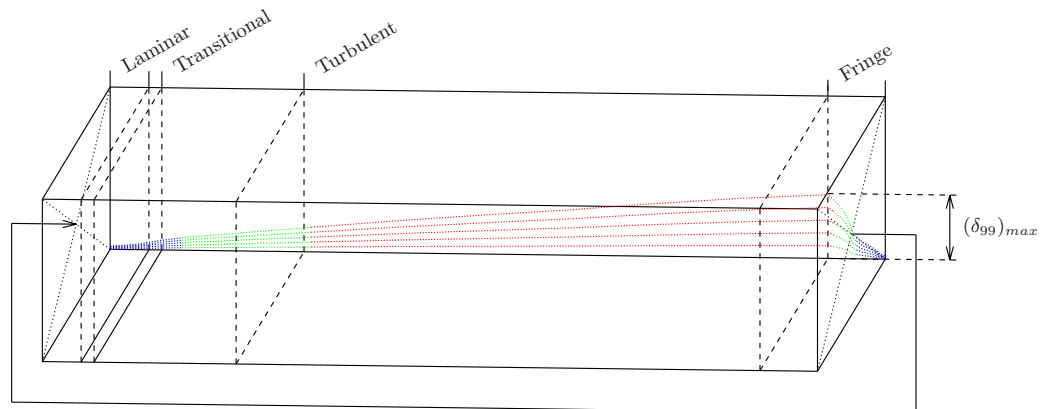
Figure 2.10: *Illustrations of a flow domain for modelling a spatially developing boundary layer flow using resolved laminar-turbulent transition and artificial streamwise periodicity.*

Recent studies have already revealed the potential of a local application of flow control methods to produce beneficial effects far downstream in spatially developing flows. Stroh *et al.* (2016) investigated the downstream effects induced by common

drag reduction techniques applied in a local region of a spatially developing boundary layer. Methods of uniform blowing and a near-wall damping force produced a local drag reduction of more than 50% during application. As the flow moved downstream, the influence on the drag fell, with the damping force producing a local drag increase. However, within the region of $Re_\theta < 2500$ the total flow resistance showed a reduction of more than 5%, due to the strong initial response to the control mechanism. They further suggested that the lingering influence on the local flow resistance may be expressed by a simple streamwise translation of the effective boundary layer origin. These observations illustrate that expanding the application of flow control mechanisms in turbulent channel flow to spatially developing flows, is a crucial next step in the development of drag reduction techniques.

2.6.2 Resolving Transition

The most accurate and realistic numerical solution for spatially developing turbulent boundary layers comes from resolving the laminar-turbulent transition process in a single continuous domain. For this process, a steady-state laminar boundary layer is destabilised to prematurely induce transition. The means of destabilising the boundary layer is referred to as the 'trip'. The trip may consist of a physical obstruction at the wall, referred to as a 'geometric trip', or a perturbation applied directly to the velocity field, referred to as a 'numerical trip'. Table 2.4 provides details of previously published results and investigations concerning the modelling of laminar-turbulent transition within spatially developing boundary layers over a smooth wall. The table specifies the classification of turbulence resolution (i.e. the turbulence model), the method of inducing laminar-turbulence transition, the range of momentum Reynolds number involved (when provided by the source), and the total cell count N_T, rounded to three

Table 2.4: Overview of key numerical studies of laminar-turbulent transition in spatially developing boundary layers over smooth surfaces.

Publication	Model	Transition	$Re_{\theta(min)}$ (min/max)	N_T $(\times 10^6)$
Durcos *et al.* (1996)	LES	Numerical tripping	386,N/A	0.416
Schlatter *et al.* (2009)	DNS	Numerical tripping	180, 2500	237
Wu & Moin (2009)	DNS	Free stream turbulence	80, 940	210
Schlatter *et al.* (2010)	LES	Numerical tripping	180, 4300	606
Schlatter & Orlu (2012)	DNS	Numerical Tripping	180, 2500	237
Eitel-Amor *et al.* (2014)	LES	Numerical Tripping	180, 8300	817

significant figures.

In 1996, a probing investigation by Durcos *et al.* (1996) produced a highly coarse solution of laminar-turbulent transition (large-eddy simulation). Cell dimensions equated to approximately 5% of the near-wall velocity streak length, and 35% of their width. The smallest cell height was approximately equal to the width of the viscous sub-slayer. Although the wall shear stress varied from experimental results by -25%, and similar errors were found for the spanwise and wall-normal components of turbulence, these efforts indicated that transitional behaviour could be reproduced at low spatial resolutions.

Sayadi & Moin (2012) used the combined periodic domain and numerical tripping techniques shown in Figure 2.10 to test the performance of various sub-grid scale models in large-eddy simulation for accurately replicating the unresolved, sub-grid stress in laminar-turbulence transition. Their results showed that even when the turbulence

model can successfully minimise dissipation in the laminar regime, the excessive dissipation in the transitional regime and the fully turbulent regime reduces the unresolved stress, and therefore, underpredicts the wall shear stress. Bae *et al.* (2018) suggested that one potential cause lies in an inability to correctly capture the destabilisation and break-up of the streamwise velocity streaks close to the wall. This will be of particular importance during transition, where the turbulent mechanisms will be more unpredictable than in fully developed flow, and will depend heavily on the type of transition.

By resolving the complex, time-dependant turbulent motions at all length scales to a high spatial and temporal accuracy with direct numerical simulation (DNS), the downstream effect from the tripping conditions can be singled out to optimise the configuration of the destabilisation mechanism (Schlatter & Orlu 2012) with minimal influence from numerical uncertainty. To reduce the computational cost to more practical levels, length scales associated with smaller turbulent eddies can be filtered out of the flow field, thereby reducing the required spatial and temporal resolution of the simulation. In this case, behaviour associated with the downstream tripping effects will be blurred with errors deriving from a combination of the resolved spatial resolution and the method used to approximate the energy transfer to the unresolved length scales.

As computational power grew, the laminar-turbulent transition region could be solved with fully resolved turbulence, as seen for periodic channel flow. In one such case, Wu & Moin (2009) simulated the destabilisation of a laminar boundary layer, using artificial free stream turbulence, and resolved the resulting turbulence development up to $Re_\theta \approx 1000$. Despite the high resolution, and the indication of a fully turbulent boundary layer beyond $Re_\theta \approx 750$, the solution overpredicted the shear stress, partic-

ularly in the outer region, with errors reaching as high as 10%. Through a comparison of published numerical solutions (up to the year 2010), Schlatter & Orlu (2010) identified repeated discrepancies in integral parameters, the wall shear stress and near-wall velocity fluctuations in supposedly identical flows. Further investigation would confirm that the means of destabilising the initially laminar flow can impact the boundary layer structure long after laminar-turbulent transition is complete.

The potential impacts of the trip were observed during the early experimental studies of Erm & Joubert (1991). Their investigations destabilised a spatially developing laminar boundary layer using three different geometric trips of varying shapes to investigate the influence of the trip on the downstream turbulent flow. In this case, with the trip lying in the range of $Re_\theta \approx 210$ and $Re_\theta \approx 320$, they concluded an upper limit of $Re_\theta \approx 3000$ beyond which the influence of the trip becomes negligible. The more recent experiments of Marusic *et al.* (2015) preformed a similar investigation at higher Reynolds numbers with more extreme tripping conditions. Where Erm & Joubert (1991) compared geometric trips of similar heights, the heights of the trips in Marusic *et al.* (2015) varied by one order of magnitude. For this excessive size difference they observed a persistent discrepancy in the flow fields as far as $Re_\theta \approx 2 \times 10^5$, though this was confined to outer layer of the boundary layer. From a detailed DNS analysis of trip configurations, Schlatter & Orlu (2012) concluded that the boundary layer must be tripped within $Re_\theta < 300$ to minimise the required development length. Even under optimal conditions, the flow did not reach self-similarity throughout the boundary layer until $Re_\theta = 2000$. By this point, the outer length scale is more than 600 times greater than the inner length scale.

2.6.3   Turbulent Inflow Generation

Due to the high computational costs of modelling laminar-turbulent transition, current efforts into industrial scale applications or detailed exploratory studies, typically require compromises to improve economic efficiency. These compromises commonly take the form of utilising models with a lower order of accuracy, or operating within a finite domain that is confined to the fully turbulent region (Boomsma & Sotiropoulos 2015; Lee & Sung 2011; Lee *et al.* 2012; Arolla & Durbin 2015).

The streamwise length of the computational domain can be limited by discarding the laminar and transitional regimes and replacing the inflow condition with a fully developed turbulent boundary layer (Wu 2017). Whilst it is possible apply an approximation of a time-dependant turbulent flow field (Mare *et al.* 2006), such an approach would fail to replicate the fundamental three-dimensional coherent structures. Alternatively, time-dependant inflow conditions can be generated by artificially growing a turbulent boundary layer within an axillary periodic domain using the 'recycling/rescaling' technique of Lund *et al.* (1998). In this method, the flow velocity field at the cyclic outlet is rescaled by calculating the boundary layer thickness and comparing this value to the desired thickness specified by the user. The rescaled velocity field, with a reduced boundary layer thickness, is fed into the inlet. The auxiliary domain does not need to be a separate domain. It can exist within the main flow domain, as shown in Figure 2.11, by linking the inflow boundary condition at the inlet to the flow field of a plane which is located shortly upstream of the inlet. Table 2.5 provides details of previous investigations which model spatially developing turbulent flow over a smooth surface, whilst applying a fully turbulent boundary layer at the inflow.

By utilising the recycling/rescaling technique Lee & Sung (2011) computed a fully
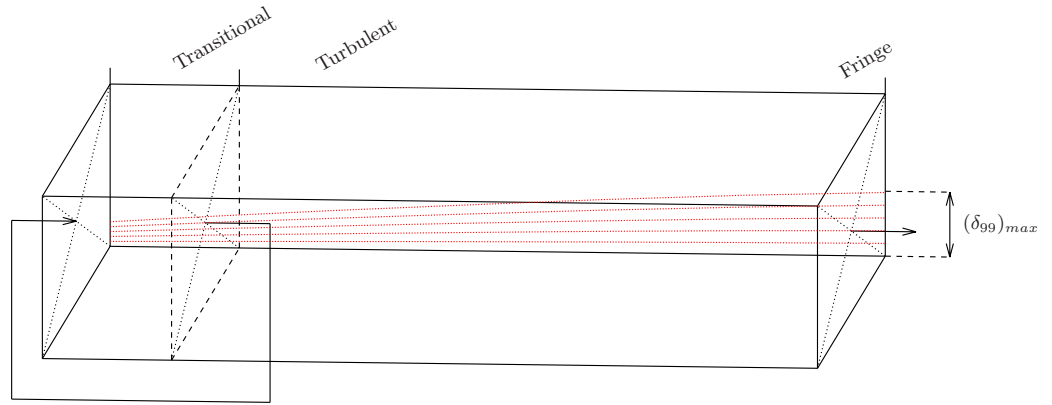
Figure 2.11: *Illustrations of flow domain for modelling a spatially developing boundary layer flow using recycling/rescaling over the initial portion of the domain.*

Table 2.5: Overview of key numerical studies for spatially developing turbulent boundary layers over smooth surfaces, with turbulent inflow conditions.

Publication	Model	Transition	$Re_{\theta(min)}$ (min/max)	N_T $(\times 10^6)$
Inoue & Pullin (2011)	LES	Recycling/ rescaling	$10^3, 10^{12}$	12.6
Lee & Sung (2011)	DNS	Recycling/ rescaling	570, 2560	315
Sayadi & Moin (2012)	LES	Numerical trip	N/A,N/A	1.2
Arolla & Durbin (2015)	LES	Recycling/ rescaling	1520,N/A	2.87
Mukha & Liefvendahl (2017)	LES	Varying inflow methods	835,2400	20.4

resolved turbulent boundary layer up to $Re_\theta \approx 2500$, with the domain beginning at a fully turbulent inflow of $Re_\theta \approx 1410$. However, to minimise the influence of artificial periodicity, the domain for the recycling/rescaling inflow generation spanned a range of $Re_\theta \approx 570$ to $Re_\theta \approx 1600$ and contained an equal number of cells as the fully turbulent domain. Furthermore, the inflow location of $Re_\theta \approx 1600$ lay below the critical limits of $Re_\theta \approx 2000$ (Schlatter & Orlu 2012), prior to which a practical flow cannot be assumed to be independent of its upstream tripping conditions.

If the structure of the boundary layer and its turbulent behaviour is known to a sufficient accuracy, then the resolution of turbulence may be restricted to the outer region of the boundary layer, whilst flow behaviour in the inner region is approximated through a suitable numerical model (Bose & Park 2018). Such approximations, combined with the recycling/rescaling techniques for inflow generation, can reduce the computational workload sufficiently enough to allow solutions reaching up to $Re_\theta \approx 1 \times 10^{12}$ (Inoue & Pullin 2011). However, such methods rely on the flow maintaining ideal patterns of behaviour which are known in advance. In the pursuit of beneficial flow control through near-wall turbulence manipulation, the structure of the inner region cannot be predicted to any reasonable accuracy. The economic benefits come at a cost of an overprediction of the turbulent kinetic energy in the near-wall region, and an underprediction of the wall shear stress.

The investigations of Arolla & Durbin (2015) and Mukha & Liefvendahl (2017) have aimed to apply similar methodologies for boundary layer modelling to the open source computational code OpenFOAM. Compared with spectral methods, OpenFOAM possesses greater adaptability at the cost of lower orders of numerical accuracy. Arolla (2016) applied a recycling/rescaling method to a single domain for a turbulent boundary layer of $Re_\theta > 1500$. Only the streamwise component of the velocity was rescaled based on the momentum thickness, and a single factor of scaling was applied to all regions of the boundary layer. In reality, the inner region scales with the viscous length; however, as this approach is applied with a low resolution large-eddy simulation, the direct influence of this discrepancy is difficult to assess. Mukha & Liefvendahl (2017) investigated the applicability of supplying the flow field from a periodic turbulent channel flow as the inflow to a spatially developing turbulent boundary layer. This approach was compared to the standard recycling/rescaling approach for an inflow of $Re_\theta = 835$,

and a reference case of fully resolved laminar-turbulent transition, beginning at a uniform laminar inflow of $Re_\theta = 0$. The periodic channel inflow method had no significant effect on reducing the required development length compared to the recycling/rescaling inflow method. Both inflow methods required the boundary layer to develop beyond $Re_\theta \approx 1400$ before the downstream influence of non-physical behaviour in the inflow was sufficiently reduced.

2.6.4 Textured Surface Modelling

The introduction of non-planar surfaces into the computational domain places additional burdens on the model, which only raises the computational workload. The mechanisms of drag reduction over streamwise riblets takes place at the smallest scales in the flow, and are often only observable with full DNS resolution. The thin crests of optimised riblets usually require further resolution, which only serves to increase the detail of the surface, whilst having a negligible benefit to the detail of the turbulent flow itself. Table 2.6 outlines key numerical simulations of spatially developing turbulent boundary layers over streamwise riblets and transverse bars. The maximum and minimum Reynolds numbers are stated, when provided by the source.

Table 2.6: Overview of key numerical studies for spatially developing turbulent boundary layers over surfaces of various textured geometries.

Publication	Model	Transition	$Re_{\theta(min)}$ (min,max)	N_T $(\times 10^6)$	Surface
Boomsma & Sotiropoulos (2015)	LES	Recycling/ rescaling	1200, N/A	124	scalloped riblets
Lee *et al.* (2012) Ahn *et al.* (2013)	DNS	Recycling/ rescaling	300,1100	150	shallow bars/cubes
Nadeem *et al.* (2015)	DNS	Recycling/ rescaling	300,1400	150	shallow bars/cubes

Boomsma & Sotiropoulos (2015) investigated scalloped riblets in a spatially developing turbulent boundary layer. Each riblet required more than 30 near-wall cells to cover its spanwise width, which varied between 10 and 27 viscous units. The resultant spanwise width of the cells was around 10% of those typically used in smooth surface DNS (Schlatter & Orlu 2012). To compensate, they supplied an inflow condition from two auxiliary domains. The first domain grew a boundary layer to $Re_\theta = 860$ using the recycling/rescaling technique. The second domain allowed this flow to grow naturally, prior to the main simulation, in order to minimise the required development length in the main simulation. Despite this approach, only 50% of the riblets could be resolved at the full spatial resolution.

Lee *et al.* (2012), Ahn *et al.* (2013) and Nadeem *et al.* (2015) conducted numerical parametric studies for a spatially developing turbulent boundary layer over 20 different configurations of two-dimensional and three-dimensional cubic structures. The flow domain and a typical geometry are displayed in Figure 2.12. They constrained their domain to a range of $Re_\theta < 1400$ and discarded the laminar and transitional regions to enforce a fully turbulent inflow of $Re_\theta = 300$. The inflow was developed from the recycling/rescaling method. Whilst these methods made this parametric study economically viable, they produced results of limited practical application, since a natural boundary layer would have remained dependant on the upstream tripping conditions within $Re_\theta < 2000$ (Schlatter & Orlu 2012).

Figure 2.12: *Flow domain for a spatially developing boundary layer over transverse bars. After Nadeem* et al. *(2015)*

2.7 Summary

Whilst both laminar and turbulent flows experience shear drag, the additional Reynolds stresses in the latter contribute to a significant drag increase. Passive drag reducing surfaces aim to reduce the Reynolds stresses by suppressing turbulent behaviour close to the wall. In the case of riblets, a large portion of the wetted area is shielded from turbulence structures which remain pinned above the crest. Riblets aim to reduce the Reynolds stresses in the groove by transferring it towards the bulk flow. However, such riblets operate among the smallest length scales of the flow, in addition to requiring sharp, narrow crests to achieve a significant drag reduction. These features hamper their manufacturability and durability in practical application.

Introducing additional streamwise vorticity into the flow can suppress the movement of turbulent energy towards the small length scales motions, thus reducing turbulent stress in the near-wall region. In turbulent channel flows, surfaces of shallow dimples have been shown to recreate this effect, whilst requiring no energy input or complex mechanical systems in their application, unlike active methods. Meanwhile, macroscale surface textures of simple geometric shapes have shown limited benefits for drag reduction in laminar flows. However, such investigations involving either laminar to turbulent flow have provided modest evidence which identifies the potential

of further improvement through optimisation of the geometric profile. The present review has considered potential approaches for such an optimisation through investigation of the unique, asymmetric bedforms which frequently form from flat sediment beds submerged in both laminar and turbulent flows. As in the case of simplified periodic groove, these bedforms typically result in a significant viscous drag reduction, but an overall drag increase due to the inevitable pressure drag. However, increasing the complexity of the representative bedform geometries under investigation, in a way which more closely matched their natural shapes, has revealed key geometric features which can improve the drag performance of the surface. Based on these observations, the present investigation builds upon a hypothesis that asymmetric profiles of naturally occurring bedforms represent a natural optimisation of a symmetrical geometrical profile in relation to drag reduction applications.

In spatially developing flows, localised drag reducing effects have been observed to translate downstream. In practical applications this would reduce the area required for application of a given method (surface texturing in the present investigation), in order to provide a beneficial drag reduction over a large area in external flow. This is opposed to internal flow, which requires a continuous application along the full length of the channel to maintain a local drag reducing effect. A reduced area of application would increase the viability of economically manufacturing practical surface textures with an increased geometric complexity. However, numerical analysis of spatially developing flows is hindered by the increasing complexity of the flow domain and the required computational resources, when compared to periodic channel flows. Methodologies for overcoming these difficulties, i.e. generating turbulent inflows and reducing spatial resolution, introduce additional uncertainties which could impact the accuracy and validity of the numerical solution.

CHAPTER 3

Modelling of Laminar and Turbulent Flows: OpenFOAM

3.1 Introduction

This Chapter presents the numerical methodologies which will be applied in the present analysis. The numerical models for the present analysis are built, solved and post processed using the code OpenFOAM (version 4.0.1). OpenFOAM, "Open Source Field Operation And Manipulation", is an open source, finite volume solver for computational fluid problems. First proposed as an object-oriented open source code in 1998 (Weller *et al.* 1998), which is based on the extensive work of Hrvoje (1996), the OpenFOAM toolbox has grown to encompass a vast selection of numerical solvers, numerical schemes and pre-processing, and post-processing, utilities.

For the present analysis, OpenFOAM was been selected due its wide range of fea-

tures, utilities and numerical tools, combined with its high parallelisation, whilst not requiring additional licensing costs for large-scale computation which are commonly required for commercial codes. Furthermore, the present analysis aimed to make use of OpenFOAM's inbuilt open source, automated meshing software, known as snappyHexMesh. A key feature of snappyHexMesh is the ability to construct irregular, unstructured cells along a surface, whilst preserving regular Cartesian cells throughout the bulk of a domain. This tool was highly beneficial for the parametric studies in Chapter 5 and Chapter 6 which contain a wide variation of irregular sand ripple profiles, which hold a fairly inform bulk flow away from the wall.

3.2   The Finite Volume Method

OpenFOAM solves flow dynamics systems through the finite volume method. In reality, a fluid consists of particles which are far smaller than the scale of interest moving through a space. The fundamental aspect of continuum mechanics is an assumption that the empty space and solid particles can be accurately represented by a solid block of fluid, known as a control volume. Figure 3.1 displays a cubic control volume with six faces in a Cartesian coordinate system.
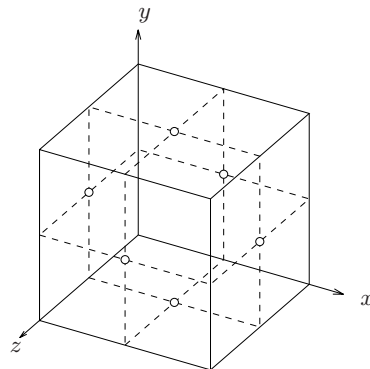
Figure 3.1: *Diagram of a cubic cell containing a continuous body of fluid.*

Equation (3.1) displays the momentum conservation equations (Navier-Stokes equations) for an incompressible, Newtonian fluid. Equation (3.2) displays the requirements for the conservation of mass. The streamwise, wall-normal and spanwise components are denoted by u, v and w respectively.

$$\frac{\partial u}{\partial t} + u\frac{\partial u}{\partial x} + v\frac{\partial u}{\partial y} + w\frac{\partial u}{\partial z} = -\frac{1}{\rho}\frac{\partial p}{\partial x} + \nu(\frac{\partial^2 u}{\partial x^2} + \frac{\partial^2 u}{\partial y^2} + \frac{\partial^2 u}{\partial z^2}),$$
$$\frac{\partial v}{\partial t} + u\frac{\partial v}{\partial x} + v\frac{\partial v}{\partial y} + w\frac{\partial v}{\partial z} = -\frac{1}{\rho}\frac{\partial p}{\partial y} + \nu(\frac{\partial^2 v}{\partial x^2} + \frac{\partial^2 v}{\partial y^2} + \frac{\partial^2 v}{\partial z^2}), \qquad (3.1)$$
$$\frac{\partial w}{\partial t} + u\frac{\partial w}{\partial x} + v\frac{\partial w}{\partial y} + w\frac{\partial w}{\partial z} = -\frac{1}{\rho}\frac{\partial p}{\partial z} + \nu(\frac{\partial^2 w}{\partial x^2} + \frac{\partial^2 w}{\partial y^2} + \frac{\partial^2 w}{\partial z^2}),$$

$$\frac{\partial u}{\partial x} + \frac{\partial v}{\partial y} + \frac{\partial w}{\partial z} = 0, \qquad (3.2)$$

The fluid domain is decomposed into a number of control volumes (cells). Open-FOAM is designed to work with polyhedron cells of arbitrary shape and size, and with an arbitrary number of faces. Figure 3.2 displays examples of the layout and notations for two types of polyhedron meshes. In part (b) the mesh resolution has been reduced through local refinement, resulting in sharp transitions in cell volume between adjacent regions. In part (a) the cells within the region of a boundary have been cut and reshaped to conform to the boundary line. A single cell (labelled P) has a volume $V^{[P]}$, and pressure and velocity values located at the point P. It is surrounded by an arbitrary number of cells N_E. It is connected to the surrounding cells (superscript $[E] = 1, 2, 3...N_E$), by an equal number of faces (superscript $[e] = 1, 2, 3...N_E$). A line of vector $\vec{d}^{[PE]}$ and length $|\vec{d}^{[PE]}|$ connects point P and point E and intersects the connecting face at point e. The vector $\vec{S}^{[e]}$ lies perpendicular to the face e.

For a given flow property ϕ, each cell contains a single value located at the cell centre; a setup referred to as a colocated grid. This in contrast to the staggered grid arrangement, where pressure values are stored at the cell centres and velocity values
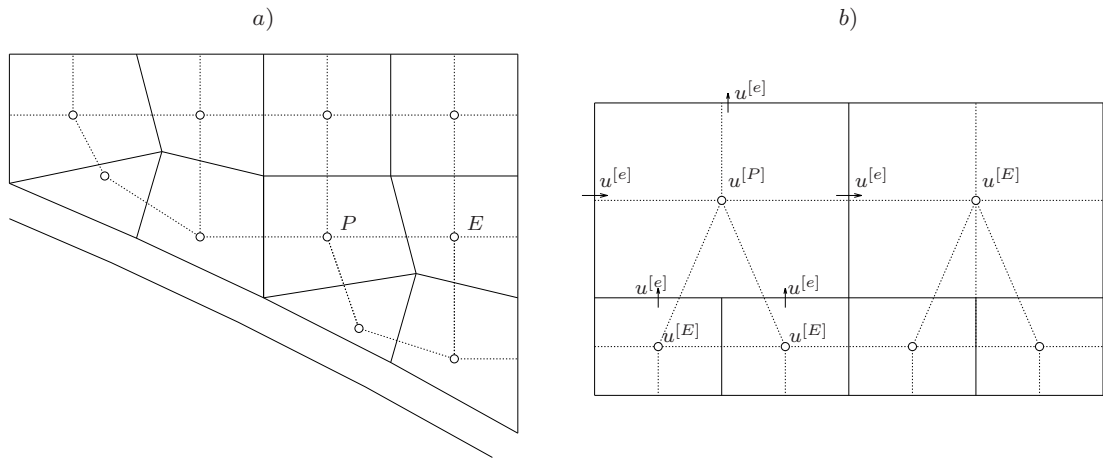
Figure 3.2: *Discretisation of a domain by hexahedral cell volumes using a) cut-cell boundaries in the near-wall region and b) local cell refinement.*

are stored at the cell faces. By comparison, the colocated grid is more versatile as it provides greater stability in cells which deviate from simple, ideal geometries (i.e. non-orthogonal) (Peric *et al.* 1988). However, the velocity and pressure values in the cell of a colocated grid are decoupled, such that the pressure value would not influence the pressure gradient at that point, which could produce localised, non-physical pressure fluctuations in the solution. The solution of Rhie & Chow (1983) expresses the mass-flux through the cell faces from an interpolation between cell centres, to replicate the layout of a staggered grid during the solution of the momentum-conservation equations.

3.3 Structure of OpenFOAM

Each simulation in OpenFOAM consists of a case directory containing three main subdirectories; '< time >', 'constant' and 'system'. All commands for operating Open-FOAM must be run at the case directory level. Figure 3.3 displays the layout and contents of a case directory for OpenFOAM. The expanse of files included in Figure 3.3 encompasses all inputs which are utilised in the present analysis.
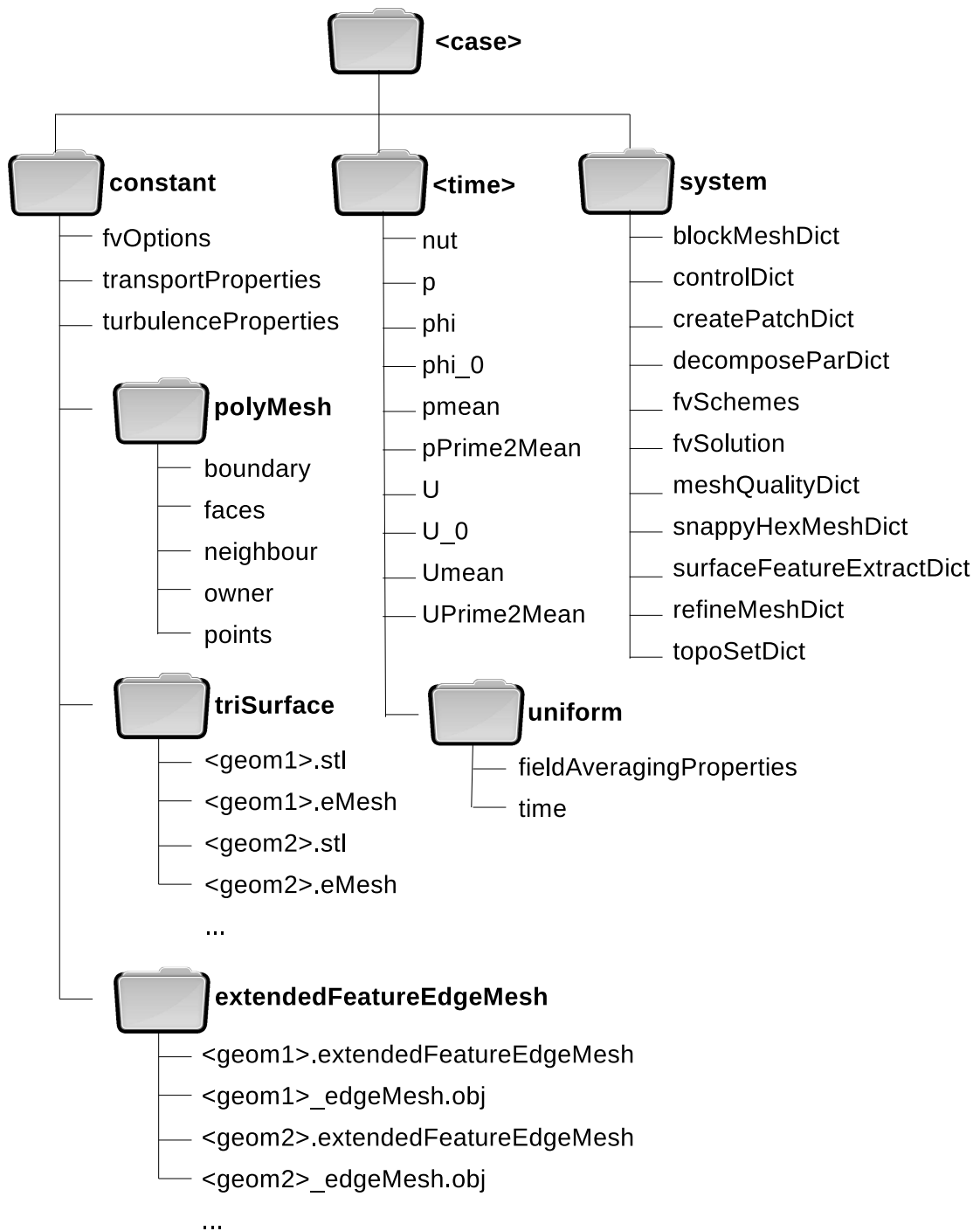
Figure 3.3: *Structure of an OpenFOAM case directory in the present analysis.*

The 'system' directory defines the routines, functions and schemes for mesh generation, pre-processing, solution generation and post-processing. The 'fvSchemes' and 'fvSolution' files (discussed in Section 3.5 and Section 3.6 respectively) define the numerical methodology for solving the governing equations in the flow domain. The 'controlDict' file contains the settings for the physical time and time step for the solver,

and the settings for outputting the results. The remaining files in the 'system' directory govern the creation and manipulation of the computational domain, mesh and boundary conditions. The contents and applications of these files are discussed further in Section 3.4.

The computational mesh is stored in the 'constant' directory, along with additional surface geometries, and directories specifying the physical properties of the flow. The 'polyMesh' subdirectory defines the cells of the computational mesh through lists of vertices ('points'), faces, and a pair of cells adjoining those faces (i.e. 'owner' and 'neighbour'). The boundary file assigns external faces in the mesh to groups which can be used to assign boundary conditions to the external surfaces of the flow domain. When additional surface geometries are required, typically for use in mesh generation/manipulation and post-processing, the files which define the surface geometries are stored in the 'triSurface' subdirectory. The surface geometries may possess key geometric geometric features (such as sharp angles) which must be captured during the mesh generation process. Information concerning such features is stored in the 'extendedFeatureEdgeMesh' subdirectory, and also as .eMesh files in the 'triSurface' subdirectory. The 'transportProperties' file contains the information of the physical properties of the flow, such as the kinematic viscosity of the fluid. The 'fvOptions' specifies the parameters of any source terms to be implemented into the momentum-conservation equations. The 'turbulenceProperties' file specifies the turbulence model to be used, and specifies the parameters which are required for its implementation. The turbulent models and parameters which are used in the present analysis are discussed further in Section 3.7.

Each time directory contains information about the boundary conditions and flow fields at a given point in physical time. Initial conditions are supplied by a uniform field

value for the internal mesh and constraints for the patches on the external boundary. Subsequent time directories are written by the numerical solver, and they specify the solved flow field at a given time step as a list of field values specifying the value in each cell. The time directory displayed in Figure 3.3 displays additional flow fields for the time-averaged values ('mean') and root mean square values ('Prime2Mean') for a given property as calculated from the solved flow field, as discussed in Section 3.8.

3.4 Mesh Generation

3.4.1 snappyHexMesh

The snappyHexMesh utility is an automatic mesh generation/manipulation programme within OpenFOAM. Starting with a coarse cartesian mesh, snappyHexMesh builds a refined mesh which conforms to a new boundary of a surface of an arbitrary geometry. The term 'split-hexahedral' refers to cells which contain more than six faces, but which are produced by the splitting and morphing of hexahedral cells, as displayed in Figure 3.2. The snappyHexMesh procedure is demonstrated throughout this section using the jaggedBoundary.stl geometry supplied in the following location in OpenFOAM.

- *openfoam4/tutorials/foamyQuadMesh/jaggedBoundary/constant/triSurface /jaggedBoundary.stl*

The final mesh produced by the snappyHexMesh utility is displayed in Figure 3.4.

The snappyHexMesh utility requires an initial Cartesian mesh, files describing the surface geometry and, in some cases, information of the key geometric features of the supplied surface geometries.
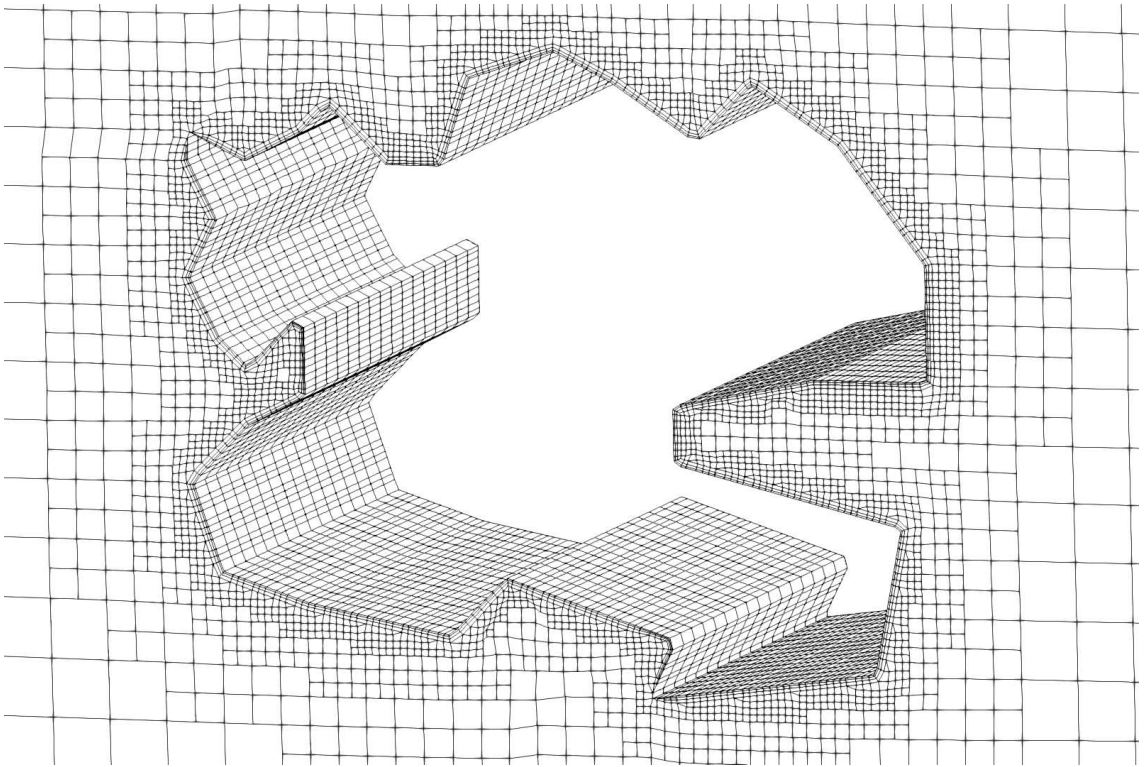
Figure 3.4: *A split-hexahedral mesh which was generated for the jaggedBoundary.stl surface geometry through utilisation of the snappyHexMesh utility.*

Preparation stages:

- **Initial Mesh** Creation of an initial computational domain with coarse Cartesian mesh.

- **Feature Extraction** Extract the geometric features from one or more surface profiles.

The first stage constructs a simple Cartesian mesh as defined in the 'blockMeshDict' dictionary. The initial Cartesian mesh should ideally contain cells with an aspect ratio of 1 in the region of the inserted surface geometries. However, this aspect ratio can be increased beyond 1 when required, as demonstrated in Chapter 6 and Chapter 7. In the second stage the features of each surface are extracted from the .stl geometry files in the 'triSurface' subdirectory. Figure 3.5 displays the features edges of the jagged boundary geometry. The extracted features include all open edges, and closed edges at which the two faces meet at an angle smaller than 175° (or a user-specified value).
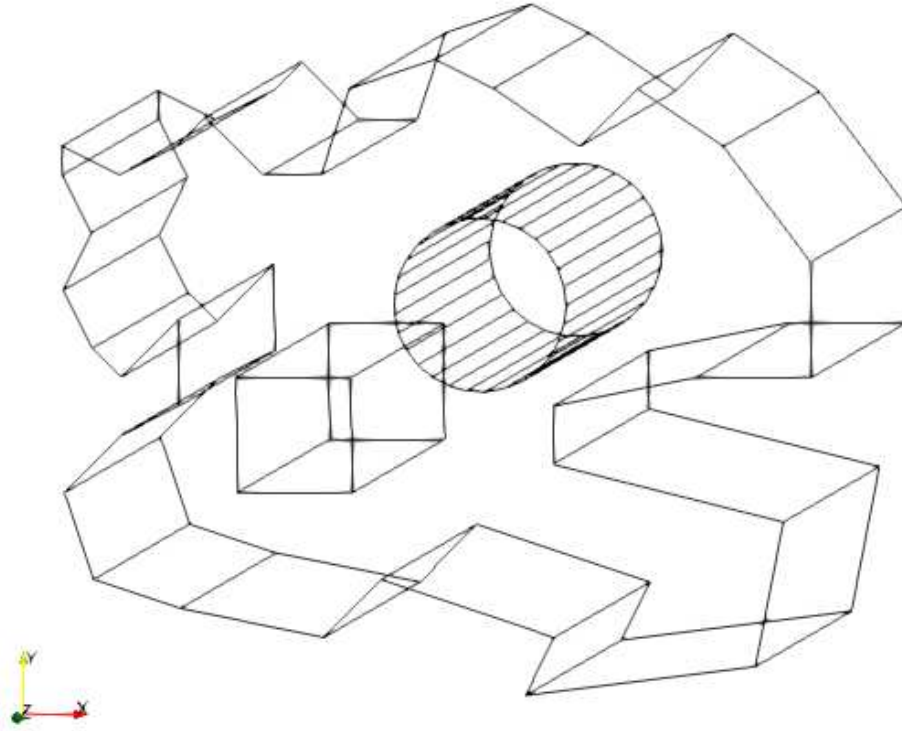
Figure 3.5: *Feature lines extracted by performing 'surfaceFeatures' on the jagged-Boundary.stl file.*

The snappyHexMesh utility operates in three key stages: castellation, snapping and layer addition. The outputs of each stage is demonstrated in Figure 3.6, using the jaggedBoundary.stl geometry as a test case.

- **Castellation** Insert of the surface profile into their corresponding location within the computational domain.

- **Snapping** Morph the cells in the near-wall region such that the mesh conforms to surface profiles.

- **Layers** Morph the mesh away from the surface profile and insert layers between the surface and the mesh.

The castellation stage performs local refinement of cells based upon the surface

(a) *Refinement and castellation*
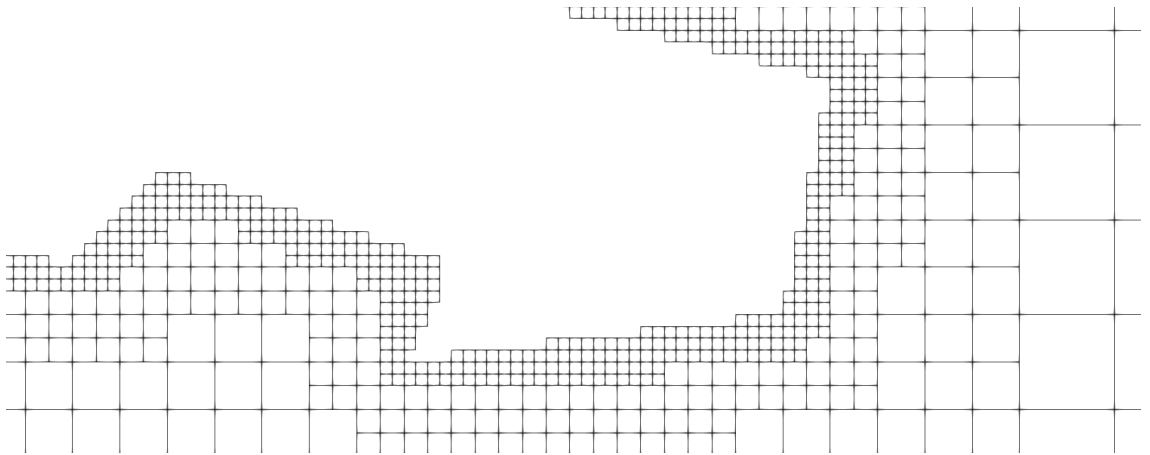
(b) *Surface snapping*
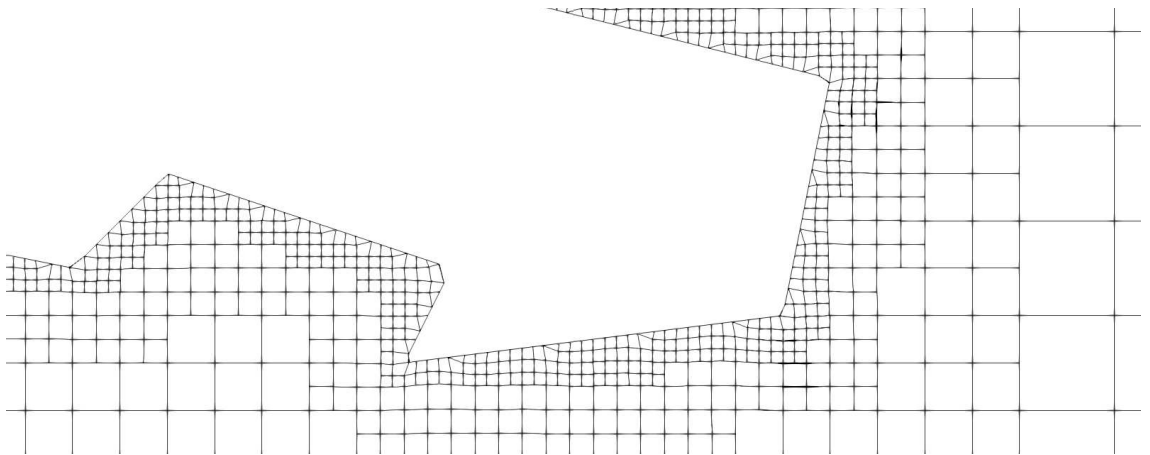
(c) *Layer addition*
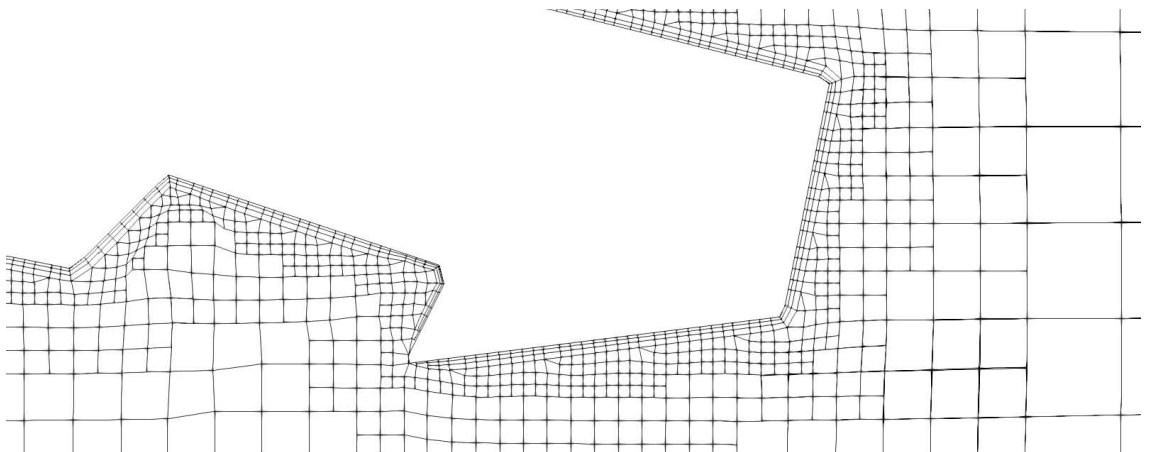
Figure 3.6: *Three stages of the snappyHexMesh utility in building a mesh around a boundary consisting of a two-dimensional irregular geometry.*

features and user-specified refinement regions. The location and the level of refinement can be performed to an exact value, or automatically, depending on the local curvature of the surface and the angle between surface features. The surface geometry forms a new boundary of the flow domain. All cells for which 50% (or a user-specified value) of their volumes lies beyond the new domain boundary are removed from the domain. In the example in Figure 3.6a a uniform level of refinement has been specified over the whole jagged boundary surface, with a minimum of 3 cells between refinement levels.

The snapping stage morphs the edges of the refined and castellated mesh to align with the original surface geometries. Each vertex on the new boundary of the domain is displaced towards the nearest surface face. Then the internal mesh is smoothed to accommodate this new displacement. The displacement of each vertex is constrained by a user-supplied value of tolerance, which defines the maximum distance that a vertex can move, given as a fraction of the length of the edges of the local cells. The newly distorted mesh is scaled back until it complies with the user-specified requirements of mesh quality as discussed in Section 3.4.2. The method of snapping can be either implicit or explicit. Implicit snapping identifies features from the surface geometries which were supplied from the castellation stage. Explicit snapping gives priority to the feature lines which where extracted using the 'surfaceFeatureDict' dictionary prior to the castellation stage, as displayed in Figure 3.5. Explicit snapping typically provides greater surface conformity at the cost of additional pre-processing time, as the user can ensure the acknowledgement and prioritizing of specific features, such as sharp corners, which would otherwise be missed by the automated Implicit snapping procedure. The mesh in Figure 3.6b has been snapped using explicit features snapping, based on the features displayed in Figure 3.5, in order to capture the sharp angles which are present at numerous locations on the jagged boundary surface.

Figure 3.6c displays the output from the final stage, in which additional layers are inserted into the mesh at the solid surface. In this case, three layers have been added along the jagged boundary, with the cell widths being specified as a fraction of the near-wall cell size. Alternatively, the cell widths can be specified in absolute units, in order to produce a uniform layer thickness on surfaces which have cells at varying levels of octree refinement. Note that in Figure 3.6c the snappyHexMesh utility has collapsed the layers around the sharpest corner in order to avoid the creation of poor quality cells. Unlike the castellation stage and the snapping stage, the addition of layers is optional in many applications. However, since the added layers grow perpendicular to the boundary, the addition of layers can provide two crucial benefits. Firstly, layers can significantly reduce the near-wall cell size without producing a large increase in streamwise and spanwise resolution. Hence, increasing spatial resolution through the addition of layers will provide greater efficiency than additional octree refinement. This is particularly important when resolving near-wall flows, where the wall-normal velocity gradient is typically several orders of magnitude greater than the streamwise and spanwise velocity gradients. Secondly, layers will improve the alignment of the near-wall cells with the flow direction. In the present analysis, the application of layers is utilised in Chapter 7, where a series of layers is applied to a spatially developing turbulent boundary layer over a two-dimensional surface.

3.4.2 Mesh Quality

The geometry of each cell greatly influences both the stability of the solver and the accuracy of the final solution. A cells quality derives from several criteria which describe the spatial relation between cell centres and their connecting faces. In OpenFOAM, the 'meshQualityDict' dictionary contains the user-defined settings for the desired limits

of mesh quality. The criteria in the 'meshQualityDict' are used by the snappyHexMesh utility as a guide when morphing the mesh during the snapping and layer stages. Two of the most important criteria; non-orthogonality and skewness, are defined below, and the vectors which are required for these definitions are illustrated in Figure 3.7.

(a) *Skewed face* **(b)** *Non-orthogonal cell*
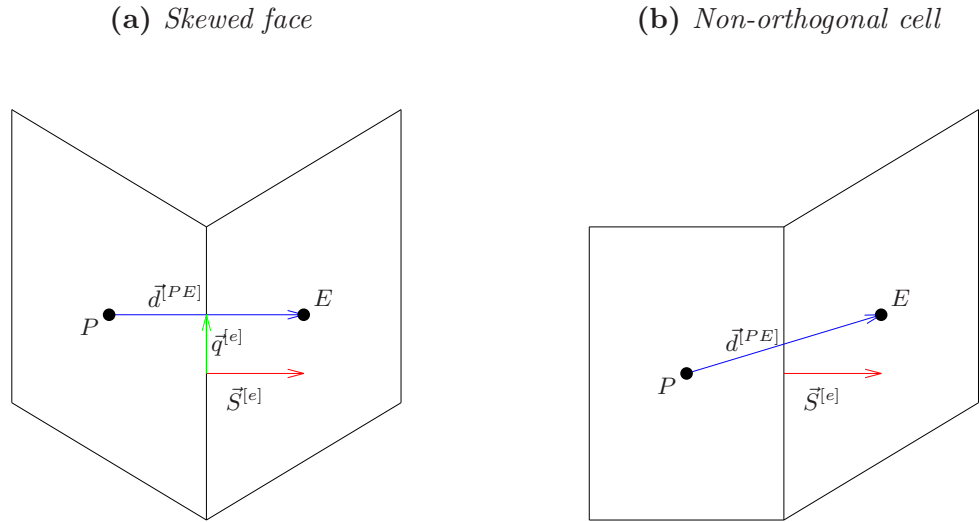
Figure 3.7: *Diagrams illustrating the cell geometric properties which are used to calculate face skewness and cell non-orthogonality.*

Face skewness (Equation 3.3) represents the distance by which the point of intersection between the cell-to-cell vector and the face deviates from the centre of area for that face. The skewness takes the form of a ratio between the magnitude of the offset vector and the magnitude of the cell-to-cell vector.

$$\text{face skewness} = \frac{|\vec{q}^{[e]}|}{|\vec{d}^{[PE]}|}, \tag{3.3}$$

Cell non-orthogonality (Equation 3.4) refers to the angle at which a vector connecting two cell centres intersects the connecting face. Non-orthogonality references a vector which is normal to the face, such that if the cell-to-cell vector is perpendicular to the face, the non-orthogonality is 0°. Similarly, a cell-to-cell vector which is parallel

to the face, though realistically impossible, would indicate a non-orthogonality of 90°.

$$\text{non-orthogonality} = \frac{\vec{S}^{[e]} \cdot \vec{d}^{[PE]}}{|\vec{S}^{[e]}||\vec{d}^{[PE]}|}, \tag{3.4}$$

Noriega *et al.* (2018a) identified that the primary error associated with mesh non-orthogonality occurred when non-orthogonal cells lie on the boundary faces with fixed flow properties or fixed gradient values. They concluded that periodic boundary conditions could maintain schemes of second order accuracy, even in the presence of non-orthogonality along the boundary. Similarly, non-orthogonality had a minimal effect far into the flow.

3.4.3 Parallel Processing

For a discretised flow domain, the computational workload can be shared by multiple processors in order to decrease the workload on a single processor and reduce CPU time. The 'decomposePar' command in OpenFOAM divides a single flow domain into multiple segments, whereby each segment can be assigned to an individual processor for computation. The method for splitting the domain is defined in the 'decomposeParDict' file. Figure 3.8 displays a simple, two-dimensional domain which has been divided into four segments with divisions along the streamwise axis and wall-normal axis. Along the boundary of each segment a new boundary condition is formed which links adjoining boundaries from two processors (processor boundaries).

The decomposition of the domain can be performed in various ways, depending on the geometric complexity of the computational domain. The 'simple' method and the 'hierarchical' method decomposes the domain into a number of segments along each directional vector. The 'hierarchical' method allows user to determine the order in which
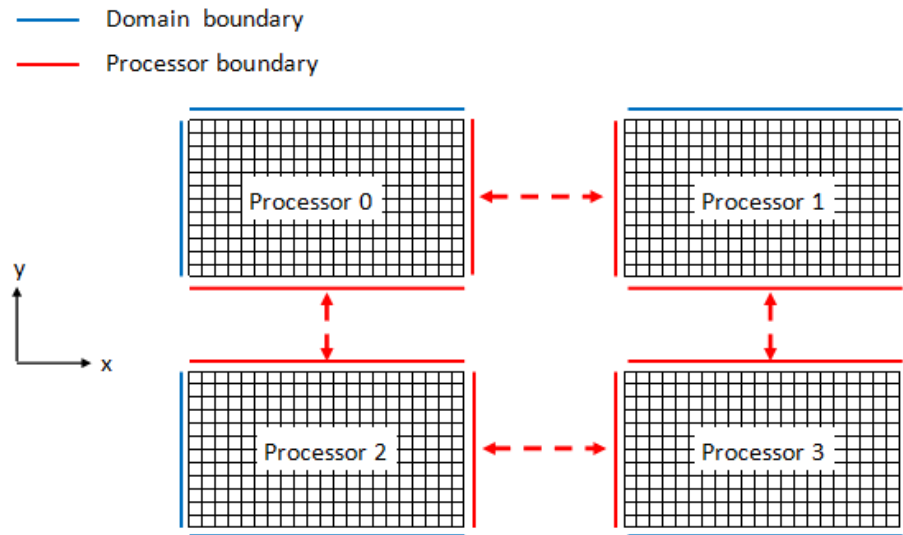
Figure 3.8: *Illustration of a discretised computational domain decomposed across 4 processors.*

to prioritise each directional vector. The 'scotch' method calculates the area of domain decomposition automatically whilst prioritising the minimisation of processor boundaries. In the present analysis, all domain discretisation applies the 'simple' method, due to the general uniformity of cell distribution throughout the computational domain in each case.

Haddadi *et al.* (2017) recommends a distribution of no fewer than 100,000 cells per processor. They suggested that efficiency could be maintained with no fewer than 50,000 cells per processor, for more basic solvers. Further reduction of the number of cells per processor, below these limits, is expected to provide a limited benefit in reducing the CPU time for the simulation. Further improvements in the efficiency of the simulation can be achieved by reducing the bandwidth of the coefficient matrix. The 'renumberMesh' command can reduce the bandwidth by rearranging the placement of each cell in the matrix to cluster the coefficients around the diagonal of the matrix.

Finally, parallel processing can be used to reduce pre-processing time by applying the snappyHexMesh utility to a discretised domain across multiple processors. During the castellation stage, the mesh is accessed after each refinement step. If the refinement

created an uneven distribution of cells between processors, the mesh is redistributed to bring the processors into balance before continuing with further mesh refinement. The 'reconstructParMesh' command can then combine the discretised domain from each segment back into a single domain. Similarly the 'reconstructPar' command combines the segmented flow fields back into a single field for the combined domain.

3.5 Numerical Schemes: fvSchemes

The transport equation for an incompressible fluid is displayed in Equation (3.5), where $\vec{u}$ denotes the velocity vector. The term B_ϕ contains all of the relevant source terms, including the contribution of the pressure gradient in the case of the momentum transport (i.e. $\phi = u_i$), where $u_i = u, v, w$ denotes the velocity component along the x-, y- and z-axis respectively.

$$\frac{\partial \phi}{\partial t} + \bigtriangledown \cdot (\vec{u}\phi) = B_\phi + \nu \bigtriangledown^2 \phi, \tag{3.5}$$

The standardized approach of discretisation in OpenFOAM is through the Gaussian Integration Theorem. Gauss's Theorem states that the integration over the control volume equals the sum of the flux through each face. Equation (3.6) displays the integrated momentum equation over a single control volume.

$$\int_{V^{[P]}} \frac{\partial \phi^{[P]}}{\partial t} \quad dV^{[P]} = B_\phi^{[P]} + \int_{V^{[P]}} \bigtriangledown \cdot (\nu \bigtriangledown \phi)^{[P]} \quad dV^{[P]} - \int_{V^{[P]}} \bigtriangledown \cdot (\vec{u}\phi)^{[P]} \quad dV^{[P]} \tag{3.6}$$

Temporal terms = Source terms + Laplacian terms + Convective terms

The 'fvSchemes' file defines the discretisation schemes used to apply Equation (3.6) over the discretised flow domain. In the 'fvSchemes' file different discretisation schemes can be assigned to each flow variable, such that the stability and order of accuracy can

be adjusted for the needs of each individual variable.

3.5.1 Convective Terms: divSchemes

The 'divSchemes' entry defines the discretisation schemes for the convective terms. Applying Gauss integration to the integrated convection term in Equation (3.6), as shown in Equation (3.7), simplifies change in a property from convection through the cell a product of two variables; the kinematic velocity flux $\left(\vec{S}^{[e]} \cdot \vec{u}^{[e]} \right)$, and the value at a given cell face $\phi^{[e]}$.

$$\int_{V^{[P]}} \bigtriangledown \cdot (\vec{u}\phi)^{[e]} \quad dV^{[P]} = \sum_{1}^{e=N_e} \vec{S}^{[e]} \cdot (\vec{u}\phi)^{[e]} = \sum_{1}^{e=N_e} \left(\vec{S}^{[e]} \cdot \vec{u}^{[e]} \right) \phi^{[e]}, \qquad (3.7)$$

The following divergence schemes are either first-order or second-order accurate schemes for determining value at each cell face by extrapolating the values from the cell centres of the corresponding owner and neighbour cells.

Gauss linear

The Gauss linear scheme applies standard central differencing, which determines the value of $\phi^{[e]}$ from a simple linear interpolation along the cell centre vector $\vec{d}^{[P,E]}$, as shown in Equation (3.8).

$$\phi^{[e]} = \left(\frac{|\vec{d}^{[Pe]}|}{|\vec{d}^{[PE]}|} \right) \phi^{[P]} + \left(\frac{|\vec{d}^{[Ee]}|}{|\vec{d}^{[PE]}|} \right) \phi^{[E]}, \qquad (3.8)$$

The Gauss linear scheme is second-order accurate, but remains unbounded from the value of the surrounding flow fields, and hence, cannot guarantee stability.

Gauss upwind

The Gauss upwind scheme (upwind differencing scheme) determines the value of

$\phi^{[e]}$ by directly duplicating the value at the cell centre which lies upstream of the mass flow through the face, as shown in Equation (3.9).

$$\phi^{[e]} = \begin{cases} \phi^{[P]} & \text{for } \left(\vec{S}^{[e]} \cdot \vec{u}^{[e]}\right) \geq 0, \\ \phi^{[E]} & \text{for } \left(\vec{S}^{[e]} \cdot \vec{u}^{[e]}\right) < 0, \end{cases} \tag{3.9}$$

The Gauss upwind scheme is highly stable, as the value of $\phi^{[e]}$ is bounded to the value of either $\phi^{[P]}$ or $\phi^{[E]}$. However, the scheme can only provide first-order accuracy. Therefore, it is typically only useful for converging the early stages of an initially unstable flow field in transient problems, before a more accurate, but less stable, scheme is applied to produce the main solution.

Gauss linearUpwind grad(U)

The Gauss linearUpwind scheme provides a compromise between the first-order accurate Gauss upwind scheme, and the second-order accurate Gauss linear scheme. The resultant hybrid scheme, shown in Equation (3.10), maintains the second-order accuracy of the Gauss linear scheme and, although the Gauss linearUpwind scheme remains unbounded, it possesses an improved stability over the Gauss linear scheme.

$$\phi^{[e]} = \begin{cases} \phi^{[P]} + \vec{x}^{[e]} \cdot \nabla \phi^{[P]} & \text{for } \left(\vec{S}^{[e]} \cdot \vec{u}^{[e]}\right) \geq 0, \\ \phi^{[E]} + \vec{x}^{[e]} \cdot \nabla \phi^{[E]} & \text{for } \left(\vec{S}^{[e]} \cdot \vec{u}^{[e]}\right) < 0, \end{cases} \tag{3.10}$$

Firstly, the gradient at the upwind cell centre is determined from values at the previous time step. The change in a property between the upwind cell centre and the connecting face is determined from the calculated gradient, and the cell-to-face vector $\vec{x}^{[e]}$. This change is applied as a correction to the upwind differencing scheme (Equation 3.9) which reduces dissipation.

3.5.2 Gradient Terms: gradSchemes

The 'gradSchemes' entry defines the discretisation method for the gradient terms. The volume integrated gradient term, and the associated Gaussian integration is shown in Equation (3.11).

$$\int_{V^{[P]}} (\triangledown \phi)^{[P]} \quad dV^{[P]} = \sum_{1}^{e=N_e} \vec{S}^{[e]} \phi^{[e]}, \tag{3.11}$$

Gauss linear

The Gauss linear scheme, shown in Equation (3.12), applies the standard central differencing method, in which the gradient is determined from the variation between two cell centres and the magnitude of a vector connecting those centres.

$$(\triangledown \phi)^{[e]} = \frac{\phi^{[E]} - \phi^{[P]}}{|\vec{d}^{[PE]}|}, \tag{3.12}$$

As for the corresponding divergence scheme in Equation (3.8), the gradient scheme in Equation (3.12) is second-order accurate but remains unbounded. The validation studies of Robertson *et al.* (2015) suggested that all cases where cell non-orthogonality exceeds 50° may require limiting to ensure stability.

Gauss cellMDLimited $< \gamma_1 >$

To improve stability, OpenFOAM provides a variety of gradient schemes which add additional diffusion to the Gauss linear scheme by applying a limiting factor γ_1, as shown in Equation (3.8).

$$(\triangledown \phi)^{[e]} = f(\gamma_1) \frac{\phi^{[E]} - \phi^{[P]}}{|\vec{d}^{[PE]}|}, \tag{3.13}$$

The degree of limiting is determined as a function of the user-defined value of γ_1,

which depends on the type of limiting scheme that is selected. The Gauss cellMDLimited scheme determines the degree of limiting based on the maximum and minimum cell centre values for the surrounding cells, and applies limiting to each Cartesian vector component. However, Robertson *et al.* (2015) warned that if the maximum cell non-orthogonality exceeds 65° the Gauss linear scheme cannot be relied on to maintain stability even when limiting is applied.

3.5.3 Laplacian Terms: laplacianSchemes

The 'laplacianSchemes' entry defines the discretisation schemes for the Laplacian terms in Equation (3.6). Equation (3.14) displays the Laplacian term with Gaussian integration.

$$\int_{V^{[P]}} \nabla \cdot (\nu \nabla \phi)^{[P]} \quad dV^{[P]} = \nu \sum_{1}^{e=N_e} \vec{S}^{[e]} \cdot (\nabla \phi)^{[e]}, \tag{3.14}$$

In OpenFOAM, each Laplacian scheme contains two keywords; the first keyword specifies the type of discretisation that is applied to the gradient of $\nabla \phi$ (i.e. linear for all schemes presented here), whilst the second keyword specifies the treatment of the face normal vector $\vec{S}^{[e]}$.

Gauss linear orthogonal

The Gauss linear orthogonal scheme, shown in Equation (3.15), does not apply any modification to the face normal vector. As such it can only maintain second-order accuracy for purely orthogonal cells, for which $\vec{S}^{[e]}$ is parallel to the vector connecting the adjacent cell centres $\vec{d}^{[PE]}$.

$$\vec{S}^{[e]} \cdot (\nabla \phi)^{[e]} = |\vec{S}^{[e]}| (\nabla \phi)^{[e]}, \tag{3.15}$$

Gauss linear corrected

The Gauss linear corrected scheme, shown in Equation (3.17), accounts for cell non-orthogonality by splitting the face normal vector $\vec{S}^{[e]}$, into two components, as shown in Equation (3.16) and Equation (3.17). The first component $\vec{\chi}_{ortho}^{[e]}$, lies parallel to the line joining the cell centres $\vec{d}^{[PE]}$. The second component $\vec{\chi}_{non}^{[e]}$, lies across the plane of the connecting face (i.e. perpendicular to $\vec{S}^{[e]}$).

$$\vec{S}^{[e]} = \vec{\chi}_{ortho}^{[e]} + \vec{\chi}_{non}^{[e]}, \tag{3.16}$$

$$\vec{S}^{[e]} \cdot (\nabla\phi)^{[e]} = \vec{\chi}_{ortho}^{[e]} \cdot (\nabla\phi)^{[e]} + \vec{\chi}_{non}^{[e]} \cdot (\nabla\phi)^{[e]}, \tag{3.17}$$

The first term on the RHS of Equation (3.17) represents the weight of the orthogonal contribution, whilst the second term represents the weight of the non-orthogonal contribution.

Gauss linear limited corrected $< \gamma_2 >$

As the non-orthogonality of a cell increases, the contribution from the non-orthogonal term also increases. On a mesh which contains highly non-orthogonal cells, the non-orthogonality term may become so excessive that the solution becomes unstable. The non-orthogonal contribution can be limited to preserve the stability of the solution. The Gauss linear limited scheme applies a limiting constant γ_2, to the non-orthogonal term in the corrected scheme (Equation 3.17), as shown in Equation (3.18).

$$\vec{S}^{[e]} \cdot (\nabla\phi)^{[e]} = \vec{\chi}_{ortho}^{[e]} \cdot (\nabla\phi)^{[e]} + \gamma_2 \left(\vec{\chi}_{non}^{[e]} \cdot (\nabla\phi)^{[e]} \right), \tag{3.18}$$

The limiting constant takes a value between $\gamma_2 = 0$ and $\gamma_2 = 1$. Unfortunately, the application of the limiting constant reduces the effective value of $\vec{S}^{[e]}$, and hence,

redefines the decomposition in Equation (3.16), as shown in Equation (3.19).

$$\vec{S}^{[e]} \geq \vec{\chi}_{ortho}^{[e]} + \gamma_2 \vec{\chi}_{non}^{[e]}, \tag{3.19}$$

When $\gamma_2 = 1$, Equation (3.18) returns to the unlimited Gauss corrected formulation in Equation (3.17). Reducing the value of γ_2 increases the stability, whilst reducing accuracy, due to reduction in value of the RHS in Equation (3.19). Hence, the Gauss linear limited corrected scheme is only recommended when the maximum cell non-orthogonality lies between 70° and 80°.

3.5.4   Temporal Terms: ddtSchemes

The 'ddtSchemes' entry defines the discretisation schemes for the temporal terms in Equation (3.6). Temporal discretisation schemes express the spatial integral of the time-derivative in terms of the discrete values at the cell centre from one or more flow fields at different time steps.

$$\int_{V^{[P]}} \frac{\partial \phi^{[P]}}{\partial t} \; dV^{[P]} = \frac{\partial}{\partial t} \int_{V^{[P]}} \phi^{[P]} \; dV^{[P]}, \tag{3.20}$$

Temporal schemes can be sub-divided into two main types: explicit and implicit. Explicit schemes produce only one unknown variable for the cell centre value at the current time step $\phi^{[P,t]}$, and obtain the values of all other variables from the output of previous time steps. Therefore, the solver needs only to perform a single calculation of the scalar transport equation in each cell. Implicit schemes calculate the value of $\phi^{[P,t]}$ from the unknown values in the flow field from the current time step. Hence, the solver must perform multiple iterations to obtain a converged value of $\phi^{[P,t]}$.

Euler

OpenFOAMs Euler scheme applies an implicit backward Euler method, in which the temporal derivative is calculated from two flow fields separated by a single time step, as shown in Equation (3.21). The face values in the spatial terms are taken from the unknown values of the flow field at the current time step $\phi^{[e,t]}$, such that both the spatial and temporal terms must be solved implicitly. Note, that the backward Euler method in the Euler scheme is not to be confused with the backward scheme in Equation (3.26).

$$\frac{\partial}{\partial t} \int_{V^{[P]}} \phi^{[P,t]} \; dV^{[P]} = \frac{V^{[P]}}{\Delta t} \left(\phi^{[P,t]} - \phi^{[P,t-1]} \right), \tag{3.21}$$

Since the Euler scheme depends on the flow fields from two time steps, the solver only needs to store a single flow field corresponding to the previous time step $\phi^{[P,t-1]}$, at any given time. Since the Euler scheme only provides first-order accuracy it typically requires impractically small time steps to produce a sufficient temporal accuracy. However, due it its high stability and boundedness, the Euler scheme maintains practical usefulness in transient cases for which the time-dependant behaviour is not of interest. This includes the early stages of transient simulations, in which the initial flow field has yet to stabilise, and steady-state flow fields which cannot be stabilised with steady-state numerical solvers, as discussed in Section 3.6.

CrankNicolson $< \gamma_{cn} >$

The CrankNicolson scheme applies a variant of the second-order Crank-Nicolson method. The main feature which separates the Crank-Nicolson method from the implicit Euler method is in the treatment of the spatial terms in Equation (3.6). The Crank-Nicolson scheme determines the face values by blending the unknown values of the flow field in the current time step with the known values from flow field from the

previous time step. This blending is shown for the convective terms in Equation (3.22) and the Laplacian terms in Equation (3.23).

$$\sum_1^{e=N_e} \left(\vec{S}^{[e]} \cdot \vec{u}^{[e]} \right) \phi^{[e]} = \frac{1}{2} \left(\sum_1^{e=N_e} \left(\vec{S}^{[e]} \cdot \vec{u}^{[e]} \right) \phi^{[e,t]} \right) \\ + \frac{1}{2} \left(\sum_1^{e=N_e} \left(\vec{S}^{[e]} \cdot \vec{u}^{[e]} \right) \phi^{[e,t-1]} \right), \tag{3.22}$$

$$\nu \sum_1^{e=N_e} \vec{S}^{[e]} \left(\bigtriangledown \phi \right)^{[e]} = \frac{1}{2} \left(\nu \sum_1^{e=N_e} \vec{S}^{[e]} \left(\bigtriangledown \phi \right)^{[e,t]} \right) \\ + \frac{1}{2} \left(\nu \sum_1^{e=N_e} \vec{S}^{[e]} \left(\bigtriangledown \phi \right)^{[e,t-1]} \right), \tag{3.23}$$

For the temporal derivative, the Crank-Nicolson method applies an identical approach to the backward Euler method as shown in Equation (3.24).

$$\frac{\partial}{\partial t} \int_{V^{[P]}} \phi^{[P,t]} \quad dV^{[P]} = \frac{V^{[P]}}{\Delta t} \left(\phi^{[P,t]} - \phi^{[P,t-1]} \right), \tag{3.24}$$

The pure Crank-Nicolson method provides second-order accuracy, without requiring the solver to store the flow field at more than one time step at any given time. It can reliably maintain stability provided that the cell size Δx, time step Δt, and local velocity $\vec{u}$, fulfil the condition which is given in Equation (3.25). The LHS of Equation (3.25) is referred to as the Courant number Co.

$$\frac{\Delta x |\vec{u}|}{\Delta t} \leq 2, \tag{3.25}$$

The CrankNicolson scheme in OpenFOAM applies a variant of the Crank-Nicolson method, which combines second-order accurate method of pure Crank-Nicolson in Equation (3.24) with the first-order accurate backward Euler method in Equation (3.21). The contribution from each scheme is controlled using the weighting factor

γ_{cn}. The weighting factor possesses a value between $\gamma_{cn} = 0$ and $\gamma_{cn} = 1$. As the value of γ_{cn} decreases, the stability of the CrankNicolson scheme increases at the cost of decreasing the effective order of accuracy. For typical engineering applications, a value of $\gamma_{cn} = 0.9$ is recommended (Greenshields 2016) to provide sufficient balance between the stability and the effective order of accuracy.

backward

The backward scheme, shown in Equation (3.26), interpolates over three-time steps, including the unknown flow field of the current time step, and weights each contribution with fixed constants. The backward scheme achieves full second order accuracy in time, however, it is less stable than the weighted CrankNicolson scheme as it is unbounded.

$$\frac{\partial}{\partial t} \int_{V^{[P]}} \phi^{[P]} \quad dV^{[P]} = \frac{V^{[P]}}{2\Delta t} \left(3\phi^{[P,t]} - 4\phi^{[P,t-1]} + \phi^{[P,t-2]} \right), \tag{3.26}$$

As for the first-order Euler scheme, the backwards schemes determines the spatial terms from the unknown values of the flow field from the current time step, which requires the spatial terms to be solved implicitly. The formulation of the temporal term in Equation (3.26) means that, at any point in time, the backward scheme requires the solver to store two flow fields for the previous two time steps, with values of $\phi^{[P,t-1]}$ and $\phi^{[P,t-2]}$, which increases the computational workload compared with the first-order Euler scheme.

3.6 Numerical Solvers: fvSolution

The OpenFOAM source code encompasses a vast library of solvers for a large variety of flow scenarios. The present study utilised three different OpenFOAM solvers; the

simpleFoam, pimpleFoam and pisoFoam solvers. Each solver is applicable to incompressible flow in either laminar or turbulent states. All three solvers apply a segregated approach, such that they work by decoupling the pressure terms and velocity terms, as described in Section 3.6.1. They produce a converged solution by alternating between the velocity field and the pressure field, and correcting each in turn.

3.6.1 Pressure-Velocity Coupling

The discretisation of Equation (3.6) relates the unknown scalar value in cell P with the surrounding scalar values, velocity values and pressure values in the surrounding cell in the form of Equation (3.27). The coefficients $\mathcal{A}^{[P]}$ and $\mathcal{A}^{[E]}$ are dependant on the discretisation schemes which are selected for the diffusive and convective parts of Equation (3.6), whilst the pressure gradient is not yet discretised. The term $\mathcal{B}^{[P]}$ represents the source terms of mass flux for cell P, including the temporal terms but excluding the pressure gradient.

$$u_i^{[P]}\mathcal{A}^{[P]} = -\sum_1^{E=N_E} \mathcal{A}^{[E]}u_i^{[E]} + \mathcal{B}^{[P]} - (\bigtriangledown p)^{[P]}, \tag{3.27}$$

For a given cell P the contributions of the surrounding cells, along with the source terms, are collected into a single term $\mathcal{H}^{[P]}$, as shown in Equation (3.28).

$$\mathcal{H}^{[P]} = \mathcal{B}^{[P]} - \sum_1^{E=N_e} \mathcal{A}^{[E]}u_i^{[E]}, \tag{3.28}$$

The solver determines the face value $\phi^{[e]}$, through linear interpolation between two cell centres and the connecting face (Equation 3.29, 3.30, 3.31 and 3.32) in the form of a weighting factor $\mathcal{W}^{[e]}$, determined from location of the fact in relation to the cell-to-cell

vector.

$$u^{[e]} = \mathcal{W}^{[e]} u^{[E]} + \left(1 - \mathcal{W}^{[e]}\right) u^{[P]}, \tag{3.29}$$

$$p^{[e]} = \mathcal{W}^{[e]} p^{[E]} - \left(1 - \mathcal{W}^{[e]}\right) p^{[P]}, \tag{3.30}$$

$$\mathcal{A}^{[e]} = \mathcal{W}^{[P]} \mathcal{A}^{[P]} + \left(1 - \mathcal{W}^{[E]}\right) \mathcal{A}^{[E]}, \tag{3.31}$$

$$\left(\frac{\mathcal{H}^{[P]}}{\mathcal{A}^{[P]}}\right)^{[e]} = \mathcal{W}^{[e]} \left(\frac{\mathcal{H}^{[P]}}{\mathcal{A}^{[P]}}\right)^{[E]} + \left(1 - \mathcal{W}^{[e]}\right) \left(\frac{\mathcal{H}^{[P]}}{\mathcal{A}^{[P]}}\right)^{[P]}, \tag{3.32}$$

Momentum predictor:

The first stage of the solution determines a new velocity field for time t, using the previous velocity and pressure fields at time $t - 1$, by solving a conservation equation of the form in Equation (3.33). The pressure field for the face values $p^{[e]}$, is taken from the previous time step and remains constant throughout the implicit calculation of Equation (3.33).

$$u_i^{[P,t]} = \gamma_u \left(\frac{\mathcal{H}^{[P]}}{\mathcal{A}^{[P]}} - \frac{1}{\mathcal{A}^{[P]}} \sum_1^{e=N_e} \vec{S}^{[e]} \cdot p^{[e]}\right) + \left(1 - \gamma_u\right) u_i^{[P,t-1]}, \tag{3.33}$$

The final value of velocity is produced by weighting the effective velocity, which is obtained from the interpolation of momentum flux and point pressure values, against an exact value taken by simply interpolating the cell centre velocity values of the previous time step, $\phi^{*[e]}$. The last term on the RHS, along with the relaxation factor, γ_u, weights the new velocity field against the initial velocity field to aid in convergence.

Pressure correction:

Equation (3.34) is derived from the continuity equation and links the pressure gradient at each face with the updated velocity field for the neighbour cells collected

in $\mathcal{H}^{[P]}$.

$$\sum_1^{e=N_e} \vec{S}^{[e]} \cdot \left(\frac{1}{\mathcal{A}^{[P]}} \nabla p \right)^{[e]} = \sum_1^{e=N_e} \vec{S}^{[e]} \cdot \left(\frac{\mathcal{H}^{[P]}}{\mathcal{A}^{[P]}} \right)^{[e]}, \qquad (3.34)$$

By discretising the pressure gradient term, as described in Section 3.5.2, the pressure gradient in Equation (3.34) is expressed in term of cell centre values, which can be solved iteratively to produce an updated pressure field.

Velocity correction:

Equation (3.35) provides the velocity flux through a face, based on the momentum predictor and the pressure field. The corrected pressure field from Equation (3.34) is supplied to Equation (3.35) to produce a series of face fluxes which conform more closely to the corrected pressure field.

$$\vec{S}^{[e]} \cdot u_i^{[e]} = \vec{S}^{[e]} \cdot \left(\left(\frac{\mathcal{H}^{[P]}}{\mathcal{A}^{[P]}} \right)^{[e]} - \left(\frac{1}{\mathcal{A}^{[P]}} \right)^{[e]} (\nabla p)^{[e]} \right), \qquad (3.35)$$

Similarly, the velocity values at each cell centre $u^{[p]}$, are recalculated using the corrected pressure field using Equation (3.36).

$$u_i^{[P]} = \frac{\mathcal{H}^{[P]}}{\mathcal{A}^{[P]}} - \frac{1}{\mathcal{A}^{[P]}} (\nabla p)^{[P]}, \qquad (3.36)$$

The correction in Equation (3.36) is performed explicitly, with all velocity terms on the RHS being taken from the velocity field from the momentum predictor step in Equation (3.33).

3.6.2   simpleFoam

The simpleFoam solver solves the discretised equation using the OpenFOAM variant of the SIMPLE (Semi-Implicit Method for Pressure-Linked Equations) algorithm, which

disregards all temporal terms. Hence, the simpleFoam is only applicable to steady-state problems. It can solve incompressible laminar flow problems, and incompressible turbulent flow problems with a steady-state mean flow and the application of time-averaged turbulence approximations (i.e. Reynolds-averaged stress models). The exact value of time step Δt, only serves as a marker for the number of iteration loops.

At the start of each time step the simpleFoam solver calculates a new velocity field by solving the momentum equation in Equation (3.33). The velocity terms in the momentum equation are solved implicitly, whilst the pressure terms are kept constant; being taken from the pressure field at the previous time step. At this stage, the velocity field is relaxed by using an under-relaxation factor of $\gamma_u < 1$.

Equation (3.34) is solved after the momentum equation, using the values of the updated velocity field to produce an updated pressure field. An under-relaxation factor of $0 < \gamma_p < 1$ is applied, as shown in Equation (3.37), to limit the contribution of the error in the pressure correction and aid stability. The value of $p*^{[P,t]}$ in Equation (3.37) denotes the pressure field obtained from solving Equation (3.34).

$$p^{[P,t]} = \gamma_p p^{*[P,t]} + \left(1 - \gamma_p\right) p^{[P,t-1]}, \tag{3.37}$$

The solver repeats this procedure until the change in the pressure field and velocity field between time steps satisfies the user-defined convergence criteria given in the 'fvSolution' dictionary.

3.6.3 pisoFoam

The pisoFoam solver is a transient solver for incompressible laminar and turbulent flows through the PISO algorithm (Pressure Implicit with Splitting of Operators). This solver can also produce solutions for steady-state flow fields, although at a greater cost than the steady-state simpleFoam solver. As with the steady-state simpleFoam solver, the pisoFoam solver begins each time step by solving the momentum equation (Equation (3.33)), to produce an initial prediction for the velocity field based on the pressure field from the previous time step. In this case, the term $\mathcal{B}^{[P]}$ in Equation (3.28) will contain the source which is attributed to the non-zero temporal terms. Typically no relaxation is applied to the velocity field , such that $\gamma_u = 1$.

To ensure that a converged solution is produced within each time step, the piso-Foam solver replaces the single pressure correction step from the simpleFoam solver with a pair of corrector loops. Each corrector loop begins by solving Equation (3.34) to produce a corrected pressure field. Then the velocity field is corrected through implicitly recalculating the face fluxes (Equation (3.35)), based on the corrected pressure field, and then correcting the cell centre values by explicitly solving Equation (3.35). The weighted flux coefficients of the primary cell, neighbour cells and source terms; $\mathcal{A}^{[P]}$, $\mathcal{A}^{[E]}$ and $\mathcal{B}^{[P]}$ are constant throughout the corrector loops. However, the solver calculates new parameters of $\mathcal{H}^{[P]}$ for each corrector loop.

3.6.4 pimpleFoam

The pimpleFoam solver is a transient solver for incompressible laminar and turbulent flow, which combines the transient PISO algorithm with the steady-state SIMPLE algorithm. Multiple steps of the SIMPLE algorithm, referred to as 'outer corrector

loops', are applied during each time step. A user-specified number of 'inner' corrector steps determines the number of pressure correctors in each iteration of the SIMPLE algorithm. The outer corrector loop is repeated until the solution achieves a desired tolerance, or the number of outer corrector loops reaches a use-specified limit, as defined in the 'fvSolution' dictionary. At this point, one final iteration loop is applied without relaxation factors, with the output being carried over as the initial flow field for the following time step.

Since the pimpleFoam solver produces a converged solution during each time step, it can maintain stability over larger time steps than the standard PISO algorithm. Hence, the time step is constrained by the requirements of the physical flow field as opposed to those of numerical stability.

3.7   Large-Eddy Simulation

The direct numerical simulation (DNS) approach aims to model the full turbulent energy cascade, by solving the flow at a spatial and temporal resolution which is sufficient to capture all turbulent coherent structures and eddies across the full range of length scales. By contrast, 'Reynolds-Averaged Navier-Stokes' (RANS) methods reduce computational cost by applying temporal averaging across all length scales to remove the time-dependant motions of the turbulent eddies. The influence of the unresolved eddies is determined by suitable approximation methods. Through this, RANS methods forgo resolving three-key properties of turbulent flow; chaotic, time-dependant and three-dimensional motions, and instead apply a numerical model to approximate the resulting effects of these behaviours. Therefore, in addition to having a reduced accuracy, RANS models are fundamentally unrepresentative of true turbulent flow be-

haviour. The large-eddy simulation approach attempts a compromise between these two primary methodologies by restricting the resolved flow field to only those length scales which contain the majority of the turbulent energy, and approximating the effect of the eddies at the smaller length scales.

The capabilities of utilising large-eddy simulation in OpenFOAM have been demonstrated and validated for benchmark cases of flow separation (Cao & Tamura 2016; Lysenko *et al.* 2013), and a fully developed channel flow . However, the question remains as to its performance for modelling laminar-turbulent transition under comparable tripping conditions.

3.7.1 Spatial Filtering

The length scale Λ represents a user-defined limit below which a simulation ceases to resolve time-dependant turbulent motions. This length scale is referred to as the spectral cut-off limit. The time-dependant velocity and pressure fields are spatially filtered to remove any fluctuations which correspond to a length scale smaller than Λ. The filtering process acts to replace the local velocity at each point with a spatially averaged value across a region of Λ dimensions. The filter function G_L includes or excludes surrounding cells in the averaging procedure based upon their distance in relation to Λ. Equation (3.38) displays the filtering procedure of a three-dimensional field.

$$\tilde{\phi} = \int_{-\infty}^{+\infty} \int_{-\infty}^{+\infty} \int_{-\infty}^{+\infty} G_L\left(x', y', z', \Lambda\right) \phi\left(x', y', z'\right) dx'dy'dz',\qquad(3.38)$$

Spatially filtered fields are denoted by $(\tilde{\circ})$. The top-hat filter, shown in Equation (3.39), defines two outputs of G_L, with a discrete limit based on a spherical volume centred on the filtering point. The top-hat filter displays good spatial accuracy in preserving

localised flow behaviour (Meneveau & Katz 2000).

$$
G_L\left(\vec{x}, \vec{x'}, \Lambda\right) =
\begin{cases}
\Lambda^{-3}, & \text{for} \quad \vec{x} - \vec{x'} \leq \Lambda/2, \\[2ex]
0, & \text{for} \quad \vec{x} - \vec{x'} > \Lambda/2,
\end{cases}
\tag{3.39}
$$

The filtered momentum conservation equations for incompressible flow take the form in Equation (3.40).

$$
\frac{\partial \tilde{u}_i}{\partial t} + \frac{\partial \left(\tilde{u}_i \tilde{u}_j\right)}{\partial x_i} = -\frac{1}{\rho}\frac{\partial \tilde{p}}{\partial x_i} + \nu \frac{\partial^2 \tilde{u}_i}{\partial x_i \partial x_j} - \frac{\partial \tau_{ij}}{\partial x_j},
\tag{3.40}
$$

The tensor τ_{ij} represents tensor of sub-grid stresses, as defined in Equation (3.41).

$$
\tau_{ij} = \widetilde{u_i u_j} - \tilde{u}_i \tilde{u}_j,
\tag{3.41}
$$

The strain-rate tensor of the filtered velocity field is given in Equation (3.42).

$$
\tilde{S}_{ij} = \frac{1}{2}\left(\frac{\partial \tilde{u}_i}{\partial x_j} + \frac{\partial \tilde{u}_j}{\partial x_i}\right) \quad \tilde{S} = \sqrt{2\tilde{S}_{ij}\tilde{S}_{ij}},
\tag{3.42}
$$

3.7.2 Smagorinsky Models

Smagorinsky (1963) developed a simple sub-grid stress model which formed the basis for a whole class of models in use today. Smagoinsky assumed that a single value of effective viscosity ν_t, is sufficient to represent the effect of the small-scale motions on the mean flow at each point. This assumption requires an equal flow of energy into and out of the unresolved portion of the energy cascade. The 'Smagorinsky' model proposes that the effective turbulent viscosity is proportional to an operator that is related to the velocity gradient tensor of the resolved scales as defined in Equation

(3.43).

$$OP_1(\vec{x}, t) = \sqrt{\tilde{S}_{ij}\tilde{S}_{ij}}, \tag{3.43}$$

Hence, the viscosity of the unresolved sub-grid stresses is determined by Equation (3.44), where C_{sgs} is the user-defined sub-grid scale constant.

$$\nu_t = C_{sgs}\Lambda\sqrt{\widetilde{OP_1(\vec{x}, t)}}, \tag{3.44}$$

Whilst the Smagorinsky model is simple; requiring only a single value of the constant C_{sgs} throughout the entire domain, this constant must be able to represent the damping effects in both the laminar region and the turbulent region of the flow. In reality, the Smagorinsky model produces excessive dissipation in shear flows. This is particularity problematic when modelling the transition of spatially developing boundary layers where an initially laminar flow needs to initiate low turbulence production. In modelling laminar-turbulent transition with a coarse streamwise and spanwise resolution (equal to 90 and 42 viscous lengths respectively), Sayadi & Moin (2012) demonstrated that the basic Smagorinsky model was too dissipative to induce transition in the laminar boundary layer.

To reduce artificial dissipation due to shearing, Germano *et al.* (1991) proposed a method of replacing the global, user-defined value of C_{sgs} with a variable which is recalculated locally during each time step. Firstly, they proposed a second filtering width Λ_{test}, which is larger than the standard filter Λ. The filtering operation is performed a second time using Λ_{test} as the cut-off length scale, where a second set of sub-grid stress tensors ξ_{ij}, are produced corresponding to a length scale of Λ_{test}.

$$\xi_{ij} = \widetilde{\widetilde{u_i u_j}} - \tilde{\tilde{u}}_i\tilde{\tilde{u}}_j, \tag{3.45}$$

Subtracting the stress tensors for ξ_{ij} and $\tilde{\tau}_{ij}$ leaves a fully resolved stress from length scales within the test filter.

$$\psi_{ij} = \tau_{ij} - \widetilde{\xi_{ij}}, \tag{3.46}$$

$$\psi_{ij} - \frac{1}{3}\psi_{kk}\delta_{ij} = \left(C_{sgs}\right)^2 \xi_{ij}, \tag{3.47}$$

$$\zeta_{ij} = 2\Lambda^2 \left(\widetilde{\left|\tilde{S}\right| \tilde{S}_{ij}} - \left(\frac{\Lambda_{test}}{\Lambda}\right)^2 \left|\tilde{\tilde{S}}\right| \tilde{\tilde{S}}_{ij} \right), \tag{3.48}$$

Lilly (1992) proposed a new definition of the sub-grid constant shown in Equation (3.49)

$$C_{sgs} = \sqrt{\frac{\langle \psi_{ij}\zeta_{ij}\rangle}{\langle \zeta_{ij}\zeta_{ij}\rangle}}, \tag{3.49}$$

This approach assumes that the sub-grid scale coefficient is independent of the local length scale, such that a single value of C_{sgs} can be applied for the scales of Δ and Δ_{test}.

3.7.3 WALE Model

The wall-adapting local eddy-viscosity model was developed by Nicoud & Ducros (1999) for the purpose of improving the accuracy of sub-grid scale modelling in the low turbulence, near-wall region of a turbulent shear layer. As for the constant Smagorinsky model, the WALE model applied a single global value to the sub-grid scale constants at all points in the domain. The behaviour of the WALE model is controlled through a modified configuration of the operator $OP_1\left(\vec{x}, t\right)$, which is derived from the velocity gradient tensor, as shown in Equation (3.50). The symbol δ_{ij} represents the Kronecker delta function.

$$S_{ij}^d = \frac{1}{2}\left(\bigtriangledown \tilde{u}_{ik} \bigtriangledown \tilde{u}_{kj} + \bigtriangledown \tilde{u}_{jk} \bigtriangledown \tilde{u}_{ki}\right) - \frac{1}{3}\delta_{ij} \bigtriangledown \tilde{u}_{kk}^2, \tag{3.50}$$

In an attached shearing flow of purely laminar behaviour the only non-negligible gradient will be $\partial u/\partial y > 0$. In a spatially developing laminar boundary layer, the streamwise length scales are considered to be far greater than the wall-normal length scales ($x >> y$), such that $\partial u/\partial y >> \partial u/\partial x$ and $\partial u/\partial y >> \partial v/\partial x$. In both of these cases it may be assumed that $S_{ij}^d S_{ij}^d \approx 0$. Hence, Nicoud & Ducros (1999) produced a new operator $OP_2(\vec{x}, t)$, shown in Equation (3.51), by scaling $S_{ij}^d S_{ij}^d$ with the combination of the strain rate tensor.

$$OP_2(\vec{x}, t) = \frac{\left(S_{ij}^d S_{ij}^d\right)^{1.5}}{\left(\tilde{S}_{ij}\tilde{S}_{ij}\right)^{2.5} + \left(S_{ij}^d S_{ij}^d\right)^{1.25}}, \tag{3.51}$$

The WALE model determines the unresolved sub-grid viscosity through the relationship in Equation (3.52).

$$\nu_t = \left(C_{sgs}\Lambda\right)^2 OP_2(\vec{x}, t), \tag{3.52}$$

The numerator in Equation (3.52) will maintain a positive, non-zero value, both in cases of laminar shear flow and rotational flow. Hence, unlike the dynamic variant of the Smagorinsky model (Lilly 1992) the WALE model does not require spatial averaging to maintain stability. This is beneficial within flows which do not have a clearly defined, or unknown, plane which is statistically homogeneous.

The findings of Rezaeiravesh & Liefvendahl (2018) provide a good indication of the maximum spatial resolution for which the WALE model is suitable. Rezaeiravesh & Liefvendahl (2018) compared the influence of near-wall spatial resolution in modelling a periodic turbulent channel flow with WALE models in OpenFOAM. Their solutions achieved an accurate replication of the inner region, for streamwise and spanwise resolutions of < 17 and < 10 viscous lengths respectively. These requirements lie close

to the high-resolution which is utilised in modelling spatially developing turbulent boundary layer to a high spectral accuracy (Schlatter *et al.* 2010). At this resolution, the use of the WALE model by Rezaeiravesh & Liefvendahl (2018) had a negligible, if not detrimental, effect on the accuracy. The error was derived primarily from the spanwise spatial resolution, and its resulting over prediction in the streamwise velocity fluctuation in the region of high-speed and low-speed streaks.

3.8 Post-Processing

Analysis of the turbulent boundary layer simulations in Chapter 4 and Chapter 7 require velocity profiles for the mean flow, which can be compared with the ideal case of a fully developed, spanwise invariant, boundary layer profile. The time-dependant turbulent flow fields are first temporally averaged to produce ideally steady-state flow fields, with the time-dependant turbulent behaviour removed. Then, through the use of bash scripts which were created by the author for the present analysis, the velocity profiles are automatically extracted, spatially-averaged and collapsed to produce the integral boundary layer properties.

3.8.1 Temporal Averaging in OpenFOAM

The temporal averaging procedure is performed by the 'fieldAverages' function, which is configured in the 'controlDict' dictionary. It allows the calculation of both the time-averaged value of a given property, along with its time-averaged root-mean square value. The user must specify the size of the temporal averaging window T_{av}. This window will contain a number of time steps denoted by $n_t = (1, 2, 3...N_t)$. When the time increment Δt, is fixed, as in the present analysis, the number of time steps in

the averaging window can simply be taken as $N_t = T_{av}/\Delta t$, where the physical time is denoted by t.

In the LES simulations in Chapter 4 and Chapter 7, a continuous averaging procedure was used. For each cell in the domain, OpenFOAM stores a single time-averaged property at each time step, beginning from initial conditions at the first time step. During the first averaging period the instantaneous values are added to the mean (Equation 3.53) and root mean squared (Equation 3.54) with equal weighting.

$$\bar{\phi}\left(x, y, z, t\right) = \left(\frac{t - \Delta t}{t}\right)\bar{\phi} + \left(\frac{\Delta t}{t}\phi\right), \tag{3.53}$$

$$\bar{\phi'}_{rms}^{[t]} = \left(\frac{t - \Delta t}{t}\right)\bar{\phi'}_{rms} + \left(\frac{\Delta t}{t}\right)\phi^2 - \bar{\phi}^2, \tag{3.54}$$

Once the physical time passes the averaging period T_{av}, the time-averaged fields and the instantaneous fields are weighted against the averaging period, as shown in Equation (3.55) and Equation (3.56). Therefore, the influence of the early transient states diminishes with time.

$$\bar{\phi}\left(x, y, z, t\right) = \left(\frac{T_{av} - \Delta t}{T_{av}}\right)\bar{\phi} + \left(\frac{\Delta t}{T_{av}}\right)\phi, \tag{3.55}$$

$$\bar{\phi'}_{rms}^{[t]} = \left(\frac{T_{av} - \Delta t}{T_{av}}\right)\bar{\phi'}_{rms} + \left(\frac{\Delta t}{T_{av}}\right)\phi^2 - \bar{\phi}^2, \tag{3.56}$$

This approach allows for a continuous output of temporal averaging across all time steps. If temporal averaging begins early in the initial transient stage, the time-dependant turbulent profiles can be monitored to assess the minimal settling time required for development of the turbulent boundary layer structure. Thus temporal averaging is applicable when the required settling time is unknown. Furthermore, it allows for optimisation of the CPU time required to obtain a fully developed solution.

3.8.2 Alternative Approach: Continuous Averaging

In many investigations of equilibrium boundary layers, the numerical solution does not apply temporal averaging procedures, or output time-averaged results, for the first series of time steps. Temporal averaging is only applied once the boundary layer reaches a developed state with minimum influence of the initial conditions or initial transient behaviour. The time-averaged value at each point can obtained by simply taking the mean of the flow field at all time increments within an averaging window that begins after equilibrium has been achieved, as shown in Equation (3.57). However, this approach requires the development time to be pre-known.

$$\bar{\phi}(x, y, z) = \frac{1}{N_t} \sum_{n_t=1}^{N_t} \phi(x, y, z, n_t), \tag{3.57}$$

3.8.3 Spanwise Averaging

The final post-processing stages in Chapter 4 and Chapter 7 used bash scripts, which were created by the author for use in the present analysis, to log the boundary layer structure at discrete points along the streamwise direction of a spatially developing turbulent boundary layer.

The first script, contained in Appendix A.1, extracts spatially averaged velocity profiles from user-specified locations along the computational domain. Firstly, a planar slice of the mesh is extracted from the main domain using the 'topoSet' and 'subsetMesh' commands. This slice is typically one cell thick in the streamwise direction. Each subset of the mesh is placed into the 'constant/polyMesh' directory, in place of the full domain. Finally, the 'postChannel' command is performed on that local subset on the domain, to produce an averaged profile at a given streamwise location.

The 'postChannel' command is designed for extracting time-averaged data from planar channels, and as such, it performs the averaging procedure over the spanwise and streamwise directions. However, by extracting a subset of the mesh, the 'postChannel' averaging procedure can be restricted to one cell in the streamwise direction.

Each sample volume spans for N_x cells in the streamwise direction, and N_z cells in the spanwise direction. For each discrete x-z plane at a distance of y away from the wall, all cells are collapsed to a single, spatially-averaged point value using Equation (3.58).

$$\langle \bar{\phi}(y, t) \rangle = \frac{1}{\Delta N_x \Delta N_z} \sum_{n_x=1}^{\Delta N_x} \sum_{n_z=1}^{\Delta N_z} \bar{\phi}(n_x, y, n_z, t), \tag{3.58}$$

The script in Appendix A.1 produces a set of wall-normal profiles of spanwise-averaged, time-averaged properties at each user-specified streamwise location. These properties include pressure $\langle \bar{p} \rangle$, velocity components $\langle \bar{u} \rangle$, $\langle \bar{v} \rangle$ and $\langle \bar{w} \rangle$, in addition to four root mean square components of velocity $\langle \bar{u}'_{rms} \rangle$, $\langle \bar{v}'_{rms} \rangle$ and $\langle \bar{w}'_{rms} \rangle$, and the Reynolds shear stress $-\langle \overline{u'v'} \rangle$. The final property is the kinetic energy which is determined from the output of the time-averaged and spanwise-averaged components, as defined in Equation (3.59).

$$k = \frac{1}{2} \left(\langle \bar{u}'_{rms} \rangle + \langle \bar{v}'_{rms} \rangle + \langle \bar{w}'_{rms} \rangle \right), \tag{3.59}$$

The final script in Appendix A.2 cycles through each discrete wall-normal location, starting with the cell value adjacent to the wall, to calculate the integral boundary layer, including thickness values which are defined in Equation (1.13), Equation (1.14) and Equation (1.15), in addition to various Reynolds numbers, free-stream conditions and wall shear stress.

3.9 Summary

This Chapter has presented a detailed discussion of the capabilities of the open source code OpenFOAM for modelling fluid flows. Given the wide variety of utilities available within OpenFOAM, primary focus has been given to those which were utilised in the present analysis.

OpenFOAM operates with the finite volume approach, in which the velocity and pressure fields are solved over a discretised domain. The steady-state simpleFoam solver, and the transient pimpleFoam and pisoFoam solvers are all applicable to incompressible flows in both the laminar and turbulent regimes. Together these three solvers will be sufficient to cover the range of flows in the present analysis.

All numerical schemes presented are of first-order to second-order accuracy, and are applicable to both orthogonal meshes, which were utilised in Chapter 4, and non-orthogonal meshes, which were utilised in Chapters 5,6 and 7. The majority of these non-orthogonal meshes were generated using the snappyHexMesh utility. This chapter has demonstrated the capabilities of snappyHexMesh for generating robust, split-hexahedral meshes around arbitrary geometries, without a significant increase in the required pre-processing time which is typically associated with increasing geometric complexity.

The capabilities of modelling turbulence through large-eddy simulation in OpenFOAM have been discussed. Whilst OpenFOAM has been validated for modelling turbulence in fully developed channel flow, the question remains as to its performance for modelling laminar-turbulent transition in spatially developing boundary layers under comparable tripping conditions. This question was be investigated in detail, as discussed in Chapter 4.

Spatially Developing Turbulent Boundary Layers in OpenFOAM

4.1 Introduction

The present chapter details a process of developing a numerical methodology for modelling spatially developing laminar-turbulent transition in OpenFOAM, with further optimisation to balance physical detail and accuracy with economic efficiency. Firstly, the flow domain is configured and approximate solutions are used to produce a detailed approximation of the boundary layer properties along the length of the domain. Secondly, two simulations compare two different configurations for the numerical trip at a fixed spatial resolution. This stage aims to assess the response of the initially laminar boundary layer to the velocity fluctuations of the tripping plane, independently of the spatial resolution. As a minimum, it is desired that the boundary layer must

reach a state of equilibrium within 25% of the domain length. Assessing the boundary layers state of development involves both a comparison of the base flow parameters (shape factor, coefficient of friction) and the local structure of the boundary layer, with particular attention to the outer region (Schlatter & Orlu 2012). The final stage of development investigates the direct influence of the global spatial resolution on the accuracy of the numerical solution. This approach assumes that the initial spatial resolution is sufficient to capture a realistic representation of the physical behaviour of the numerical trip and the boundary layer development during the transitional region.

4.2   Numerical Setup

4.2.1   Flow Domain

The boundary layer simulations which are developed in the present analysis are designed in the context of an existing open wind tunnel within Liverpool John Moores University. A detailed description of the facility can be found in Wharton (2017). The wind tunnel consists of a high speed air blower which is capable of producing a bulk flow velocity of up to $120m/s$. The air blower connects to the inlet of a working section which is $400mm$ in length, $200mm$ in width and $20mm$ in height. Wharton (2017) designed and constructed a force balance which can incorporate interchangeable plates upon the lower wall between $x = 0.07m$ and $x = 0.25m$ downstream of the inlet to the working section. This region will be taken as the 'point of interest', for which the smooth surface will be replaced with transverse grooves in Chapter 7. The working section of the wind tunnel is shown in Figure 4.1, whilst the features of the force balance are highlighted in Figure 4.1b.

(a) *Side view*

(b) *Top view*
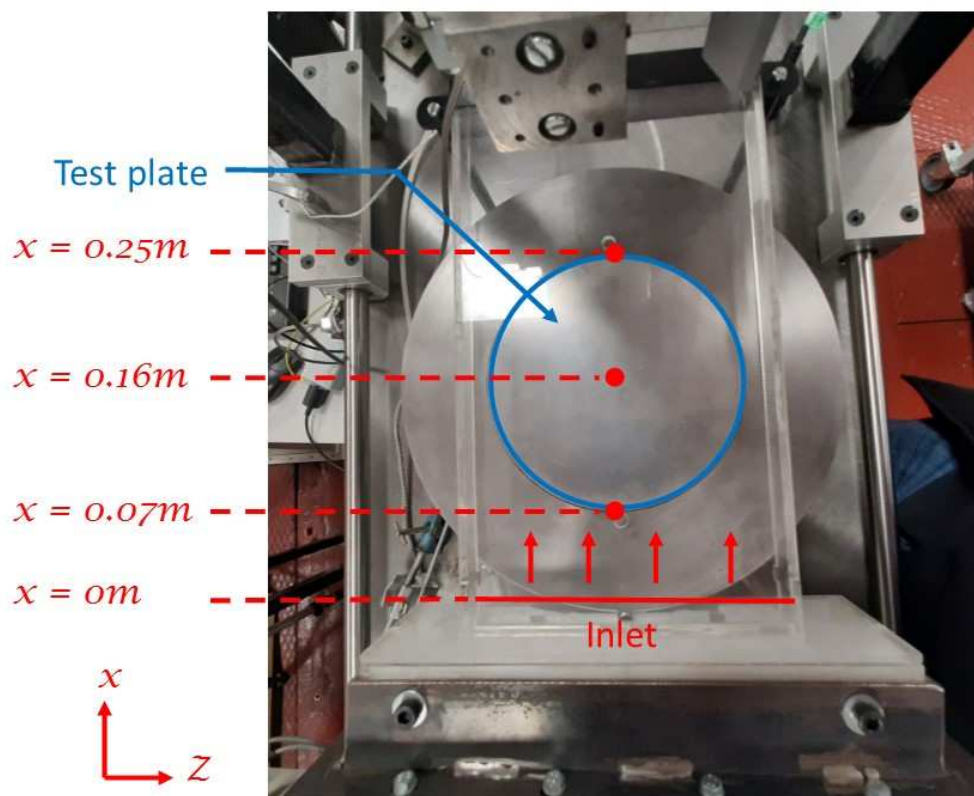
Figure 4.1: *Image of the open wind tunnel facility; air blower and working section.*

Figure 4.2 displays the flow domain which is taken to represent the wind tunnel working section in the present analysis. The boundary layer outline shown in Figure 4.2a demonstrates the ideal process of boundary layer growth in the computational domain. The working fluid is air with a constant kinematic viscosity of $\nu = 1.568 \times 10^{-5} m^2/s$ and a constant density of $\rho = 1.177 kg/m^3$. It is assumed that the flow will enter the working section in a fully laminar state, with a small laminar shear layer having already developed over the lower wall. The origin of the streamwise Cartesian vector x is taken to lie at the inflow plane of the working section. The inflow plane will lie upstream of the location of the effective 'leading edge' from which the inflowing laminar boundary layer originates. The length parameters x_l and x_t denotes the distance between a point x and the location of the effective 'leading edges' of the laminar boundary layer and turbulent boundary layer respectively, as illustrated in Figure 4.2.

For the computational domain, the spanwise width of the working section is reduced to a width L_z, by assuming that the width of the working section is large enough such that the solid walls which form the spanwise boundaries have a negligible influence on the flow field towards the centre of the working section. The front plane and back plane are specified as periodic boundaries by linking the velocity and pressure fields at both faces through a 'cyclic' boundary condition, as illustrated in Figure 4.2b. The domain height L_y is restricted to half the height of the working section. Free-stream boundary conditions are applied at the upper boundary, by assuming that the thickness of the boundary layer on the smooth upper wall of the working section has a negligible influence on bulk flow through the working section.

(a) *Streamwise and wall-normal plane*
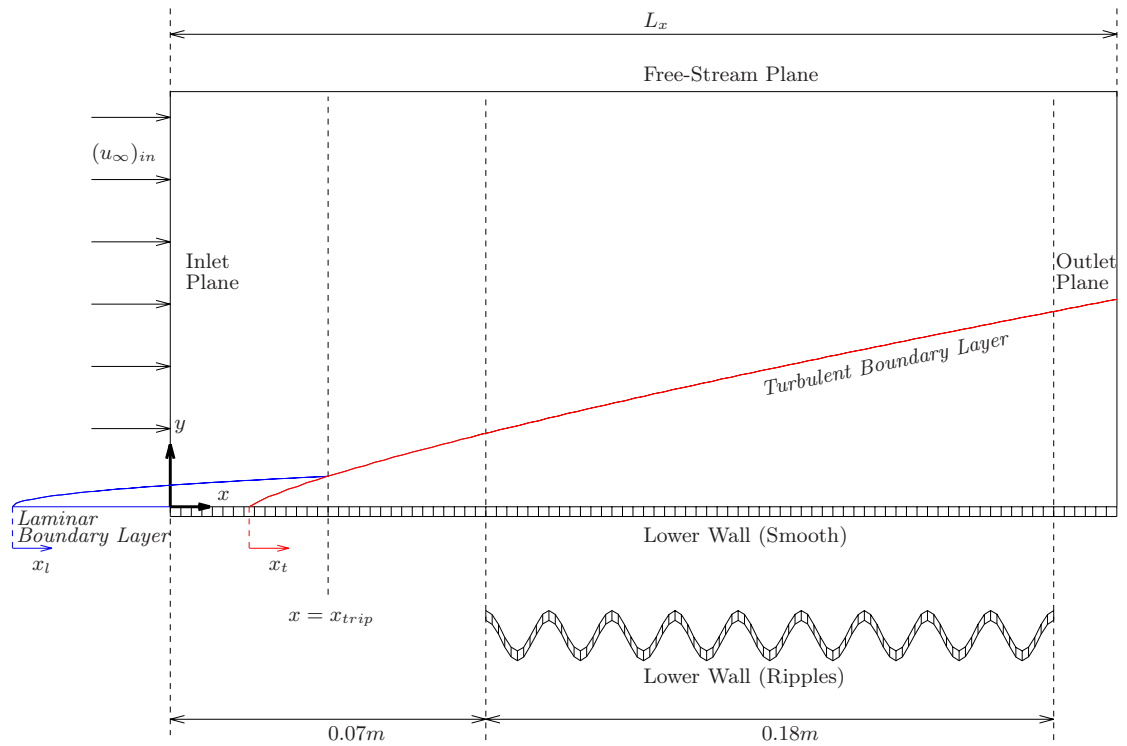
(b) *Wall-normal and spanwise plane*
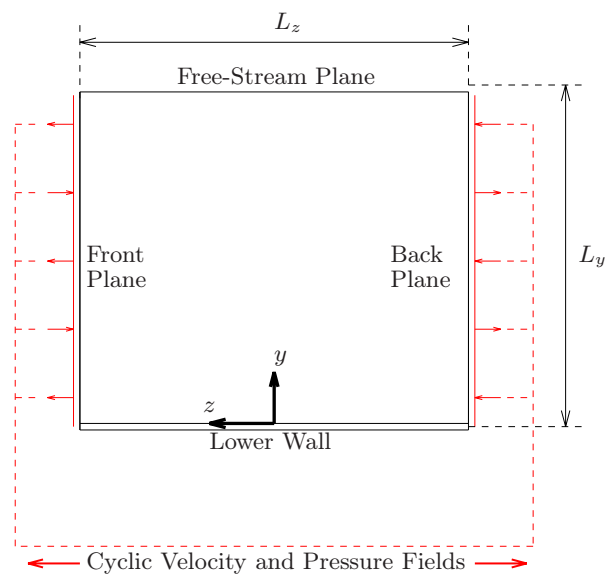
Figure 4.2: *Diagram of the flow domain and boundary conditions for the spatially developing boundary layer flow.*

4.2.2 Inflow Conditions

Blasius identified that, in a spatially developing laminar boundary layer, the velocity scales with u_∞ and the wall-normal distance scales with the variable $\sqrt{vx_l/u_\infty}$. The scaled velocity is given by the differential of a function $g' = u/u_\infty$, where g is a function of the scaled wall-normal distance, such that $g = f(y\sqrt{u_\infty/vx_l})$, and g satisfies the relationship in Equation (4.1).

$$gg'' + 2g''' = 0, \tag{4.1}$$

By substituting the analytical solution for boundary layer thickness δ_{99} in Equation (4.3), the wall-normal distance y, and function g, can be rewritten in the form $g = f(5y/\delta_{99})$. Although an exact form of g is unknown, Table 4.1 displays the solutions for the function g and its derivatives as determined by Howarth (1938) (referenced from Schlichting (1978)).

In reality, no single equation describes the distribution of velocity across the full width of a turbulent boundary layer. Whilst the outer region scales with the mean flow properties (i.e. u_∞, δ_{99}), the velocity distribution in the inner region is independent of these variables. However, when initial predictions are required, it is sufficiently accurate to assume that the velocity in the inner region scales with δ_{99}, and that the relation takes the form of the 1/7th power law in Equation (4.2).

$$\frac{u}{u_\infty} = \left(\frac{y}{\delta_{99}}\right)^{\frac{1}{7}}, \tag{4.2}$$

Substituting Equation (4.2) and the discrete laminar solutions (Table 4.1) into the integral relations in Equations (1.13),(1.14),(1.15) and (1.16) leads to approximations for boundary layer thickness (Equation 4.3), displacements thickness (Equation 4.4), momentum thickness (Equation 4.5) and wall shear stress (Equation 4.6) at a point

Table 4.1: Solutions to the Blasius Equation for the velocity distribution in a spatially developing laminar boundary layer (Howarth 1938).

y/δ_{99}	g	g'	g''	y/δ_{99}	g	g'	g''
0.00	0.00000	0.00000	0.33206				
0.04	0.00664	0.06641	0.33199	0.92	2.88826	0.98260	0.02948
0.08	0.02656	0.13277	0.33147	0.96	3.08534	0.98779	0.02187
0.12	0.05974	0.19894	0.33008	1.00	3.28329	0.99155	0.01591
0.16	0.10611	0.26471	0.32739	1.04	3.48189	0.99425	0.01134
0.20	0.16557	0.32979	0.32301	1.08	3.68094	0.99616	0.00793
0.24	0.23795	0.39378	0.31659	1.12	3.88031	0.99748	0.00543
0.28	0.32298	0.45627	0.30787	1.16	4.07990	0.99838	0.00365
0.32	0.42032	0.51676	0.29667	1.20	4.27964	0.99898	0.00240
0.36	0.52952	0.57477	0.28293	1.24	4.47948	0.99937	0.00155
0.40	0.65003	0.62977	0.26675	1.28	4.67938	0.99961	0.00098
0.44	0.78120	0.68132	0.24835	1.32	4.87931	0.99977	0.00061
0.48	0.92230	0.72899	0.22809	1.36	5.07928	0.99987	0.00037
0.52	1.07252	0.77246	0.20646	1.40	5.27926	0.99992	0.00022
0.56	1.23099	0.81152	0.18401	1.44	5.47925	0.99996	0.00013
0.60	1.39682	0.84605	0.16136	1.48	5.67924	0.99998	0.00007
0.64	1.56911	0.87609	0.13913	1.52	5.87924	0.99999	0.00004
0.68	1.74696	0.90177	0.11788	1.56	6.07923	1.00000	0.00002
0.72	1.92954	0.92333	0.09809	1.60	6.27923	1.00000	0.00001
0.76	2.11605	0.94112	0.08013	1.64	6.47923	1.00000	0.00001
0.80	2.30578	0.95552	0.06424	1.68	6.67923	1.00000	0.00000
0.84	2.49806	0.96696	0.05052	1.72	6.87923	1.00000	0.00000
0.88	2.69238	0.97587	0.03897	1.76	7.07923	1.00000	0.00000

x in a spatially developing laminar or turbulent boundary layer (Schlichting 1978).
These approximations assume that the boundary layer immediately transitions from a laminar state to a fully developed turbulent state at a point $x = x_{trip}$, where x_{trip} represents the exact point of transition due to either a natural or enforced instability.

Approximation of the boundary layer thickness:

$$
\delta_{99} \approx
\begin{cases}
5x_l^{\frac{1}{2}} \left(\dfrac{u_\infty}{\nu} \right)^{-\frac{1}{2}}, & \text{for} \quad x_l < x_{trip}, \\[2ex]
0.37x_t^{\frac{4}{5}} \left(\dfrac{u_\infty}{\nu} \right)^{-\frac{1}{5}}, & \text{for} \quad x_l > x_{trip},
\end{cases}
\tag{4.3}
$$

Approximation of the displacement thickness:

$$\delta^* \approx \begin{cases} 1.721 x_l^{\frac{1}{2}} \left(\dfrac{u_\infty}{\nu} \right)^{-\frac{1}{2}}, & \text{for} \quad x_l < x_{trip}, \\[3mm] 0.0463 x_t^{\frac{4}{5}} \left(\dfrac{u_\infty}{\nu} \right)^{-\frac{1}{5}}, & \text{for} \quad x_l > x_{trip}, \end{cases} \tag{4.4}$$

Approximation of the momentum thickness:

$$\theta \approx \begin{cases} 0.664 x_l^{\frac{1}{2}} \left(\dfrac{u_\infty}{\nu} \right)^{-\frac{1}{2}}, & \text{for} \quad x_l < x_{trip}, \\[3mm] 0.036 x_t^{\frac{4}{5}} \left(\dfrac{u_\infty}{\nu} \right)^{-\frac{1}{5}}, & \text{for} \quad x_l > x_{trip}, \end{cases} \tag{4.5}$$

Approximation of the wall shear stress:

$$\tau_0 \approx \begin{cases} 0.332 \rho u_\infty^{\frac{3}{2}} \left(\dfrac{\nu}{x_l} \right)^{\frac{1}{2}}, & \text{for} \quad x_l < x_{trip}, \\[3mm] 0.0225 \rho u_\infty^{\frac{7}{8}} \left(\dfrac{\nu}{\delta_{99}} \right)^{\frac{1}{4}}, & \text{for} \quad x_l > x_{trip}, \end{cases} \tag{4.6}$$

Based upon the recommendations of Schlatter & Orlu (2012), the boundary layer must be tripped within the limit $Re_\theta < 300$. If the conditions of the trip are suitable to the flow, the turbulent regime of the boundary layer should become fully developed by the point $Re_\theta \geq 2000$. Two reoccurring estimates involve fixing either the displacement Reynolds number to $Re_\delta \approx 450$ or the momentum Reynolds number to $Re_\theta \approx 180$ (Eitel-Amor $et\ al.$ 2014; Schlatter & Orlu 2010; Schlatter & Orlu 2012). For all approximations in the present analysis, the Reynolds number of the inflow boundary layer is taken as $Re_\theta = 180$ and it is assumed that acceleration in the free-stream due to boundary layer growth is negligible. Since boundary layer growth during laminar-turbulent transition is difficult to predict, it is assumed that the boundary layer immediately transitions to a fully developed turbulent state at the tripping point, whilst maintaining the same value of boundary layer thickness δ_{99}.
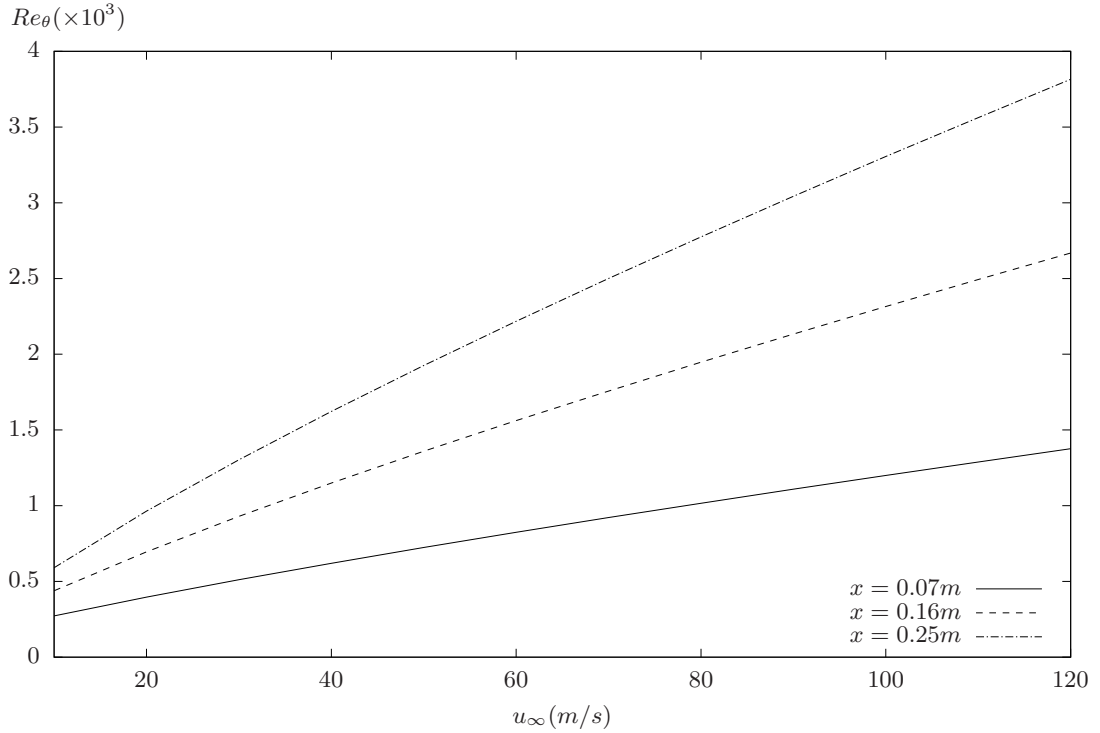
Figure 4.3: *Prediction of Re_θ for different values of free-stream velocity at the inflow.*

The momentum Reynolds number at a point increases non-linearly with both the free-stream velocity and streamwise location. The magnitude of the free-stream velocity must be sufficient to ensure that the flow has reached a state of fully developed turbulence by the start of the region of interest $x = 0.07m$, and that a state of ideal turbulence; i.e. without significant influence from the tripping conditions, covers a significant portion of this region. For varying values of free-stream velocity at the inlet, Figure 4.3 displays the predicted values of Re_θ at three key points along the streamwise length of the domain. These three points mark the start point ($x = 0.07m$), midpoint ($x = 0.16m$) and end point ($x = 0.25m$) of the region of interest. It is estimated that a free-stream velocity of $u_\infty > 40m/s$ is required for the boundary layer to complete its transition to turbulence by the point $x = 0.07m$, however, the flow behaviour will continue to be influenced by the trip whilst the flow remains within the limits of incompressibility. The influence of the trip is predicted to be sufficiently diminished by the midpoint ($x = 0.16m$) when the inflow velocity exceeds $90m/s$. Of course, this only

applies if optimal tripping conditions can be determined. Based upon these observations, the inflow free-stream velocity is set to $u_\infty = 100m/s$ (or 110% of the minimum required value), in order to ensure that a full development exists over half of length of the region of interest; between $x = 0.16$ and $x = 0.25m$.

The laminar boundary layer must be tripped within $x < 0.02m$, for which $Re_\theta < 300$. If the tripping is optimal, the boundary layer will reach an independent state ($Re_\theta > 2000$) at $x > 0.14m$. Whilst air with a velocity of $100m/s$ lies close to the limit of incompressibility ($M = 0.3$), for which temperature and density variations in the fluid become significant, the flow in the present analysis is assumed to remain incompressible along the full length of the domain.

4.2.3 Tripping Mechanism

Schlatter & Orlu (2012) demonstrated that a steady-state laminar boundary layer can be destabilised by a wall-normal body force with a temporal variation and a spanwise spatial variation. They identified that this trip should lie within $Re_\theta < 300$ to ensure rapid transition.

The present OpenFOAM simulations demonstrate that these wall-normal motions, and their destabilising effects, may be replicated by applying a field of synthetic turbulence to the wall-normal velocity components at the no-slip wall. The 'turbulentInlet' boundary condition of the OpenFOAM library applies a simple representation of turbulent behaviour to a uniform inflow, as a field of time-dependant velocity fluctuations to one or more components of a uniform velocity inflow condition. The velocity fluctuations for a given velocity component are fully random in space, and pseudo-random in time, at each point on the inflow plane. All points are anchored to a uniform value of

reference velocity $(u_{ref}, v_{ref}, w_{ref})$ and scale with a user specified velocity fluctuation scale $(u'_{ref}, v'_{ref}, w'_{ref})$. Equation (4.7) displays the weighted adjustment of instantaneous wall-normal velocity on the tripping plane at time t, where G_g represents a Gaussian random number, and α_t represents the weighting factor.

$$v^{[t]} = (1 - \alpha_t) \, v^{[t-\Delta t]} + \alpha_t \left(v_{ref} + v'_{ref} G_g \right), \tag{4.7}$$

In this case, the tripping inflow plane lies parallel to the wall at $y = 0m$. It spans the full spanwise width of the domain and lies between $x = 0.004m$ and $x = 0.006m$ along the streamwise direction. The streamwise and spanwise velocity components comply with the no-slip condition of a traditional solid wall; $u^+ = 0$ and $w^+ = 0$, along with a zero value Neuman constraint for the pressure variable. Table 4.2 displays the settings of each trip configuration which is considered in the present investigation. The wall-normal reference velocity contains a non-zero uniform value of $v_{ref} = (u_\infty)_{in} \times 10^{-5}$ to produce a negligible value of bulk mass flow rate through the plane. The velocity fluctuation values are scaled against the theoretical value of friction velocity for a turbulent boundary layer at the midpoint of the tripping location assuming that $\delta_{99(t)} = \delta_{99(l)}$. This study investigates on two values of tripping velocity; $v'^+_{ref} = 0.551$ and $v'^+_{ref} = 1.105$, which preliminary investigations confirmed were sufficient to initiate transition within the first 20% of the streamwise domain.

Table 4.2: Configurations of two numerical trips used in the present analysis.

Trip	$v'_{ref}(m/s)$	$v_{ref}(m/s)$	α_t	v'^+_{ref}
T1	1.817	0.001	0.1	0.551
T2	3.633	0.001	0.1	1.105

The distribution of the time-averaged wall-normal velocity and the time-averaged root mean square of the wall-normal velocity is not homogeneous across the tripping plane; varying at each face. The maximum and minimum variation from the specified

value of v'^+_{ref} grew as the value of v'^+_{ref} increased. For the weakest trip of $v'^+_{ref} = 0.551$, the variation in $\bar{v}^+_{rms}$ was less than $\pm 1\%$ of v'^+_{ref}, but rose to $\pm 10\%$ for the strongest trip of $v'^+_{ref} = 1.105$. Notably, two different solutions which applied $v'^+_{ref} = 1.105$ produced nearly identical responses in the local variations of $\bar{v}^+_{rms}$ and $\bar{v}^+$. This comparison suggests that although the exact form of the trip is unknown in a given case, the averaging period is sufficient to filter out the random fluctuations at each point to produce a consistent and predictable effect on the time-averaged flow field.

4.2.4 Investigation Configuration

Figure 4.4 displays the layout of the flow domain, and the stages of the spatially developing boundary layer. The flow enters the domain as a steady-state, laminar boundary layer with a fixed Reynolds number of $Re_\theta = 180$, based upon the momentum thickness at the inlet θ_{in}, and the free-stream velocity u_∞. The boundary layer reaches the outflow plane as a fully turbulent flow of $Re_\theta \approx 3000$. The streamwise and wall-normal lengths of the computational domain were kept constant for all simulations. The streamwise length is $L_x = 0.27m$ in real units, or $L_x \approx 9566\theta_{in}$, in relation to the inflow momentum thickness. The wall-normal height extends for half the height of the corresponding experimental domain; $L_y = 0.01m$ ($L_y \approx 354\theta_{in}$) or, based upon initial approximations, 1.77 times the maximum thickness of the boundary layer in the domain. All smooth wall simulations contain identical boundary conditions, with the exception of the numerical tripping plane. A free stream boundary condition was applied to the boundary plane of $y = 0.01m$ by specifying a zero gradient for the pressure and all three components of velocity. The outlet boundary plane at $y = 0.27m$ was specified as a fixed, uniform value of pressure, with zero gradient velocity components. Cyclic boundary conditions were applied to two boundary planes at

$z = L_z/2$ and $z = -L_z/2$. The inflow plane at $x = 0m$ contained fixed values of zero for the spanwise and wall-normal velocity components, and a zero gradient constraint on the pressure. The streamwise velocity component was applied as a steady-state, non-uniform field, which varies across the wall-normal direction in the form of the Blasius profile in Table 4.1.
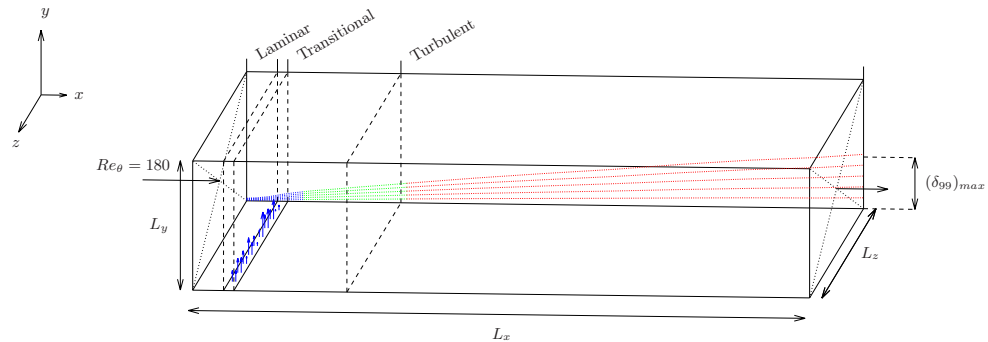
Figure 4.4: *The flow domain for a spatially developing boundary layer comprising, laminar, transitional and fully turbulent regimes within a single domain.*

Table 4.3 provides the configurations of the five simulation cases in the present analysis, in terms of the mesh, numerical trip and spanwise domain width. Case M2-T1-L1 and case M2-T2-L1, investigate the two configurations of the numerical trip; trip T1 and trip T2, given in Table 4.2, with a fixed spatial resolution (i.e. mesh M2). Case M1-T2-L2, case M2-T2-L2 and case M3-T2-L2 investigate influence of spatial resolution by comparing three different meshes with a fixed configuration for the numerical trip. Table 4.4 displays the inner-scaled cell dimensions of the three meshes; M1, M2 and M3. The friction velocity for the inner-scaling of the cell dimensions is taken from the point $x = 0.07m$ ($x/\theta_{in} = 2480$). The spanwise length varied as the methodology developed. For the first stage of simulations (case M2-T1-L1 and case M2-T2-L1) this width corresponded to over three times the predicted boundary layer thickness; $L_z = 0.012m \approx 2.25\delta_{99(max)}$. The resulting solution produced more accurate predictions of $\delta_{99(max)}$, and hence, for the remaining investigation of varying spatial resolution (case M1-T2-L2, case M2-T2-L2 and case M3-T2-L2) the computational

domain was reduced from $L_z = 0.012m \approx 3\delta_{99}$ to $L_z = 0.008m \approx 2\delta_{99}$, based on δ_{99} at

$x = 0.25m$.

Table 4.3: Configurations of tripping velocity, spatial resolution and spanwise width for the cases of spatially developing flow over a smooth wall.

Case	Mesh	Trip	L_z/θ_{in}	$N_T \left(\times 10^6\right)$	$\Delta t \left(u_\infty\right)_{in}/L_x \left(\times 10^{-5}\right)$
M2-T1-L1	M2	T1	425	42.4	6.11
M2-T2-L1	M2	T2	425	42.4	6.11
M1-T2-L2	M1	T2	283	12.6	7.96
M2-T2-L2	M2	T2	283	28.3	6.11
M3-T2-L2	M3	T2	283	62.9	4.70

Table 4.4: Inner-scaled cell dimensions for three meshes of varying spatial resolution.

Mesh	Δx^+	Δy^+_{max}	Δy^+_{min}	Δz^+
M1	54.9	54.9	1.30	27.6
M2	42.2	42.2	1.00	21.2
M3	32.5	32.5	0.77	16.3

Mesh M2, which is displayed in Figure 4.5, constitutes the base mesh which is applied in the investigation of the numerical trip in case M2-T1-L1 and case M2-T2-L1. For this base mesh, the near-wall cells are uniformly distributed in the streamwise and spanwise directions with a resolution of $\Delta x^+ \approx 42.2$ and $\Delta z^+ \approx 21.2$, based upon u_τ at the start of the fully developed region; $x/\theta = 2481$ ($Re_\theta = 1066$).The cells have a wall-normal resolution of $\Delta y^+_{min} \approx 1$ adjacent to the wall and expand uniformly between $y = 0m$ and $y = 0.04m$, where the maximum height is $\Delta y^+_{max} \approx \Delta x^+$.

The sub-grid stress from the unresolved turbulent length scales are modelled using the WALE sub-grid scale turbulence model. A recent validation of OpenFOAM for turbulent channel flow by Rezaeiravesh & Liefvendahl (2018) produced a recommended resolution of $\Delta x^+ \approx 18$ and $\Delta z^+ \approx 9$. However, this resolution rendered the WALE sub-grid scale either ineffective or detrimental in influencing the accuracy of the solution. Whilst omitting the WALE model reduced the excessive near-wall streamwise fluctuations, it degraded the accuracy of the friction velocity if the spanwise resolution was not increased. The streamwise and wall-normal resolution in mesh M2 lies close to
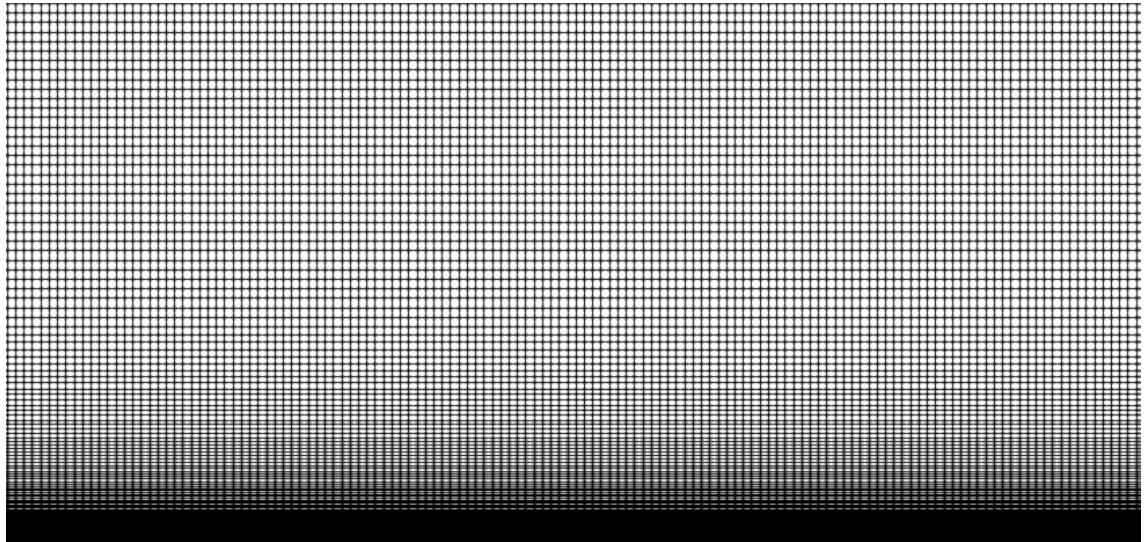
Figure 4.5: *Streamwise and wall-normal mesh distribution for a flow domain with mesh M2.*

that of solution of Arolla (2016), $\Delta x^+, \Delta z^+ \approx 45, 12$. The spanwise resolution is lower by a factor of 1.7, which more recent investigations have confirmed to be capable of supporting a resolved laminar-turbulent transition process (Mukha *et al.* 2019).

Second-order accurate central differencing schemes are used for spatial discretisation of the gradient (Equation 3.12) and divergence terms (Equation 3.8). Limiting is not applied to the gradient scheme in Equation (3.12) since all cells are fully orthogonal. All Laplacian terms are discretised using the Laplacian scheme in Equation (3.18). The second order accurate backward differencing scheme (Equation 3.26) is used to discretise all temporal terms.

The values of time shown in Table 4.3 are normalised by the time taken for the free-stream flow at the inlet to pass through the streamwise length of the domain; $L_x/(u_\infty)_{in}$. The time steps correspond to a maximum value of the Courant number of $Co < 0.7$, which produces a global average of $Co \approx 0.1$. The time-averaged value $\bar{\phi}$, and root mean square components ϕ_{rms}, of velocity and pressure are averaged continuously during the period of initial transience and full development. Once the physical time passes the averaging period, the time-averaged fields and the instantaneous fields are

weighted against the averaging period, such that the influence of the early transient state diminishes with time.

Spatial averaging, denoted by $\langle \cdot \rangle$, is applied to the time-averaged velocity values across the spanwise direction post run time. The wall shear stress value is then determined from the near-wall velocity gradient, based on the first cell at the wall, and the stationary wall boundary (Equation 4.8).

$$\langle \bar{\tau}_0 \rangle = \mu \left(\frac{\partial \langle \bar{u} \rangle}{\partial y} \right)_{y=0} \approx \mu \frac{\langle \bar{u} \rangle_{min}}{0.5 \Delta y_{min}}, \tag{4.8}$$

The spanwise averaged wall shear stress is normalised using the local free-stream velocity to produce the dimensionless coefficient of friction (Equation 4.9).

$$C_f = \frac{2}{\rho} \frac{\langle \bar{\tau}_0 \rangle}{\langle \bar{u}_\infty \rangle^2}, \tag{4.9}$$

The total run time in each case equalled 20 passes through the domain; $t = 20L_x/(u_\infty)_{in}$. The continuous averaging period spanned for $T_{av} = 10L_x/(u_\infty)_{in}$. Table 4.5 displays the temporal convergence in each case by comparing the shape factor H, and coefficient of friction C_f, at physical times of $t = 18L_x/(u_\infty)_{in}$ and $t = 20L_x/(u_\infty)_{in}$, and assessing the shift in H and C_f over a period of $2L_x/(u_\infty)_{in}$. Figure 4.6 and Figure 4.7 illustrate the variation in H and C_f over time in relation to the error associated with spatial resolution.

The temporal convergence is assessed at three points along the computational domain $x = 0.07m$, $x = 0.16m$ and $x = 0.25m$. The shape factor displays the strongest convergence compared with the coefficient of friction. At all three locations, the shape factor does not vary more than 0.1% between $t = 18L_x/(u_\infty)_{in}$ and $t = 20L_x/(u_\infty)_{in}$ in each simulation. As the boundary layer moves along the streamwise direction, the

(a) $x = 0.07m$
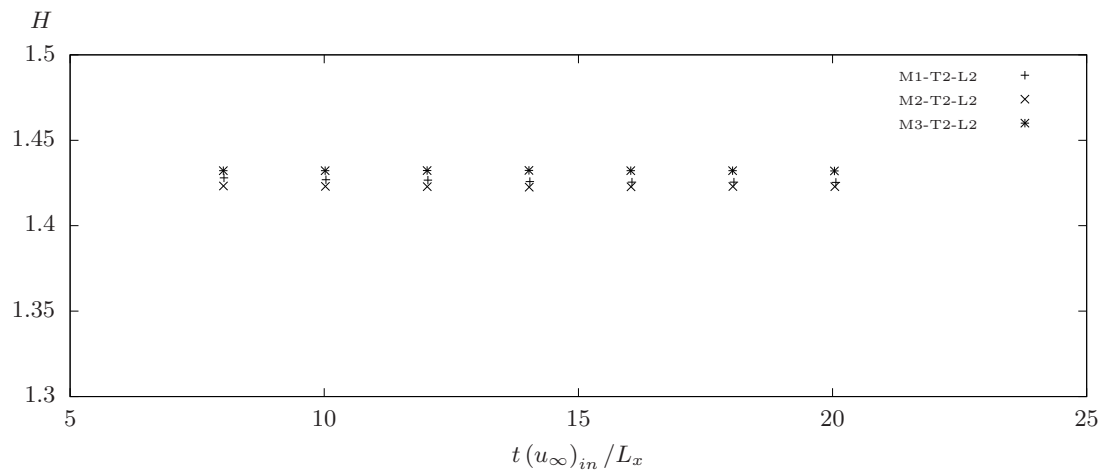
(b) $x = 0.16m$
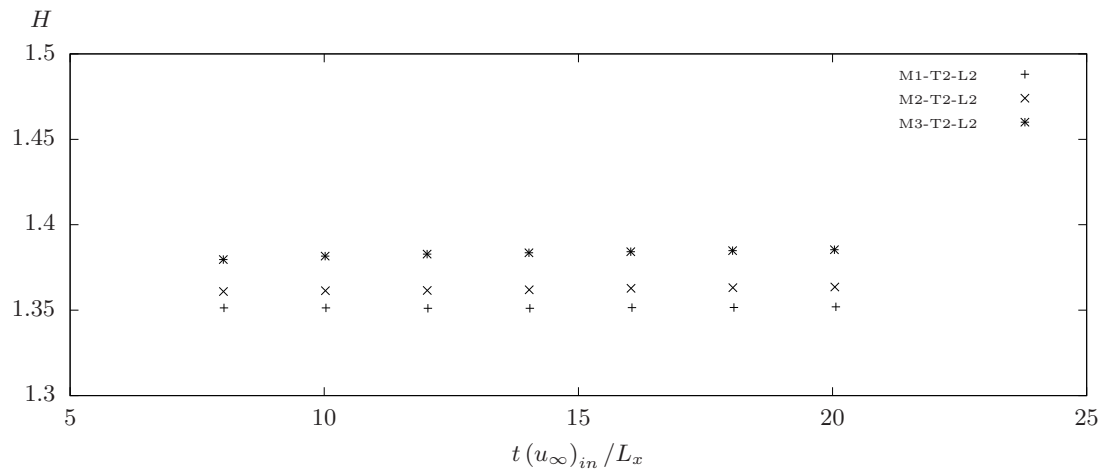
(c) $x = 0.25m$
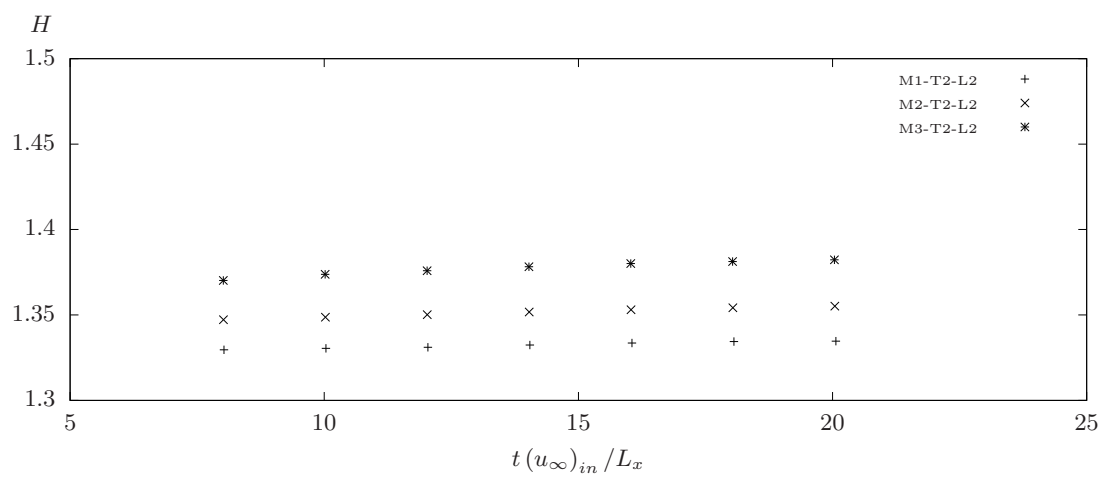
Figure 4.6: *Temporal convergence of the shape factor H, for three levels of spatial resolution over a smooth wall.*

(a) $x = 0.07m$
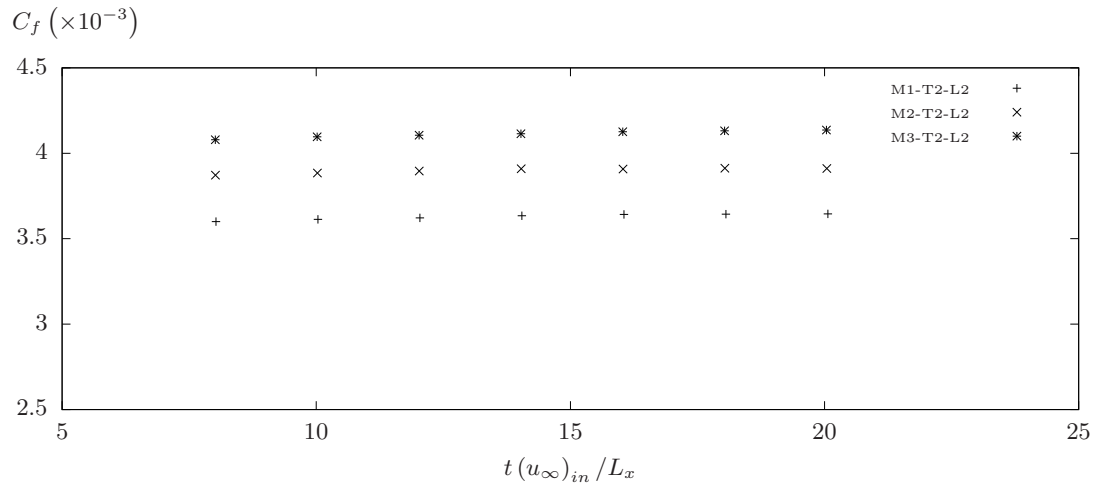
(b) $x = 0.16m$
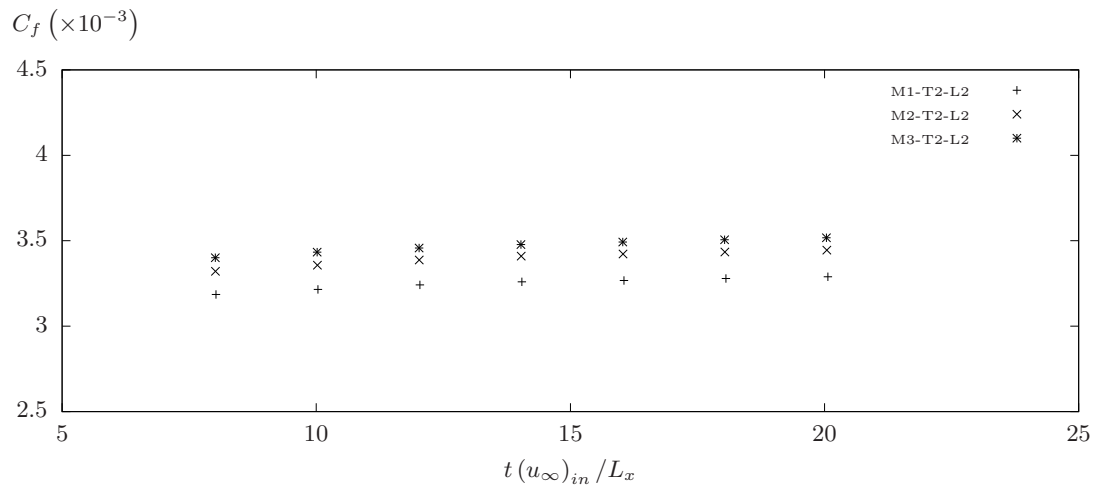
(c) $x = 0.25m$
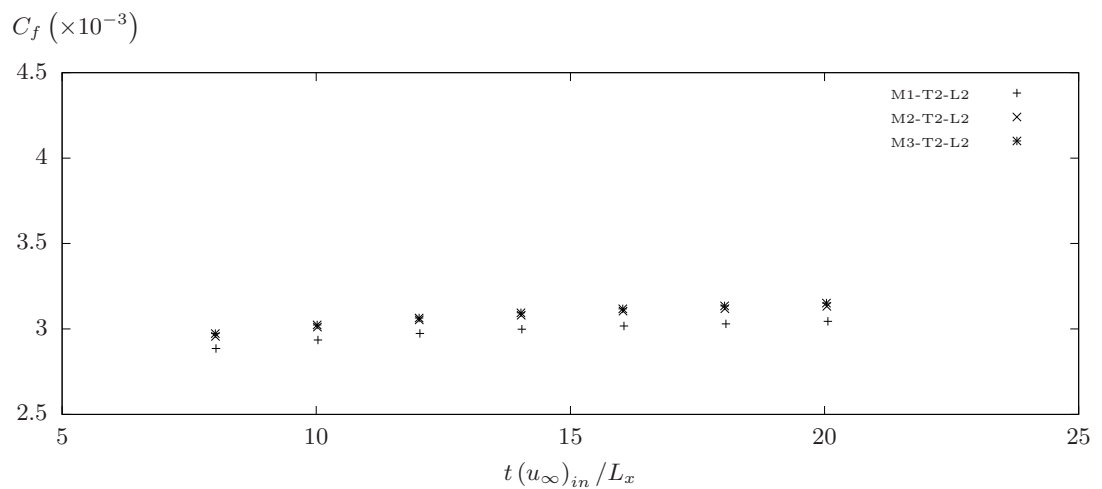
Figure 4.7: *Temporal convergence of the coefficient of friction C_f, for three levels of spatial resolution over a smooth wall.*

Table 4.5: Temporal variation of shape factor and coefficient of friction in each smooth wall boundary layer simulation.

Case	$x\,(m)$	$t\,(u_\infty)_{in}\,/L_x$	H	$C_f\,(\times 10^{-3})$	$\Delta H\,(\%)$	$\Delta C_f\,(\%)$
M2-T1-L1	0.07	18	1.494	4.157		
		20	1.494	4.162	+0.01	+0.11
	0.16	18	1.374	3.512		
		20	1.373	3.532	−0.04	0.55
	0.25	18	1.356	3.158		
		20	1.357	3.177	+0.02	+0.61
M2-T2-L1	0.07	18	1.423	3.907		
		20	1.423	3.910	+0.00	+0.07
	0.16	18	1.364	3.437		
		20	1.364	3.443	+0.03	+0.20
	0.25	18	1.354	3.124		
		20	1.355	3.136	+0.06	+0.37
M1-T2-L2	0.07	18	1.426	3.644		
		20	1.425	3.646	−0.03	+0.05
	0.16	18	1.352	3.279		
		20	1.352	3.289	+0.03	+0.31
	0.25	18	1.334	3.030		
		20	1.335	3.044	+0.02	+0.48
M2-T2-L2	0.07	18	1.423	3.913		
		20	1.423	3.911	+0.00	−0.04
	0.16	18	1.363	3.434		
		20	1.364	3.445	+0.03	+0.32
	0.25	18	1.354	3.119		
		20	1.355	3.133	+0.07	+0.45
M3-T2-L2	0.07	18	1.432	4.131		
		20	1.432	4.136	−0.01	+0.12
	0.16	18	1.385	3.506		
		20	1.385	3.517	+0.04	+0.34
	0.25	18	1.381	3.135		
		20	1.382	3.151	+0.08	+0.52

variation between the three levels of spatial resolution grows, such that the influence of spatial resolution on H exerts an influence which greatly exceeds that of the error due to temporal convergence, as shown in Figure 4.6c.

In contrast to the shape factor, the variation in the coefficient of friction between $t = 18L_x/(u_\infty)_{in}$ and $t = 20L_x/(u_\infty)_{in}$ grows along the domain, whilst the influence of the spatial resolution decreases. This only become significant at the point $x = 0.25m$ (Figure 4.7c), where the variation in C_f between mesh M2 and mesh M3 is of equal magnitude to the error due to temporal convergence. At the points $x = 0.07m$ and

$x = 0.16m$, the spatial resolution continues to exert a dominant influence on C_f. Of the three cases displayed in Figure 4.7, case M3-T2-L2 displayed the greatest variation in C_f of +0.52%. However, running case M3-T2-L2 for a further time of $t = 24L_x/(u_\infty)_{in}$ altered the coefficient of friction by less than +0.1% for $Re_\theta < 2000$ and by +0.3% towards the end of the domain, when compared to the solution at $t = 20L_x/(u_\infty)_{in}$.

4.3 Trip Response

4.3.1 Coherent Structures

Firstly, consider the response of the physical flow in the region of the trip. Figure 4.8 displays the initiation and growth of coherent turbulent structures downstream of the trip for tripping velocities of $v'^+_{ref} = 0.551$ (Figure 4.8a) and $v'^+_{ref} = 1.102$ (Figure 4.8b). These structures are visualised through the second invariant of the velocity gradient tensor Q. The Q criterion defines a vortex based on the the strain-rate tensor S_{ij}, and the asymmetric vorticity tensor Ω_{ij}. The definitions of S_ij and Ω_ij are presented in Section 1.3.4. A vortex exists where the square of the norm of the asymmetric vorticity tensor $\Omega_{ij}\Omega_{ij}$, is greater than the square of the norm of the symmetric strain-rate tensor $S_{ij}S_{ij}$, such that $Q > 0$ (Equation 4.10).

$$Q = \frac{1}{2}\left(\Omega_{ij}\Omega_{ij} - S_{ij}S_{ij}\right), \tag{4.10}$$

Each boundary layer in Figure 4.8 is divided into two segments to visualise different length scales. One segment displays the large-scale structures in the outer region with a criterion of $Q > 5 \times 10^5 1/s$ (left). The other segment displays small-scale structures closer to the wall with a criterion of $Q > 5 \times 10^8 1/s$ (right).

(a) *Case M2-T1-L1*
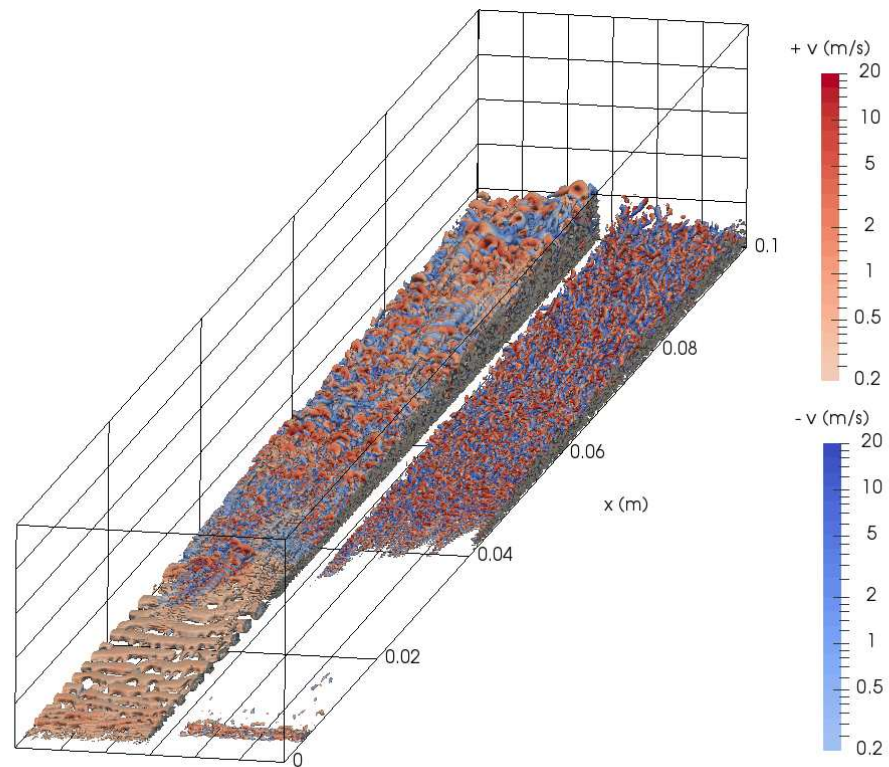
(b) *Case M2-T2-L1*
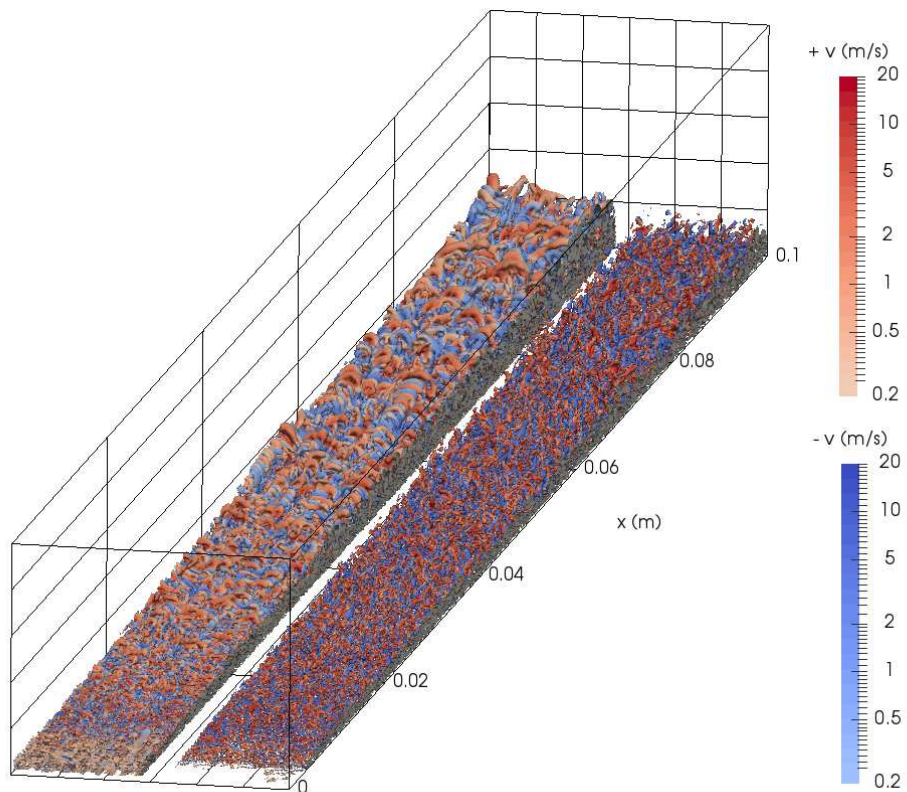
Figure 4.8: *Development of coherent turbulent structures in the laminar and transitional regimes downstream of a numerical trip for two values of the tripping velocity.*

Initial testing investigated a tripping velocity equal to 0.91% of the free stream velocity at the inlet. The low trip velocity induces large, two-dimensional disturbances, with minimal spanwise variation, into the laminar boundary layer, similar to those visible early on in Figure 4.8a. The collection of small scale structures which form at the trip rapidly dissipate downstream. The two-dimensional disturbances then continue to propagate downstream and the flow maintains a growth rate for Re_θ which correlates to the theoretical Blasius solution with an upstream shift in the streamwise boundary layer origin.

Raising the tripping velocity to $v'^+_{ref} = 0.551$ produces the same large-scale disturbances as before, whilst the small-scale, three-dimensional structures rapidly dissipate beyond the trip. Once the flow reaches $x = 0.04m$ these large-scale disturbances give way to three-dimensional periodic structures, although the resolution is not sufficient, even in the highest resolution of mesh M3 (case M3-T2-L2), to confirm the existence of hairpin vortices. This weaker trip does not initiate transition until the flow has reached the upper limits of the recommended range for the transition point; $Re_\theta < 300$. Doubling the strength of the trip to $v'^+_{ref} = 1.105$ produces a rapid destabilisation of the laminar flow, in which the point of transition lies firmly within $Re_\theta < 200$. The small-scale coherent structures which form at the trip continue to propagate downstream.

As a result the weaker trip of $v'^+_{rms} = 0.551$ reached a Reynolds number of $Re_\theta = 1000$ at a distance of $x = 3500\theta_{in}$ downstream of the inlet. Increasing the strength to $v'^+_{ref} = 1.105$ reduces this distance to $x = 2480\theta_{in}$. After $Re_\theta = 1000$, the two boundary layers continue to grow at similar rates. The lag of the weaker trip case at a fixed streamwise location behaves as a simple shift of the boundary layer origin. This shift reduces the effective domain length by approximately 10% in comparison to a trip of $v'^+_{ref} = 1.105$.

4.3.2 Free-Stream Constriction

As expected, the growth of the boundary layer within the confines of the domain produces a favourable pressure gradient as the effective free-stream area shrinks downstream of the trip. For a spatially developing boundary layer at equilibrium, the Clauser pressure gradient parameter β, (Clauser 1956) defined by Equation (4.11), will be constant along the streamwise length of the domain.

$$\beta = \frac{\delta^*}{\langle \bar{\tau}_0 \rangle} \frac{d\langle \bar{p} \rangle_\infty}{dx},\qquad(4.11)$$

Downstream from the onset of transition, the time-averaged mean static pressure of the free-stream flow falls non-linearly along the domain. The magnitude of the negative pressure gradient parameter increases as the boundary layer grow along the streamwise direction. The maximum value, located shortly upstream of the end of the domain $(x = 7795\theta_{in})$, lies within the range $|\beta| = 0.038 \approx 0.043$. The fixed atmospheric conditions at the outlet of the domain produces short, periodic pressure distortions along the domain. However, the effect of these fluctuations is limited to the time-averaged root mean square of the pressure variables over the full averaging window.

4.3.3 Boundary Layer Growth

The shape factor is the ratio of the local displacement thickness to the local momentum thickness $H = \delta^*/\theta$, and provides a strong indicator of the local state of boundary layer development. The value of H falls asymptotically as the scaled free-stream velocity $\langle \bar{u} \rangle_\infty^+$, rises. The profile in Equation (4.12) approximates the distribution of H as a

function of Reynolds number, local variable I_u and the constants κ and C.

$$H_{est} = \left(1 - \frac{I_u}{\kappa^{-1}ln\left(\langle\bar{u}\rangle_\infty \delta^*/\nu\right) + C} \right)^{-1}, \tag{4.12}$$

$$I_u = \frac{1}{\delta^*\langle\bar{u}\rangle_\infty^+} \int_0^\infty \left(\langle\bar{u}\rangle_\infty^+ - \langle\bar{u}\rangle^+\right)^2 \quad dy, \tag{4.13}$$

In a zero-pressure gradient boundary layer at equilibrium, the value of I_u is ideally constant along the domain, based upon a collapse of published experimental datasets (Chauhan *et al.* 2009). The constants take the form of $\kappa = 0.384$ and $C = 3.3$. Figure 4.9 displays the evolution of the shape factor H, with the Reynolds number, Re_θ, for two different values of tripping velocity (Equation 4.7). The results are compared against the Clauser relations for an ideal zero-pressure gradient flow.
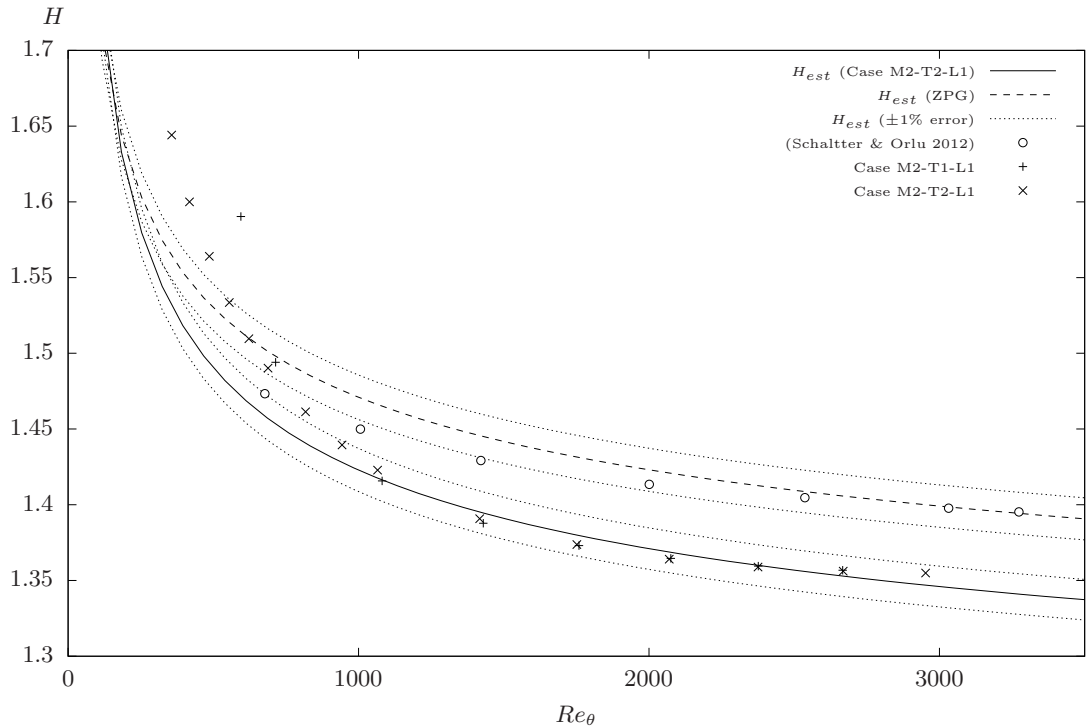
Figure 4.9: *Evolution of the shape factor H, with the growth of Re_θ downstream of the tripping plane.*

Given the non-zero value of β, and the uncertainty of the downstream influence of the trip, new coefficients are determined for Equation (4.12), based upon the flow field of case M2-T2-L1. The best fit line for u_∞^+ as a function of $\langle\bar{u}\rangle_\infty \delta^*/\nu$ produces values

of $\kappa = 0.3052$ and $C = -1.908$. The value of I_u is dependant on Re_θ during transition and the early turbulent regime, but stabilised at $I_u = 6.502 \pm 0.12$ within the region of $Re_\theta > 1415$. These adjusted constants shift the asymptotic limit for the Clauser relation whilst maintaining the general profile shape. By $Re_\theta > 1350$, the value of H_{est} for case M2-T2-L2 lingers below the approximation for a zero-pressure-gradient solution by roughly 5%.

The tripping velocity displays a mild influence on the shape factor distribution at low Reynolds numbers. For $Re_\theta > 1000$ this influence diminishes as both boundary layers collapse onto the adjusted shape factor approximations within an error bound of $\pm 1\%$, and stays within these bounds along the remainder of the domain. At this point, the relation of H in relation to Equation (4.12) is consistent with the $\pm 1\%$ variation for similar zero-pressure gradient DNS solutions resulting from differences in domain dimensions and tripping effects Schlatter & Orlu (2010). However, in case M2-T1-L2 and case M2-T2-L2 the trend of H is not consistent with H_{est} towards the end of the domain. Beyond $Re_\theta = 2000$ the rate of change of H once again deviates from H_{est} and H starts to stabilize around $H \approx 1.35$.

Figure 4.10 compares the evolution of the coefficient of friction, C_f (Equation 4.9), downstream of the numerical trip for two different values of tripping velocity (Equation 4.7). This distribution is assessed against the Coles-Felnholz (Coles 1956) log-law relation in Equation (4.14), in addition to the results from the numerical solutions displayed in Figure 4.9.

$$\left(C_f\right)_{Coles} = 2 \left(\frac{1}{0.384} \ln Re_\theta + 4.127 \right)^{-2}, \tag{4.14}$$

The strength of the numerical trip and the numerical spatial resolution produce
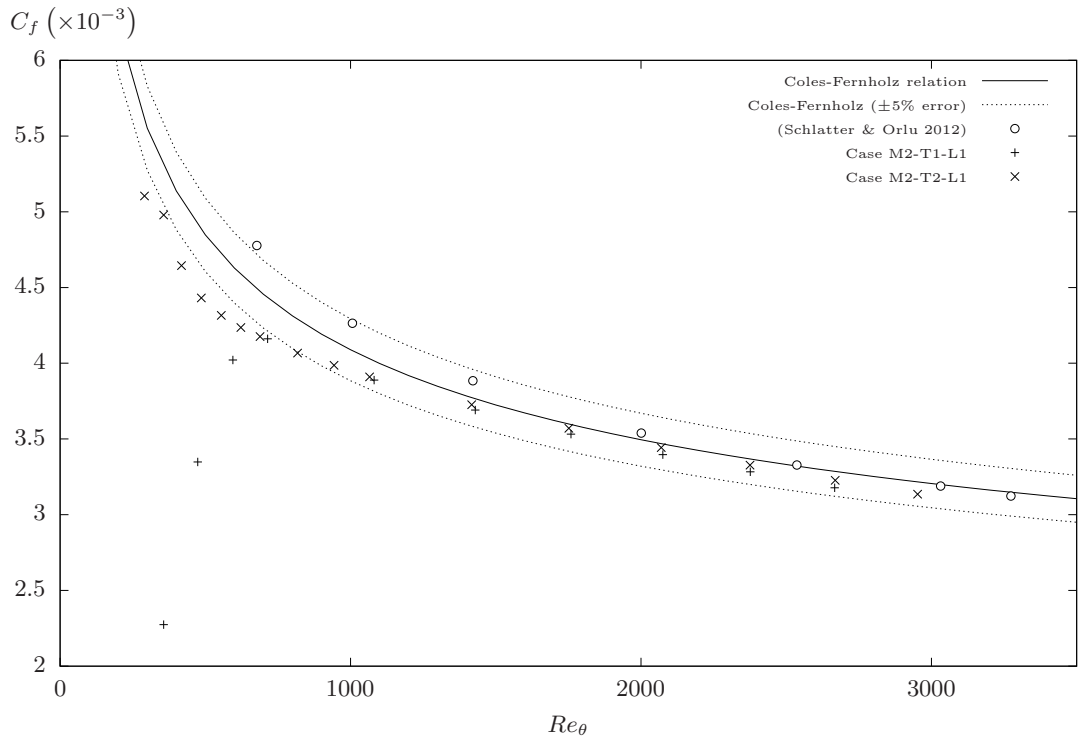
Figure 4.10: *Evolution of the coefficient of friction C_f, with the growth of Re_θ downstream of the tripping plane.*

their strongest influence on C_f within the transitioning boundary layer. For case M2-T2-L1, the delay in transition caused by the weaker trip T1, greatly extends the early stages of the transitional regime, such that the development of C_f provides no relation to the log-law relation until $Re_\theta = 700$. Beyond this point, the flow rapidly conforms to the magnitude and form expected for a fully turbulent flow. For both trip configurations, the downstream boundary layer approaches to within a $\pm 3\%$ tolerance of the log-law relation by $Re_\theta = 1000$. However, it is at this point that the location of the numerical trip appears to exert its strongest influence. As the boundary layer grows beyond $Re_\theta = 1000$, all flows tripped within the limit of $Re_\theta < 300$, continue convergence towards the log-law relation.

4.3.4 Turbulent Profiles

The time-averaged mean and root mean squared velocity values are taken as spatial averages across the full width of the domain, and are scaled against a spatially and temporally averaged friction velocity. Figure 4.11 displays the profiles inner-scaled mean streamwise velocity profiles for discrete values of Re_θ. Figure 4.12 and Figure 4.13 display the distribution of the inner-scaled streamwise velocity fluctuations $\langle \bar{u}'_{rms} \rangle^+$, wall-normal velocity fluctuations $\langle \bar{v}'_{rms} \rangle^+$, and Reynolds shear stress $-\langle \bar{u'v'} \rangle^+$, across the boundary layer for discrete values of Re_θ. For reference, these graphs display profiles of the flat plate OpenFOAM solutions of Arolla (2016) at $Re_\theta = 1410$, and highly resolved spectral solution of Schlatter & Orlu (2010) for Re_θ up to $Re_\theta \approx 3030$.
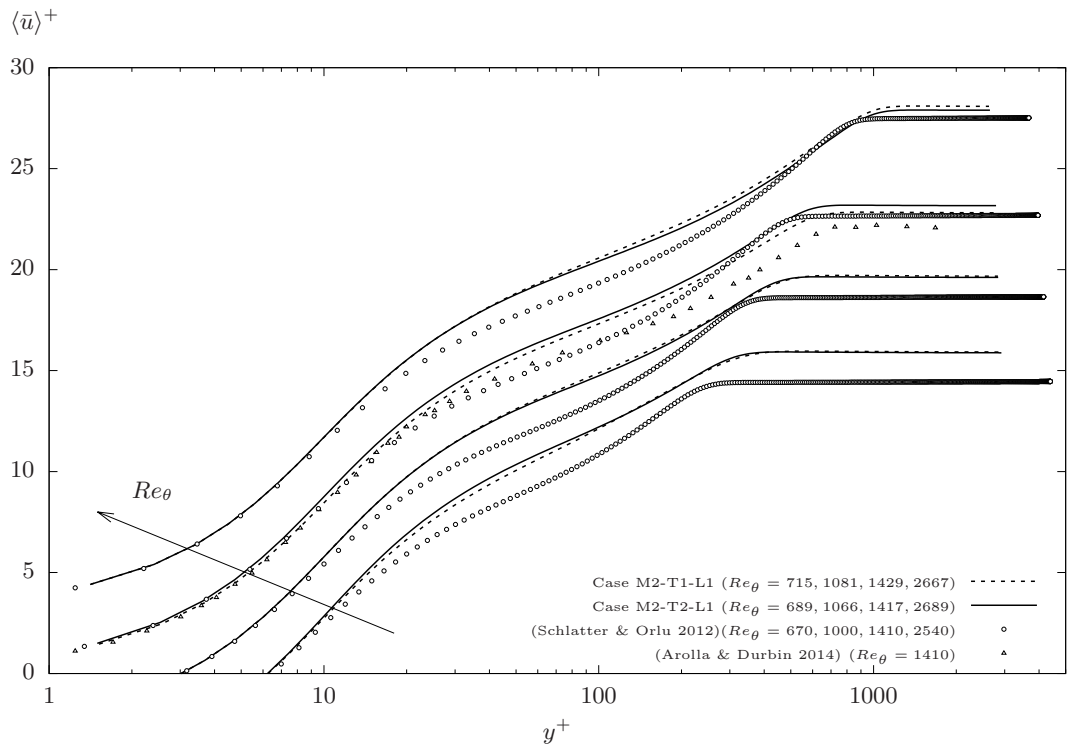
Figure 4.11: *Distribution of the inner-scaled, time-averaged streamwise velocity. For clarity, each set of profiles for a given magnitude of Re_θ have been vertically offset in intervals of 5 viscous units.*

For the streamwise velocity, all profiles maintain a strong fit to the expected relation of $u^+ = y^+$ throughout the viscous sub-layer. Within the log-law region, there is a clear log-law mismatch which improves only marginally beyond $Re_\theta \approx 1000$. The upwards

(a) *RMS of streamwise velocity fluctuations*
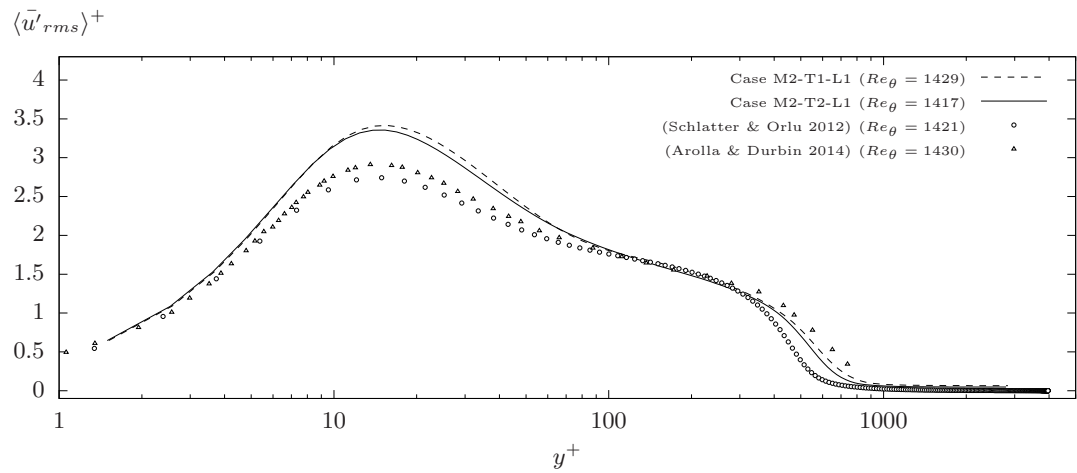
(b) *RMS of wall-normal velocity fluctuations*
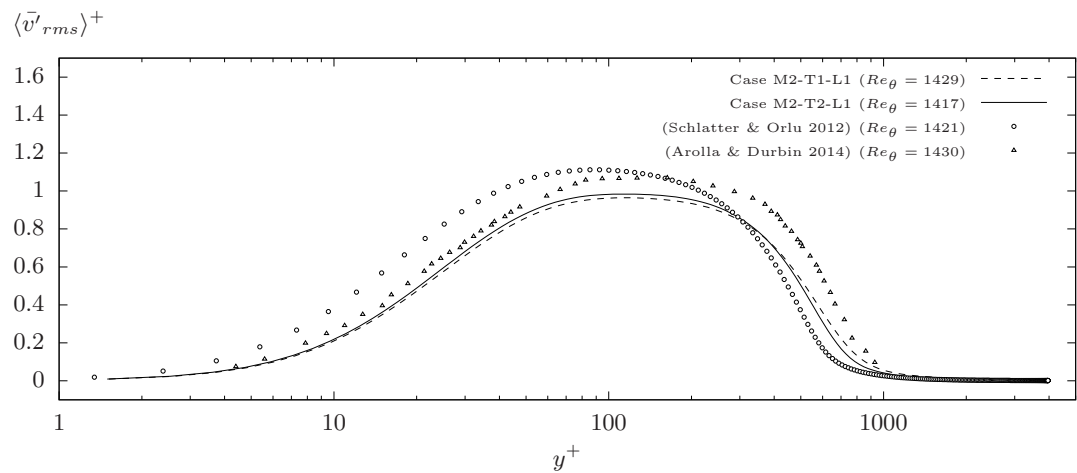
(c) *Reynolds shear stress*
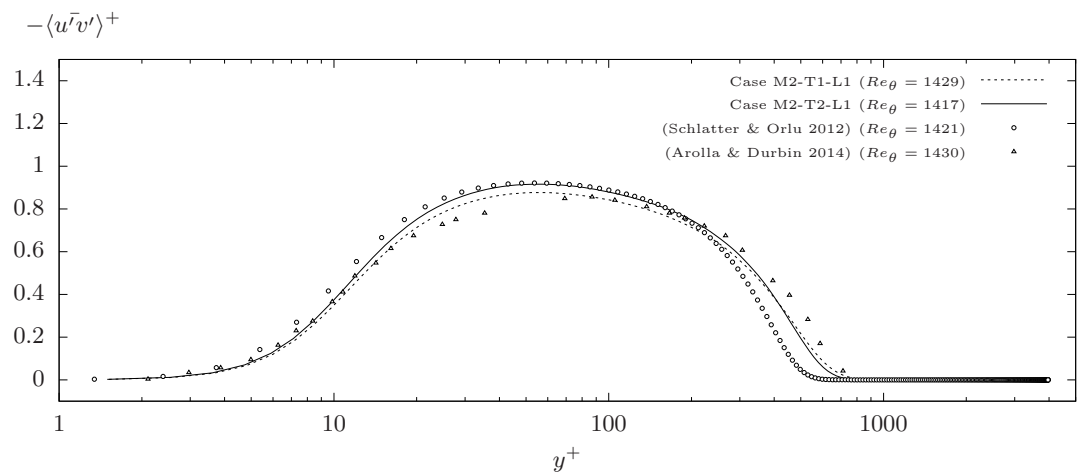
Figure 4.12: *Comparison of the distribution of turbulent stress components over a smooth wall for various tripping velocities.*

(a) *RMS of streamwise velocity fluctuations*
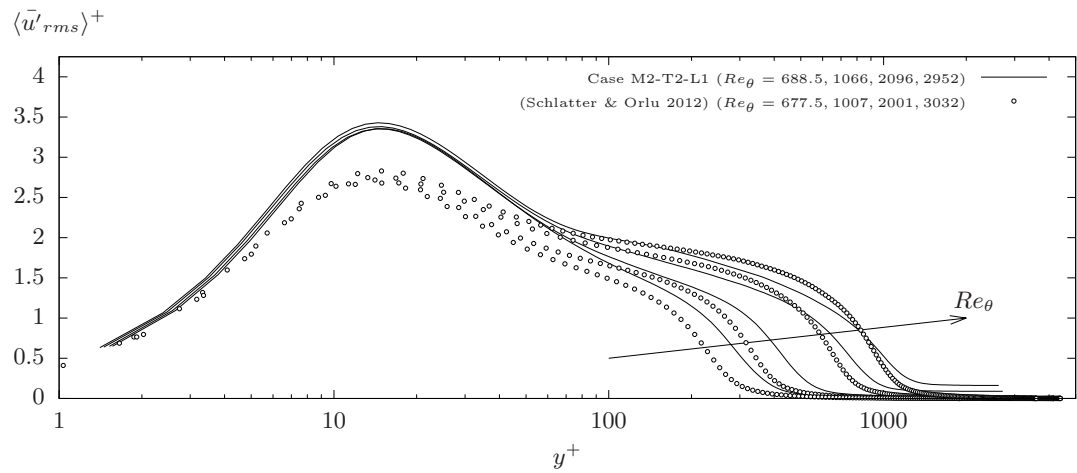
(b) *RMS of wall-normal velocity fluctuations*
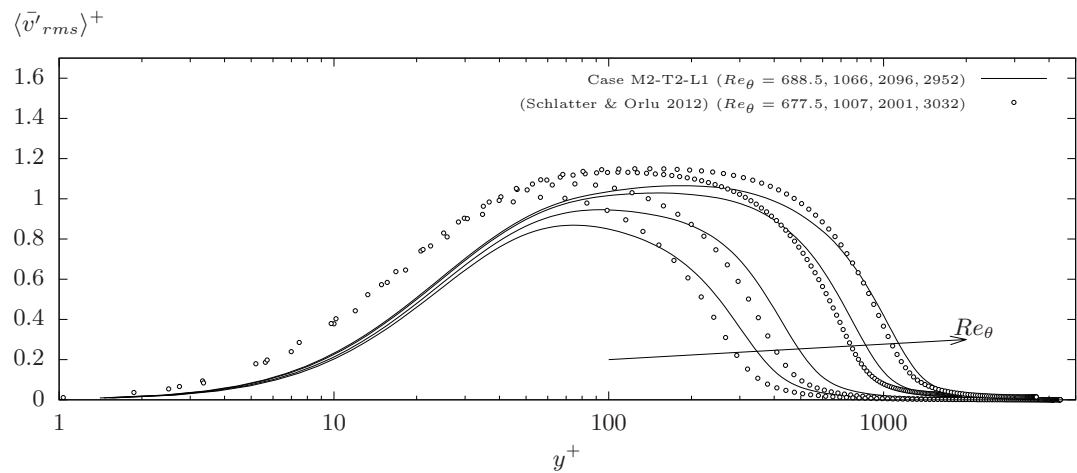
(c) *Reynolds shear stress*
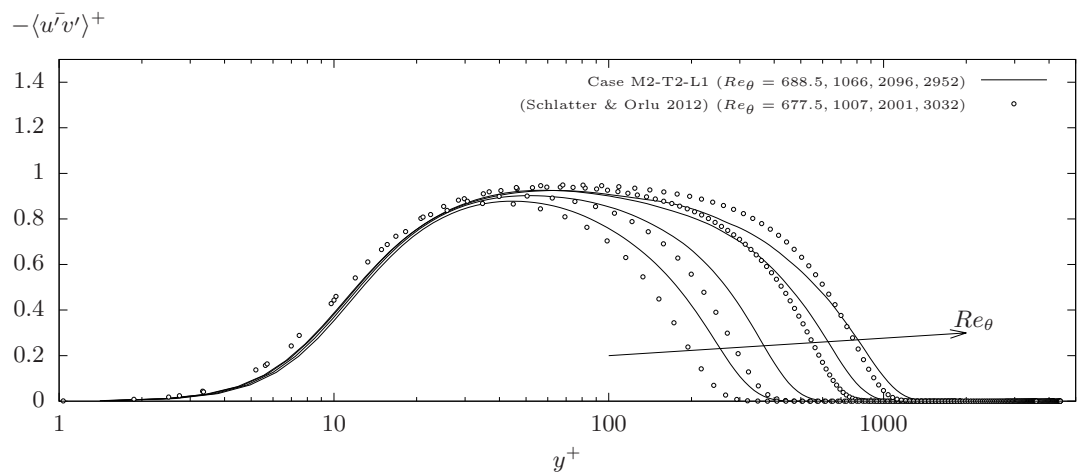
Figure 4.13: *Evolution of turbulent stress components over a smooth wall downstream of the optimal numerical trip.*

shift is consistent with an reduction in the flow resistance for drag reducing flow control, or in this case, an underprediction of C_f.

For the turbulent shear stresses produced by the current model, the direct influence of the tripping strength begins to vanish by $Re_\theta = 1000$. Figure 4.12 displays minimal variation between the weaker and stronger trip in the current model at $Re_\theta \approx 1410$. In relation to the reference DNS solution, the current model overpredicts the maximum streamwise velocity fluctuations, and underpredicts the wall-normal velocity fluctuations, throughout the shear layer. The scale of these discrepancies remains consistent along the length of the domain. This includes the region from $Re_\theta > 2000$, for which the effects of the tripping condition are expected have dissipated, and the shape factor collapses onto the adjusted Clauser relation (Figure 4.10). Notably, despite having a smaller streamwise resolution, the profiles of Arolla do not contain such a significant overprediction of $\langle \bar{u}'_{rms} \rangle^+$ across the across the logarithmic region and more than half the distance of the outer region $5 < y^+ < 300$. The improvement in $\langle \bar{v}'_{rms} \rangle^+$ is less significant in the inner region, whilst the larger maximum at $y^+ \approx 100$ translates into excessive wall-normal fluctuations throughout the outer region.

As observed in the channel flow of Rezaeiravesh & Liefvendahl (2018), recall that the accuracy of the wall shear stress for large-eddy simulation in OpenFOAM, at least within the WALE model, depends first and foremost on the spanwise resolution near the wall. On the other hand, the outer region, which scales with flow geometry, depends primarily on the downstream inflow or development conditions. Finally, the Reynolds shear stress $-\langle \bar{u}'v' \rangle^+$ displays the strongest agreement with the DNS solution through the domain. As for $\langle \bar{u}'_{rms} \rangle^+$ and $\langle \bar{v}'_{rms} \rangle^+$, the inner region collapses onto the DNS solution first, showing a good, consistent collapse by $Re_\theta = 700$. The outer region follows with a gradual collapse as Re_θ grows.

4.4 Influence of Spatial Resolution

Since the maximum boundary layer thickness resulting from $v'^+_{ref} = 1.105$ is known, the domain dimensions can be optimised by reducing the spanwise width to the minimum length that is required to contain two large-scale coherent turbulent structures, which each have a spanwise width of roughly $0.85\delta_{99}$ (Schlatter *et al.* 2010). Reducing the spanwise domain width to twice the width of the maximum boundary layer thickness (case M2-T2-L1 $\rightarrow$ case M2-T2-L2) altered the value of C_f by less than $\pm0.2\%$ along the region of $Re_\theta > 1000$. A comparison of the wall-normal profiles of $\langle\bar{u}'_{rms}\rangle^+$, $\langle\bar{v}'_{rms}\rangle^+$ and $-\langle\bar{u'v'}\rangle^+$ at $x = 8858\theta_{in}$ displayed no visible change at all points across the full width of the boundary layer.

The accuracy and validity of the current model in solving a spatially developing, zero-pressure gradient boundary layer depends on a combination of the usual numerical errors and the lingering effects of the upstream laminar-turbulent transitional flow. To isolate and observe the contribution from the spatial resolution errors case M1-T2-L2, case M2-T2-L2 and case M1-T2-L2 compare three levels of spatial resolution with a fixed numerical trip of $v'^+_{ref} = 1.105$. The influence of spatial resolution on boundary layer growth is assessed by the shape factor (Figure 4.14) and the coefficient of friction (Figure 4.15). Increasing the spatial resolution to $\Delta x^+ = 32.5$ and $\Delta z^+ = 16.3$ produced a minor delay in the onset of transition. However, downstream of the transition the rate of growth, in terms of Re_θ, appears to accelerate with increasing spatial resolution.

Under a near-wall cell width of $\Delta x^+, \Delta z^+ = 54.9, 27.6$ in mesh M1 (case M1-T2-L2) and $\Delta x^+, \Delta z^+ = 42.2, 21.2$ in mesh M2 (case M2-T2-L2), the boundary layer growth conforms to the general trend of the Coles-Fernholz log-law relation by $Re_\theta \approx 300$.
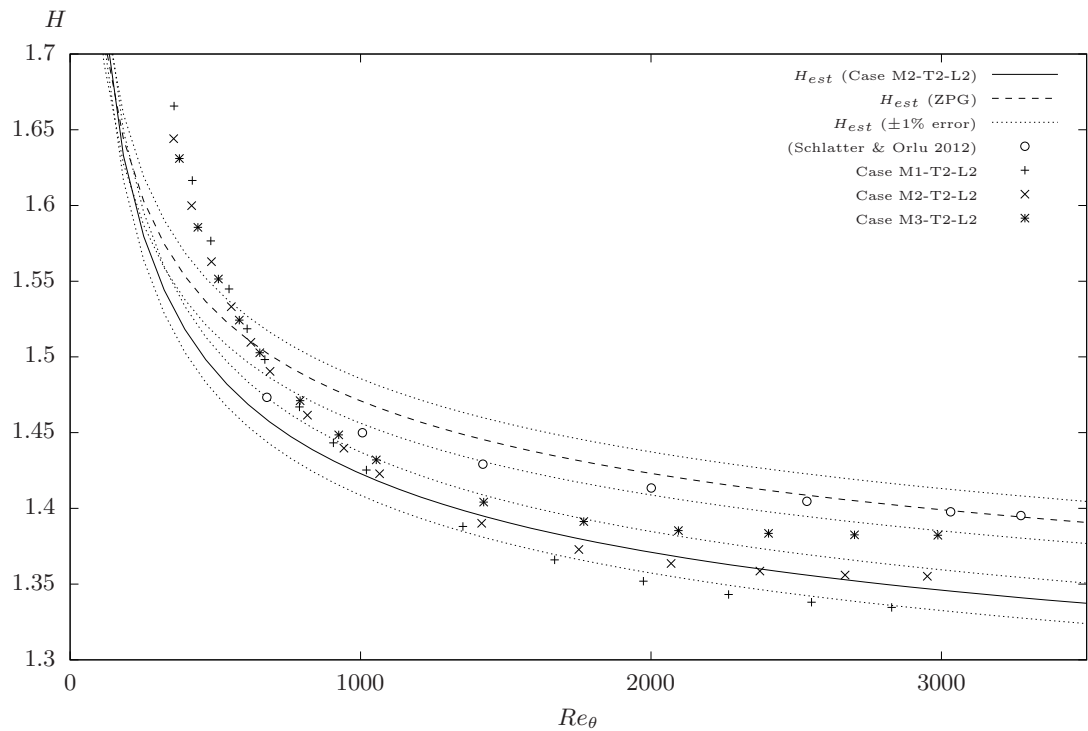
Figure 4.14: *Evolution of the shape factor H, with the growth of Re_θ downstream of the tripping plane for three levels of spatial resolution.*
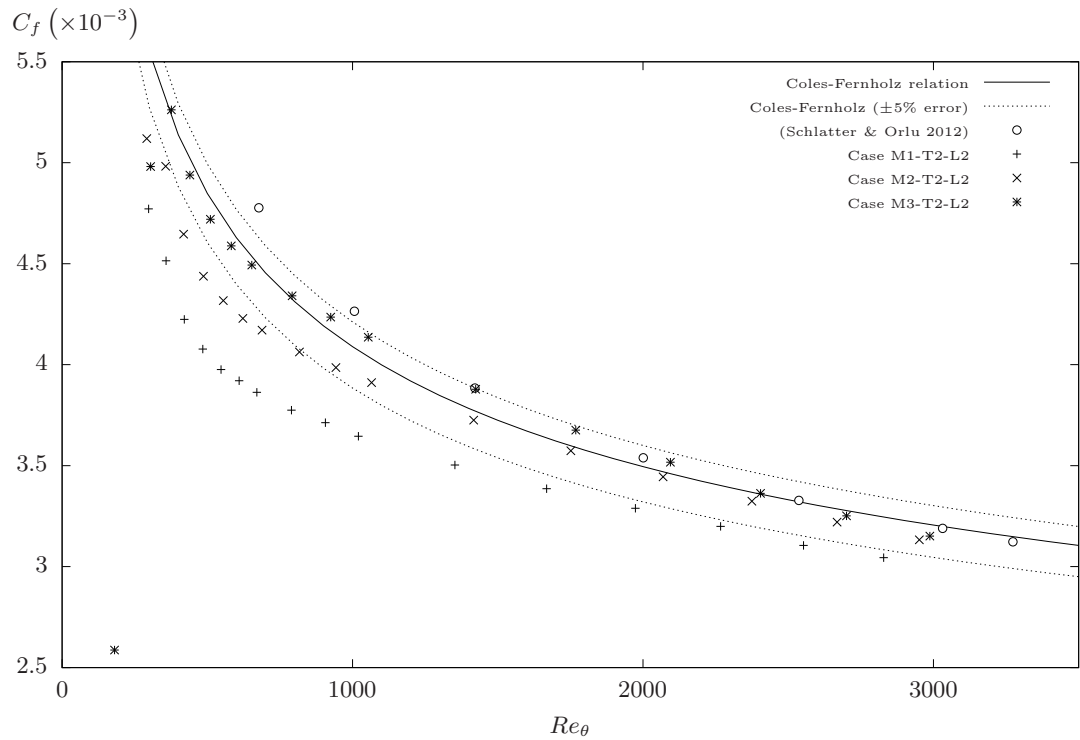
Figure 4.15: *Evolution of the coefficient of friction C_f, with the growth of Re_θ downstream of the tripping plane for three levels of spatial resolution.*

However, whereas case M2-T2-L2 converges onto Equation (4.14) as the boundary layer grows, case M1-T2-L2 displays an irregular development within the transitional and early turbulent region of $Re_\theta < 1000$, by diverging from the form of Equation (4.14). Eventually, the growth follows the trend of Equation (4.14) and remains outside the 5% tolerance bounds whilst not showing signs of further convergence, leaving a continual under prediction of more than 5%. Despite a minor delay in transition, case M3-T2-L2 displays the fastest convergence towards the Coles-Fernholz relation, and reaches the $\pm 3\%$ error band as early as $Re_\theta \approx 400$, or a distance of $x = 531\theta_{in}$ downstream of the inlet. Case M3-T2-L2 showed an improved agreement with both the Coles-Fernholz log-law relation in Equation (4.14) and the reference DNS results beyond $Re_\theta \approx 2000$.

In contrast to the coefficient of friction, the shape factor growth, shown in Figure 4.14, displays a negligible dependence on the spatial resolution throughout the transitional region. As the boundary layer develops beyond $Re_\theta = 800$, the rate of convergence, and the apparent asymptotic limit, increase with the spatial resolution. The finest resolution brings the shape factor to within 1.5% of the zero-pressure gradient Clauser relation towards the end of the domain, $Re_\theta \approx 3000$.

Figure 4.16, Figure 4.17 and Figure 4.18 display the distribution of streamwise and wall-normal velocity fluctuations, and Reynolds shear stress, across the boundary layer, for increasing levels of spatial resolution in cases M1-T2-L2, M2-T2-L2 and M3-T2-L2 at streamwise locations of $x = 0.07m$ ($Re_\theta \approx 1000$), $x = 0.16$ ($Re_\theta \approx 2000$) and $x = 0.25m$ ($Re_\theta \approx 3000$). Additional plots for the distribution of the time-averaged streamwise velocity and the spanwise velocity fluctuations are provided in Appendix B. Refining the spatial resolution between the three cases had a minimal impact on the turbulent stress distribution across the outer region, whilst reducing the streamwise velocity overshoot in the inner region and scaling the profile of $\langle \bar{u}'_{rms} \rangle^+$

(a) *RMS of streamwise velocity fluctuations ($x = 0.07m$)*
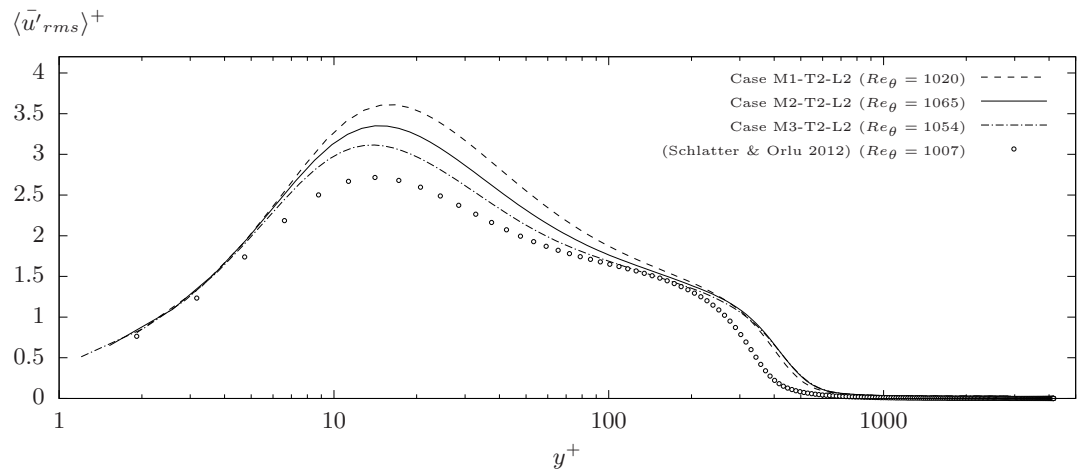
(b) *RMS of wall-normal velocity fluctuations ($x = 0.07m$)*
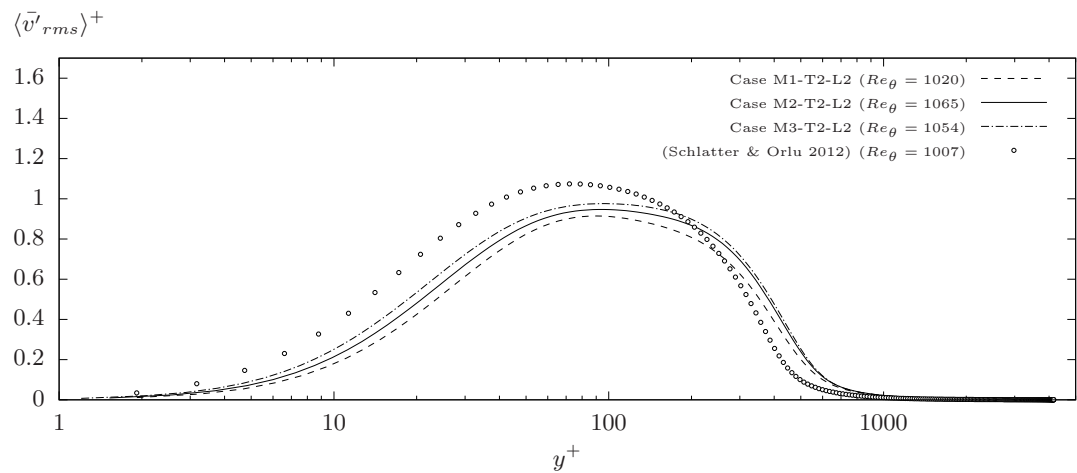
(c) *Reynolds shear stress ($x = 0.07m$)*
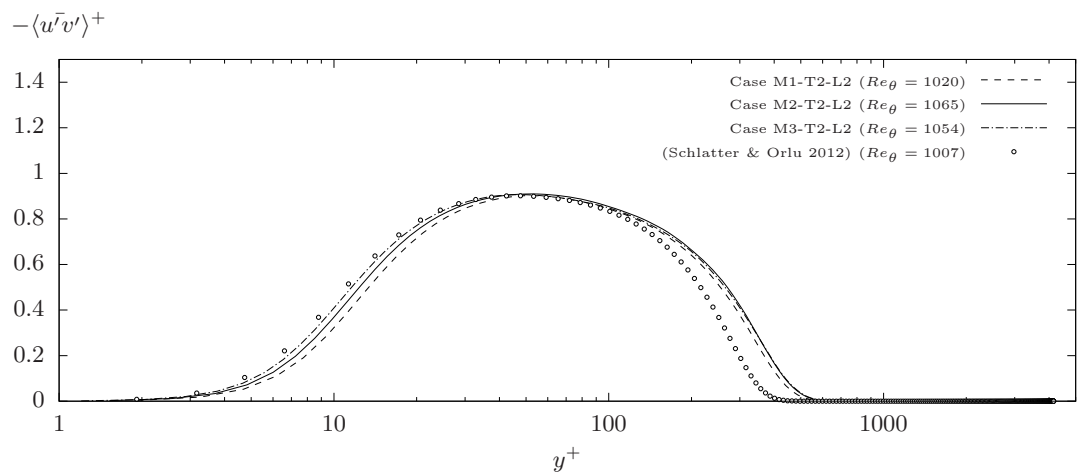
Figure 4.16: *Comparison of the distribution of turbulent stress components at $x = 0.07m$ along a smooth wall for three levels of spatial resolution.*

(a) *RMS of streamwise velocity fluctuations ($x = 0.16m$)*

$\langle \bar{u}'_{rms} \rangle^+$

y^+

(b) *RMS of wall-normal velocity fluctuations ($x = 0.16m$)*

$\langle \bar{v}'_{rms} \rangle^+$

y^+
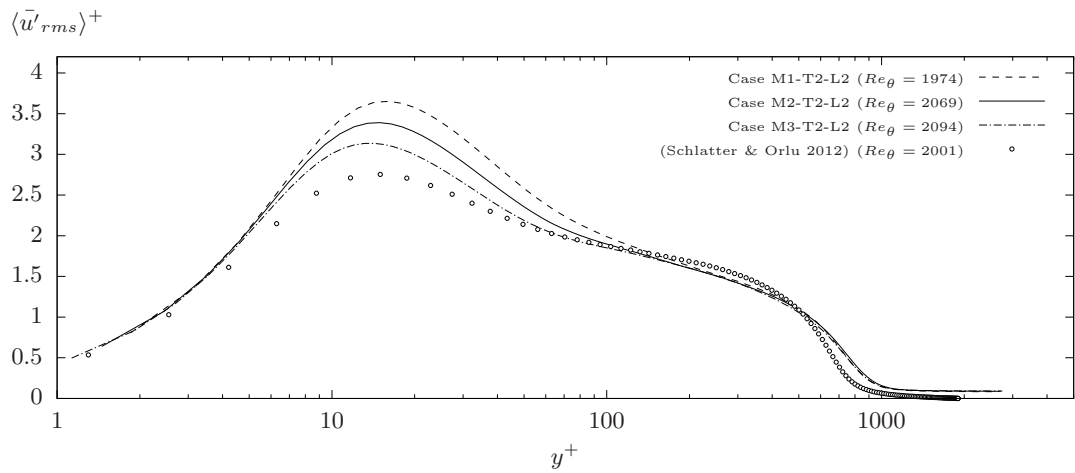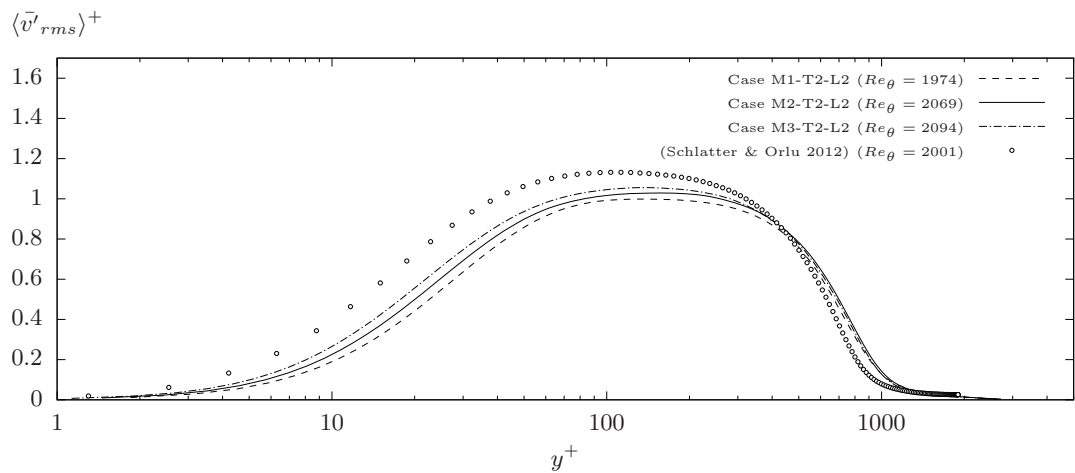
(c) *Reynolds shear stress ($x = 0.16m$)*

$-\langle \bar{u'v'} \rangle^+$

y^+
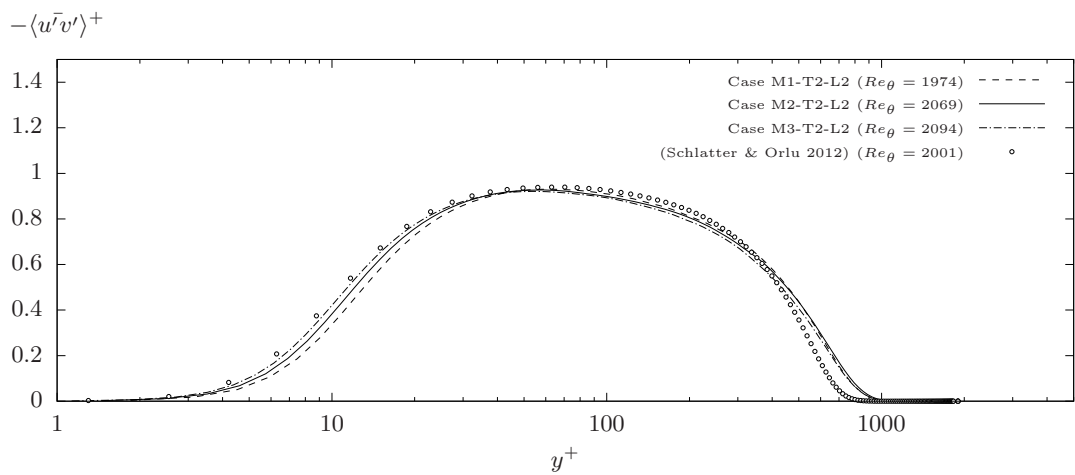
Figure 4.17: *Comparison of the distribution of turbulent stress components at $x = 0.16m$ along a smooth wall for three levels of spatial resolution.*

(a) *RMS of streamwise velocity fluctuations (x = 0.25m)*
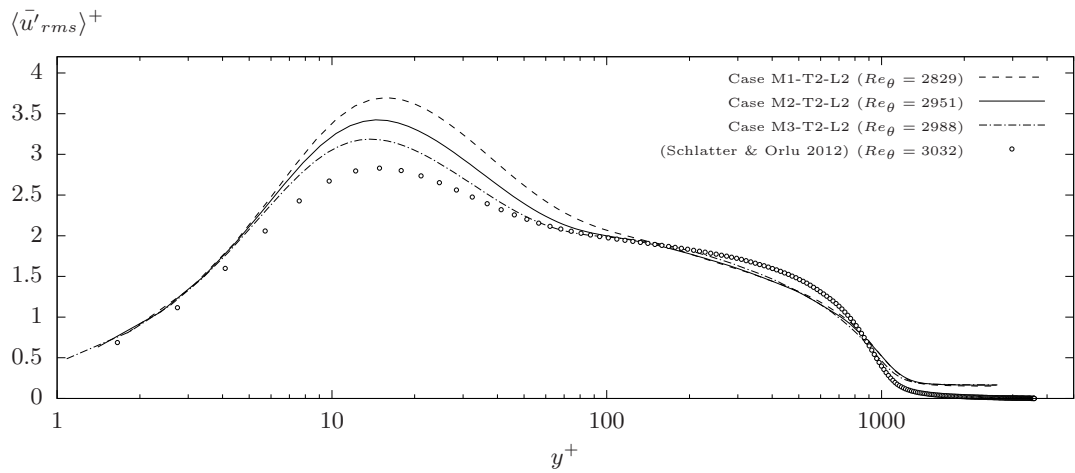
(b) *RMS of wall-normal velocity fluctuations (x = 0.25m)*
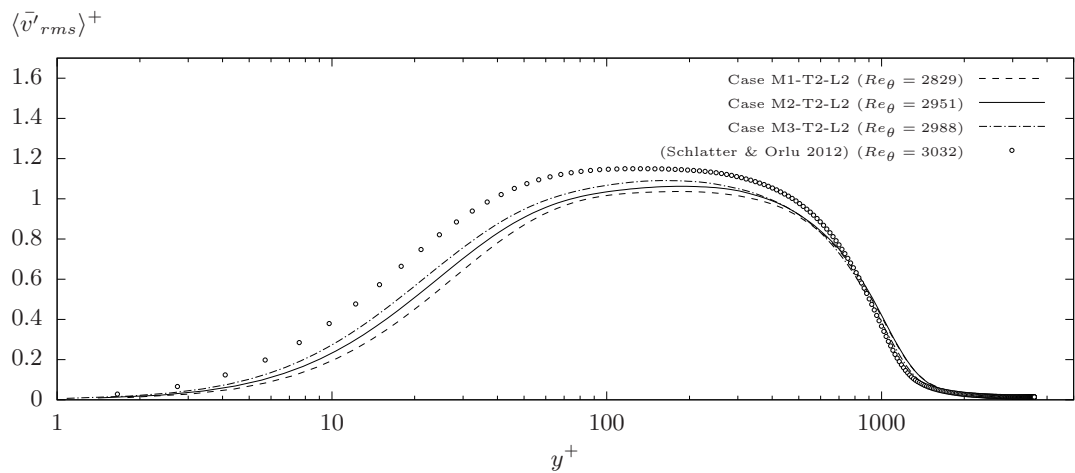
(c) *Reynolds shear stress (x = 0.25m)*
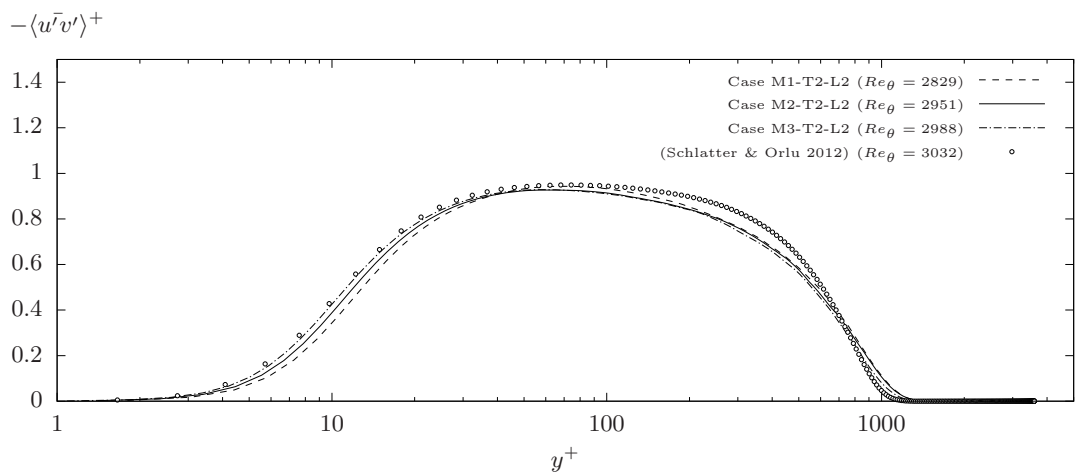
Figure 4.18: *Comparison of the distribution of turbulent stress components at $x = 0.25m$ along a smooth wall for three levels of spatial resolution.*

towards the DNS solution within $10 < y^+ < 100$. Similarly, the reduction in the streamwise velocity overshoot accompanies a growth in the under predicted wall-normal and spanwise velocity fluctuations near the wall. Such behaviour may be attributed to the inability of the current spatial resolution to capture the break-up of the high velocity streaks and low velocity streaks in the near-wall region (Bae *et al.* 2018). Bae *et al.* (2018) compared the resulting effect with that of small-scale, drag reducing riblets, which suppress the wall-normal and spanwise velocity fluctuations near to the wall. This effect is seen in the underprediction of C_f shown in Figure 4.15, and the improved agreement as the flow moves from the transitional to the fully turbulent region. For a spatial resolution of $\Delta x^+ = 32.5, \Delta z^+ = 16.3$, an improved resolution of the break-up cycle may account for the delayed reaction to the trip in case M3-T2-L2, in addition to the minimisation of artificial 'drag reducing' effects for $Re_\theta < 300$.

4.5 Summary

A spatially developing boundary layer comprising of laminar, transitional and fully turbulent regimes has been modelled using the open source libraries of OpenFOAM. The full boundary layer extends from a steady-state laminar boundary layer of $Re_\theta = 180$ to a fully turbulent flow of $Re_\theta = 3000$.

A tripping plane of wall-normal velocity fluctuations, with pseudo-random temporal variance and random spatial variance, destabilises a steady-state laminar boundary layer. The tripping plane can reproduce time-averaged velocity fluctuations with a root mean square values within $\pm 10\%$ of the desired strength, provided that the averaging window is sufficiently large. The highest fluctuation velocity which was investigated was comparable to the maximum value of the $\bar{v}'^+_{rms}$ component in a turbulent boundary

layer of an identical thickness. For this tripping configuration, the onset of transition was nearly instantaneous, such that initial period of large-scale, two-dimensional disturbances was not observable. This reaction suggests that, under the current tripping mechanism, the strength of the wall-normal fluctuations in the near-wall region of a turbulent boundary layer represents a critical optimised limit for the rapid initiation of laminar-turbulent transition.

By $Re_\theta = 1000$ the strength of the numerical trip on the local flow resistance and turbulent stress profiles diminishes. In the inner region, the variations between profiles of velocity fluctuations and the Reynolds shear stress are negligible, in comparison to the discrepancies produced by spatial numerical error. Limiting the near-wall streamwise and spanwise spatial resolution to $\Delta x^+ \approx 42.2$ and $\Delta z^+ \approx 21.2$ brings the coefficient of friction to within a $\pm 3\%$ tolerance of the Coles-Fernholz relation within a region of $1000 < Re_\theta < 3000$. Refining this resolution to $\Delta x^+ \approx 32.5$ and $\Delta z^+ \approx 16.3$ maintains the $\pm 3\%$ tolerance limits in the fully turbulence regime, but expands this tolerance far into the transitional regime; $400 < Re_\theta < 3000$.

The simulations in the present Chapter were initially designed through theoretical approximations of ideal boundary layer. To the authors knowledge, this is the first study of its kind to produce a systematic verification and validation of OpenFOAM for revolving laminar-turbulent transition with controlled tripping and large-eddy simulation. The results of the present analysis provide more detailed design criteria for modelling laminar turbulent transition in OpenFOAM, and building future simulations for the investigation of large-scale textured geometries. The present results suggest that a spatial resolution of $\Delta x^+ \approx 42.2$, $\Delta y^+_{min} \approx 1$ and $\Delta z^+ \approx 21.2$ provides an optimal starting point for determining the initial spatial resolution, prior to incorporating textured geometries into the domain. This base resolution should only be increased if such

textures are to be applied within the transitional regime. Whilst the flow contains the influence of the trip up to $Re_\theta \approx 2000$, the coefficient of friction and the shape factor can converge to within the theoretical error bounds by the point $Re_\theta \approx 1000$. Hence, when applying LES in OpenFOAM, the design criteria may take $Re_\theta < 1000$ as a suitable approximation of the location of the transitional regime. These recommendations will be carried forward into Chapter 7 to construct simulations of spatially developing flow over two-dimensional periodic ripples. The numerical trip will be applied with a tripping velocity of $v'^+_{ref} = 1.105$ to achieve $Re_\theta \approx 1000$ by the time the flow has reached the textured region, which lies 0.07m downstream of the inlet.

Laminar Channel Flow: Arbitrary Geometry

5.1 Introduction

Chapter 4 validates a method for modelling chaotic turbulent flows over planar surfaces, with high economic efficiency. The current chapter provides and validates a new methodology for automated modelling of grooved surfaces of arbitrary geometry and complexity. This method is first applied (in isolation from the methodology in Chapter 4) to a simpler steady-state laminar flow in an infinite channel. The first section outlines the procedure which was used for producing digital samples which replicate naturally occurring sand ripples from the sediment surface of a natural beach. The numerical methodology outlined in the following sections is developed with these specific surface profiles in mind. However, the model is designed to accommodate a wide range

of geometric profiles, features and length scales.

5.2 Natural Profile Development

Samples of naturally occurring sand ripple profiles were obtained at Crosby Beach, Merseyside. The ripple bedforms had formed under the action of free surface tidal motions. Once the tide had receded, the emerged bedforms were left for two hours to dry. Two individual locations were identified, each corresponding to a different form of ripple structure; one sample of symmetrical sinusoidal ripples (Figure 5.1a) and one sample of asymmetric vortex ripples (Figure 5.1b). Liquid gypsum plaster was applied to the sand surface in the sample area and left to solidify with one rigid surface conforming to a mirror image of the ripple profile, as shown in Figure 5.1c.
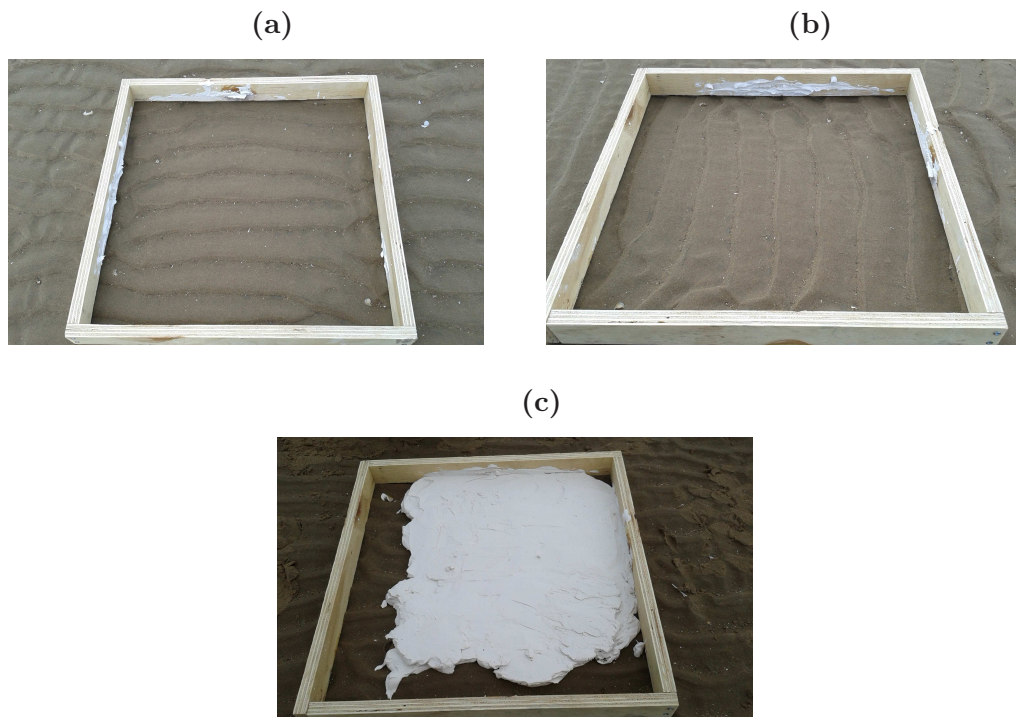
Figure 5.1: *Photographs displaying the sample sand ripple surfaces, wooden frame and gypsum plaster.*

The geometric profile of each gypsum plaster cast was measured using The ROMER Absolute Arm, model RA-7520S1, shown in Figure 5.2. The arm uses a positional laser

to produce a three-dimensional point cloud field of a geometric object. The sand ripple profiles contained a crest-to-crest wavelength on the order of $70mm$, and a crest-to-trough depth on the order of $7 \sim 10mm$. The ROMER arm provided a stated accuracy of $\pm 0.079mm$. The raw point cloud data was filtered until there was a minimum distance of 0.2mm between adjacent points. Considering that the exact dimensions only serve as a baseline for designing a suitable geometry, these measurement errors and filtering limits were considered to be acceptable. The filtered point cloud data was triangulated to construct a continuous surface consisting of connected two-dimensional triangular planes which was stored in an '.stl' format.

Figure 5.2: *Photograph of the Romer Absolute Arm, Model RA-7520S1.*

Figure 5.3 displays the final triangulated digital profiles for the two natural sand ripple surfaces. These digital profiles capture the complex geometric profiles with a streamwise periodicity that remains generally consistent over the area of each sample.

However, the surfaces also contain random perturbations from debris embedded within the sand surface. In addition, the unpredictable flow behaviour has induced small, but significant, random geometric variations in both the streamwise and spanwise directions.
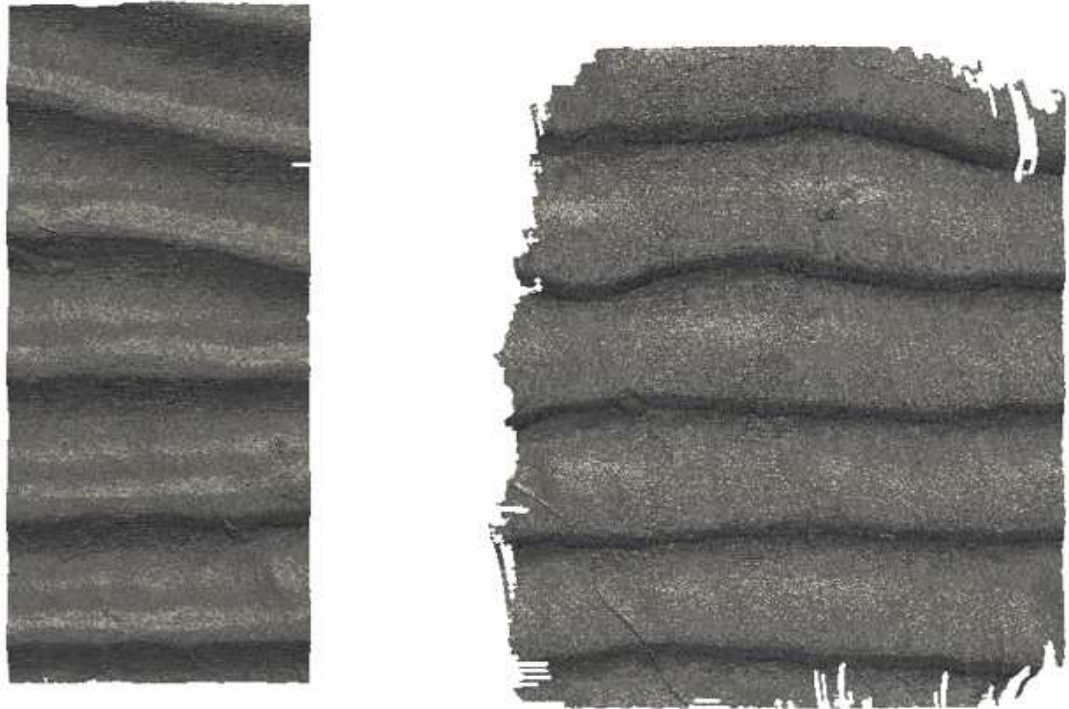
Figure 5.3: *Three-dimensional digital images of the sand ripple casts.*

The numerical methodology aims to reduce the computational workload by assuming periodicity in one or more flow directions. As such, the final sand ripple surfaces require periodicity in both the streamwise and spanwise directions. Hence, the final surfaces require a predictable, periodic geometry which correctly replicates only the key repeating features of the natural surfaces displayed in Figure 5.3. Rather than attempting to achieve ideal periodicity by smoothing the digital profiles, periodic profiles were created manually. For each surface, sample slices of the surface profile, from a plane which lay normal to the spanwise direction, were taken at five evenly spaced spanwise locations. The approximate coordinates of key geometric features (curves, straight edges, inflection points etc.) were determined visually by projecting each slice onto a grid of streamwise and wall-normal dimensions. Average coordinate values for

each surface were calculated from the five spanwise profiles. From these coordinates, a two-dimensional profile was developed by constructing a series of segments, each consisting of either a single plane or curve and connecting a single pair of adjacent coordinates. Each segment was intended to join with two adjacent segments at as close to a tangent as possible. The resulting coordinates were shifted by a small distance, relative to each other, to minimise the angle between connecting surface segments. As a result, each ripple profile closely resembles a single continuous line with minimal instantaneous variations in the surface direction. Figure 5.4 and Table 5.1 define the streamwise width a_i, and wall-normal depth b_i, of each surface segment, along with the streamwise crest length s_1, and trough length s_2, as a scaling of either the streamwise wavelength λ_x, or the groove depth k_g. For future reference, the final forms of the two-dimensional sand ripple profiles are referred to as RN1 and RN2.

Table 5.1: Scaled values of the streamwise and wall-normal length of each profile segment, as illustrated in Figure 5.4

	RN1	RN2		RN1	RN2
a_1/λ_x	0.167	0.08	b_1/k_g	0.5	0.25
a_2/λ_x	0.167	0.073	b_2/k_g	0.5	0.5
a_3/λ_x	0.331	0.08	b_3/k_g	0.5	0.25
a_4/λ_x	0.216	0.514	b_4/k_g	0.5	1
s_1/λ_x	0.119	0.119	s_2/λ_x	0	0.134

The crests of RN1 and RN2 contain a short, flat plateau of length s_1, as opposed to the more common single point maximum. The scaled groove depth k_g^*, as a ratio between depth and wavelength, disregards the width of the flat crest and only considers the groove wavelength λ_g, such that $k_g^* = k_g/\lambda_g$. With the exception of its crest, profile RN1 closely replicates the geometric pattern which Blondeaux *et al.* (2015) predicted would occur under the combined action of a uniform current flow and an oscillating wave induced flow. As in Blondeaux *et al.* (2015), the lee-side of RN1 consists of a pair of curves which form a continuous sinusoidal profile. However, the similarity is most notable in the unique stoss-side profile, which resembles two unequal pairs of

(a) *Profile: RN1, Orientation: $\varphi = 0°$*
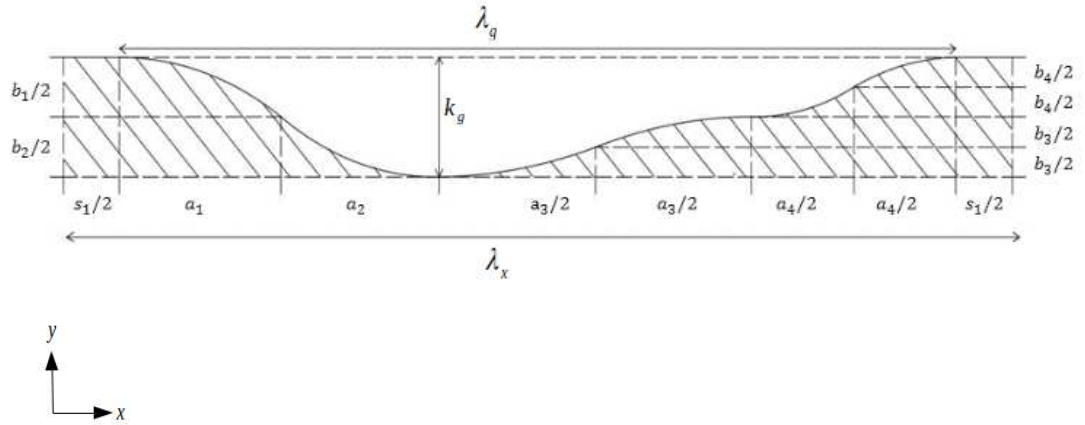
(b) *Profile: RN2, Orientation: $\varphi = 0°$*
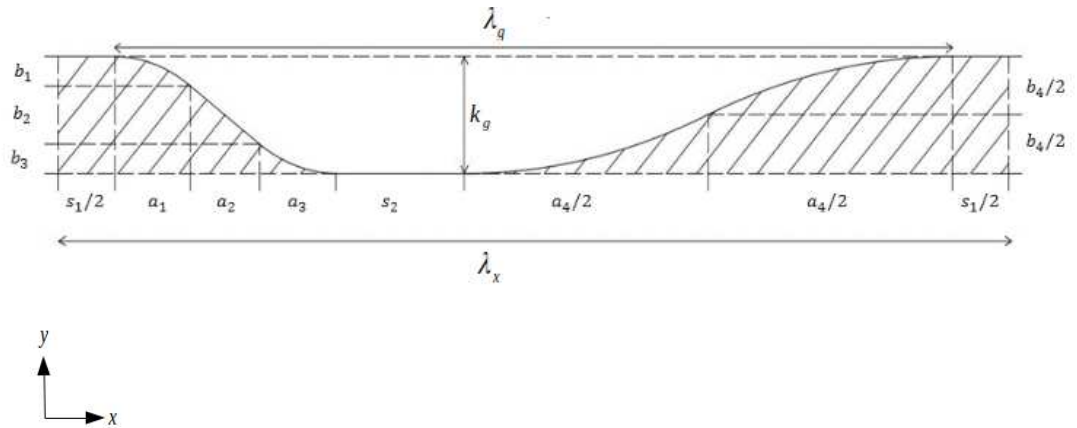
Figure 5.4: *The geometric definitions of the two-dimensional sand ripple profiles RN1 and RN2.*

sinusoidal curves. The two pairs intersect at a tangent, forming an inflection point, the orientation of which lies parallel to the streamwise axis. Note that the sample surface contains a depth to wavelength ratio of $k_g^* \approx 0.15$, which lies beyond the predicted theoretical limit of flow separation ($k_g^* = 0.1$), and hence, the range of the stability analysis in Blondeaux *et al.* (2015).

Similar to the geometries considered in Lefebvre *et al.* (2016), the lee-side of profile RN2 consists of a planar slip face which is connected to the crest and trough by a pair of additional geometric features. However, the additional features in RN2 are rounded such that they intersect the trough and crest close to a tangent, forming an

almost continuous lee-side profile. The stoss-side of RN2 consists of a sinusoidal profile produced from a pair of continuous curves, similar to the lee-side of RN1, as opposed to simpler geometries of flat, inclined segments. In turbulent flows, Lefebvre *et al.* (2016) suggested that the former case can produce small, but significant, benefits to flow resistance when applied alongside an optimised geometrical feature connecting the lee-side slip face and the crest (defined in RN2 by the segment of a_1, b_1). Note that their numerical analysis utilised Reynolds-Averaging to model all turbulent length scales, which would suggest that the mechanism responsible for this observation is not related to the presence or behaviour of time-dependant coherent turbulent structures. The final deviation lies in the trough, which consists of a flat plane of length s_2, which lies parallel to the streamwise direction, as opposed to a single point minimum. The natural profiles of RN2 have a depth to wavelength ratio of $k_g^* = k_g/\lambda_g \approx 0.11$

To produce a fully periodic three-dimensional surface, the two-dimensional planar profiles in Figure 5.4 are extruded in the spanwise direction along a line in the streamwise-spanwise plane, as illustrated in Figure 5.5. This extrusion profile is periodic along the spanwise direction, with a spanwise wavelength of λ_z, and a streamwise orientated maximum-to-minimum length of k_z, which is normalised by the spanwise wavelength ($k_z^* = k_z/\lambda_z$). It has a sinusoidal spatial variation, as defined in Equation (5.1) When $k_z^* = 0$ the surface geometry is invariant in the spanwise direction and is referred to as 'two-dimensional', whilst a surface of $k_z^* > 0$ is referred to as 'three-dimensional'.

$$x = \frac{k_z}{2}\left(cos\left(\frac{2\pi z}{\lambda_z}\right) - 1\right), \tag{5.1}$$
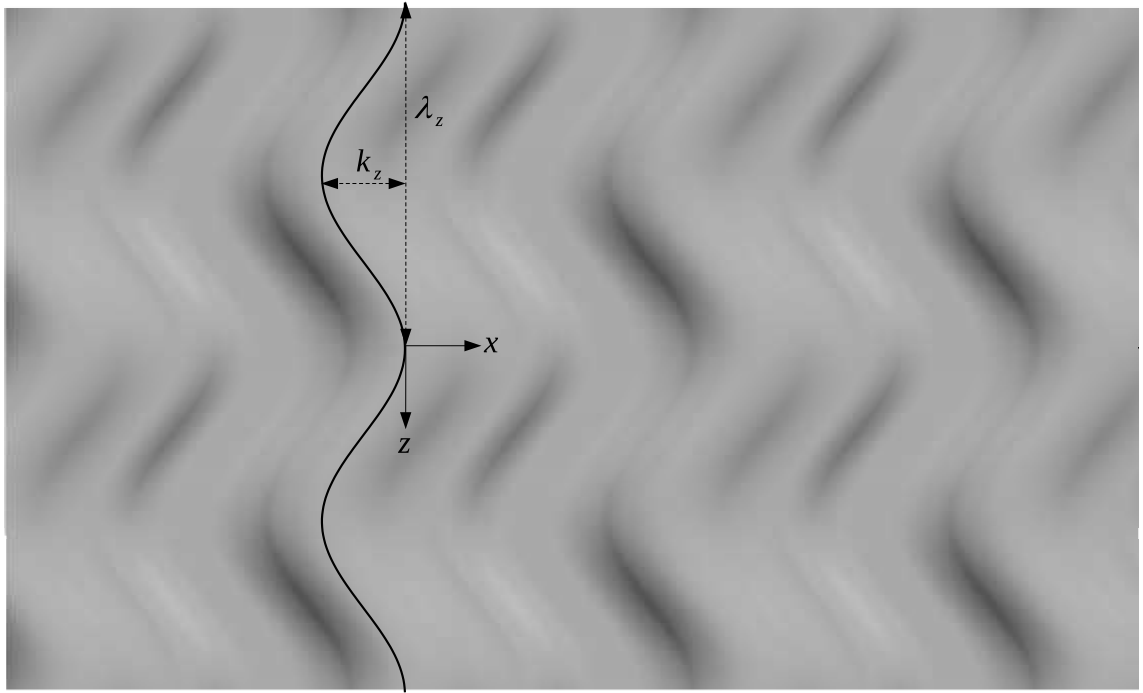
Figure 5.5: *Diagram of the spanwise sinusoidal profile of a three-dimensional sand ripple.*

5.3 Numerical Methodology

5.3.1 Overview

The present analysis considers a laminar flow through a three-dimensional channel with one smooth wall and one textured wall. The domain contains a single phase flow, which consists of an incompressible, Newtonian fluid. However, the current methodology is designed to be adaptable to multiple flow conditions and surface configurations. The following types of surface profile should be accommodated with similar applications of the domain configuration, the near-wall mesh and the meshing procedure between different cases.

- The simulation must be capable of incorporating arbitrary profiles in place of the lower and/or upper walls.

- The simulation must accommodate groove profiles of either two-dimensional or three-dimensional periodic spatial variation.

- The simulation must enable free rotation of the surface about the y-axis.

5.3.2 Flow Domain and Boundary Conditions

Figure 5.6 illustrates the layout of the channel domain and its boundaries. The channel is assumed to have a sufficient length and width that the flow is fully developed, and that the bulk flow field does not vary along the streamwise or spanwise directions. Hence, the channel consists of a three-dimensional section of an infinite domain, with periodic constraints applied to the streamwise (inlet and outlet) boundary planes and the spanwise (front and back) boundary planes. In a practical flow the motion of the fluid results from a pressure gradient along the streamwise length of the channel. Within a periodic domain, the bulk streamwise pressure gradient is equal to zero. In its place a body force drives the flow in a streamwise direction to produce a pre-defined value of bulk velocity U_{av}, along the channel.

The streamwise and spanwise lengths of the domains are denoted by L_x and L_z respectively. The channel has a full height of $L_y = 2h_0$, where h_0 is the unadjusted channel half-height. The lower wall consists of either a planar surface at $y = 0$, or a non-planar surface with crests located on the plane $y = 0$ and a trough which lies within the region $y < 0$. Similarly, the upper wall of the channel may consist of either a planar surface at $y = L_y$ or a non-planar surface with crests located at $y = L_y$ and a trough which lies within the region of $y > L_y$. The average depth for a textured surface k_{av}, refers to the magnitude of the wall-normal distance between its crests and its centre of area. The effective channel half-height becomes $h = 0.5 \left(L_y + (k_{av})_{lower} + (k_{av})_{upper} \right)$.

(a) *Streamwise and wall-normal directions*
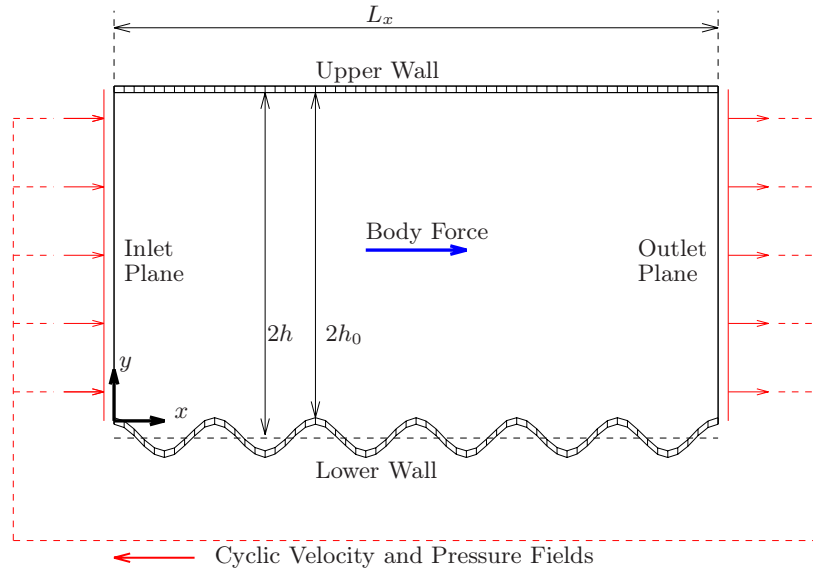
(b) *Wall-normal and spanwise directions*
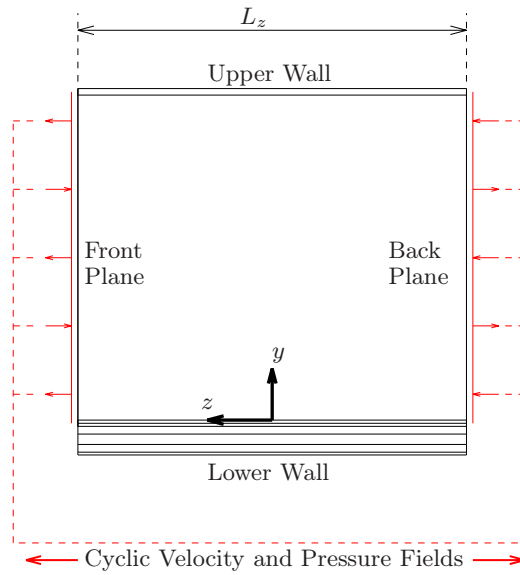
Figure 5.6: *Diagram of the flow domain and boundary conditions for present channel flow simulations, displayed with a textured lower wall and a smooth upper wall.*

In this way, the structure of the mesh across the bulk of the channel is independent of the surface geometry. The flow Reynolds number is defined by $Re_h = U_{av}h/\nu$.

The upper and lower surfaces are solid boundaries enforced by a 'no-slip' constraint for the velocity components $(u, v, w = 0)$, and a zero value Neumann constraint for the pressure $(p \cdot \nabla = 0)$. The boundaries at the inlet plane and outlet plane, as shown

in Figure 5.6a, form the inlet boundary ($y = 0$) and the outlet boundary ($y = L_x$) along the streamwise direction. The 'Cyclic Arbitrary Mesh Interface'('Cyclic AMI') boundary condition links the inlet and outlet boundaries on the finalised mesh to enforce periodicity.

The boundaries at the front plane and back plane, as shown in Figure 5.6b, form the front boundary ($z = +0.5L_z$) and back boundary ($z = -0.5L_z$) along the spanwise direction. The spanwise boundary conditions are varied depending on the stability of the flow field. Under the ideal approach, periodicity would be applied to the spanwise direction using the 'Cyclic AMI' boundary conditions. Noriega *et al.* (2018b) identified that cell non-orthogonality does not reduce the order of accuracy when applied to domain boundaries with periodic conditions. More importantly, periodicity in the spanwise direction is necessary for accommodating arbitrary surface rotation, as such surfaces may produce a considerable bulk flow across the spanwise direction (Mohammadi & Floryan 2013b; Ghebali *et al.* 2017). However, when surfaces of three-dimensional ripples were applied in place of the lower wall, the solution could not maintain stability towards the higher end of the laminar regime ($Re_h > 400$) whilst periodic boundary conditions were enforced in the spanwise direction. To maintain stability in these cases, the cyclic boundary condition at the front plane and back plane was replaced with a symmetry boundary condition enforced by a zero value Neumann constraint for the velocity. Note that this phenomenon occurred in test cases for which the ripple profiles lay parallel to the streamwise direction, which creates a geometric symmetry at the spanwise boundaries. Towards the higher end of the laminar regime, the three-dimensional surface geometry manipulates the bulk flow field away from the wall to create a rotational secondary flow which induces additional streamwise and wall-normal motions along the spanwise boundary planes, in the absence of any sig-

nificant spanwise velocity component. Hence, whilst the present analysis is limited to parallel and perpendicular surface orientations, further work which expands the model to a greater range of surface orientations, for which the surface geometry induces strong spanwise motions through the spanwise boundary planes, is required to enhance the stability of the solution in the presence of fully periodic spanwise boundary conditions.

The simpler 'Cyclic' boundary condition links each face on a boundary patch with a single face on its neighbour patch, and assigns a single value of a given flow property to the pair. This approach assumes that the shape and decomposition of each patch is identical, such that each face connects with a single face through a global transformation of translation and rotation. The 'Cyclic AMI' boundary condition may compensate for any deviation between two patches. After applying a user specified translation and rotation to a pair of patches, the value of a property on a given face is determined from the value of all overlapping faces on the neighbour patch. Each value from each overlapping face on the neighbour patch is weighted as a fraction of the area of its contact with the boundary face and the total area of the boundary face. Although this method requires the connected faces to be similar in geometry and decomposition, it allows for minor distortion of the boundary cells.

Figure 5.7 illustrates the layout of a channel with a three-dimensional sand ripple profile forming the lower wall. Steady-state laminar channel flow may often be restricted to a single wavelength of the surface geometry. This maximises economic efficiency when the structure and stability of the flow field is predictable. In the current model, channel dimensions are expanded to cover 6 wavelengths in the streamwise direction and 2 wavelengths in the spanwise direction. These dimensions lie closer to the common limits for modelling large-scale motions in turbulent flow. The dimensions are selected to ensure a full realisation of secondary flow which may materialise,

and to minimize the impact of cell misalignment between connected pairs of periodic boundary patches.
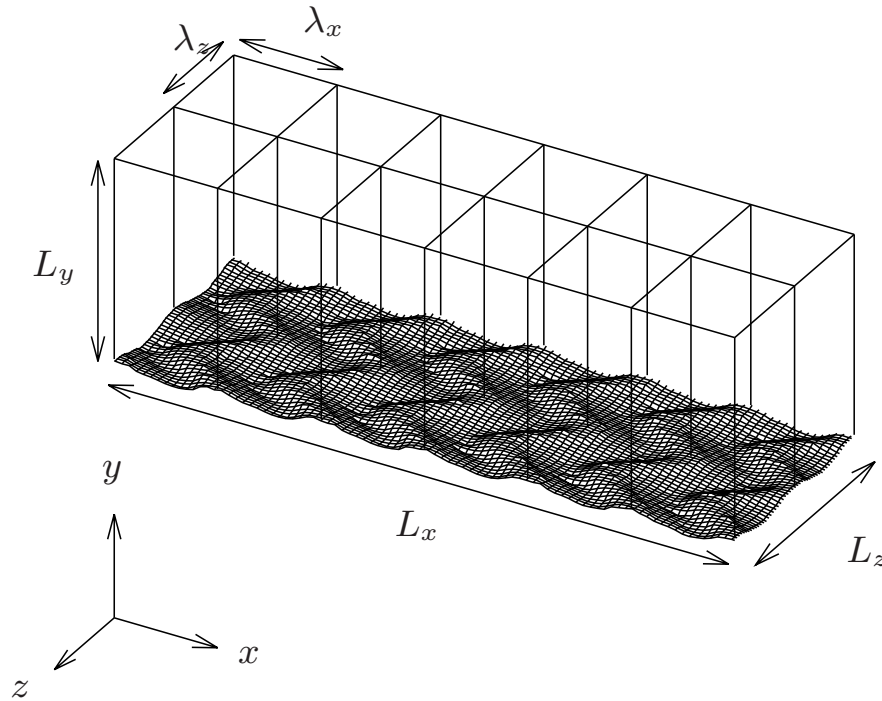
Figure 5.7: *Layout of the fluid domain with a lower wall consisting of a sample three-dimensional ripple profile.*

5.3.3 Characterisation of Flow Resistance

In a confined flow, the flow resistance acts against a driving force which propels the fluid along the streamwise direction. In practical applications, the driving force results from a change in static pressure along the streamwise direction. For a numerical model which assumes the flow to be periodic, the pressure gradient may be replaced with an artificial body force to produce a specified flow velocity or mass flow rate. Mohammadi & Floryan (2012) described the pressure loss over grooved surfaces in a laminar channel as a decomposition of three main components. The viscous drag component describes the effects of wall shear stress between the fluid and the solid surface. Two pressure drag components describe the contribution of the spatial variation in the bulk pressure field, and the contribution of the interaction between the pressure field and the surface

profile.

The unscaled flow resistance is obtained as a spatially averaged drag force over the full surface area of each wall. It comprises of two viscous forces; F_{v1} on the lower wall, and F_{v2} on the upper wall, and two pressure forces; F_{p1} on the lower wall, and F_{p2} on the upper wall. The dimensionless friction factor represents the flow resistance by a scaling of drag force with a reference surface area and velocity scale. The present analysis assumes a velocity scale of bulk velocity averaged across the modified channel U_{av}. In the current analysis, the total friction factor is decomposed into two components (Equation 5.4). The pressure component of the friction factor f_p (Equation 5.3), refers only to the sum of the contribution from pressure interaction drag on the lower wall f_{p1}, and upper wall f_{p2}. All remaining drag contributions are expressed in the viscous drag component f_v (Equation 5.2) as a sum of remaining drag on the lower wall f_{v1}, and upper wall f_{v2}.

$$f_v = f_{v1} + f_{v2}, \quad f_{v1} = \frac{\langle F_{v1} \rangle}{\rho(L_x L_z)U_{av}^2}, \quad f_{v2} = \frac{\langle F_{v2} \rangle}{\rho(L_x L_z)U_{av}^2}, \tag{5.2}$$

$$f_p = f_{p1} + f_{p2}, \quad f_{p1} = \frac{\langle F_{p1} \rangle}{\rho(L_x L_z)U_{av}^2}, \quad f_{p2} = \frac{\langle F_{p2} \rangle}{\rho(L_x L_z)U_{av}^2}, \tag{5.3}$$

$$f = f_v + f_p, \tag{5.4}$$

With a velocity scale of U_{av}, and a Reynolds number defined by U_{av} and h, the friction factor in a reference smooth channel is proportional to the Reynolds number such that $Re_h f_{smooth} = 6$ (Mohammadi & Floryan 2013b). Note that in the presence of non-planar walls, the value of the channel half-height which determines Re_h accounts for the modification to bulk channel opening, based on groove geometry. In such cases, the value of $(Re_h f)_{smooth}$ corresponds to a reference flow between two flat walls located at the centre of area for each textured surface. Furthermore, the friction factor

compensates for changes in the wetted surface area, with quantities of force on a wall being divided by the area of a reference smooth wall $L_x L_y$, as opposed to the total physical area of the surface.

5.3.4 Automatic Meshing Procedure

The files containing the textured surface geometries were supplied in an '.stl' format which describes the surface as a series of triangular planes. The natural sand ripple profiles consists of a series of connected geometric forms which cannot be described by a single universal form. In addition, the current investigations examine a limited range of profile shapes, with a focus on length scales and orientation. Therefore, in the present investigation, the '.stl' files were created manually through the GUI of the SALOME CAD package.

Firstly, a two-dimensional profile was created within an x-y oriented plane and extruded along the spanwise direction to create a three-dimensional surface. For a two-dimensional surface geometry the path of extrusion was a single continuous line. For a three-dimensional surface geometry the path of extrusion was another two-dimensional profile comprised of discrete segments with a length equal to half of the intended width of the near-wall cells. Finally, the surface was meshed using two-dimensional quadrilateral cells. This mesh was exported as an '.stl' file, in which each two-dimensional quadrilateral cell was split in a pair of triangular planes. The triangular planes of the three-dimensional geometric profiles had a maximum length equal to at least half the width of the near-wall cells ($\Delta x_{min} \approx \Delta z_{min}$) in both the spanwise and streamwise directions. The two-dimensional geometric profiles contained a single pair of triangular planes in the spanwise direction, with a streamwise length equal to that used for the three-dimensional geometric profiles.

The mesh for each domain and geometry was generated using the snappyHexMesh utility, as outlined in Section 3.4.1. Figure 5.8 displays the streamwise and wall-normal distribution of a locally refined mesh in a smooth wall channel. The region around the centreline contains cubic cells of $5.88 \times 10^{-3} h_0$ in width. The cells in the near-wall refine have been refined to 4 octree levels. The cells of the highest refinement levels are located above the plane $y = L_y - 6\Delta y_{min}$, and below the plane $y = 6\Delta y_{min}$. Figure 5.9 displays the streamwise, wall-normal and spanwise distribution of cells over surfaces of a two-dimensional ripple profile (Figure 5.9a) and a three-dimensional ripple profile (Figure 5.9b). The cells in Figure 5.9a and Figure 5.9b contain spanwise spacings of $\Delta z = 3.5\Delta x$ and $\Delta z = \Delta x$ respectively.
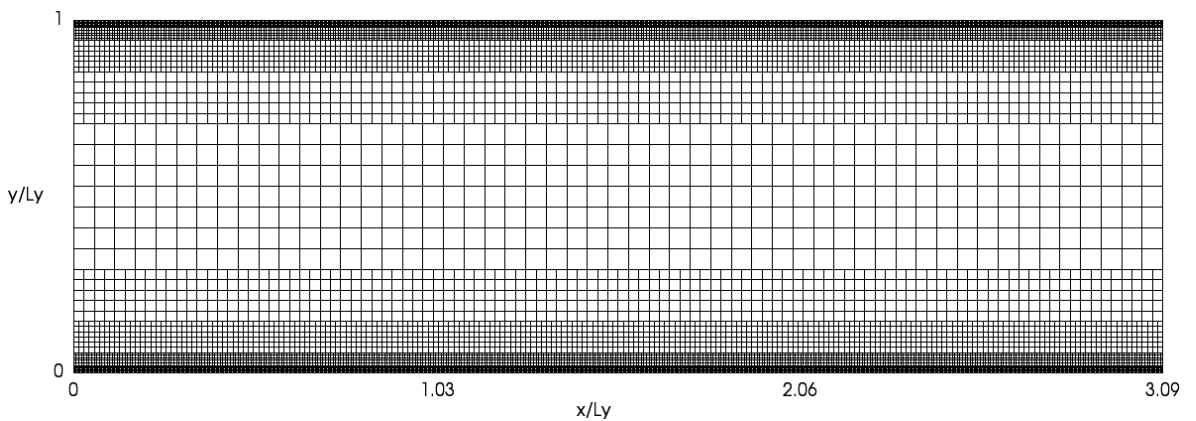
Figure 5.8: *Distribution of the locally refined mesh along the streamwise and wall-normal directions in a smooth channel.*

An initially coarse mesh was refined near the upper and lower walls using local octree refinement. Each orthogonal cell (before surface snapping) had an equal width in the streamwise and wall-normal directions; $\Delta x = \Delta y$. The spanwise width was varied depending on the surface profile; $\Delta z = 3.5\Delta y$ for spanwise uniformity ($k_z^* = 0$), and $\Delta z = \Delta y$ for spanwise variation ($k_z^* > 0$). Local mesh refinement in snappyHexMesh may be specified manually, based upon user specification, or automatically, based upon requirements in the vicinity of fine geometric features. In order to preserve the form of the bulk flow, and maintain acceptable levels of non-orthogonality in the bulk flow, the

(a) *RN1, $k_g^* = 0.15$, $k_z^* = 0$, $\varphi = 0°$*
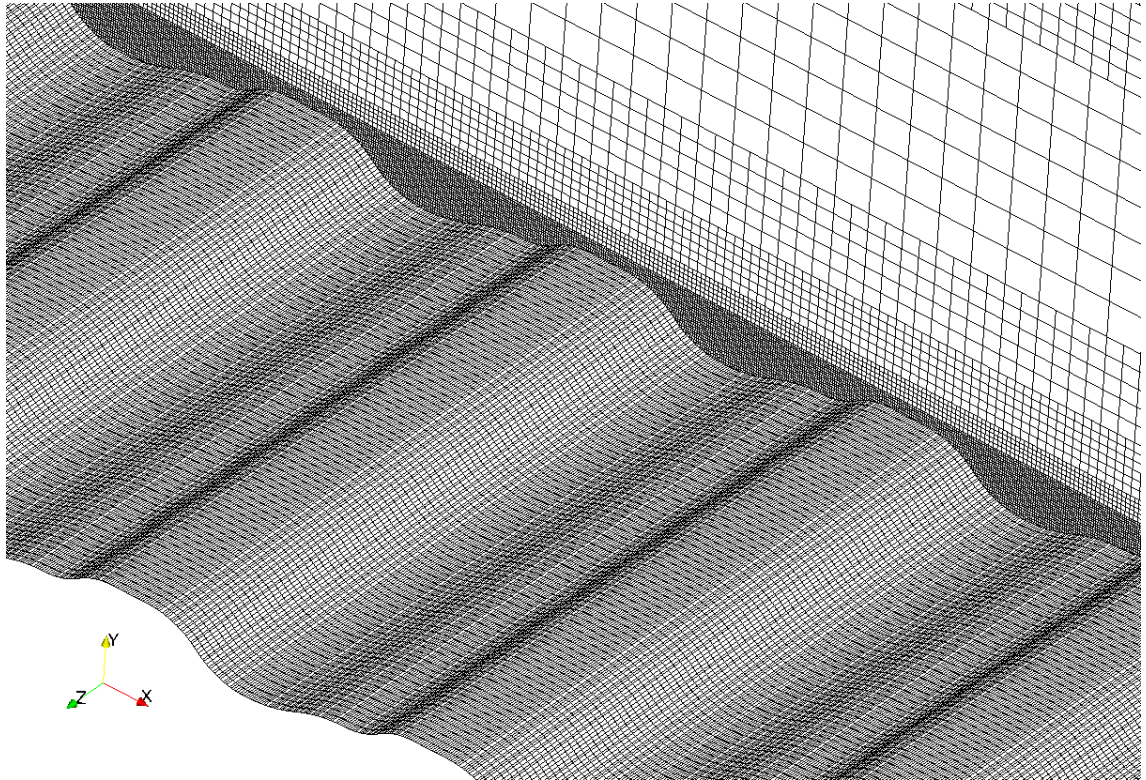
(b) *RN1, $k_g^* = 0.15$, $k_z^* = 0.25$, $\varphi = 0°$*
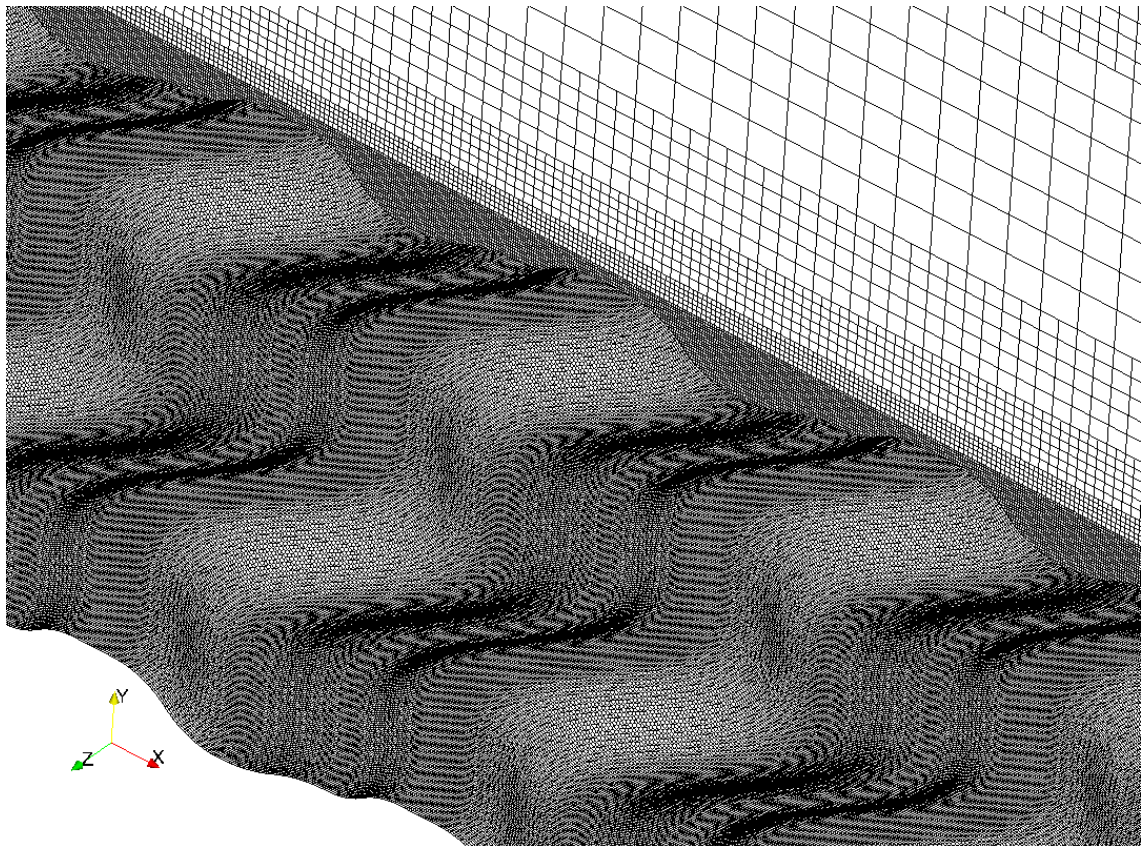
Figure 5.9: *The three-dimensional mesh consisting of split-hexahedral cells and local refinement; as shown by images of cell distribution over the lower textured wall and the boundary plane $z = -0.5L_z$.*

mesh was refined manually in layers defined by ordered rectangular regions. Hence, the boundary of the region for the finest refinement level was defined by a pair of flat x-z planes, located at a distance of $6\Delta y_{min}$ from the upper and lower walls. In this way, a single cell in the domain was connected to no more than 9 neighbour cells. Allowing the local refinement regions to conform to the surface geometry could have potentially doubled the maximum number of neighbour cells possessed by a single cell in the domain. Furthermore, the maximum non-orthogonality in the smooth wall channel (i.e. throughout the bulk flow) lay below 52°. Hence, based on the observations of Robertson *et al.* (2015), the solution in the bulk channel would not require limiting constraints on the numerical schemes. Each layer of refinement contained a minimum of 5 cells and a maximum of 6 cells. The boundary between refinement regions was constant in the streamwise and spanwise directions.

5.3.5 Solver Configuration

All investigation cases involving the infinite channel domain sought a temporally steady-state solution. The Reynolds number and the geometry of the lower wall profile had a significant impact on the stability of the flow field. Hence, multiple configurations of the flow solver and discretisation schemes were utilised to compensate for these insta-bilities where necessary. The numerical schemes and algorithms which are discussed in the present section here been presented in Section 3.5 and Section 3.6. In general, flow scenarios may be subdivided into four distinct groups based upon the stability of the solution;

- Two-dimensional surface profiles in low Reynolds number flow ($Re_h \approx 50, 100$).

- Three-dimensional surface profiles in low Reynolds number flow ($Re_h \approx 50, 100$).

- Two-dimensional surface profiles in high Reynolds number flow ($Re_h \approx 500, 1000$).

- Three-dimensional surface profiles in high Reynolds number flow ($Re_h \approx 500, 1000$).

Since the solutions in all cases are assumed to be temporally steady-state, the steady-state simpleFoam solver was the natural choice for pressure-velocity coupling. However, during preliminary testing, this solver could only maintain stability towards the lower end of the laminar regime. Based upon observations from preliminary testing, the flow would become unstable and diverge for flows of $Re_h > 400$, even within a smooth wall channel. Replacing the periodic spanwise boundaries with symmetrical Neuman boundary conditions, and adding limiting terms to the gradient schemes, failed to improved stability.

The steady-state SIMPLE algorithm produced solutions for all flows at the lower end of the laminar regime; $Re_h \approx 50$ and $Re_h \approx 100$. Each iteration loop solved the velocity and pressure fields to a relative tolerance of 0.1, with maximum absolute tolerances of 1×10^{-10} and 1×10^{-12}. The correction step used under relaxation factors of $\gamma_p = 0.1$ for the pressure field and $\gamma_u = 0.7$ for the velocity field. At low Reynolds numbers the geometric complexity of the surface negatively impacted the rate of convergence towards a steady-state solution, however, it produced no noticeable impact on stability.

Flows at higher Reynolds numbers of $Re_\theta > 400$ required a temporal term to maintain stability, but successfully converged to a steady-state solution through successive time steps (known as a psuedo-transient solution). This was implemented using the PIMPLE algorithm in the pimpleFoam solver, which, as a hybrid of the SIMPLE and PISO algorithms can maintain stability at larger time steps than the purely transient PISO algorithm. To improve the convergence rate, the pseudo-transient solver took

the output from a low-Reynolds number, steady-state solution as the initial velocity and pressure fields. The psuedo-transient model reduced the viscosity by a factor of ten, which produced a higher Reynolds number for an identical value of bulk velocity. For the more stable cases involving two-dimensional surface geometries, the flow field was marched through 200 time steps for $Re_h \approx 500$ and 400 time steps for $Re_h \approx 1000$. The time increment was fixed producing a maximum Courant number (Equation 3.25) of approximately 40. The temporal terms were discretised using the first order accurate Euler scheme in Equation (3.21). Each outer loop iteration converged the velocity and pressure fields to a relative tolerance of 0.1. Once the pressure values varied by less than $\pm 1 \times 10^{-5}$, and the three velocity components varied by $\pm 1 \times 10^{-5}$ between consecutive outer loops, the solver entered a final outer loop, which converged the velocity and pressure fields to tolerances of 1×10^{-10} and 1×10^{-12} respectively. The pressure correction had an increased relaxation ($\gamma_p = 0.3$) compared to that used for the simpleFoam solver at low Reynolds numbers.

For the pseudo-transient approach, the more complex three-dimensional profiles required finer time steps and a greater accuracy in the temporal term to maintain stability. In these cases, the time increment was allowed to vary at each time step to ensure a maximum Courant number of 1. For the temporal terms, the first order accurate Euler scheme was replaced by the second order accurate Crank-Nicolson scheme in Equation (3.24), with a weighting factor of $\gamma_{cn} = 0.9$. The pimpleFoam solver was modified to contain only one outer correction step, as in the fully transient PISO algorithm. Since these near-wall cells contained a maximum non-orthogonality of up to 65° at the lower wall, two non-orthogonal correction steps were included in each time step. Furthermore, the final tolerances for pressure and velocity were raised to 1×10^{-8}.

The gradient terms for pressure and velocity were discretised using a second-order

central differencing scheme (Equation 3.12). The convective velocity terms were discretised using the second order accurate linear upwind differencing scheme (Equation 3.10), with interpolation derived from the velocity gradient. When the maximum non-orthogonality across all cells in the domain exceeded 53°, limiting was applied to the gradient and Laplacian terms. The gradient was limited using a multi-direction cell-centred scheme. In cases of $k_z^* = 0$, for which the maximum non-orthogonality and skewness did not exceed 50° and 0.8 respectively, limitless gradient terms and full non-orthogonal correction were applied; $\gamma_1 = 0$ and $\gamma_2 = 0$. In cases of $k_z^* \geq 0$, the maximum non-orthogonality and skewness did not exceed 65° and 1.3 respectively. In such cases, limiting was applied to the gradient and Laplacian terms with limiting factors of $\gamma_1 = 0.5$ and $\gamma_2 = 0.5$.

5.4   Validation for Simple Geometries

5.4.1   Overview

Before the model could be applied to detailed geometric profiles, its accuracy and limitations were verified over simpler geometric surface profiles with pre-known solutions. This analysis was limited to test cases involving pressure driven flow of a laminar, single phase fluid. The accurate prediction of the Poisuille number $Re_h f$, was assessed for smooth wall channel flow (Figure 5.10a) and shallow, transverse grooves of a simple sinusoidal profile (Figure 5.10b). The periodic hill in (Figure 5.10c) represents a classic benchmark scenario for assessing flow separation and reattachment.

(a) *Plane channel* **(b)** *Sinusoidal grooves*

(c) *Periodic hill*
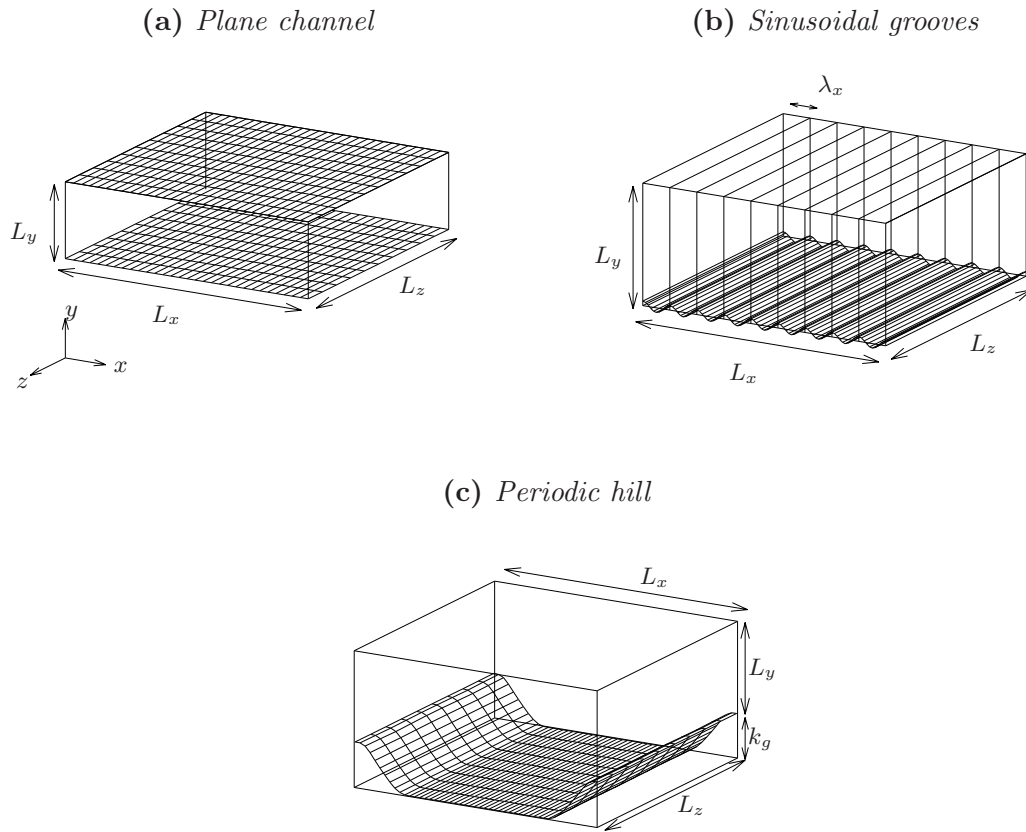
Figure 5.10: *Domain configurations for three geometries with published solutions.*

5.4.2 Smooth Channel

Firstly, the model was assessed for plain Poisuille flow with numerical solutions for $Re_h = 100$ with the steady-state approach and $Re_h = 1000$ with the pseudo-transient approach. The computational domain and mesh were identical to that displayed in Figure 5.8. Under the present definition of Re_h, the theoretical prediction of the Poisuille number is $(Re_h f)_{smooth} = 6$ (Mohammadi & Floryan 2013b). In both cases ($Re_h = 100$ and $Re_h = 1000$), results for the split-hexahedral mesh produced identical Poisuille numbers of $Re_h f_v = 5.98$; or 99.67% of its predicted value, with the error evenly distributed between the upper and lower walls.

The error in the velocity field was determined by comparison to the theoretical velocity distribution for plane Poisuille flow (Equation 5.5) (Mohammadi & Floryan

2013a).

$$u\left(y\right) = \frac{3}{2}\frac{U_{av}}{h^2}\left(2hy - y^2\right),\qquad(5.5)$$

The wall-normal distribution of streamwise velocity was obtained at discrete points across the channel, which correspond to the distribution of cell centres over the wall-normal direction. At each wall-normal location, a single velocity value was obtained from a spatial average of all cells along the streamwise direction and spanwise direction. Figure 5.11 compares the streamwise velocity field from the split-hexahedral mesh with the corresponding approximation from the theoretical solution in Equation (5.5) for a flow of $Re_h = 1000$.
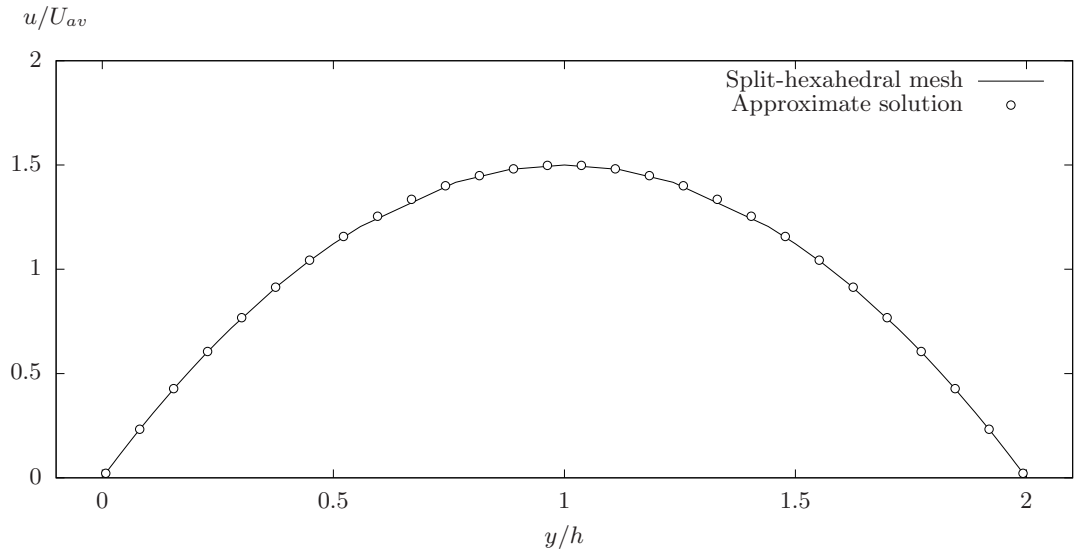
Figure 5.11: *Streamwise velocity profile across the smooth wall channel.*

Within all but the coarsest region ($y < 0.29$ and $y > 0.71$), the error varied between -0.3% and -0.5% of the local velocity value at each point. The highest errors of -0.7% occurred around the centre of the channel ($0.29 < y < 0.71$), where the cell resolution was at its lowest. The distribution of error between the numerical solution and Equation 5.5 showed negligible change between the steady-state solution for $Re_h = 100$ and the pseudo-transient solution for $Re_h = 1000$.

5.4.3 Sinusoidal Grooves

Mohammadi & Floryan (2013b) produced solutions for shallow, sinusoidal grooves which were oriented transverse to the flow direction, with a profile defined in Equation (5.6).

$$y = \frac{k_g}{2} \left(\cos \left(2\pi \frac{x}{\lambda_x} \right) - 1 \right), \qquad (5.6)$$

From their results, a groove was selected based upon the greatest depth ($k_g = 0.05h$), and a wavelength that lies close to that of the natural sand ripple profiles in the present analysis ($\lambda_x = 0.628h$). The flow domain and automatically generated mesh for the current simulation are displayed in Figure 5.12

(a) *Full channel*
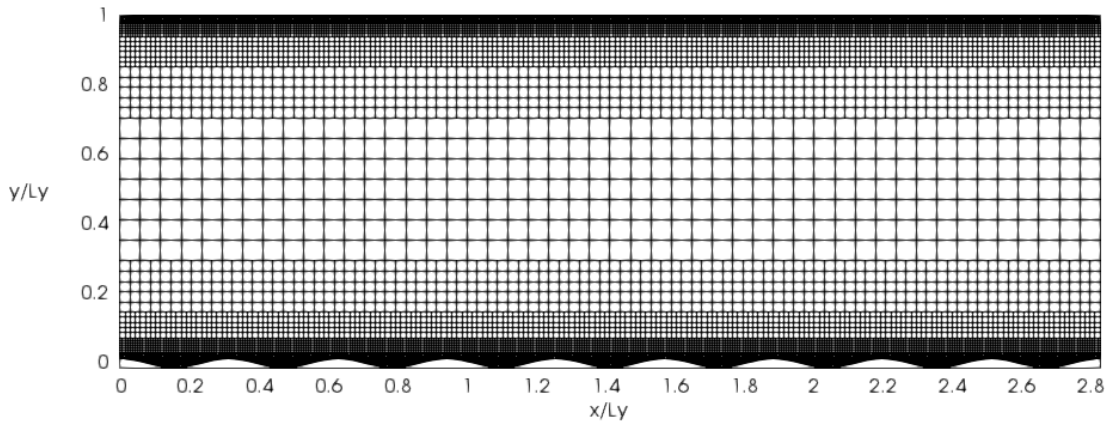
(b) *Lower wall*
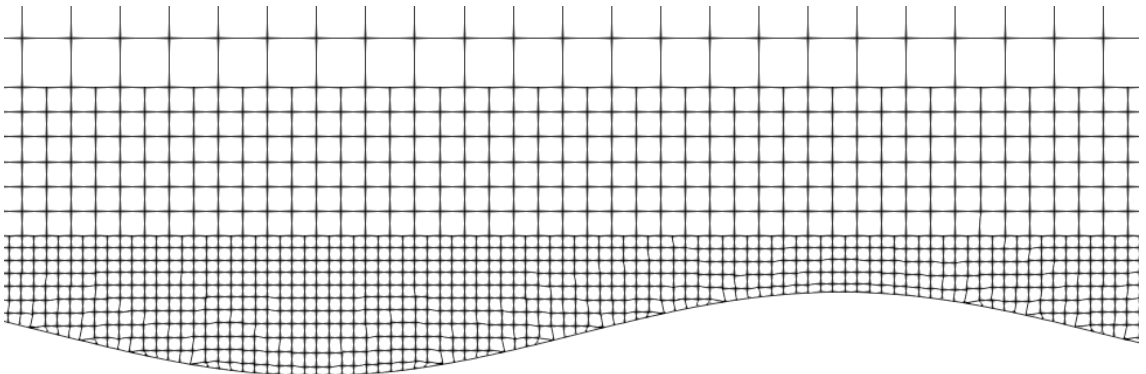
Figure 5.12: *Split-hexahedral mesh in a channel containing a lower wall of the reference sinusoidal grooves.*

Mohammadi & Floryan (2013b) evaluated the Poisuille number using the centreline

velocity of a reference smooth channel as the the velocity scale, as opposed to the bulk velocity U_{av}. Here, their findings are reported in terms of $Re_h f$ by assuming a relation of $u_{max} = 2U_{av}/3$ (Mohammadi & Floryan 2013a) for plane Poisuille flow. At $Re_h = 666.6$, a groove with a depth of $k_g^* = 0.08$ and a wavelength of $\lambda_x = 0.31L_y$ produced a total Poisuille number of $Re_h f \approx 6.075$. This amounts to a +0.075 drag increase compared to the smooth wall value of the numerical domain ($Re_h f = 6$). For the current numerical domain, identical sinusoidal grooves produced a total Poisuille number equivalent to a +0.077 increase, compared with the reference plane channel flow of $Re_h f = 5.98$. This amounts to a 2.7% error in the total drag increase. For comparison, Mohammadi & Floryan (2013b) accepted a 10% error in the predicted drag increase when utilising their spectral code, in order to reduce the detail of their geometric surface in Fourier space, and reduce economic cost. Similarly, an error in the region of 2.7% in the present analysis is considered to be tolerable given the significant reduction in the pre-processing time with the current meshing procedure.

Figure 5.13 compares the distribution of normalised shear stress over the groove profile for the current simulation and the solution of Mohammadi & Floryan (2013b). The normalised wall shear stress produced by the split-hexahedral shows a strong correlation with Mohammadi & Floryan (2013b) throughout the trough. The reduced cell quality along the lee-side produces local distortions in the shear stress profile. However, these distortions are small compared to the local magnitude of the shear stress, and hence, has a negligible impact on the overall trend of the shear stress distribution. Furthermore, the split-hexahedral mesh produces a mild under prediction of the normalised wall shear stress at the crest. This would suggest that the error observed in the value of the total Poiseuille number $Re_h f$, results from errors in either the interaction of the pressure field with the lower wall, or the viscous stresses on the

upper wall. Confirmation of this assumption would require a method of separating out the flow resistance into the pressure interaction and pressure form drag components, as defined and reported in Mohammadi & Floryan (2013b)
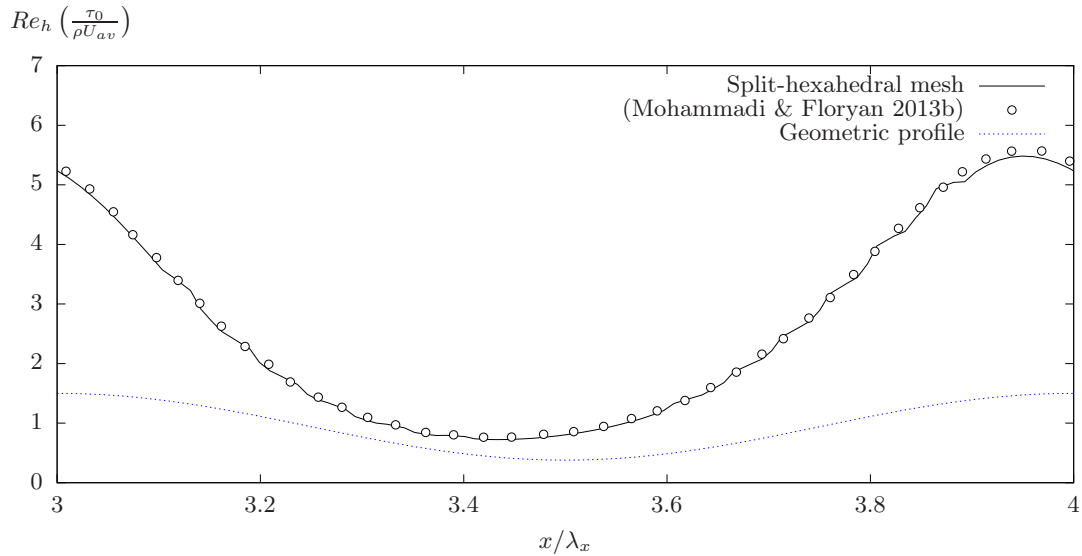
Figure 5.13: *Profiles of the normalised wall shear stress over the reference sinusoidal grooves, compared with the reference solution of Mohammadi & Floryan (2013a).*

5.4.4   Periodic Hill

The periodic hill solution is an established benchmark for separated, internal flows with streamwise periodicity, operating under steady and unsteady conditions. Breuer *et al.* (2009) presented a detailed comparison of experimental and numerical results for both laminar and turbulent flows based upon this geometry. The geometry for the current solutions is shown in Figure 5.10c. The hill has a depth of $k_g = 0.49L_y$ and a length of $\lambda_x = L_x = 4.42L_y$, whilst the hill crest is located at the points $x = 0$ and $y = 0$. The mesh shown in Figure 5.14 contains a maximum non-orthogonality of 36.4° and a maximum skewness of 0.713.

Breuer *et al.* (2009) defined the Reynolds number based upon the groove depth k_g, and the mean bulk velocity U_{av}, at the narrowest point of the channel. In the present analysis, the velocity was specified as a bulk velocity which was averaged throughout
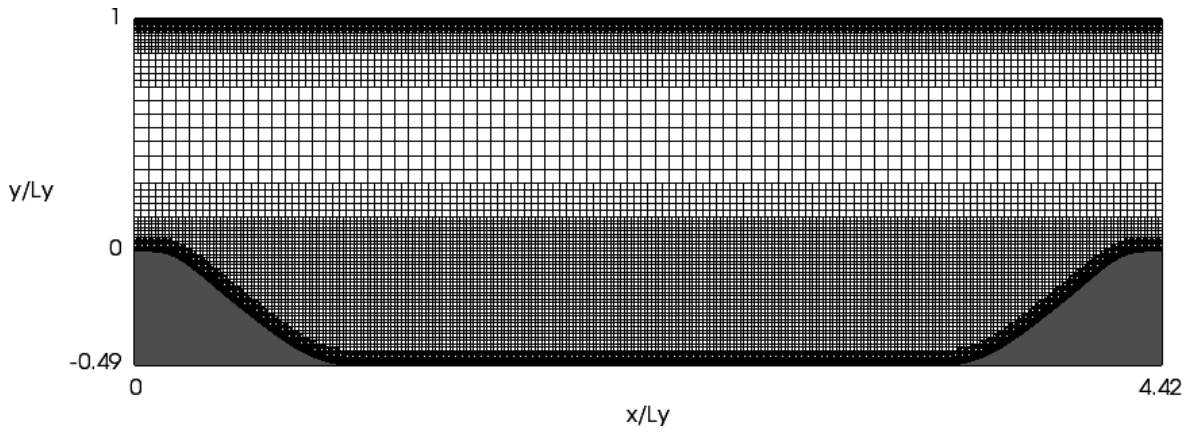
Figure 5.14: *Split-hexahedral mesh in a channel containing the periodic hill geometry of Breuer* et al. *(2009).*

the streamwise direction. The resulting Reynolds number, as defined by Breuer *et al.* (2009), was $Re = 100.7$ in the present case, compared with an ideal value of $Re = 100$ given in the benchmark solution. Under these conditions, the flow remained in the laminar regime with steady-state behaviour. The streamwise distribution of the normalised wall shear stress along the periodic hill is displayed in Figure 5.15.

Breuer *et al.* (2009) did not produce a full shear stress profile for the present configuration. However, Breuer *et al.* (2009) stated that the flow separated from the surface at a location of $x/L_x = 0.05$ and reattached to the surface at a location of $x/L_x = 0.859$. These points have been marked on Figure 5.15b, where they display strong agreement with the separation and reattachment of the flow solution produced by the split-hexahedral mesh in the current simulation. The normalised wall shear stress profile in Figure 5.15b intersects the limit of flow separation ($\tau_0/\rho U_{av} = 0$) at locations of $x/L_x = 0.051$ and $x/L_x = 0.861$. Therefore, the separation point and the reattachment point from the split-hexahedral mesh vary from the solution of Breuer *et al.* (2009) by an upstream shift of distances equal to 0.08% of L_x and 0.21% of L_x respectively.

(a) *Full profile*
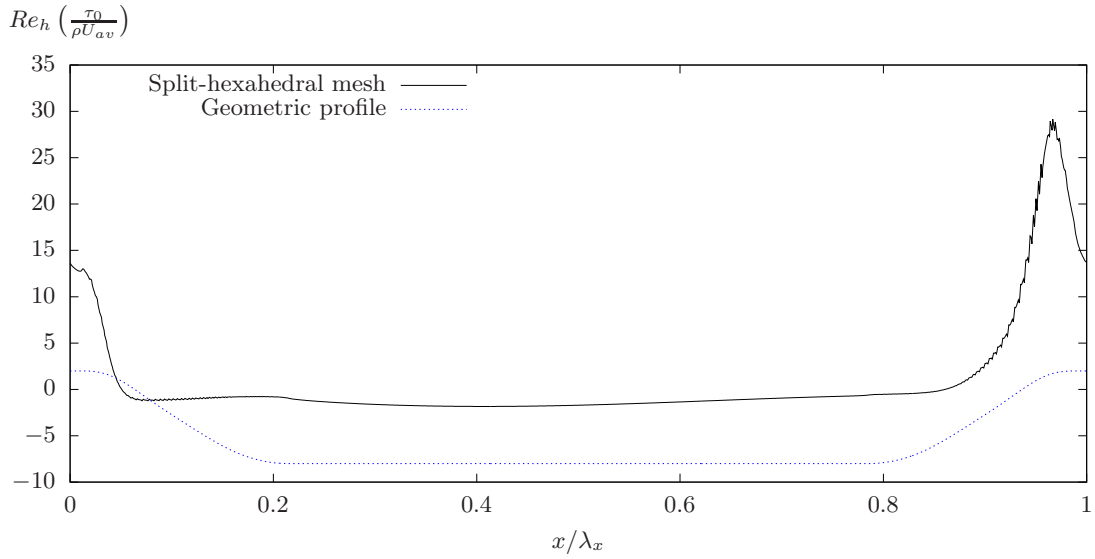
(b) *Separation zone*
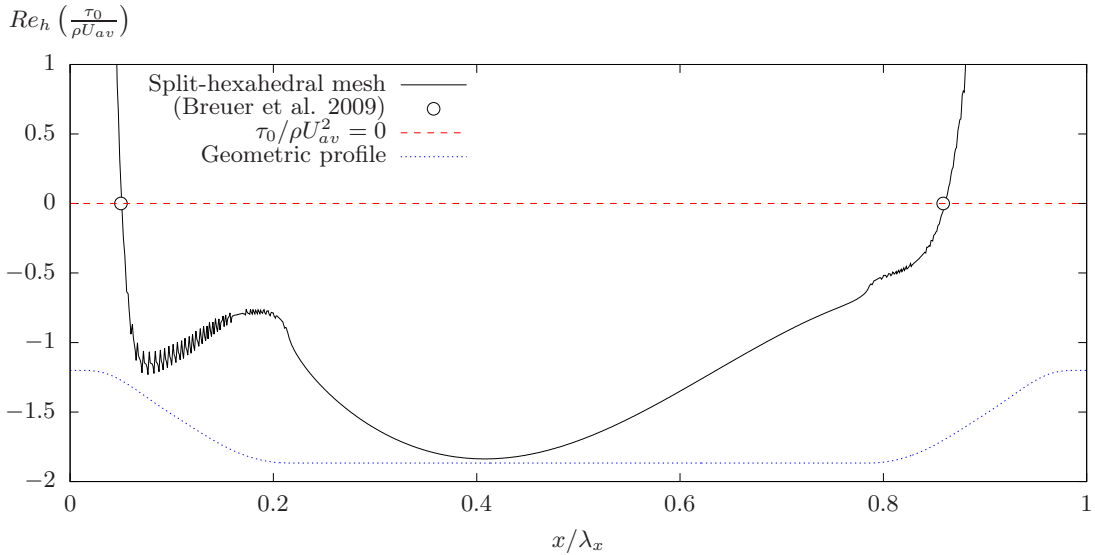
Figure 5.15: *Profiles of the normalised wall shear stress over the periodic hill geometry, compared with the reference solution of Breuer* et al. *(2009).*

5.5 Near-Wall Resolution for Sand Ripple Profiles

The computational setup was assessed using ripple profiles to determine its accuracy and efficiency for the parametric study in Chapter 6. Firstly, the impact of the refinement level for the locally refined near-wall cells was determined, using sample surfaces of two-dimensional and three-dimensional ripples. The solutions for a single sample two-dimensional ripple profile were compared for both the split-hexahedral mesh with

local refinement, which was produced by the automated meshing procedure, and a hexahedral mesh with gradient refinement, which was built and meshed in the SA-LOME Mech package. For all cases, the channel had dimensions of $L_x = 6.18h$ and $L_z = 2.06h$, whilst the lower wall consisted of a ripple geometry with streamwise and spanwise wavelengths of $\lambda_x = \lambda_z = 1.03h$.

5.5.1 Near-Wall Spatial Resolution

The influence of the near-wall spatial resolution on the natural sand ripple profiles was assessed for three sample cases of sand ripple profiles. These cases covered one two-dimensional profile at the highest Reynolds number which was considered in Chapter 6 ($Re_h \approx 1000$), and two cases of a three-dimensional profile, covering flows towards the lower end ($Re_h \approx 50$) and higher end ($Re_h \approx 500$) of the laminar regime. For each case, solutions were obtained for three different levels of near-wall spatial resolution, which were varied through local octree refinement. Table 5.2 displays the layout of each case configuration, along with the dimensions of the coarsest cells around the centreline of the channel, and the surface orientation relative to the flow φ. Although the reported value of maximum skewness is high, these cells remain confined to a small portion of the textured wall. The finest resolution of the three-dimensional ripple produced a maximum skewness of 0.995 in the domain, with 2.75% of the near-wall cells possessing a skewness greater than 0.5, and 0.02% possessing a skewness greater than 0.7. A similar resolution of the two-dimensional surface produced similar results with 3% of the cells possessing a skewness within the range of 0.5 and 0.58.

Table 5.3 provides the individual components of Poisuille number for the varying level of mesh refinement in each validation case. The two-dimensional ripple case (LV1), and the low Reynolds number, three-dimensional ripple case (LV2), displayed a similar

Table 5.2: Flow and geometry configurations for three mesh independence validation cases involving natural ripple profiles.

Case	Profile	k_z^*	k_g^*	φ	Re_h	$\frac{\Delta x_{max}}{h}$	$\frac{\Delta y_{max}}{h}$	$\frac{\Delta z_{max}}{h}$)
LV1	RN2	0.11	0	0°	1024.3	0.118	0.118	0.412
LV2	RN1	0.15	0.5	0°	51.6	0.118	0.118	0.118
LV3	RN1	0.15	0.5	0°	515.8	0.118	0.118	0.118

behaviour in the response to the near-wall refinement level. In both cases, refinement of the near-wall mesh caused the pressure component $Re_h f_p$, to fall with an equal magnitude to that by which the lower wall viscous component $Re_h f_v$, increased, such that $\Delta f_p \approx -\Delta f_v$. The change in the total Poisuille number was negligible between all levels of mesh refinement, with the maximum variation $\Delta|f| = 0.05\%$ lying within acceptable error limits.

Table 5.3: The total Poisuille and its individual components for the test cases outlined in Table 5.2

Case	$\Delta x_{max}/\Delta x_{min}$	$Re_h f_p$	$Re_h f_{v1}$	$Re_h f_{v2}$	$Re_h f$
LV1	3	1.115	2.063	3.078	6.256
	4	1.133	2.047	3.079	6.258
	5	1.140	2.040	3.079	6.259
LV2	3	0.461	2.696	3.071	6.228
	4	0.483	2.676	3.072	6.231
	5	0.494	2.663	3.072	6.229
LV3	3	0.981	2.948	3.348	7.276
	4	1.024	2.978	3.373	7.375
	5	1.043	2.977	3.381	7.401

The mesh resolution exerted a greater influence on all Poisuille components for a combination of high inertial effects ($Re_h \approx 500$) and a three-dimensional profile. In case LV3, the balance between the errors in $Re_h f_p$ and $Re_h f_v$ vanished. Firstly, increasing the refinement level from 3 to 4 caused the overall viscous and pressure contributions, $Re_h f_p$ and $Re_h f_v$, to rise on the order of 1% of $Re_h f_{smooth}$. In addition, this refinement exerted a nearly identical influence on the viscous drag on the upper and lower walls. A further increase in the near-wall refinement level to 5 displayed a negligible change in the lower wall viscous drag ($\approx 0.03\%$ of $Re_h f_{smooth}$), whilst

the upper wall component continued to increase by more than 0.1%. The results in Chapter 6 show that a three-dimensional surface variation in a laminar flow containing high inertial effects ($Re_h \approx 500$) produces strong modifications in the flow field away from the wall, including beyond the channel centreline. This behaviour is absent for all other configurations in Chapter 6, which contain either two-dimensional ripples or low Reynolds number laminar flows, and may account for the enhanced dependence of the flow resistance on the upper wall and the near-wall spatial resolution. At a refinement level of 4, the pressure drag was found to provide the greatest contribution to the error, with additional refinement producing an increase in $Re_h f_p$ of more than 0.3%.

5.5.2 Hexahedral Comparison

The results for a sample split-hexahedral mesh were compared to an alternative hexahedral mesh, for a sample two-dimensional ripple profile. The lower wall consisted of the two-dimensional profile RN1 ($k_z^* = 0$), at a depth of $k_g^* = 0.15$ and an orientation of $\varphi = 0°$, as depicted in Figure 5.9a. Two solutions were produced for each mesh, corresponding to flows of $Re_h \approx 50$ and $Re_h \approx 500$.

Figure 5.16 displays the layout of the split-hexahedral mesh and the hexahedral mesh in the near-wall region. The hexahedral mesh contained identical values of Δz at each layer of mesh refinement, and identical values of Δy for all layers, except that adjacent to the lower wall. In this region, Δy was graded in the wall-normal direction and varied across the ripple profile to aid in wall conformity. In this region, the maximum value of Δy was equal to Δy_{min} for the split-hexahedral mesh. The hexahedral mesh contained a constant value of $\Delta x = \Delta x_{min}$ throughout the domain. The split-hexahedral mesh contained over 1.633 million cells with a maximum skewness of 0.715 and a maximum non-orthogonality of 50.8° near to the wall. The hexahedral

mesh contained a over 8.66 million cells with a maximum skewness of 0.532 and a maximum non-orthogonality of 42.4° near to the wall. Applying a hexahedral mesh reduced the streamwise width of cells within the channel centre by a factor of 16. Whilst the pseudo-transient time step was reduced to compensate, the total physical time required for convergence remained unchanged. The simultaneous increase in the total cell count and the required number of time increments raised the total CPU run time by a factor of 14.

(a) *Split-hexahedral* **(b)** *Hexahedral*
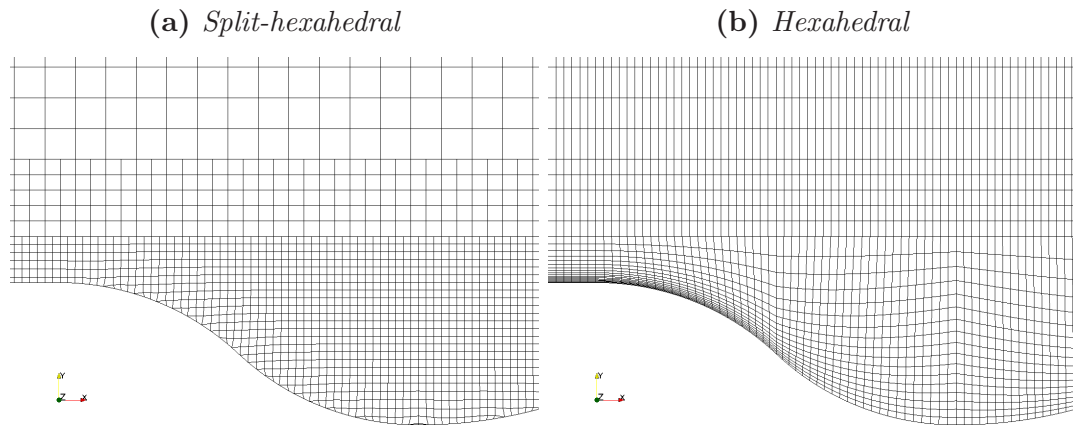
Figure 5.16: *Near-wall cells in the split-hexahedral mesh and hexahedral mesh for a two-dimensional sand ripple profile.*

Table 5.4 displays the components of Poisuille number for the four combinations of mesh type and Reynolds number. For both values of Re_h, the mesh type had a minimal effect on the flow resistance on the upper wall, with a difference in the magnitude of $\Delta Re_h f_{v2} = \pm 0.001$. This result indicates that, for the current range of two-dimensional profiles, the coarsening of the streamwise resolution of the cells at the centre of the channel does not hinder the transfer of pressure or velocity variations (induced by the lower wall) to the high resolution at the upper wall. This behaviour may be expected, where Saha *et al.* (2015) observed that the influence of sinusoidal grooves, with similar dimensions to the current profiles, was confined to the near-wall region of laminar flow.

For both the steady-state solution and the pseudo-transient solution, the absolute variation in $Re_h f_p$, was equal to the absolute variation in $Re_h f_{v1}$, between the split-

Table 5.4: Poisuille number for the steady-state and pseudo-transient solutions of a split-hexahedral mesh and a hexahedral mesh over a two-dimensional sand ripple profile.

Case	Re_h	$Re_h f_p$	$Re_h f_{v1}$	$Re_h f_{v2}$	$Re_h f$
hexahedral	51.6	0.673	2.489	3.074	6.236
	515.8	1.205	2.015	3.102	6.322
split-hexahedral	51.6	0.632	2.530	3.074	6.236
	515.8	1.173	2.047	3.103	6.323

hexahedral mesh and the hexahedral mesh. Relative to the solution, the most significant error occurs when transitioning from a hexahedral mesh to the split-hexahedral mesh in a flow of $Re_h = 51.6$, for which the value of $Re_h f_{v1}$ shifts by -8.2% of the viscous drag reduction on the lower wall. In context, even the largest shift in any component of $Re_h f$ (i.e. 8.2%) remains within the $\pm 10\%$ accuracy range which was identified by Mohammadi & Floryan (2013a) for shallow, misaligned grooves, when employing a minimal resolution of the surface geometry. In the present analysis, both simulations were computed in parallel over 22 cores using a 2.20 GHz Intel Xeon CPU combined with 125Gb RAM memory capacity. With this configuration, the error associated with the split-hexahedral cells in the near-wall region, and local mesh refinement throughout the bulk of the flow domain, is accompanied by a reduction of 93% in the required CPU time.

Figure 5.17 and Figure 5.18 compare the distribution of the normalised pressure and normalised wall shear stress along the ripple profile for the split-hexahedral and the hexahedral mesh at two values of Re_h. The locally distorted cells on the split-hexahedral boundary display localised spikes and spatial fluctuations, when compared to the smooth distribution of the hexahedral boundary. However, these local errors are most significant in the pressure field, and become masked by the large, undistorted pressure gradients at higher Reynolds numbers of $Re_h = 515.8$.

(a) *Shear stress:* $Re_h = 51.6$
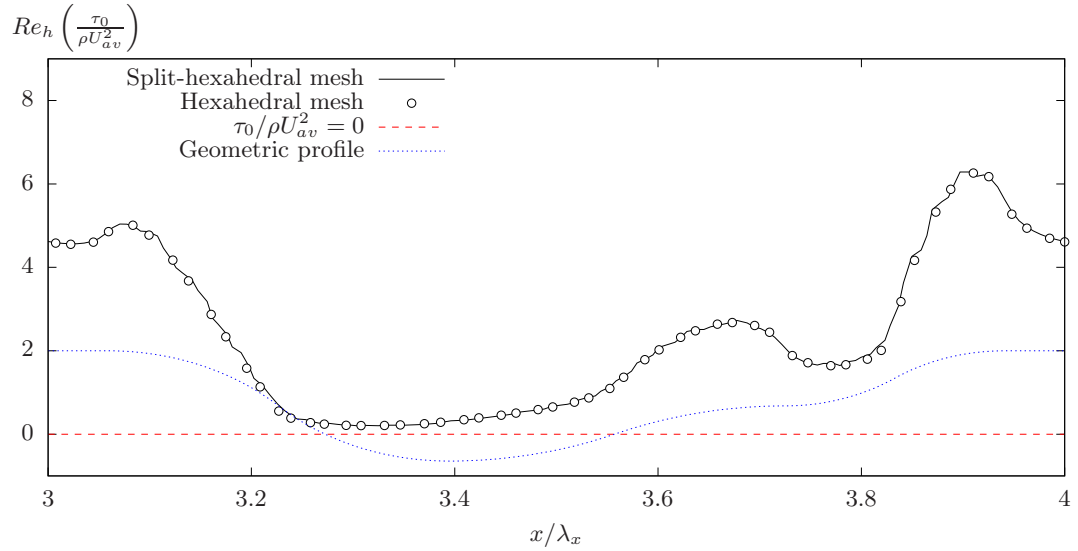
(b) *Pressure:* $Re_h = 51.6$
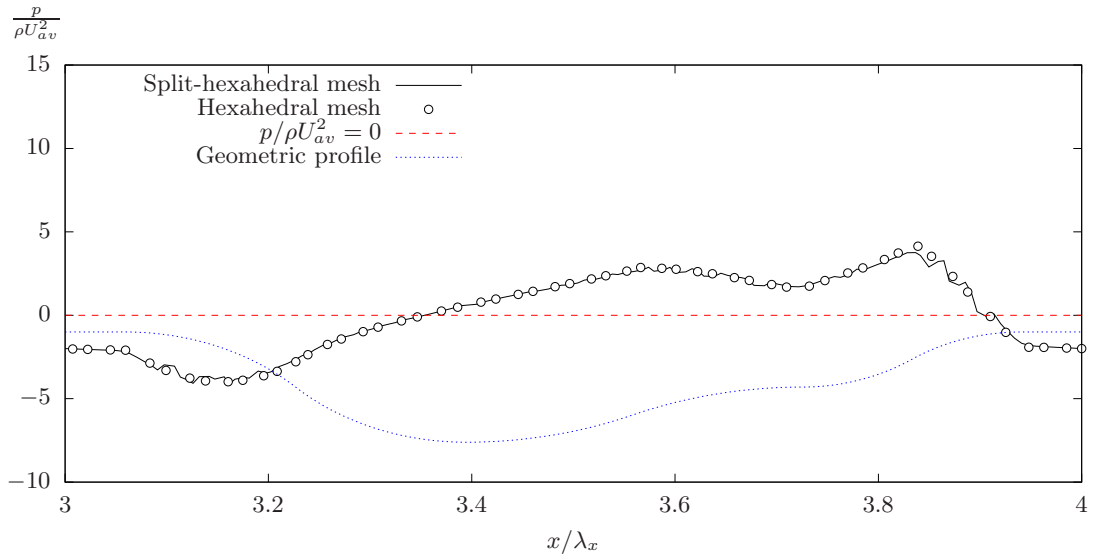
Figure 5.17: *Comparison of the distribution of the normalised wall shear stress and pressure over a sand ripple profile using a split-hexahedral mesh and a hexahedral mesh* $(Re_h = 51.6)$.

(a) *Shear stress: $Re_h = 515.8$*
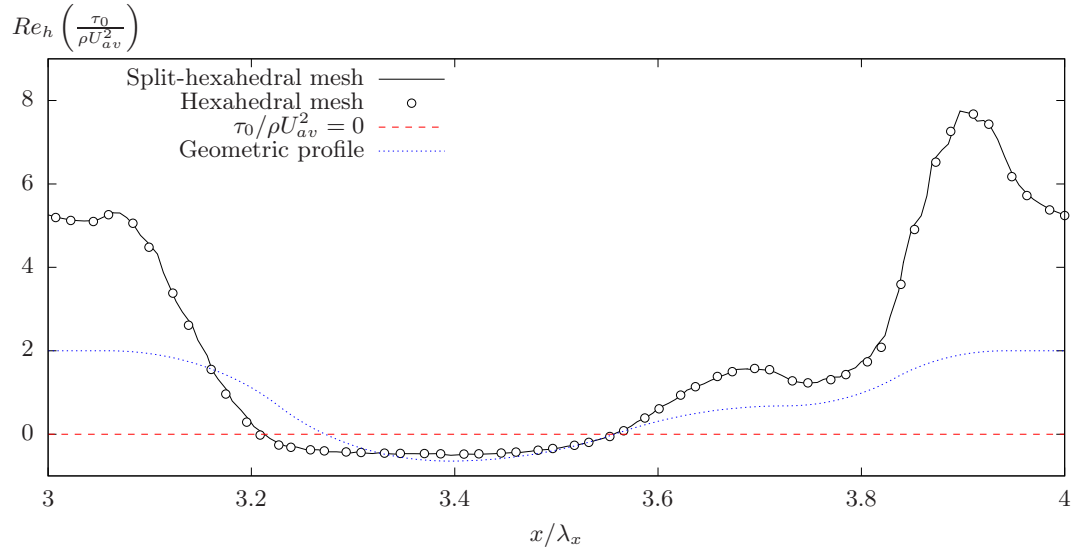
(b) *Pressure: $Re_h = 515.8$*
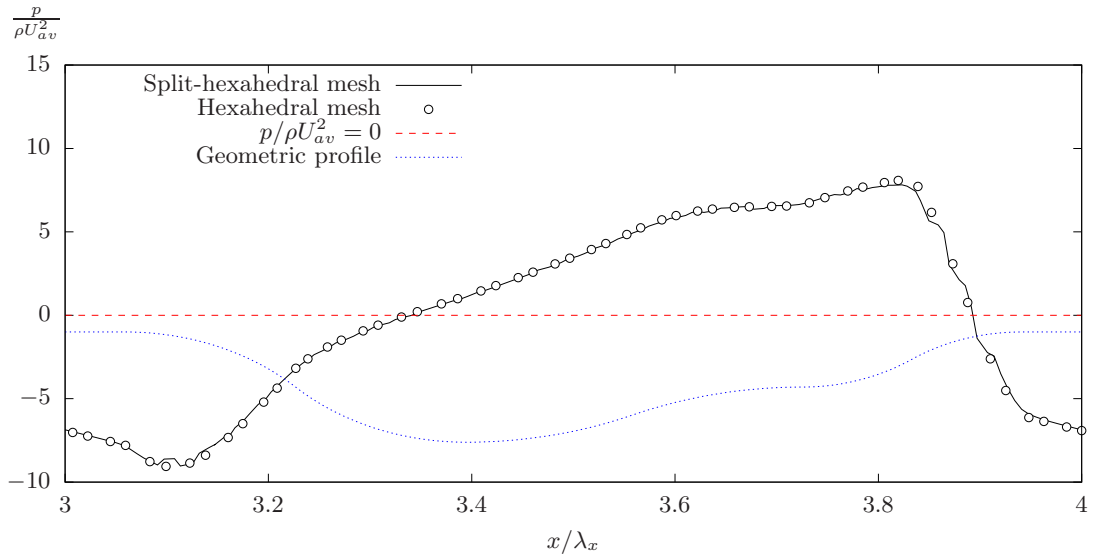
Figure 5.18: *Comparison of the distribution of the normalised wall shear stress and pressure over a sand ripple profile using a split-hexahedral mesh and a hexahedral mesh ($Re_h = 515.8$).*

5.6 Summary

The applied numerical approach is highly adaptable for different surface geometries. Both walls of the channel can comply with an arbitrary two-dimensional or three-dimensional periodic pattern, and this mesh is generated automatically. Given the instability issues arising from the union of spanwise motion and spanwise periodic boundaries, further development and testing will be required to expand its applicability to oblique surface alignments. The model was validated against existing numerical and theoretical solutions of plane Poisuille flow, shallow grooves and flow separation over large-scale periodic hills. However, the initial validation in Section 5.4 would benefit from a more direct experimental validation utilising surface profiles of a similar detail to those presented here

The spatial resolution along all three axis vectors was varied across the domain using local octree refinement to produce a split-hexahedral mesh. This is opposed to a hexahedral mesh which contains consistent spanwise and streamwise spacings throughout the bulk of the channel. For a simple two-dimensional ripple profile, applying a split-hexahedral mesh produced significant savings in resources, with reductions in the total cell count and the overall CPU time by 80% and 93% respectively. For this efficiency, the split-hexahedral mesh produced errors in the viscous and pressure drag components of up to $\pm 8\%$ of the viscous drag reduction increase, relative to the solution obtained using the hexahedral mesh. However, the balance between pressure and wall shear stress was such that the change to flow resistance was negligible.

Natural Sand Ripples in Poisuille Flow

6.1 Introduction

The following investigation comprises a detailed parametric study involving transverse grooves in Poisuille flow along an infinite channel, as outlined in Chapter 5. The parametric study covers a range of flows at varying Reynolds numbers in the laminar regime. Two-dimensional and Three-dimensional profiles of naturally occurring sand ripples are investigated for varying values of groove depth, spanwise spatial variation and surface orientation. The individual impacts and interactions of these control factors are assessed to determine their influence on the flow resistance, shear stress distribution along the groove and the velocity flow field.

6.2 Parametric Configuration

The flow domain contains a single phase fluid flow which is incompressible, laminar and fully developed. The upper wall of the channel is a smooth, planar surface at the point $y = L_y$. The lower wall consists of a non-planar surface with its crests located at the point $y = 0$. The computational domain has a streamwise length of $L_x = 3.088L_y$, and a spanwise length of $L_z = 1.029L_y$. The domain contains six periodic grooves in the streamwise direction ($L_x = 6\lambda_x$), and, in the case of spanwise variation, two wavelengths of the spanwise geometric profile ($L_z = 2\lambda_z$). The setup of this domain is explained and discussed in Section 5.3, and is illustrated in Figure 5.6 and Figure 5.7.

This study considers three geometric profiles for the two-dimensional groove profile; two profiles developed from reverse engineering naturally occurring sand ripples (denoted RN1 and RN2), and one profile of a simple sinusoid (denoted RS). The profile RS, shown in Figure 6.1e, serves as a reference case, representative of a commonly used geometric profile, by which to assess the influence of the highly detailed geometric features present in the asymmetric sand ripple profiles. The profile RS has been modified by adding a flat crest between adjacent sinusoidal curves to ensure similarity with profiles RN1 and RN2, and to allow for a direct comparison of the normalised ripple depth $k_g^* = k_g/\lambda_g$, between surfaces.

For each individual case which contains an asymmetric groove profile (i.e. RN1 and RN2) two solutions are produced, corresponding to two different values of surface orientation; $\varphi = 0°$ and $\varphi = 180°$. When the surface is oriented at $\varphi = 0°$ to the flow direction the steepest slope of the ripple forms the lee-side, as shown in Figure 6.1a and Figure 6.1c, whilst the shallower slope forms the stoss-side. This is the typical orientation of naturally occurring spanwise bedforms. An orientation of $\varphi = 180°$, as

(a) *RN1, $k_g^* = 0.15$, $\varphi = 0°$*

(b) *RN1, $k_g^* = 0.15$, $\varphi = 180°$*

(c) *RN2, $k_g^* = 0.15$, $\varphi = 0°$*

(d) *RN2, $k_g^* = 0.15$, $\varphi = 180°$*

(e) *RS, $k_g^* = 0.15$, $\varphi = 0°$*
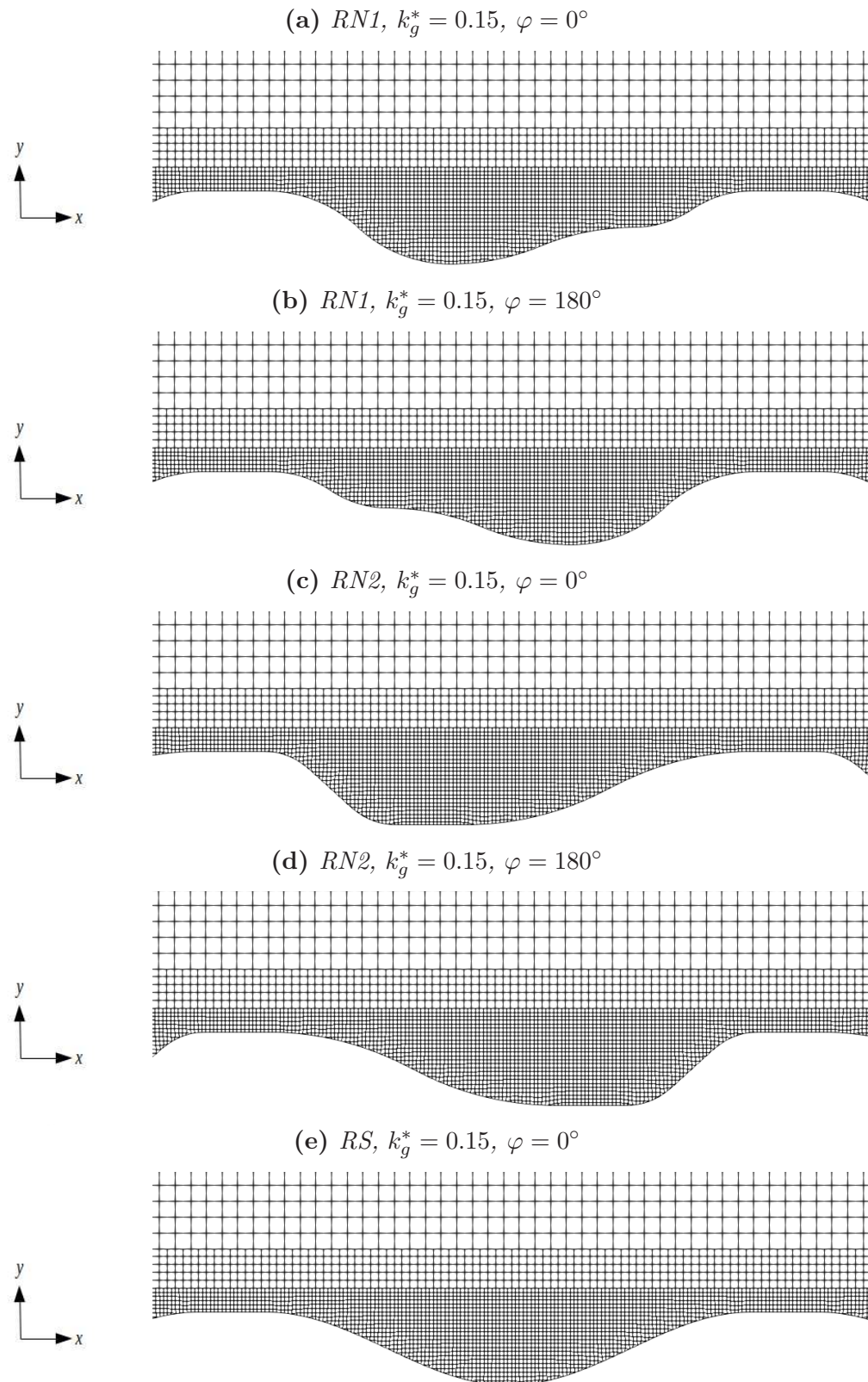
Figure 6.1: *Orientation of the two-dimensional grooves, visualised by the near-wall mesh distribution.*

shown in Figure 6.1b and Figure 6.1d, sees the placement of these slopes reversed, in direct contrast to the typical ripple formation. The normalised depth of the streamwise profile $k_g^* = k_g/\lambda_g$, varies over three discrete values of 0.075 (denoted KG1), 0.11 (denoted KG2) and 0.15 (denoted KG3). The depths of KG2 and KG3 correspond to the scales of the naturally occurring sand ripples which formed the profiles of $RN2$ and $RN1$ respectively. The shallowest depth of KG1 was selected to lie below the generally stated limit for the onset of vortex ripples ($k_g^* > 0.1$) (Vittori & Blondeaux 1990; Blondeaux *et al.* 2015).

The control factor for flow strength covers fixed values of the ratio between the bulk flow velocity and the kinematic viscosity; U_{av}/ν. For clarity, these values are converted into the Reynolds numbers by multiplying this factor by the effective channel half-height h. The value of h will vary depending the average depth k_{av}, for a given profile shape and depth. In some cases, the effective channel height will be reduced due to the 'lifting' of the flow away from the grooves (Mohammadi & Floryan 2013b). Considering all cases presented in Tables 6.1 and 6.2 for a given value of U_{av}/ν, the value of Re_h between different surface profiles varies within $\pm 1\%$ about the mean value. When referring to multiple cases of fixed flow strength (i.e. fixed U_{av}/ν), the value of Re_h is stated as an order of magnitude. The precise values of Re_h for each case are given in Table 6.1 and Table 6.2. The four different flows, defined by the value of Reynolds number, correspond to two flows which lie fully within the laminar regime; flow F1 ($Re_h \approx 50$) and flow F2 ($Re_h \approx 100$), one flow lying around the boundary of the laminar and transitional regimes; flow F3 ($Re_h \approx 500$) and one flow lying far into the transitional regime; flow F4 ($Re_h \approx 1000$).

Table 6.1 displays the full range of cases for two-dimensional grooves in Poisuille flow. A two-dimensional surface geometry is denoted by the setting $KZ0$. For the

two-dimensional natural ripple profiles, the parametric investigation covers 24 different configurations (cases) of Re_h, k_g^* and profile shape. Two solutions are produced for each case involving an asymmetric surface profile; with different flow directions parallel to the streamwise direction. For comparison, an additional 12 cases are investigated using a symmetric sinusoidal profile.

The second stage involves surface textures with a spanwise surface variation. The two-dimensional groove profile is extruded along a sinusoidal profile, as defined in Equation (5.1) in Section 5.2, oriented on the streamwise-spanwise plane. This profile has an amplitude of $0.5k_z$, a full depth k_z, and a wavelength λ_z. In the present analysis, the spanwise wavelength is equal to the wavelength of the streamwise groove ($\lambda_z = \lambda_x$).

Surfaces with a three-dimensional spatial variation give rise to an increase in the total cell count by a factor of three, and present an additional control factor for investigation; k_z. To offset the increased computational demand, this stages limits the number of possible settings for each control factor to two. The Reynolds number is varied between two magnitudes of $Re_h \approx 50$ (i.e. flow F1) and $Re_h \approx 500$ (i.e. flow F3). The relative groove depth is varied between $k_g^* = 0.075$ (i.e. KG1) and $k_g^* = 0.15$ (i.e. KG3), whilst the amplitude of the spanwise profile is varied between two discrete non-zero values, which correspond to $k_z^* = 0.25$ (denoted by KG1) and $k_z^* = 0.5$ (denoted by KG2). The surface profiles are a single asymmetric ripple profile RN1, and the reference sinusoidal profile RS. As before, each case involving an axisymmetric ripple profile produces solutions for two different surface orientations of $\varphi = 0°$ and $\varphi = 180°$. Table 6.2 displays the configurations for all cases involving surfaces of three-dimensional grooves.

The mesh decompositions and solver configurations for the respective two-dimensional and three-dimensional surfaces are identical to those described in Section 5.5.1. As

Table 6.1: Configuration of the control factors for investigating two-dimensional surface profiles.

Case	Profile	k_g^*	k_z^*	Re_h	φ
RN1-KG1-KZ0-F1	RN1	0.075	0	50.8	0° & 180°
RN1-KG1-KZ0-F2				101.6	0° & 180°
RN1-KG1-KZ0-F3				507.8	0° & 180°
RN1-KG1-KZ0-F4				1015.6	0° & 180°
RN1-KG2-KZ0-F1	RN1	0.110	0	51.2	0° & 180°
RN1-KG2-KZ0-F2				102.3	0° & 180°
RN1-KG2-KZ0-F3				511.5	0° & 180°
RN1-KG2-KZ0-F4				1023.0	0° & 180°
RN1-KG3-KZ0-F1	RN1	0.150	0	51.6	0° & 180°
RN1-KG3-KZ0-F2				103.2	0° & 180°
RN1-KG3-KZ0-F3				515.8	0° & 180°
RN1-KG3-KZ0-F4				1031.5	0° & 180°
RN2-KG1-KZ0-F1	RN2	0.075	0	50.8	0° & 180°
RN2-KG1-KZ0-F2				101.7	0° & 180°
RN2-KG1-KZ0-F3				508.4	0° & 180°
RN2-KG1-KZ0-F4				1016.9	0° & 180°
RN2-KG2-KZ0-F1	RN2	0.110	0	51.2	0° & 180°
RN2-KG2-KZ0-F2				102.5	0° & 180°
RN2-KG2-KZ0-F3				512.5	0° & 180°
RN2-KG2-KZ0-F4				1024.9	0° & 180°
RN2-KG3-KZ0-F1	RN2	0.150	0	51.7	0° & 180°
RN2-KG3-KZ0-F2				103.4	0° & 180°
RN2-KG3-KZ0-F3				517.1	0° & 180°
RN2-KG3-KZ0-F4				1034.1	0° & 180°
RS-KG1-KZ0-F1	RS	0.075	0	50.7	0°
RS-KG1-KZ0-F2				101.5	0°
RS-KG1-KZ0-F3				507.3	0°
RS-KG1-KZ0-F4				1014.6	0°
RS-KG2-KZ0-F1	RS	0.110	0	51.1	0°
RS-KG2-KZ0-F2				102.2	0°
RS-KG2-KZ0-F3				510.8	0°
RS-KG2-KZ0-F4				1021.6	0°
RS-KG3-KZ0-F1	RS	0.150	0	51.5	0°
RS-KG3-KZ0-F2				103.0	0°
RS-KG3-KZ0-F3				514.8	0°
RS-KG3-KZ0-F4				1029.6	0°

Table 6.2: Configuration of the control factors for investigating three-dimensional surface profiles.

Case	Profile	k_g^*	k_z^*	Re_h	φ
RN1-KG1-KZ1-F1	RN1	0.075	0.25	50.8	0° & 180°
RN1-KG1-KZ1-F3				507.8	0° & 180°
RN1-KG1-KZ2-F1	RN1	0.075	0.50	50.8	0° & 180°
RN1-KG1-KZ2-F3				507.8	0° & 180°
RN1-KG3-KZ1-F1	RN1	0.150	0.25	51.6	0° & 180°
RN1-KG3-KZ1-F3				515.8	0° & 180°
RN1-KG3-KZ2-F1	RN1	0.150	0.50	51.6	0° & 180°
RN1-KG3-KZ2-F3				515.8	0° & 180°
RS-KG1-KZ1-F1	RS	0.075	0.25	50.7	0°
RS-KG1-KZ1-F3				507.3	0°
RS-KG1-KZ2-F1	RS	0.075	0.5	50.7	0°
RS-KG1-KZ2-F3				507.3	0°
RS-KG3-KZ1-F1	RS	0.150	0.25	51.5	0°
RS-KG3-KZ1-F3				514.8	0°
RS-KG3-KZ2-F1	RS	0.150	0.5	51.5	0°
RS-KG3-KZ2-F3				514.8	0°

such, cases of $k_z^* = 0$ and $k_z^* > 0$ contain approximately 2×10^6 cells and 6×10^6 cells respectively. All cases with a Reynolds number of $Re_h \approx 50$ and $Re_h \approx 100$ utilise the steady-state simpleFoam solver. These particular cases were computed in parallel across 9 computational cores, with the domain decomposed along the streamwise direction. All remaining cases utilise a psuedo-transient setup of the pisoFoam solver. These psuedo-transient cases were computed in parallel across 22 processing cores, with the domain decomposed once in the wall-normal direction, and 11 times in the streamwise direction. Convergence of the steady-state solver required 3000 iteration steps for $k_z^* = 0$, and 5000 iteration steps for $k_g^* > 0$. Convergence of the psuedo-transient solver required a time period of $t \approx 430h/U_{av}$ for $Re_h \approx 500$ and $t \approx 215h/U_{av}$ for $Re_h \approx 1000$. The precision of the time-step varied depending on the complexity of the flow field. For $k_z^* = 0$, the time-step was fixed to produce a maximum Courant number

(Equation 3.25) of approximately 40. The PIMPLE algorithm maintained stability by performing multiple SIMPLE iterations during each time-step. For $k_z^* > 0$, the time-step was allowed to vary so that the maximum Courant number was restricted to 1, whilst the number of SIMPLE iterations in each time-step was limited to 1. The results presented here are taken from the instantaneous flow field at the final time-step. The full set of results for the flow resistance and shear stress distribution for each case is presented in Appendix C and Appendix D.

6.3 Two-Dimensional Ripples

6.3.1 Poisuille Number

Figure 6.2 displays values of the pressure contribution f_p/f (Figure 6.2b), viscous component of Poiseuille number $Re_h f_v$ (Figure 6.2c), and the total Poisuille number $Re_h f$ (Figure 6.2d), for discrete values of Reynolds number. Only the results for an orientation of $\varphi = 180°$ are shown for surfaces RN1 and RN2, as the small influence of $\varphi = (0°, 180°)$ would not be clearly observable from these graphs, as will be discussed.

Figure 6.2a displays the balance between the pressure component of Poisuille number and the combined viscous component. The line $Re_h f_v = 5.98 - Re_h f_p$ represents the point at which the viscous drag through a channel falls by an equal magnitude to the additional drag which arises from the interaction of pressure with the textured wall. In all cases, the viscous component of the Poiseuille number was lower than that for the reference smooth channel $Re_h f_v < 5.98$, with a maximum reduction of up to 18.7% for the natural ripple profiles and up to 15.7% for the reference sinusoidal groove. The variation of pressure along the lower wall gave rise to the inevitable 'pres-

(a) *Pressure-Viscous Balance*   **(b)** *Pressure Ratio*

(c) *Total Viscous Resistance*   **(d)** *Total Flow Resistance*
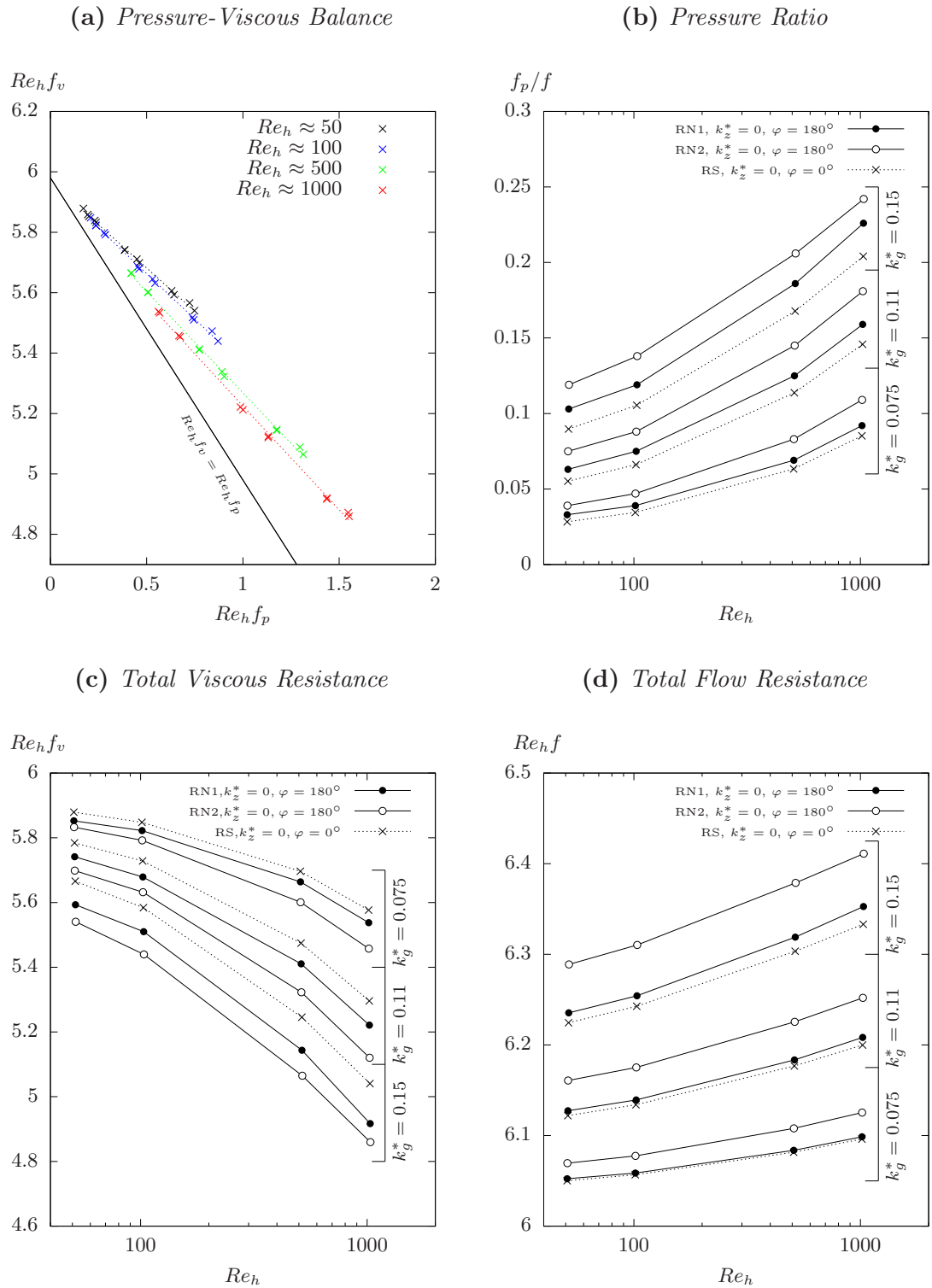
Figure 6.2: *Properties of flow resistance for the two-dimensional surface profile cases outlined in Table 6.1.*

sure interaction' drag. For all cases in Table 6.1, the results show that the additional pressure drag exceeds the reduction in viscous drag, resulting in an overall increase in the total flow resistance. At a fixed Reynolds number, the relationship between $Re_h f_v$ and $Re_h f_p$ generally follows a linear trend for which the shift of best-fit lines across different values of Re_h is significantly greater than the scatter about each line.

The 24 cases (48 solutions) involving two-dimensional surfaces of profile RN1 and RN2 (Table 6.1), are analysed using an Analysis of Variance approach to quantify the impact of four control factors on the analysis of variance approach. Since this analysis include the factor φ it excludes cases which contain the symmetrical profile of RS. For a fixed profile shape and groove depth, the total Poisuille number rises non-linearly with Reynolds number, such that the effect of Re_h diminishes as the flow moves from the lower laminar regime to the theoretical limit of laminar-turbulent transition. Whilst varying the value of ripple depth does not alter the general form of the $Re_h - Re_h f$ curve, raising the ripple depth produces two significant effects. Firstly, it increases the Poisuille number, as represented by an upwards shift in the curve. Secondly it amplifies the dependence that the Poisuille number has on the Reynolds number, as represented by a positive scaling of the curve. Comparing the variances confirms a non-negligible interaction between the ripple depth and Reynolds number, which accounts for 1.2% of the variation in the Poisuille number across all cases of natural ripple profiles. The Poisuille number is influenced overwhelmingly by the ripple depth, which accounts for 83.5% of the variation, compared with 11.3% for the Reynolds number.

Figure 6.2b shows that the relations for the pressure contribution ratio are similar those observed for the total Poisuille number. However, the upwards shift and scaling with ripple depth is smaller in relation to the gradient across the range of Reynolds numbers investigated. The variance statistics confirm that the influence of ripple depth

and Reynolds number are more balanced, with these parameters accounting for 50.7% and 44.7% of the variation respectively. The interaction between these factors becomes more significant; accounting for 2.9% of the variation. This additional effect presents a positive shift in f_p/f as k_g^* increases at higher Reynolds numbers, whilst the reverse occurs for $Re_h \lesssim 100$. At the highest depth and Reynolds number, the pressure contribution ratio accounted for less than 20% of the total drag over sinusoidal grooves, and 25% of the total drag over the natural ripple profile RN2. Compare these observations to the sinusoidal grooves of Saha *et al.* (2015), which displayed a pressure contribution ratio of over 55% for an equivalent Reynolds number of $Re_h \approx 750$ and a groove depth of $k_g^* = 0.152$. In that analysis, sinusoidal grooves covered the full circumference of a circular pipe, whereas in the present analysis the grooves lie on one wall of an infinite channel. Limiting the pressure ratio to consider the pressure drag and total drag on the lower wall only; $f_{p1}/(f_{v1} + f_{p1})$, suggests an equivalent pressure contribution ratio of f_p/f_{v1} within the range of 32% and 40.1%, based upon the Reynolds number of $Re_h = 514.8$ and $Re_h = 1029.6$, for simple sinusoidal grooves of $k_g^* = 0.15$.

For a given combination of k_g^* and Re_h, the profile RN1 produced a larger value of $Re_h f_v$ over the lower wall than RN2 in spite of its smaller surface area. Substituting RN1 for the simple sinusoidal groove raises the lower viscous component further. Furthermore, the change in $Re_h f_v$ between profiles RN1 and RS was smaller than that between profiles RN2 and RN1, despite the larger reduction in surface area. The orientation of the ripple profile φ, exerted the weakest influence on the total flow resistance. Varying φ between two discrete limits of $0°$ and $180°$ accounted for less than 0.02% of the total variation in flow resistance. This is the case whether considering either the total Poisuille number, or comparing each of its decomposed components individually. Assuming that the influence of φ is non-negligible, and primarily attributable to nu-

merical error, the present results indicate that a reversed orientation $\varphi = 180°$ produces a small reduction in both the total Poisuille number and the pressure contribution ratio. The singular profile RN2 was found to be most sensitive to φ, with maximum reductions of $\Delta Re_h f = -8 \times 10^{-3}$ and $\Delta(f_p/f) = -0.8\%$, which were observed for the largest depth and highest Reynolds number. Such behaviour would correlate with past findings for the large-scale asymmetric grooves of Osorio-Nesme & Delgado (2017) and the shallow, asymmetric dimples of Tay *et al.* (2017). By shifting the surface orientation from $\varphi = 180°$ to $\varphi = 0°$, the former case observed a 2% reduction in flow rate for steady-state laminar flow, whilst the latter case observed a 6% drag reduction for channel flow at the lower end of the turbulent regime. The negligible influence of φ in the present analysis may result from the combinations of small ripple dimensions and the laminar flow conditions.

In the present analysis, the value of φ is restricted to cases where the ripples are perpendicular to the flow. If the definition of ripple orientation is expanded to a greater number of values spanning the range $0° < \varphi < 180°$ then its influence may be expected to grow. In the case of shallow sinusoidal grooves, Mohammadi & Floryan (2013b) observed that the Poiseuille number could fall by almost 60% from a maximum over transverse grooves ($\varphi = 0°$) to a minimum over longitudinal grooves ($\varphi = 90°$). In theory, the pressure contribution will reduce to zero when $\varphi = 90°$, for which there is no streamwise variation along the lower wall.

6.3.2 Local Wall Shear Stress

Figure 6.3 displays the normalised streamwise shear stress; a product of Reynolds number and the local friction factor, along a sinusoidal groove at $Re_h = \approx 50$, $Re_h \approx 100$, $Re_h \approx 500$ and $Re_h \approx 1000$. The profiles display two phenomenon commonly

observed in sinusoidal grooves. Firstly, the streamwise shear stress distribution within the groove takes the form of a parabolic curve that lies out of phase with the geometric profile. Secondly, the reduction in shear stress throughout the groove is matched by a rise in the shear stress near the crests. Although the maximum and minimum values of $Re_h(\tau_0/\rho U_{av}^2)$ grow along with the groove depth, the enhanced resistance at the crests cannot overcome lower resistance over the larger area of the trough. Hence, the overall viscous flow resistance falls, as shown in Figure 6.2. In the present analysis, where the crest is not confined to a single point, the maximum of $Re_h(\tau_0/\rho U_{av}^2)$ moves from the stoss-side to the point where the stoss-side meets the flat crest. Here, the maximum forms a single spike just downstream of the stoss-side, which then falls to a plateau over the remainder of the crest. The pressure minimum lies at the downstream edge of the crest, whilst the pressure maximum forms around the midpoint of the stoss-side.

For all cases of $Re_h \approx 50$ and $Re_h \approx 100$ in Figure 6.3, the local shear stress remains positive along the surface for all values of k_g^*, which includes maximum lee-side angles of up to 25.2°. When the maximum lee-side angle is 19.1° ($k_g^* = 0.11$), and the surface lies in a flow of $Re_h \approx 500$, the shear stress approaches the limit of separation; $Re_h(\tau_0/\rho U_{av}^2) = 0$, towards the minimum of the trough but does not achieve separation. As case RS-KG2-KZ0-F4 shows, whilst flow separation is possible for sufficiently high inertial forces ($Re_h \approx 1000$), the point of separation does not occur until the steepest point of the lee-side is reached, leaving a flat, highly asymmetric vortex which is compressed by the shallow trough. For deeper grooves of $k_g^* = 0.15$, the separation point moves above the midpoint of the lee-side, increasing both the length and depth of the free-shear region, and hence, increasing the area that is available to the backwash. The length of the free-shear region and the strength of the backwash grow more substantially for an increasing groove depth, than they do for an increasing

(a) *RS, $k_z^* = 0$, $Re_h \approx 50$, $\varphi = 0°$*   **(b)** *RS, $k_z^* = 0$, $Re_h \approx 100$, $\varphi = 0°$*

(c) *RS, $k_z^* = 0$, $Re_h \approx 500$, $\varphi = 0°$*   **(d)** *RS, $k_z^* = 0$, $Re_h \approx 1000$, $\varphi = 0°$*
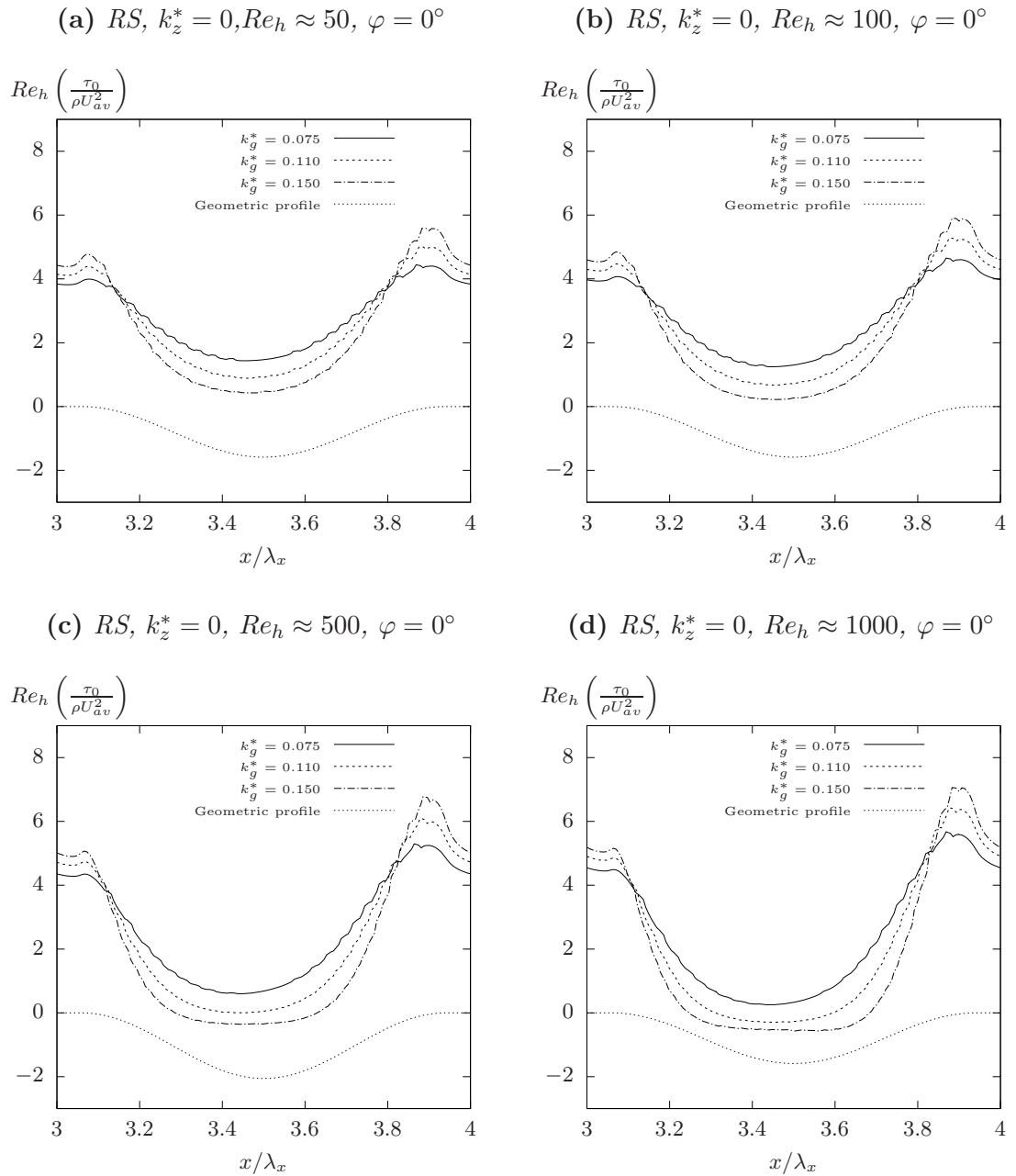
Figure 6.3: *Distribution of the normalised streamwise shear stress over two-dimensional sinusoidal profiles for flows of $Re_h \approx 50$, $Re_h \approx 100$, $Re_h \approx 500$ and $Re_h \approx 1000$.*

Reynolds number.

Now consider the effects of imposing a naturally occurring asymmetry onto a simple sinusoidal groove. Figure 6.4 displays the distribution of the normalised shear stress over the lower wall for two-dimensional geometries of natural sand ripple profile RN1 and RN2 in a flow of $Re_h \approx 500$. As in Figure 6.3, this distribution is assessed against two key values. The first value corresponds to the shear stress over the reference

smooth wall; $Re_h(\tau_0/\rho U_{av}^2) = 2.99$. The second value corresponds to the limit of
flow separation and flow reversal; $Re_h(\tau_0/\rho U_{av}^2) = 0$. For generalised sand ripples
forming under laminar flow conditions, the limits for vortex ripple formation, i.e. flow
separation, is determined by the critical depth of $k_g^* = 0.1$ (Vittori & Blondeaux 1990;
Blondeaux *et al.* 2015). This value was determined as the point at which a weakly non-
linear analysis for combined oscillating and steady bulk flow becomes unstable. For
asymmetric ripples comprised of flat planar section, Lefebvre *et al.* (2016) identified a
slip face angle of 18% as the critical limit of flow separation in unidirectional turbulent
flow. The present results indicate that the the critical limit of k_g^* for the onset of flow
separation over rigid ripple profile is heavily influenced by two additional factors; the
Reynolds number and the geometric features of the lee-side. Although, for profiles
which go beyond simple geometric profiles, a critical limit of k_g^* fails to represent a key
property of the surface profile; the steepness of the lee-side.

When considering a combination of Re_h, k_g^* and the maximum face angle, Fig-
ure 6.5a displays the first requirements for the development of a free-shear region.
The profile of RN2 at the deepest depth with its natural orientation of $\varphi = 0°$ is the
only surface to produce flow separation without approaching the limits of the laminar
regime ($Re_h \lesssim 100$). For its maximum depth of $k_g^* = 0.15$, the slip face angle becomes
42.2°. The length of the resulting free-shear region is small, within which a small span-
wise vortex remains pinned between the lee-side and the upstream portion of the flat
trough, indicating that for a flow of $Re_h \approx 100$, a slip face angle of 42.2° lies not far
above the critical limit of flow separation. Based purely upon the maximum lee-side
angle, a critical limit of $\approx 40°$ would correlate with that observed for sinusoidal grooves
in a purely viscous stokes flow (Niavarani & Priezjev 2009). As for the profile RN1,
sinusoidal grooves themselves have a single localised point at which the lee-side slope

(a) *RN1, $k_z^* = 0$, $Re_h \approx 500$, $\varphi = 0°$* **(b)** *RN2, $k_z^* = 0$, $Re_h \approx 500$, $\varphi = 0°$*

(c) *RN1, $k_z^* = 0$, $Re_h \approx 500$, $\varphi = 180°$* **(d)** *RN2, $k_z^* = 0$, $Re_h \approx 500$, $\varphi = 180°$*
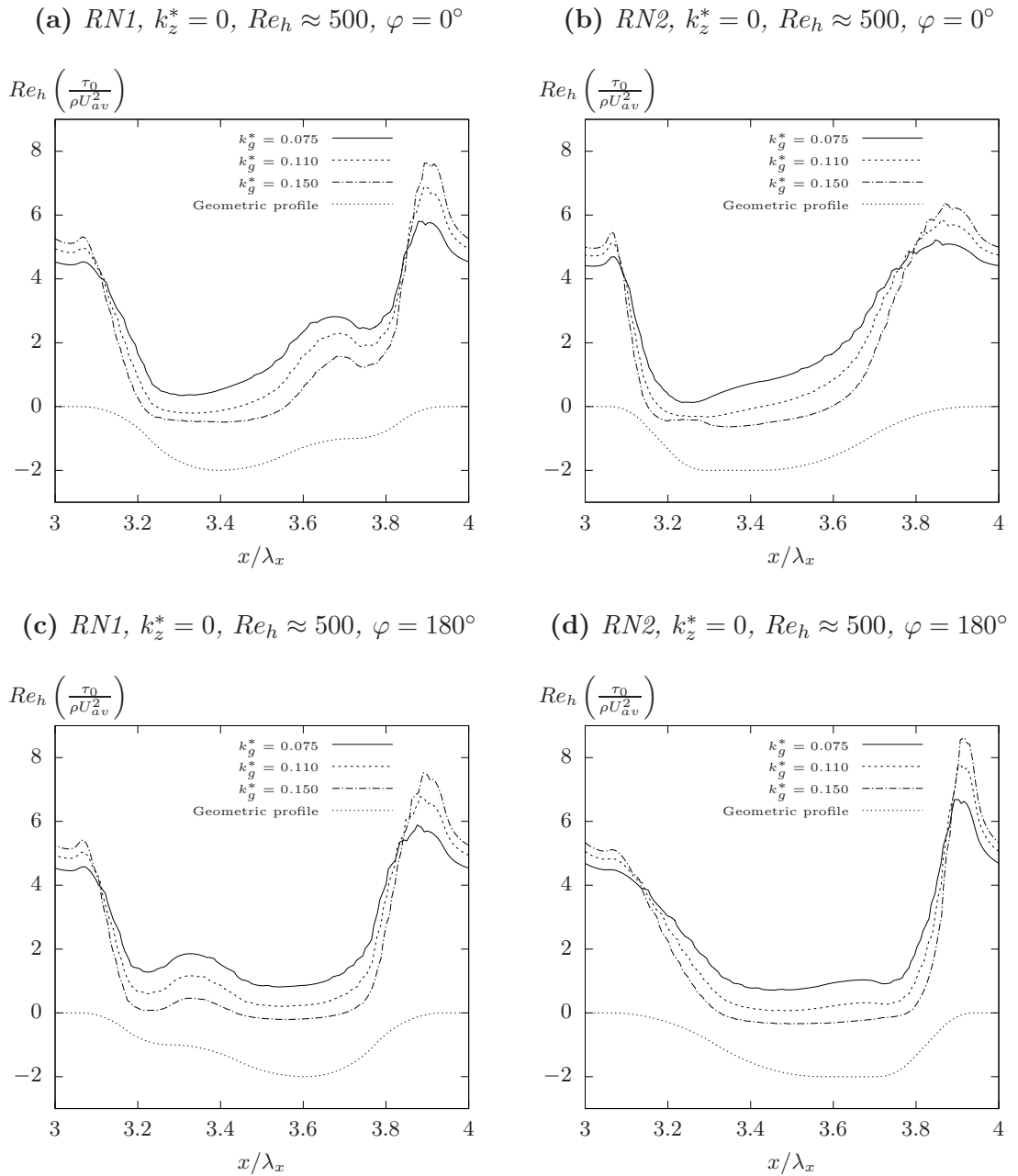
Figure 6.4: *Distribution of the normalised streamwise shear stress over two-dimensional sand ripple profiles for a flow of $Re_h \approx 500$.*

reaches an angle of $\approx 40°$. Separation does not occur for the profile of $RN1$ under identical conditions, for which the maximum steepness on the natural lee-side reaches 43.2°. Reducing the angle of the slip face in RN2 to 24.4° ($k_g^* = 0.075$) raises the required Reynolds number for flow separation by a factor greater than 5. Whilst shear layers remain attached throughout the groove at $Re_h \approx 500$, by $Re_h \approx 1000$ a large spanwise vortex covers the majority of the flat trough.

(a) *Case RN2-KG3-KZ0-F2, $\varphi = 0°$*
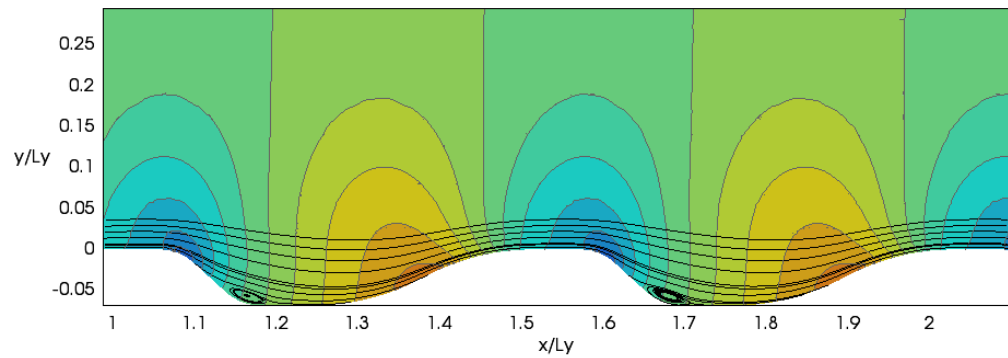
(b) *Case RN1-KG3-KZ0-F4, $\varphi = 0°$*
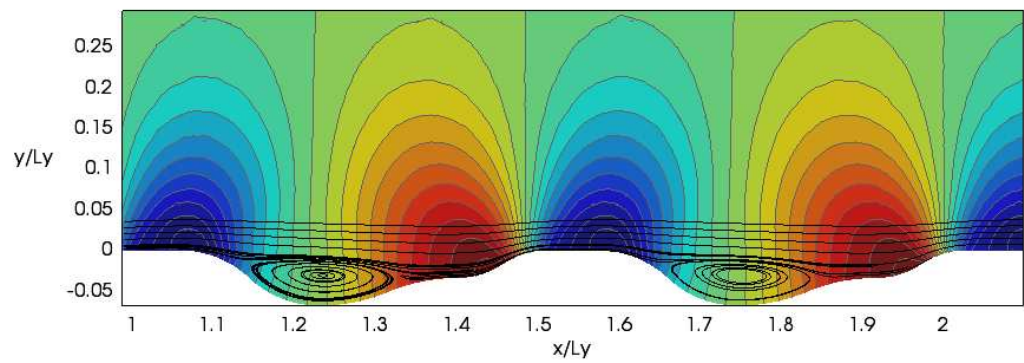
(c) *Case RN1-KG3-KZ0-F4, $\varphi = 180°$*
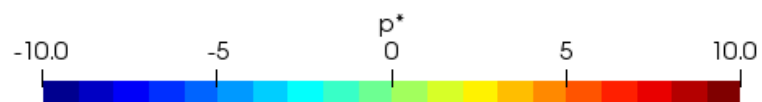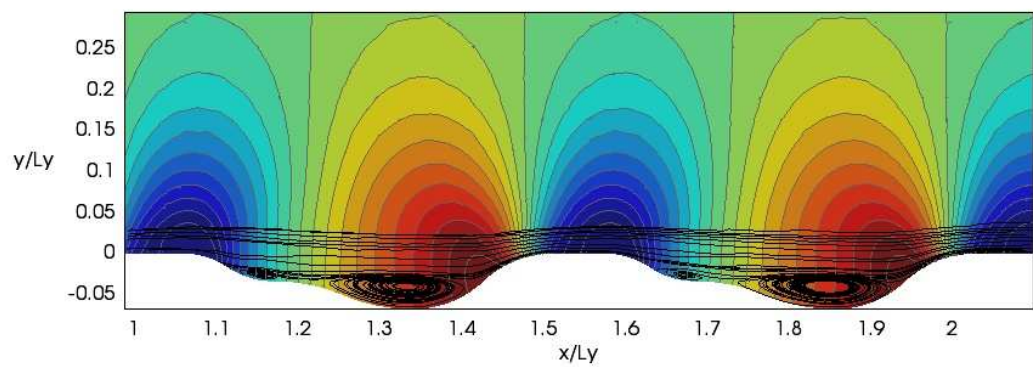
Figure 6.5: *A visualisation of flow trajectory (black lines), and normalised pressure field for three cases in Table 6.1.*

When the lee-side consists of multiple curves/faces, a single value of the maximum slope angle may be insufficient for even a general indication of flow separation. In profile RN1 the steepest point on the natural stoss-side is located at the highest point of inflection ($y = -0.25k_g$). When the natural stoss-side is placed to form the lee-side ($\varphi = 180°$), the flow remains attached to the the upper segment in any case of $Re_h \approx 500$, for which it separates below the plane of $y = -0.5k_g$. This is in spite of the reverse case promoting flow separation with a smaller angle of $32°$ ($k_g^* = 0.11$) at a similar magnitude of Re_h. When the configuration of the former surface does promote flow separation, by raising the Reynolds number to $Re_h \approx 1000$, it produces a pair of co-rotating vortices, as shown in Figure 6.5c, which form two distinct separation regions, as opposed to the single vortex which is present when the surface orientation is reversed, as shown in Figure 6.5c. At the connecting point the flow briefly reattaches to lee-side prior to the second free-shear region. As the flow that lies adjacent to the lee-side approaches the second point of inflection at $y = -0.5k_g$, it goes through a period in which the rate of acceleration/deceleration reduces, before rising again. This behaviour leads to a third localised spike in the shear stress.

For combinations of sufficiently deep, asymmetrical grooves combined with Reynolds numbers in the range of $Re_h \gtrsim 500$, the direction of the flow plays a significant role in promoting or delaying the onset of flow separation from the lee-side. This in turn significantly impacts the length of the free-shear region and the strength of the back-wash from the spanwise vortex. However, in no case did a reversal of the flow direction produce a non-negligible change to either the ratio of the pressure contribution, or the individual components of Poisuille number. As Figure 6.4 shows, even when alternating the flow orientation determines the existence of a free-shear region, the solution for $\varphi = 180°$ already produces a strong reduction in shear stress throughout the groove

and lies close to the limit of separation at $Re_h(\tau_0/\rho U_{av}^2) = 0$. Hence, the negative shear stress from the backwash only produces a marginal improvement within the trough. Furthermore, this reduction in shear stress in the trough is counteracted by higher shear stress at the crests, and particularly during the initial velocity spike. For simple sinusoidal grooves, Saha *et al.* (2015) observed that flow separation over the majority of the groove, and the formation of large spanwise vortices, are not necessary for the pressure drag to match the viscous drag on a corrugated surface. This observation existed in the context of comparing the flow field within grooves for varying values of depth and Reynolds number. In the present analysis, this phenomenon is confirmed when the geometries of the lee-side and stoss-side are altered whilst keeping both the centre of area and the total surface area constant.

6.4 Three-Dimensional Ripples

6.4.1 Poisuille Number

Figure 6.6 compares results for natural sand ripple surfaces for varying magnitudes of spanwise variation k_z^*. For all cases for which the flow lies firmly within laminar regime ($Re_h \approx 50$), the spanwise amplitude displays a negligible impact on the total Poisuille number. In no instance does raising the spanwise amplitude from $k_z^* = 0$ to $k_z^* = 0.5$ shift $Re_h f$ by more than 0.1% of $(Re_h f)_{smooth}$. The viscous component on the upper wall displays an equally small response. As observed for two-dimensional ripples, the lack of response in $Re_h f$ may be attributed to the balance between its pressure and viscous components. As k_z^* increases, $Re_h f_p$ falls by an equal magnitude to the rise in $Re_h f_v$, which reaches up to $\pm 1.8\%$ of $(Re_h f)_{smooth}$ for the deepest ripples.

(a) *Pressure Ratio*

(b) *Total Flow Resistance*

(c) *Lower Wall Viscous Resistance*

(d) *Upper Wall Viscous Resistance*
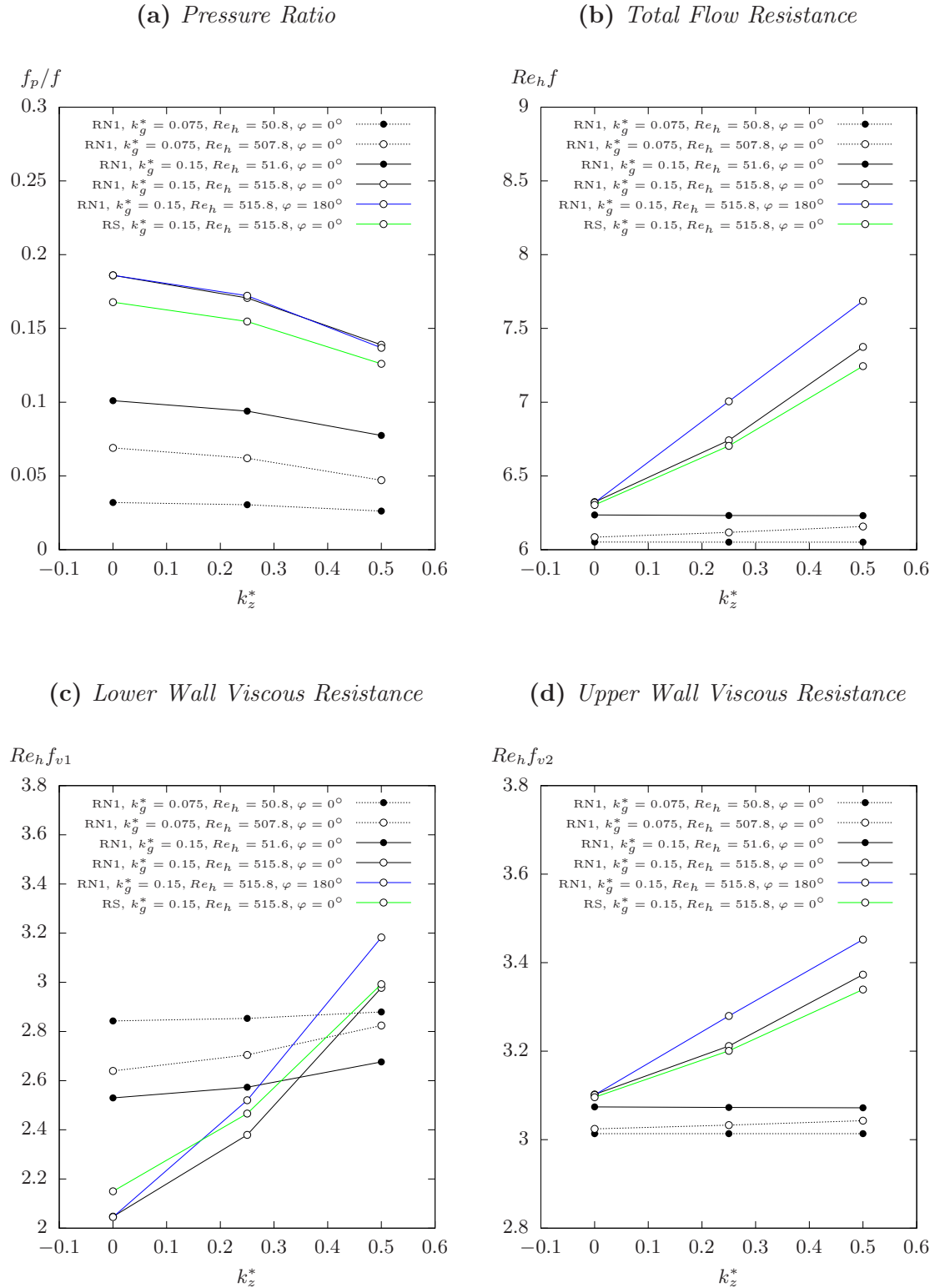
Figure 6.6: *Properties of flow resistance for the three-dimensional surface profile cases outlined in Table 6.2.*

Bringing the Reynolds number towards the upper limits of the laminar regime ($Re_h \approx 500$) strongly amplifies the effect of k_z^*. For the shallowest ripples ($k_g^* = 0.075$), as k_z^* grows the viscous drag increase begins to grow at a faster rate than the drop in the pressure component. The total shift in $Re_h f$ between $k_z^* = 0$ and $k_z^* = 0.5$ lies below $+1.26\%$ of $(Re_h f)_{smooth}$. As seen for the lower Reynolds numbers of $Re_h \approx 50$, the individual components of Poisuille number display a minimal dependence on the flow orientation. Doubling the groove depth, thus combining these higher Reynolds numbers of $Re_h \approx 500$ with the deep ripple profiles of $k_g^* = 0.15$, significantly amplifies the influence of k_z^*. Applying a spanwise amplitude of $k_z^* = 0.25$ to this two-dimensional ripple raises the Poisuille number by more than 7% of $(Re_h f)_{smooth}$ for $\varphi = 0°$. This shift is already greater than that observed for the range of any of the control factors considered in Section 6.3.1, and rises to $+17.5\%$ of $(Re_h f)_{smooth}$ at $k_z^* = 0.5$. In addition, the flow direction begins to play a significant role in determining the flow resistance. Reversing the flow over the naturally oriented ripple ($\varphi = 0° \rightarrow 180°$) raises the Poisuille number by roughly 5% of $(Re_h f)_{smooth}$ ($\approx 5 \pm 0.5\%$), depending on the value of k_z^* in contrast to the small improvement observed when $k_z^* = 0$. Reversing the flow direction produced a greater change in $Re_h f$ than replacing the ripple profile of RN1 at $\varphi = 0°$ with a symmetrical sinusoidal groove.

The sharp rise in $Re_h f$ with k_z^*, which was observed for cases of $Re_h \approx 500$ and $k_g^* = 0.15$, may be attributed primarily to the lower wall viscous drag, which increases rapidly enough that by $k_z^* = 0.5$, the value of $Re_h f_{v1}$ alone can exceed the value of a reference smooth wall. This trend is accompanied by a similar trend in the values of the viscous component on the upper wall, although to a far smaller magnitude. In comparison, the impact of k_z^* on the flow resistance from pressure remains negligible and the drop in f_p/f in Figure 6.6a reflects the rapid climb in f. The drop in $Re_h f_p$ is

of a small magnitude for all combinations of Re_h and k_g^*, such that varying k_z^* within the current range never reduces the value of $Re_h f_p$ by more than 3%.

6.4.2 Local Wall Shear Stress

The value of k_z^* only produces a significant effect on the Poisuille number when the ripple has a depth of $k_g^* = 0.15$ and lies within a flow of $Re_h \approx 500$. The changes in the Poisuille number in this case are dependant primarily on the viscous resistance of the textured lower wall and, to a lesser degree, the smooth upper wall. Figure 6.7 displays the distribution of the normalised shear stress over three-dimensional ripple patterns at two key spanwise locations; one located over the lobe ($z/L_z = 0$) and the other located over the saddle ($z/L_z = 0.5$). The cases correspond to a flow of strength of $Re_h \approx 500$ over ripples of depth $k_g^* = 0.15$ (Figure 6.7a & Figure 6.7b) and $k_g^* = 0.075$ (Figure 6.7c & Figure 6.7d). Applying a sinusoidal spanwise variation with an amplitude of $k_z^* = 0.25$ to an initially two-dimensional profile produces a redistribution of the shear stress along the lower wall, such that the streamwise distribution of $Re_h(\tau_0/\rho U_{av}^2)$ within the grooves varies in relation to the spanwise location.

First, consider the region of reduced shear stress in the region connecting two lobes ($z/L_z = 0$), as shown in Figure 6.7a and Figure 6.7b. For $k_z^* = 0.25$ and $k_z^* = 0.5$ the normalised shear stress falls below the the smooth wall reference $Re_h(\tau_0/\rho U_{av}^2) = 2.99$ along the full profile of the groove and the majority of the crest, and only exceeds this value during the usual spike upon reaching the crest. The usual correlation between the shear stress at the crest and in the trough is maintained, whereby, as k_z^* rises, the fall in the maximum value of $Re_h(\tau_0/\rho U_{av}^2)$ is matched by a rise in the minimum value. However, this marginal rise in shear stress within the trough is negligible compared to the reduction over the crest. In case RN1-KG3-KZ2-F3 ($Re_h \approx 500$, $k_g^* = 0.15$) the

(a) $k_g^* = 0.15$ *(z/λ_z = 0)*

(b) $k_g^* = 0.15$ *(z/λ_z = 0.5)*

(c) $k_g^* = 0.075$ *(z/λ_z = 0)*

(d) $k_g^* = 0.075$ *(z/λ_z = 0.5)*
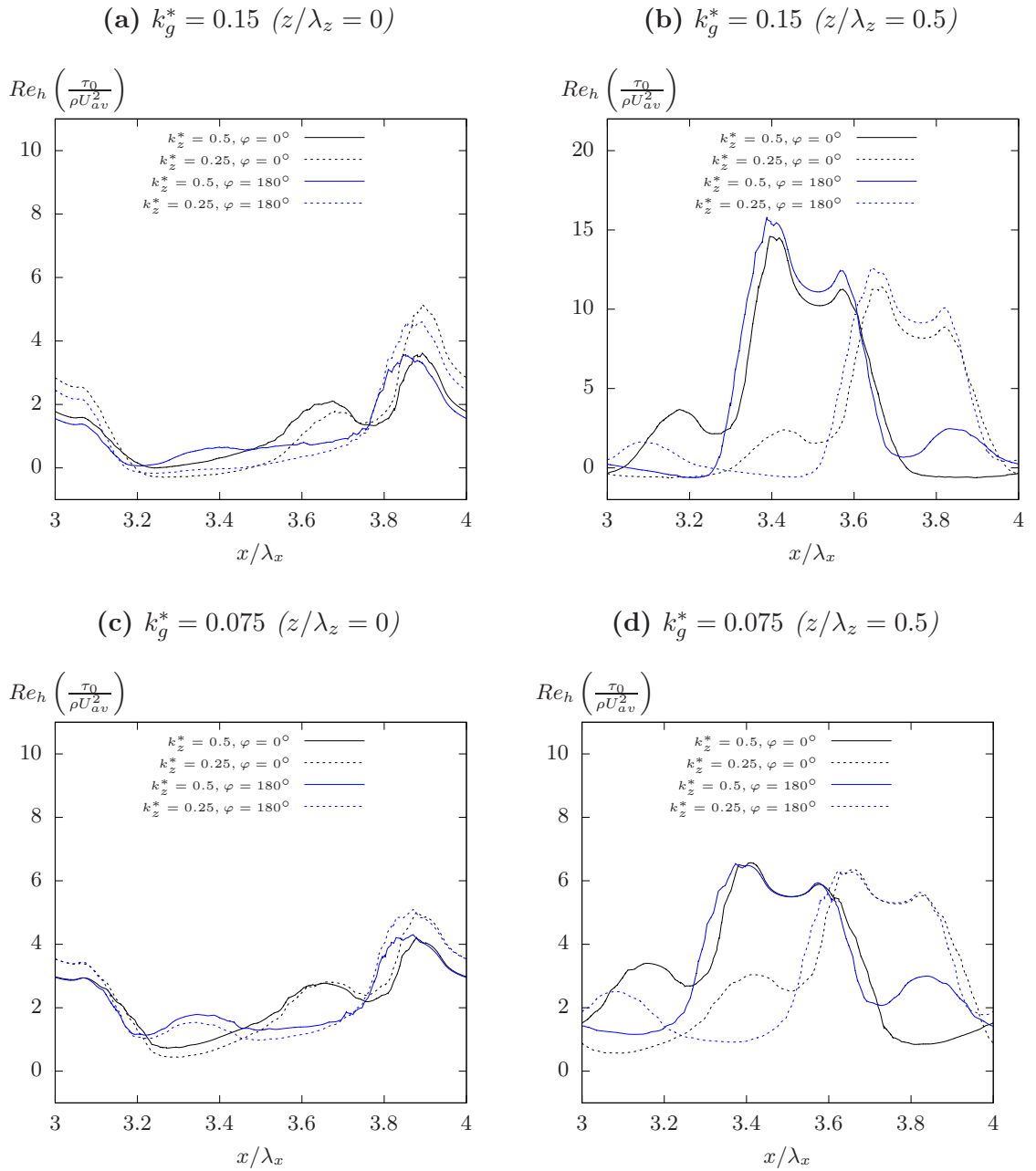
Figure 6.7: *Distribution of the normalise streamwise shear stress over surfaces of the three-dimensional ripple profile RN1 in flows of $Re_h \approx 500$.*

loss of momentum at the lobe is such that the flow passing over the lee-side of the lobe fails to separate for either solution of $\varphi = 0°$ and $\varphi = 180°$.

In cases RN1-KG3-KZ1-F3 and RN1-KG3-KZ2-F3, the reduction in the shear stress at the lobe is accompanied by a sharp rise in the shear stress in the region of the saddle $(z = \pm 0.5\lambda_z)$. This rise is primarily focused on the crests, where the value of $Re_h(\tau_0/\rho U_{av}^2)$ at both the initial localised spike and the remainder of the flat crest rises

by more than $\approx 80\%$ when compared with the two-dimensional ripple in case RN1-KG3-KZ0-F3 (Figure 6.4). The rise in shear stress over the stoss-side and the crest at the saddle exceeds the reduction in shear stress over the full width of the lobe. This difference only grows with the increasing amplitude of the spanwise profile. Reducing the ripple depth by a factor of 0.5 to $k_g^* = 0.075$ (Figure 6.7d) disproportionately reduces the shear stress at the crests whilst maintaining a similar magnitude of shear stress over the stoss-side. In addition, Figure 6.7b shows that the orientation of the groove at $k_g^* = 0.15$ and $Re_h \approx 500$ has a significant influence on the shear stress in over the crest of the lobe. The natural orientation of $\varphi = 0°$ produces a reduction in the shear stress along the whole length of the high shear region at the crests of the saddle, in comparison to $\varphi = 180°$. The flow mechanism which generates the high shear stress at the lobes has a non-negligible dependence on the geometric profiles of the lee-side and stoss-side.

Over the three-dimensional profile the flow is characterised by a pair of streamwise, counter-rotating vortex cores which form on either side of each lobe. As each pair of vortices move downstream they grow in size and move away from the wall. Half-way along the ripple profile the vortices begin to converge before reattaching to the crest of the downstream lobe. The trajectory of the flow in the streamwise-wall-normal plane between consecutive lobes ($z = 0 \pm \lambda_z$) is always primarily directed towards the upper wall. This even applies to the region over the lee-side, where the local channel opening in these two-dimensional planes is increasing with x. Although the slow moving fluid from the trough accelerates over the lee-side of the lobe, its upwards momentum is rapidly reversed as it feeds into the stronger downwash. At this point the magnitude of the minimum wall-normal velocity (located within the downwash) exceeds the maximum positive value (located within the upwash), by a factor of ≈ 2.

(a) $x/\lambda_x = 0$ **(b)** $x/\lambda_x = 0.60$

(c) $x/\lambda_x = 0.83$ **(d)** *Streamwise locations*
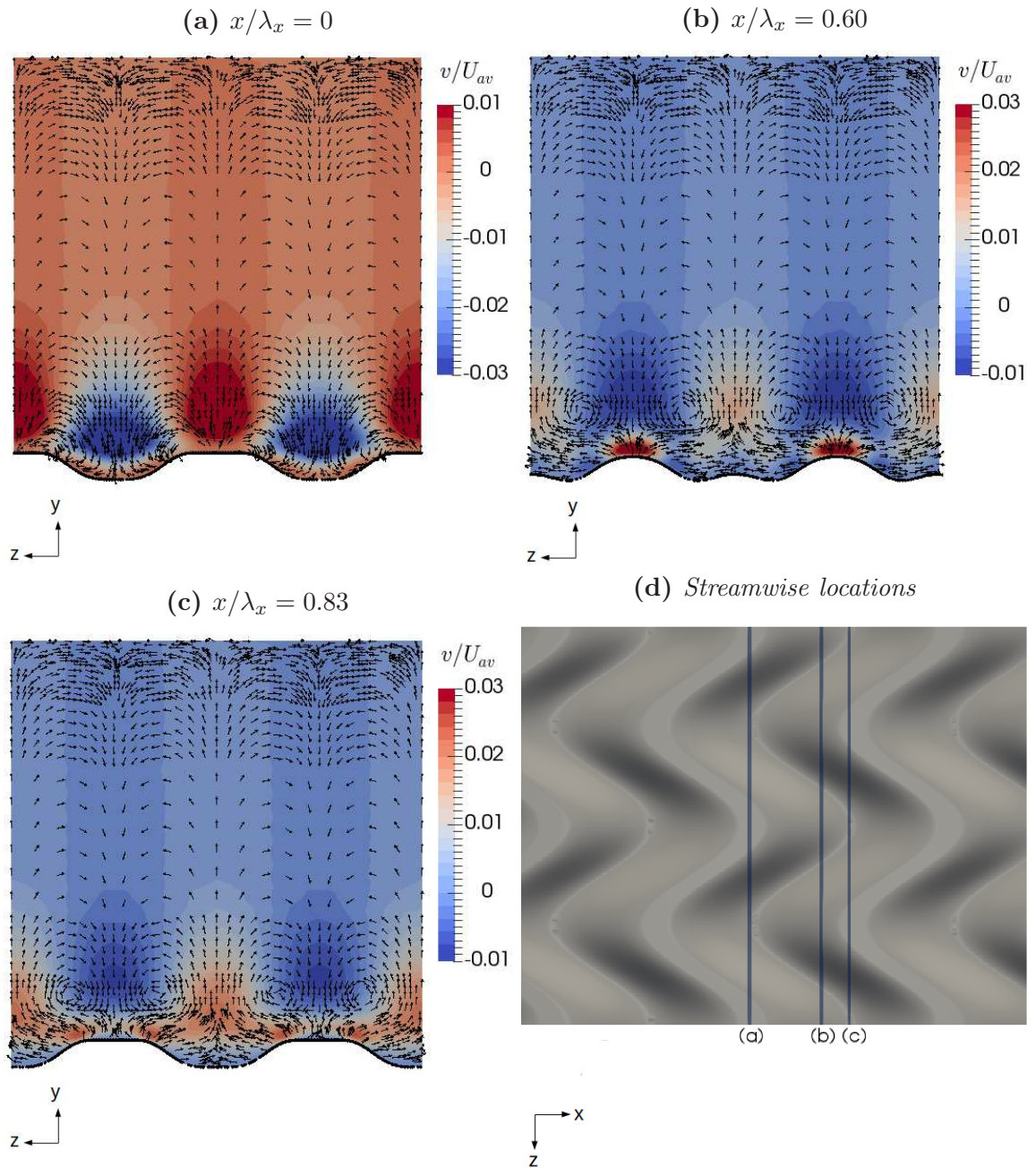
Figure 6.8: *A visualisation of spanwise vortex formation, based on the flow fields over the reference sinusoidal profile in case RS-KG3-KZ2-F3. Vectors display illustrate the wall-normal and spanwise velocity component.*

Figure 6.9 provides a clear depiction of the main impact of the upwash and downwash over the flow field. In the region over the saddle points ($z = \pm0.5\lambda_z$), within the bulk of the channel, the flow maintains a constant trajectory towards the lower wall. In contrast to that over the lobes ($z = 0 \pm \lambda_z$) the flow within the trough and in a small region above the crests, varies in wall-normal trajectory, in relation to the two-dimensional surface profile. As the flow passes beyond the crest of the saddle, the

momentum of the downwash feeds the flow directly into the groove, where it follows the contour of the lee-side, as in the case of $k_z^* = 0$. Hence, the distribution of stress stress along the lee-side maintains a similar form, although with significant scaling, with the corresponding two-dimensional cases; Figure 6.4a and Figure 6.7c. As the flow moves towards the trough the shape of the spanwise periodic profile funnels the flow towards the enclave force behind the lobe. As the flow stream accelerates over the stoss-side it collides with the high velocity flow from the bulk of the channel, which passes through the downwash between the streamwise vortices. The flow on the stoss-side is restricted, producing a greater rate of acceleration prior to the crest.

The presence of a patterned surface will modify the shape of the steady-state flow field, in relation to the planar distribution of a reference smooth channel. The ultimate effect of the spatially alternating upwash and downwash generated by the streamwise vortices is to redistribute the streamwise velocity across the spanwise surface profile. Figure 6.11 and Figure 6.10 represent the interaction between the lower wall and the three-dimensional flow field as the spatial distribution of the streamwise velocity component on a streamwise-spanwise plane over the lower wall, for asymmetric ripple profiles with a depth of $k_g^* = 0.15$. When the flow lies firmly within the laminar regime, i.e. $Re_h \approx 50$ (Figure 6.10), and the amplitude of the spanwise variation is equal to half of the streamwise wavelength ($\lambda_x = 2k_z$), the spanwise deviation in the flow field remains the dominant feature at a distance of $y/h_0 = 0.147$. When the spanwise amplitude is halved ($\lambda_x = 4k_z$), the streamwise deviation dominates. Moving into the transitional regime ($Re_h = 515.8$), the streamwise variation rapidly diminishes away from the wall, and the streamwise flow field is dominated by a two-dimensional wavy profile. The maximum and minimum values lie along a pair of parallel streamwise axis which lie over the lobe and saddle points of the lower wall. Throughout the bulk of the channel,

(a) *RN1-KG3-KZ1-F1*
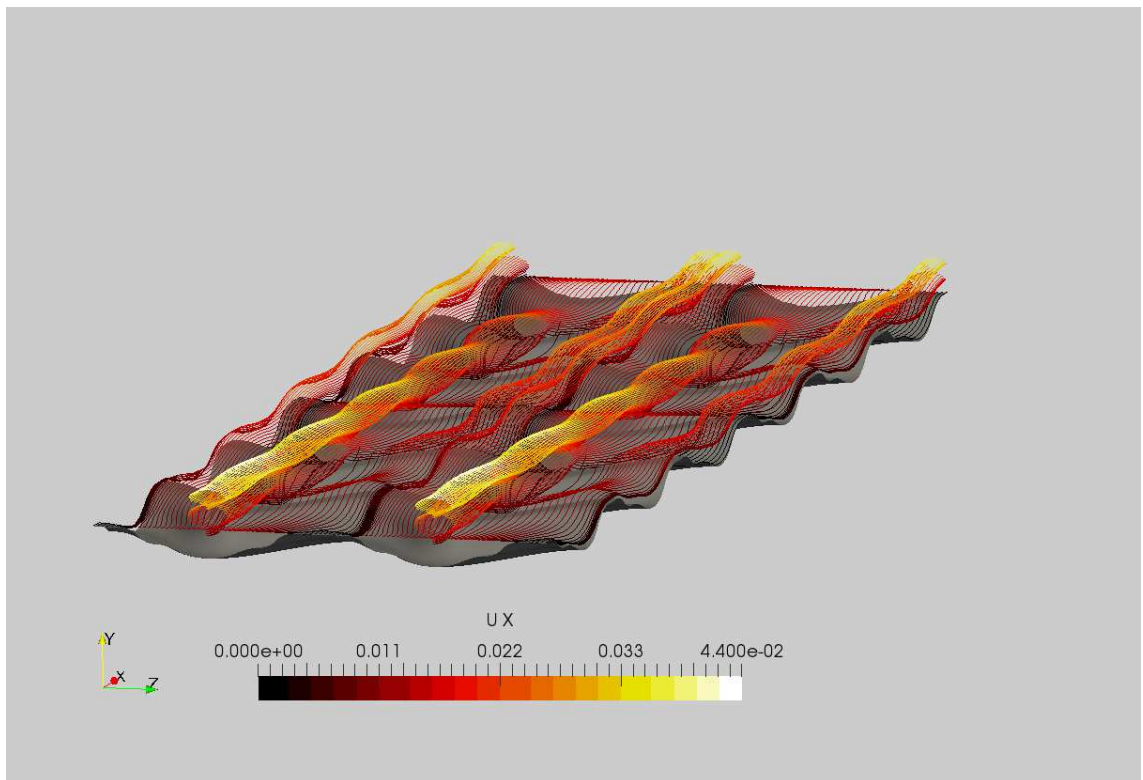
(b) *RN1-KG3-KZ1-F3*
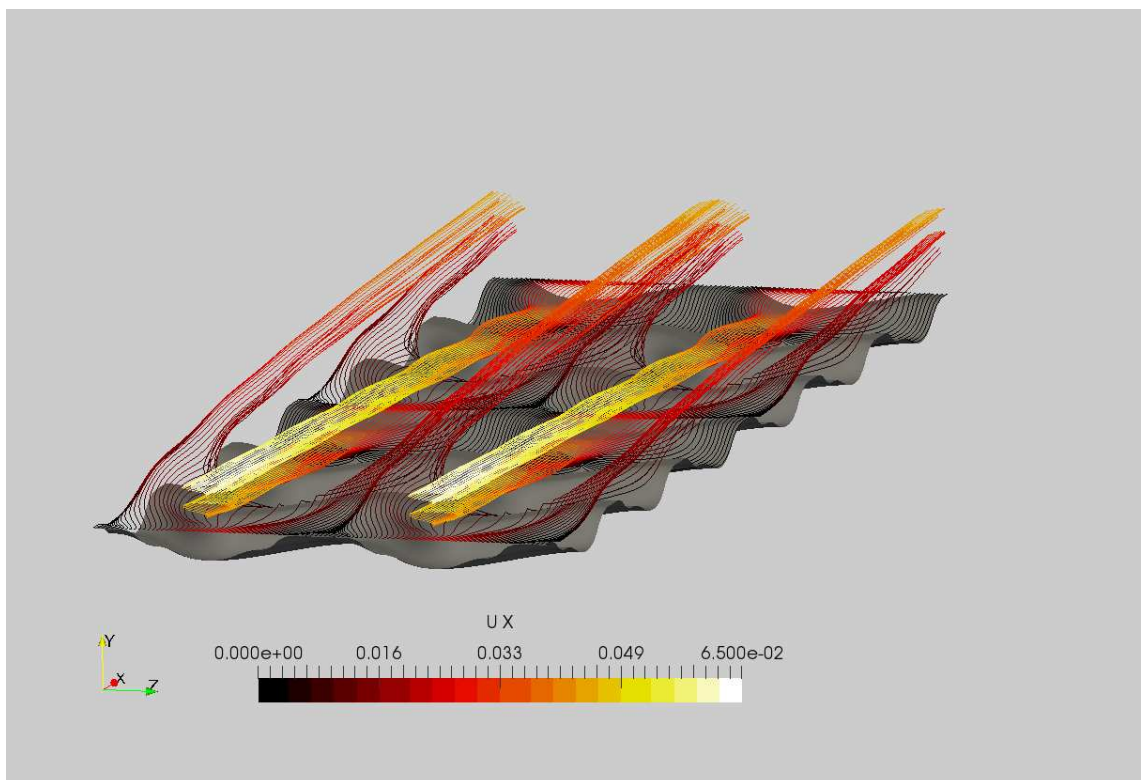
Figure 6.9: *Three-dimensional streamlines of flow trajectory passing over the crest of three-dimensional sand ripple profiles.*

including the region beyond the centreline ($y > h$), the flow field maintains this distribution, though the maximum and minimum value of streamwise velocity degrades with increasing distance from the lower wall.

(a) *RN1-KG3-KZ1-F1* ($y/h_0 = 0.029$)   **(b)** *RN1-KG3-KZ1-F1* ($y/h_0 = 0.147$)
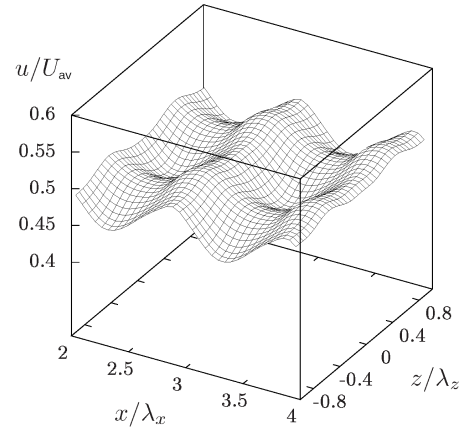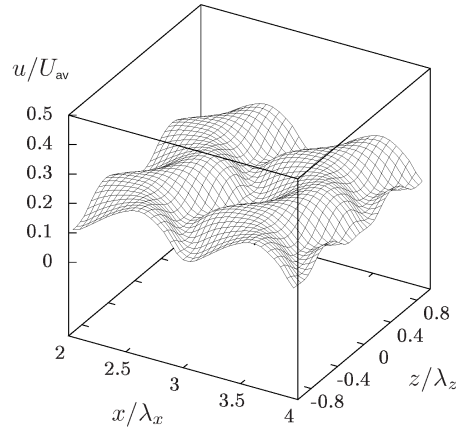
(c) *RN1-KG3-KZ2-F3* ($y/h_0 = 0.029$)   **(d)** *RN1-KG3-KZ2-F3* ($y/h_0 = 0.147$)
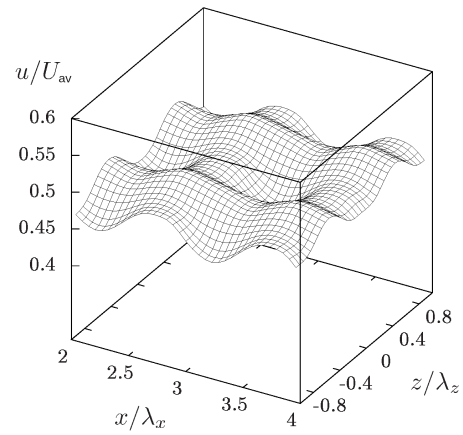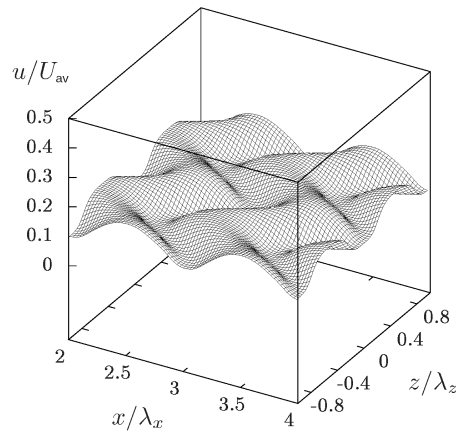
Figure 6.10: *Surfaces contours of the streamwise component of velocity in a flow of $Re_h \approx 500$ for an asymmetric sand ripple profile with varying spanwise variation.*

(a) *RN1-KG3-KZ0-F3 (y/h$_0$ = 0.029)*　　**(b)** *RN1-KG3-KZ0-F3 (y/h$_0$ = 0.147)*
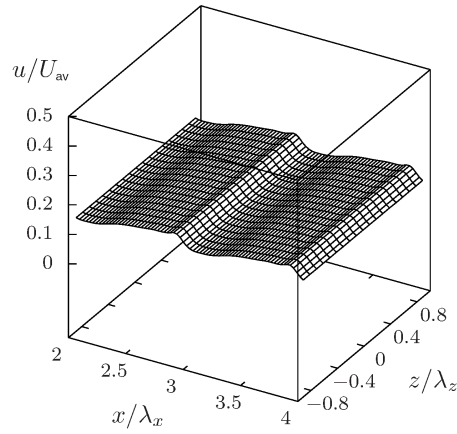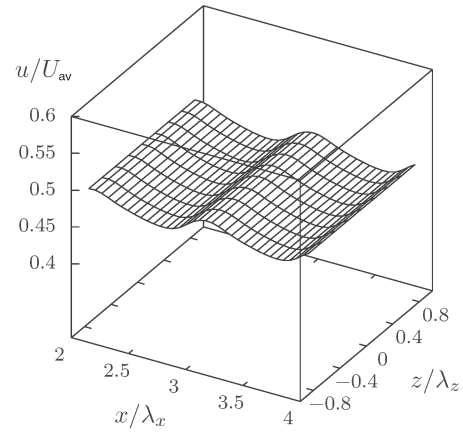
(c) *RN1-KG3-KZ1-F3 (y/h$_0$ = 0.029)*　　**(d)** *RN1-KG3-KZ1-F3 (y/h$_0$ = 0.147)*
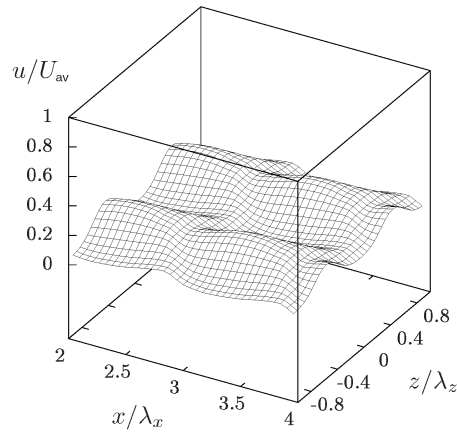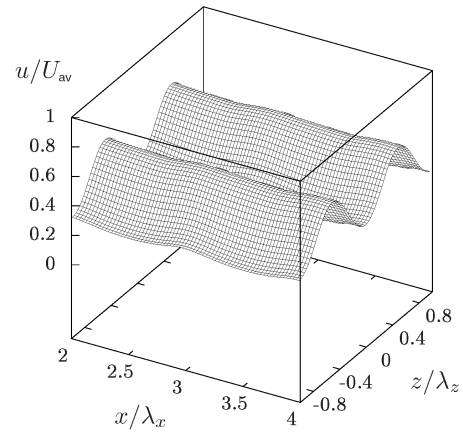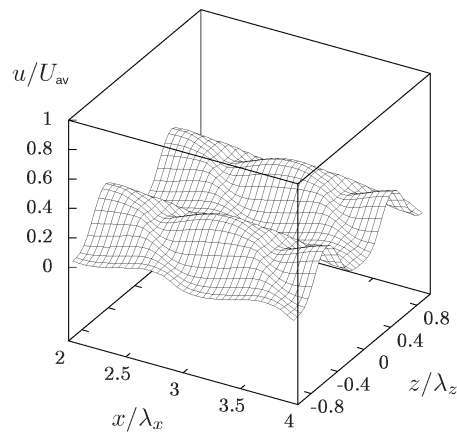
(e) *RN1-KG3-KZ2-F3 (y/h$_0$ = 0.029)*　　**(f)** *RN1-KG3-KZ2-F3 (y/h$_0$ = 0.147)*
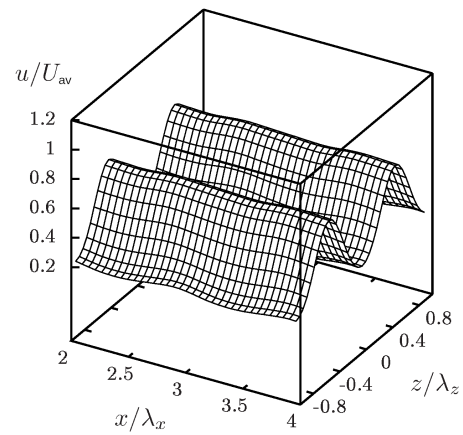
Figure 6.11: *Surfaces contours of the streamwise component of velocity in a flow of $Re_h \approx 500$ for an asymmetric sand ripple profiles for three levels of spanwise variation.*

6.5 Summary

A large-scale parametric study has been completed that investigates the theorised potential for laminar drag reduction of grooved Poisuille flows through the application and optimisation of highly detailed geometric surface features. The two primary surface profiles replicate the detailed profiles of bedforms of sand ripples which form naturally under tidal motions over a sand beach. The analysis considers the influence of groove depth, profile shape, flow direction, Reynolds number and spanwise geometric variation on the flow resistance through the channel, in addition to the near-wall flow field and the shear stress distribution along the surface. The results presented here contribute a higher understanding to the existence of critical limits, in regards to surface geometry and flow strength, for which a detailed surface modification has the potential to manipulate flow resistance.

For all cases involving two-dimensional grooves, the natural sand ripple profiles had a negative impact on the overall flow resistance, in comparison to simplified sinusoidal grooves. Across the ranges considered here, the groove depth proved to be the primary factor in determining the total flow resistance, displaying an overwhelming influence when compared to the Reynolds number. The direction of the flow, in relation to the surface profile, displayed a negligible influence on both the total Poisuille number and its individual components. This influence remained negligible in cases for which the flow field was irreversible, and the size and shape of the separation bubble varied significantly with the flow direction. Where previous investigations have failed to observe such correlations by comparing the output of varied surface geometries, the current results demonstrate that such a correlation remain absent when comparing identical domains and flow conditions. These observations do not lend support to recent theories (Mohammadi & Floryan 2013b; Saha *et al.* 2015) which suggest a potential for

achieving a drag reduction in single phase laminar flow by reducing the separation length within a groove to reduce the pressure drag, or by encouraging the growth of a separation bubble to reduce viscous drag on a surface. The current results show that the mechanisms which dominate the pressure drag and viscous drag in single phase laminar flow exist in opposition to each other, usually in close balance, and that these mechanisms have, at most, a weak connection to any free-shear region within the groove.

Imposing a sinusoidal spanwise variation onto a two-dimensional profile did not exert any significant change in the flow resistance, until applied with a combined groove depth of $k_g^* = 0.15$ and a flow of $Re_h \approx 500$. Under these conditions, the viscous resistance of the lower wall, and to a lesser degree the upper wall, grew rapidly with an increasing spanwise amplitude, whilst the effect on the pressure interaction drag was minimal. This change results from a redistribution of the shear stress between the lobes and the saddles. The crests of the lobes are supplied by an upwash of low velocity fluid from the troughs. The crests of the saddles are supplied by a counteracting downwash of high velocity flow from the bulk of the channel. With this high concentration of shear stress at the saddle, the high geometric details of the lee-side begin to exert a significant influence on the resulting shear stress at the crest, and hence, become a primary source of viscous flow resistance. It is only under such conditions that the orientation of such transverse grooves can be considered as an important design factor.

Further investigation is required to increase the precision of the control factors, and hence, improve and understanding of the critical limits of the flow phenomenon observed here. From the current parametric study, the range of geometric properties can be expanded to include a larger range of geometric parameters and profile shapes. In addition, the influence of the spatial resolution within the bulk of the channel when

the surfaces induce a large shift in the flow distribution away from the wall, (i.e. deep,

three-dimensional grooves), should be investigated further.

Ripples in Spatially Developing Turbulent Flow

7.1 Introduction

The present Chapter investigates the application of the numerical methodology developed in Chapter 4 to a spatially developing boundary turbulent layer over a surface of periodic, two-dimensional ripple profiles. One asymmetric ripple profile from Chapter 5 and Chapter 6 is simplified in order to accommodate the optimal smooth wall spatial resolution from Chapter 4, in addition to improving manufacturability.

Three simulations investigate the spatially developing boundary layer over ripple profiles with three values of ripple depth, using the spatial resolution which is optimised for the reference smooth wall, but which is relatively coarse in relation to the requirement of the ripple profile. One additional boundary layer simulation applies the

automatically generated split-hexahedral mesh from Chapter 5 to the deepest ripple profile, in order to investigate the capability of a split-hexahedral mesh to overcome the difficulties associated with modelling non-planar geometries in resolved turbulent flow.

The final section of this Chapter validates the meshing procedure by comparing coarse and fine hexahedral meshes, with the automatically generated split-hexahedral mesh, within the simplified domain of a periodic channel. A channel domain is selected due to the crippling computational costs associated with increasing spatial resolution in a hexahedral mesh; a problem which the automatically generated split-hexahedral mesh alleviates.

7.2 Physical Scenario

7.2.1 Groove Geometry and Case Configuration

The present analysis utilises the simulation setup from Chapter 4 which was designed and optimised for modelling spatially developing turbulent boundary layers over smooth walls, as shown in Figure 7.1. In Figure 7.1 a region of the smooth surface lying between $x = 0.07m$ ($x = 2480\theta_{in}$) and $x = 0.25m$ ($x = 8858\theta_{in}$) has been replaced with a surface of two-dimensional, periodic ripples which are oriented perpendicular to the streamwise direction. The ripples consist of a single profile at three different dimensionless depths, $k_g^* = 0.025$, $k_g^* = 0.05$ and $k_g^* = 0.15$. Two values correspond to the drag reducing limits of $k_g^* \leq 0.05$ observed for circular dimples in turbulent channel flow (Tay *et al.* 2015). The highest value corresponds to the natural depth ratio observed in the natural ripple profile RN1 in Chapter 5. A depth of $k_g^* = 0.15$ lies

beyond the proposed critical limit of separation $k_g^* > 0.1$ (Blondeaux *et al.* 2015). Furthermore, the analysis in Chapter 6 revealed that a ripple depth of $k_g^* = 0.15$ combined with a spanwise geometric variation could produce strong iterations with the flow field, characterised by large three-dimensional flow structures within a two-dimensional, high Reynolds number, laminar channel flow.
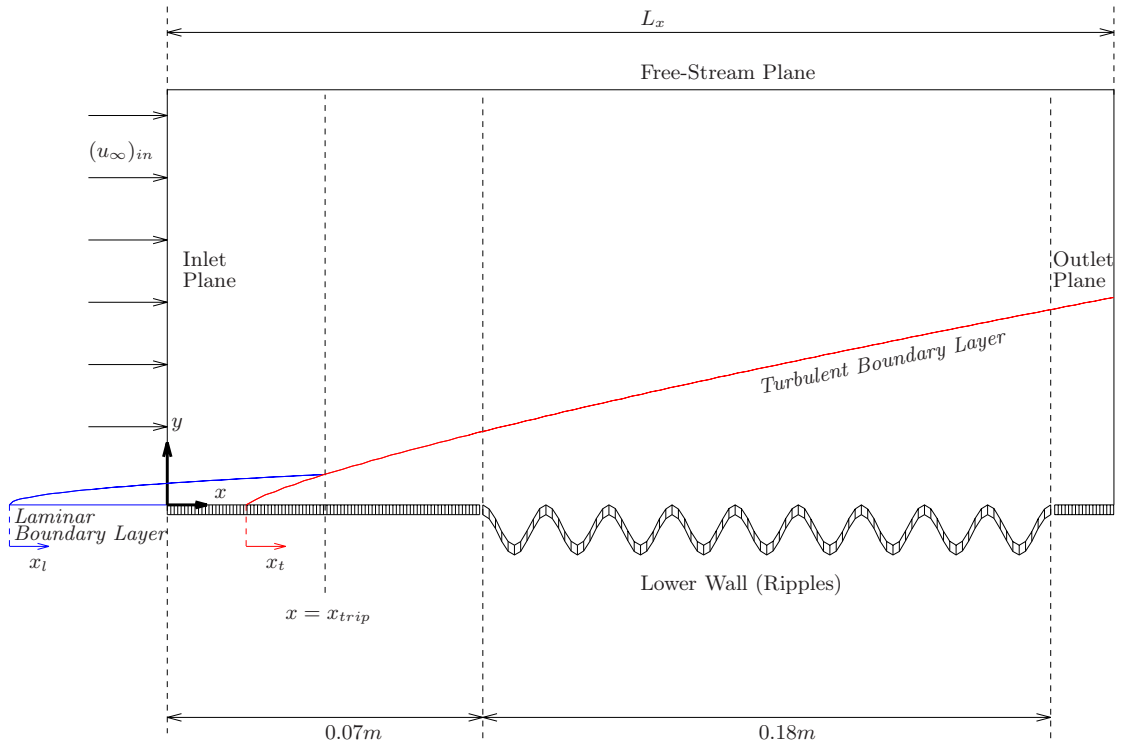
Figure 7.1: *Diagram of the flow domain and boundary conditions for the spatially developing boundary layer flow over a surface of periodic ripples.*

The original surface is a two-dimensional profile of a manufactured, groove with a ripple-inspired profile, based upon the naturally occurring profile RN1, defined in Chapter 5. The manufactured geometry is created through milling, in which a pair of overlapping arcs are cut into a flat surface. The total distance from the midpoint of a crest, to the midpoint of an adjacent crest is $\lambda_x = 7.46mm$. The length of the ripple is $\lambda_z = 3.46mm$, with a crest to trough depth of $k_x = 0.519mm$, such that $k_g^* = k_g/\lambda_g = 0.15$. The manufactured ripple profile was designed such that the length of λ_g is roughly equal to the thickness of the smooth wall boundary layer at the end of

the textured region ($\lambda_g \approx \delta_{99}$ at $x = 0.25m$). The shallower ripple profiles are created by scaling the manufactured profile in the wall-normal direction. In this initial study, the ripple is oriented with the a shallow lee-side and steep stoss-side ($\varphi = 180°$). Each geometry is defined by the centre and radius of a pair of circles which produce the pair of overlapping arcs which are cut into the surface. Table 7.1 provides these values as a scaling of the full ripple wavelength λ_x.
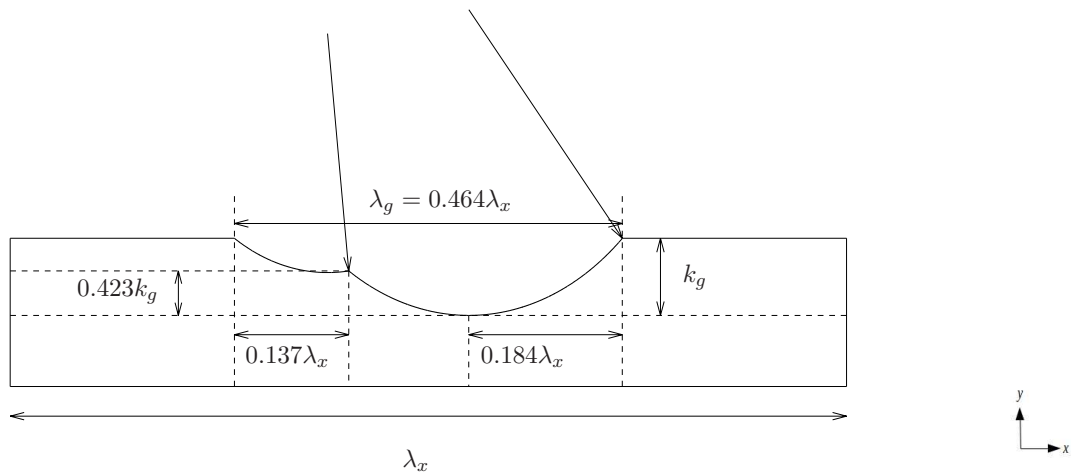
Figure 7.2: *Schematic of the two-dimensional, simplified ripple profile denoted as G3 in Table 7.1.*

Table 7.1: The geometry of each ripple profile applied in the present analysis.

$Ripple configuration$	k_g^*	$radius/\lambda_x$	x_{centre}/λ_x	y_{centre}/λ_x
G1	0.025	1.180	0.379	1.175
		1.482	0.546	1.470
G2	0.050	0.595	0.379	0.585
		0.749	0.546	0.725
G3	0.150	0.216	0.380	0.185
		0.276	0.548	0.207

The reference smooth wall boundary layer is taken from the solution for case M2-T2-L2 in Chapter 7, which is denoted as case M2-SW-TB in the present chapter. Table 7.2 displays the configuration of four simulations of the spatially developing turbulent boundary layer over two-dimensional ripple geometries. Case M2-G1-TB, case M2-G2-TB and case M2-G3-TB compare ripple profiles at three different depths of $k_g^* = 0.025$,

$k_g^* = 0.05$ and $k_g^* = 0.15$ respectively. Each case resolved the near-wall flow using a hexahedral mesh with a spatial resolution equivalent to that in case M2-SW-TB, which was optimised for the reference smooth wall flow. For the deepest ripple geometry, the steepest ripple face meets the crest at an outward angle 230°, which requires an orientation of 49° between the connecting cells at this point. The sudden changes in the geometry, combined with the high-aspect ratio of the cells, produced cells with a high skewness (≈ 0.95) near the ends of the crest. This high skewness could significantly impact the shear stress and pressure force acting at these points. Case M4-G3-TB remodels the deepest ripple geometry of $k_g^* = 0.15$ using a split-hexehedral mesh, in which the spatial resolution in the near-wall region is increased by a factor of 4. Split-hexahedral meshes were utilised extensively in Chapter 6 to resolve highly detailed sand ripple profiles in laminar channel flow, whilst minimising pre-processing time and total cell count. In the present chapter, the solutions for case M2-G3-TB and case M4-G3-TB are compared to assess the viability of this same meshing procedure, to accurately model wall-resolved turbulent boundary layers with textured surface profiles, whilst minimising the pre-processing time and cell count, compared to the optimised smooth wall flow simulations which were produced in Chapter 4.

Table 7.2: Setup for four simulation cases of a spatially developing turbulent boundary layer over periodic ripples, in addition to a reference smooth surface in case M2-SW-TB, as defined in Table 4.3.

Case	k_g^*	Mesh type	L_z/θ_{in}	$N_T \left(\times 10^6 \right)$
M2-SW-TB	0	M2	283	28.3
M2-G1-TB	0.025	M2	286.5	29.0
M2-G2-TB	0.05	M2	286.5	29.0
M2-G3-TB	0.15	M2	286.5	29.0
M4-G3-TB	0.15	M4	286.5	66.4

7.2.2 Mesh Construction

In the present analysis, three distinct types of meshes were constructed for the ripple surfaces. Figure 7.3 and Figure 7.4 display the layout of each mesh over a ripple of depth $k_g^* = 0.15$ (denoted surface G3). Table 7.3 provides the cell types and dimensionless cell spacing in each mesh. The friction velocity for the inner scale is taken as the theoretical value of $u_\tau = 4.25 m/s$, as established in Chapter 4. Mesh M2 contains a spatial resolution which was optimised for the smooth wall boundary layer in Chapter 4. Mesh M4 utilises the snappyHexMesh utility to construct a mesh with similar wall-normal spacing and spanwise spacing as mesh M2, but which increased streamwise resolution in the region of the wall. The purpose of mesh M4 is to examine the impact of streamwise resolution on resolving flow over the sharp angles, without a significant increase in mesh size throughout the bulk of the flow. In the present analysis, mesh M4 is applied to ripple G3.

Table 7.3: Inner-scaled cell dimensions over the ripple surface, based on a theoretical friction velocity of $u_\tau = 4.25 m/s$ as established in Chapter 4.

Mesh	hexahedral	Δx_{min}^+	Δx_{max}^+	Δy_{min}^+	Δz^+
M2	hexahedral	42.2	42.2	0.95	21.2
M4	split-hexahedral	10.6	42.2	0.95	21.2
M5	hexahedral	5.3	42.2	0.95	21.2

The cell dimensions in mesh M2 are equal to those of the optimised smooth surface simulations in case M2-SW-TB. For three cases of $k_g^* = 0.025$, $k_g^* = 0.05$ and $k_g^* = 0.15$, a hexahedral mesh was built over the domain with the graphical user-interface of the SALOME Mecha programme. Along the full streamwise length of the domain, the cells have inner-scaled streamwise and spanwise widths of $\Delta x^+ \approx 42.2$ and $\Delta z^+ \approx 21.2$ respectively. Below $y < 0.6L_y$, the wall-normal height uniformly decreases to produce $\Delta y_{min}^+ = 0.95$ at the wall. Mesh M5 contains identical wall-normal and spanwise cell widths as mesh M2, however, the streamwise cell width is decreased over the region

(a) *Mesh M2*

(b) *Mesh M4*

(c) *Mesh M5*
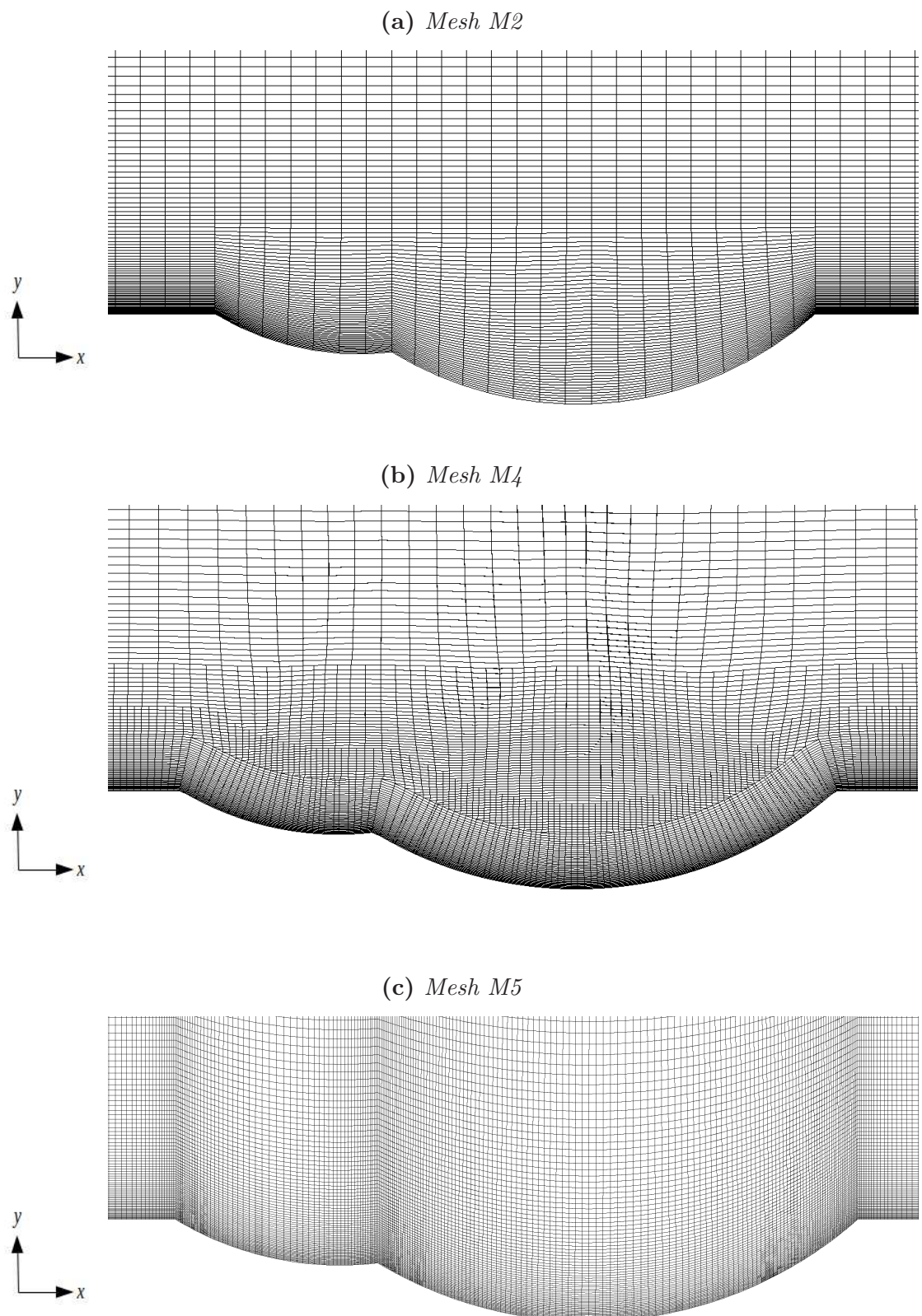
Figure 7.3: *Cell distribution over the ripple profile G3 , (as defined in Table 7.1) for the three different types of mesh which are defined in Table 7.3.*

(a) *Key feature locations*

(b) *Mesh M2 (Point A)*   **(c)** *Mesh M2 (Point B)*

(d) *Mesh M4 (Point A)*   **(e)** *Mesh M4 (Point B)*

(f) *Mesh M5 (Point A)*   **(g)** *Mesh M5 (Point B)*
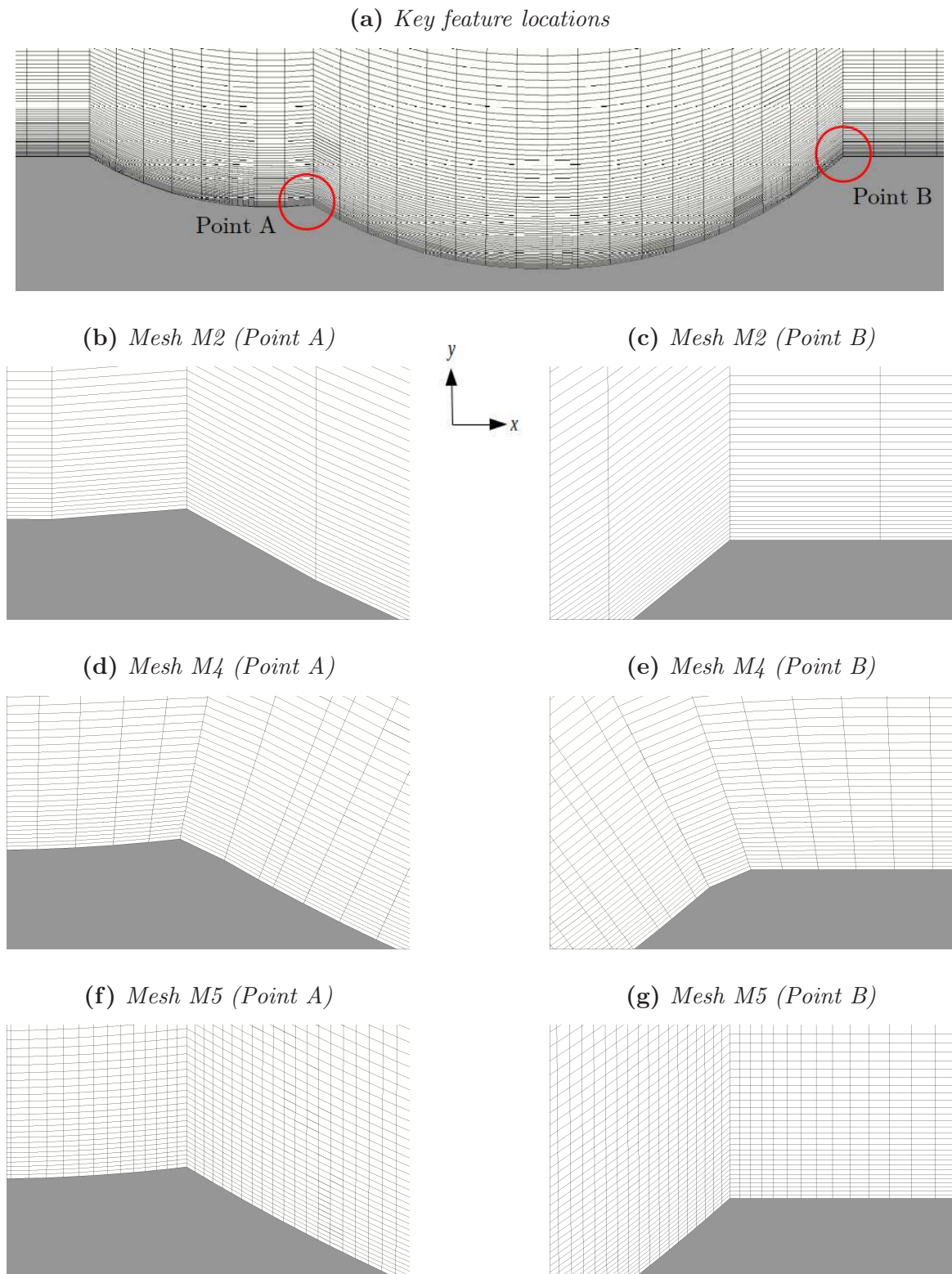
Figure 7.4: *Cell distribution around two key features of the deepest ripple profile, denoted by G3 in Table 7.1, for three different types of mesh, as defined in Table 7.3.*

of the surface containing large angles. Hence, the streamwise cell width varies from $\Delta x^+ \approx 42.2$ at the crest and in the trough, to $\Delta x^+ \approx 5$ at the edges of the ripple segments. All cells in mesh M5 are hexahedral, and hence, the increased streamwise resolution is not limited to the near-wall region as it is in mesh M4. This has the effect of increasing the Courant number at a given time step in the high velocity flow which lies away from the wall. A smaller time-step is required to maintain stability, which further increases the required computational workload, in addition to increasing the total mesh size in the domain. For this reason, the mesh M5 is computed in an simplified simulation comprising of a periodic channel domain, and compared with matching channel simulations for mesh M2 and mesh M4.

The near-wall cells in the optimised smooth wall models contain a uniform aspect ratio of 40 in the x-y plane. For the snapping process of the snappyHexMesh utility, the functionality of the algorithm improves as the aspect ratio of the initial mesh tends towards one. The aspect ratio of the initial orthogonal mesh was reduced by first, increasing the wall-normal width of the cells adjacent to the wall, and improving the streamwise resolution. Local cell refinement allowed for a further reduction in the aspect ratio of the near-wall cells, whilst minimising the increase in the overall mesh density throughout the domain. The configuration of the 'refineMesh' module applied a single division along the x-axis of each cell within a specified area of the domain. All but the final levels of refinement lay between the trough of the surface profile and a parallel x-z plane at a wall-normal point above the crests. The final level conformed to the surface profile, with an offset of 0.2mm along the normal surface vector at each point. With these changes the initial grid contained minimum cell dimensions of $\Delta x^+_{min} \approx 10.6$, $\Delta y^+_{min} \approx 3.8$ and $\Delta z^+ \approx 21.2$ in the near-wall region.

The maximum non-orthogonality showed a minimal dependence on the configura-

tion of the near-wall meshing parameters. All cases could achieve the minimum quality requirement of 65° (Robertson *et al.* 2015) for all points in the domain. Limiting the movement of edges to no more than 10% of their initial length caused a collapse of all constructed layers. In these cases, the algorithm failed to show any sign of convergence within as many as 50 smoothing iterations.

Producing a domain with a maximum skewness of less than 0.7 requires an excess of 100 million cells, bringing the domain size to within 43% of an equivalent DNS solution, with no significant improvement in the resolution of the turbulent length scales. Reducing the local refinement level in the streamwise direction requires a similar reduction in the initial wall-normal resolution to maintain a suitable aspect ratio and minimise skewness. However, the domain requires a larger number of layers which must lie within the 2nd level of local refinement. Similarly, reducing the initial wall-normal width to reduce the number of layers requires those layers to have an additional level of refinement to maintain the same skewness. The final mesh contains a maximum streamwise width of $\Delta x_{max} \approx 42.2$ for all points of above $y/L_y > 0.67$. Two levels of local refinement are applied to the streamwise width within the boundary layer, to produce a streamwise resolution of $\Delta x_{min} \approx 10.6$ over the full surface of the ripple profile. Note that the streamwise resolution varies within the ripple due to cell distortion, but it stays below a maximum limit of approximately $\Delta x_{min} < 0.5 \Delta x_{max}$. The near-wall region has a maximum non-orthogonality of 62.3° and a maximum skewness of 0.89. The average non-orthogonality throughout the domain is 4.37°.

7.3 Numerical Solution and Post-Processing

All numerical solutions were calculated using the transient PISO algorithm. The second-order accurate backward differencing scheme was used for the discretisation of the temporal terms. The total physical time was kept constant for all simulations. For the reference smooth wall boundary layer in case M2-SW-TB this corresponds to 1440 inertial time scales, based on δ_{99}/u_∞ towards the end of the domain. The time interval was kept fixed during the run time; however, in each individual case this user supplied value was reduced as required to keep the maximum Courant number below 1, in order to maintain stability. As in the reference smooth surface simulations, the discretisation of the gradient and divergence terms was performed using second-order accurate central differencing schemes, whilst the Laplacian scheme in Equation (3.18) was used for the discretisation of the Laplacian terms.

In case M4-G3-TB, which contains variable streamwise cell dimensions across the wall-normal direction, the the streamwise profile was averaged over a streamwise length of $\pm 71\theta_{in}$ from the midpoint of the crest. Since the postChannel calculation cannot collapse split-hexahedral cells, each refinement level was collapsed individually, and the resulting profiles were compiled into a complete boundary layer. Note that this process must discard one layer of cells in each refinement layer which lies beyond the near-wall layer.

Along the textured surface the boundary layer properties are determined at the midpoint of ripple crests, $x = 2480\theta_{in} + n\lambda_z$ for $n = 1, 2...24$. For each periodic ripple, a 'ripple averaged' free-stream velocity and free-stream pressure are obtained from a streamwise and spanwise spatial average from the cell-centred values adjacent to the free-stream plane directly above the ripple profile. The averaging procedures

are defined in Equation (7.1) and Equation (7.2).

$$\langle \bar{p}_\infty \rangle_n = \frac{1}{\Delta N_x \Delta N_z} \sum_{n_x=1}^{\Delta N_x} \sum_{n_z=1}^{\Delta N_z} \bar{p}_\infty(x, y, z), \tag{7.1}$$

$$\langle \bar{u}_\infty \rangle_n = \frac{1}{\Delta N_x \Delta N_z} \sum_{n_x=1}^{\Delta N_x} \sum_{n_z=1}^{\Delta N_z} \bar{u}_\infty(x, y, z), \tag{7.2}$$

Where,

$$\Delta N_x = \lambda_x / \Delta x_{max}, \quad \Delta N_z = L_z / \Delta z, \tag{7.3}$$

$$x(n_x) = 2480\theta_{in} + n\lambda_x + n_x \Delta x_{max}, \tag{7.4}$$

$$y = L_y - 0.5\Delta y_{max}, \tag{7.5}$$

$$z(n_z) = n_z \Delta z - 0.5 L_z, \tag{7.6}$$

The results in Chapter 4 identified that the smooth wall boundary layer could be considered to have reached temporal convergence once the flow completed 20 passes of the domain. At this point, the error due to temporal convergence in the coefficient of friction and shape factor was negligible compared with the error from spatial resolution and the variation due to transitional behaviour in the upstream flow. However, the presence of ripples, and varying ripples depth, may impact the rate of temporal convergence throughout the domain. Table 7.4, Figure 7.5, Figure 7.6 and Figure 7.7 show the rate of temporal convergence in relation to ripple depth through comparison of shape factor, and the individual pressure and viscous contributions to the coefficient of friction for case M2-G1-TB, case M2-G2-TB and case M2-G3-TB.

As for the smooth wall simulations, the shape factor over the ripple surfaces show the fastest convergence in time, compared to the pressure component C_p, and viscous component C_v. The largest variation in the shape factor between $t(u_\infty)_{in}/L_x = 18$ and

(a) $x = 0.07m$
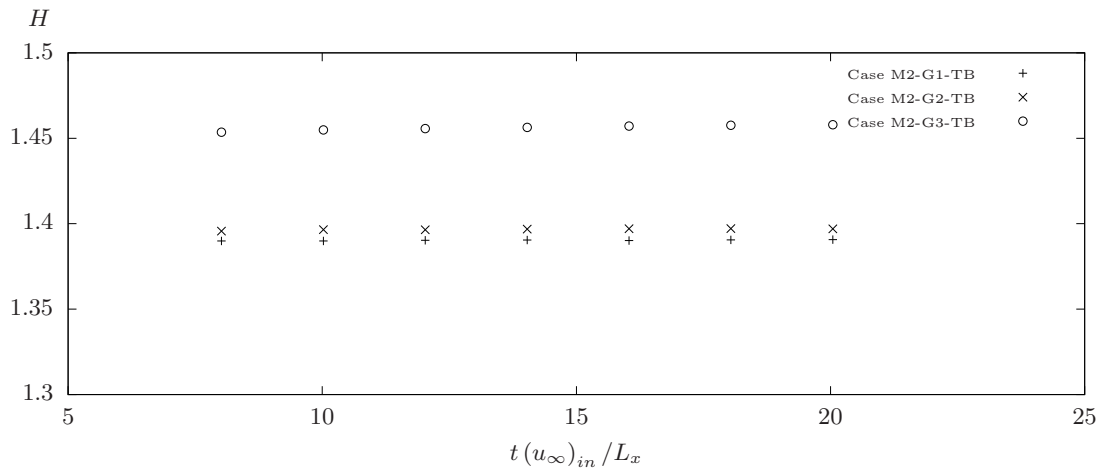
(b) $x = 0.15952m$
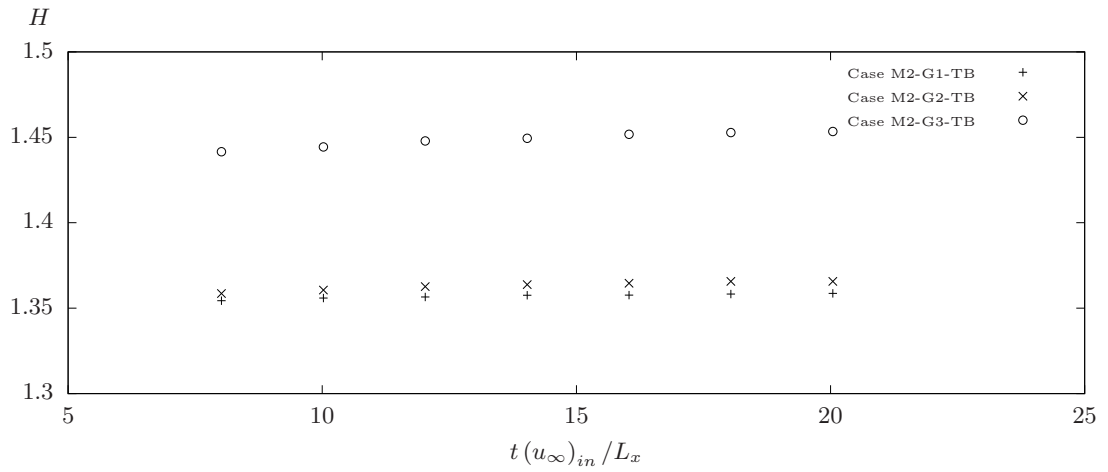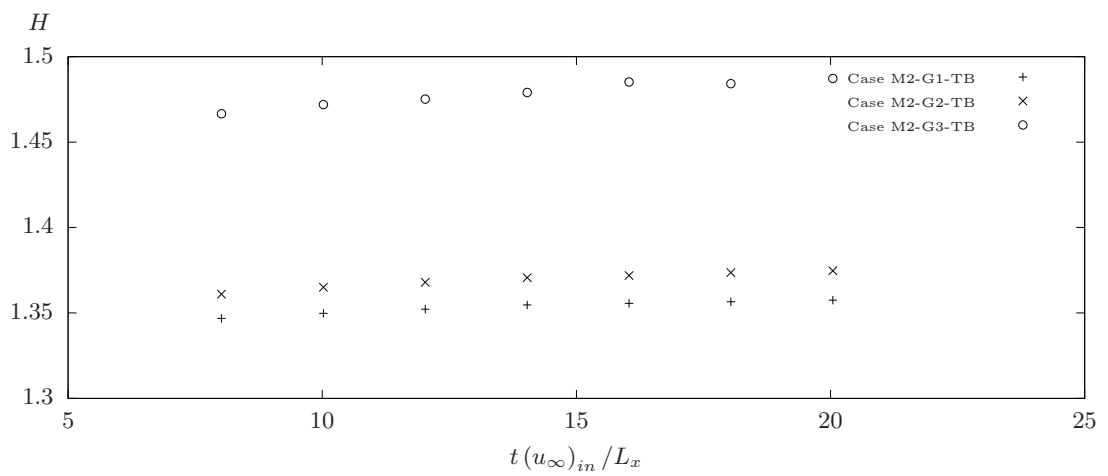
(c) $x = 0.24904m$

Figure 7.5: *Temporal convergence of the shape factor H, for three values of ripple depth with a fixed spatial resolution.*
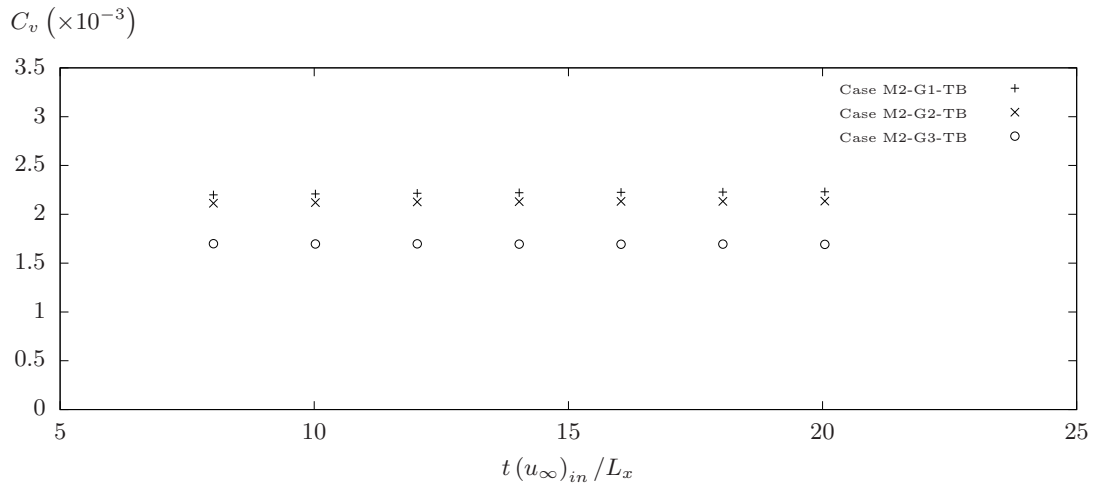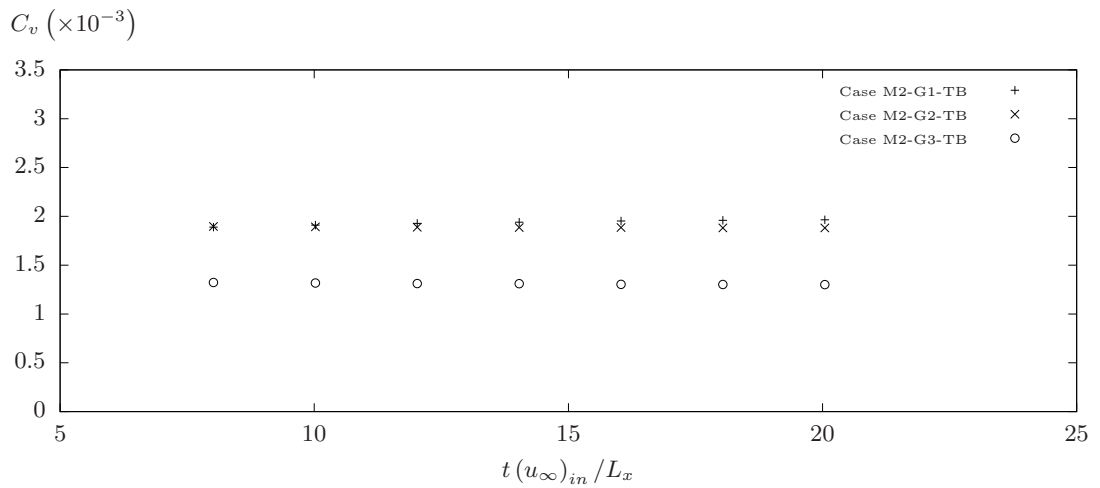
(a) $x = 0.07m$

(b) $x = 0.15952m$
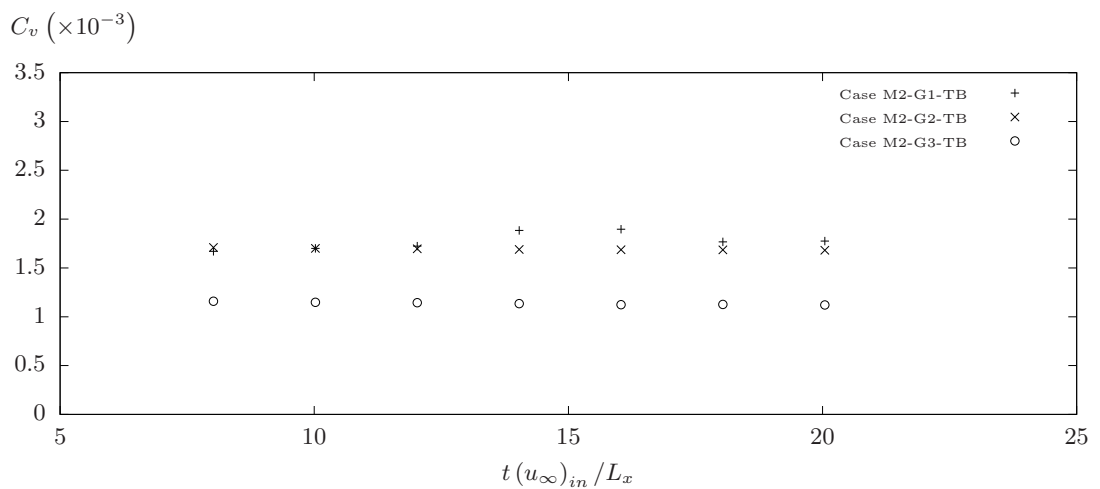
(c) $x = 0.24904m$

Figure 7.6: *Temporal convergence of the viscous component of the coefficient of friction C_v, for three values of ripple depth with a fixed spatial resolution.*

(a) $x = 0.07m$
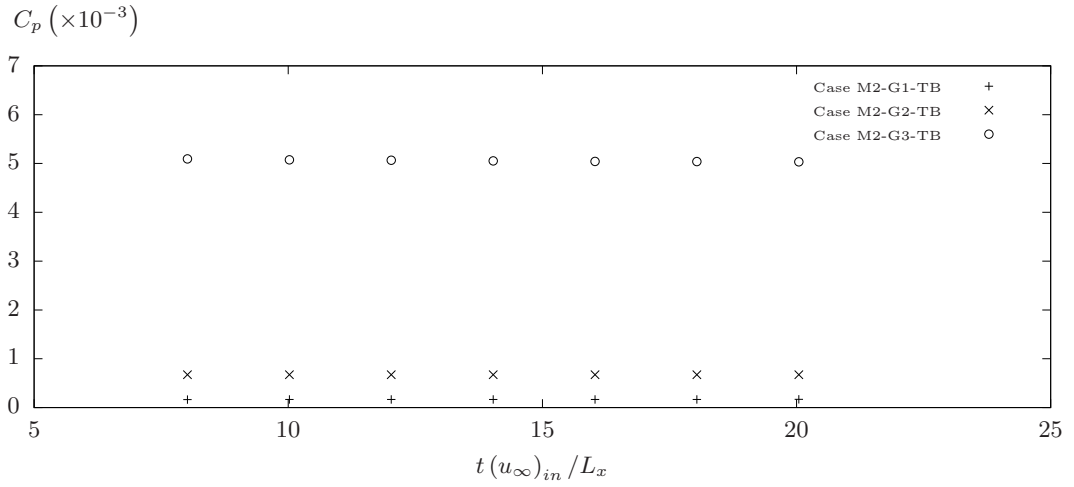
(b) $x = 0.15952m$
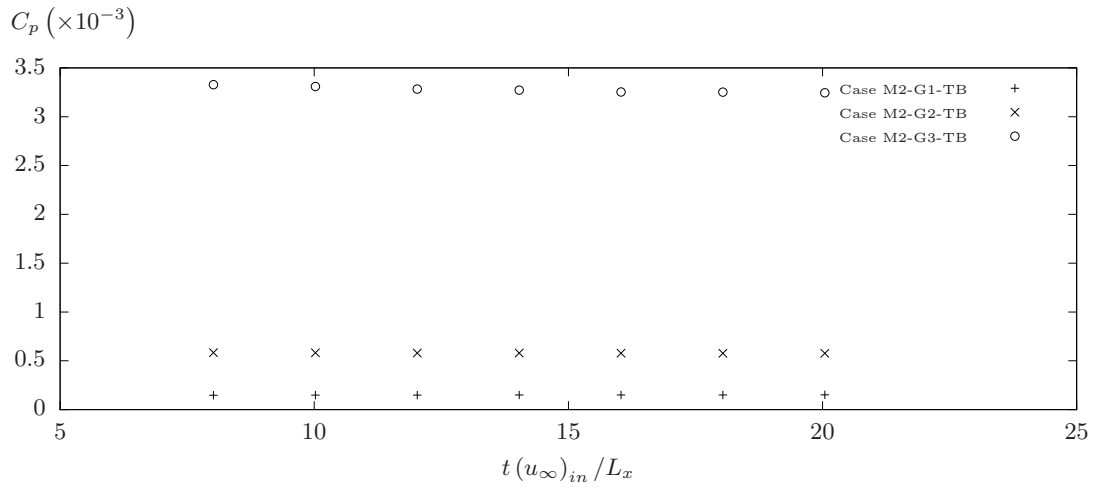
(c) $x = 0.24904m$
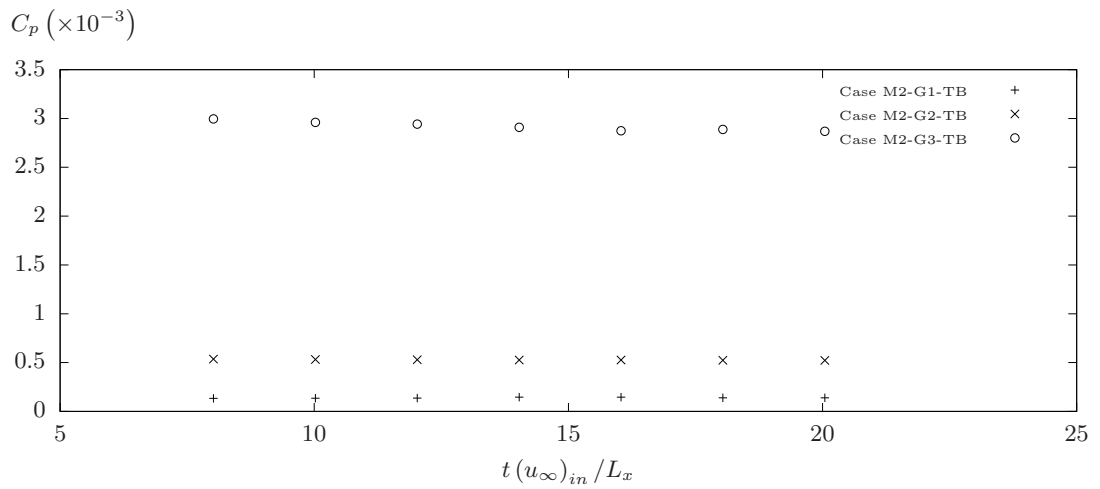
Figure 7.7: *Temporal convergence of the pressure component of the coefficient of friction C_p, for three values of ripple depth with a fixed spatial resolution.*

Table 7.4: Temporal variation of the shape factor and the pressure and viscous components of the coefficient of friction for each ripple wall simulation that is outlined in Table 7.2.

Case	$x\,(m)$	$t\,(u_\infty)_{in}/L_x$	H	$C_p\,(\times10^{-3})$	$C_v\,(\times10^{-3})$
M2-G1-TB	0.07	18	1.391	0.143	1.892
		20	1.391	0.143	1.895
	0.15952	18	1.358	1.28	1.664
		20	1.359	0.128	1.669
	0.24904	18	1.357	0.118	1.501
		20	1.357	0.118	1.508
M2-G2-TB	0.07	18	1.397	0.573	1.812
		20	1.397	0.573	1.814
	0.15952	18	1.366	0.490	1.599
		20	1.366	0.490	1.599
	0.24904	18	1.374	0.445	1.432
		20	1.375	0.444	1.428
M2-G3-TB	0.07	18	1.458	4.282	1.440
		20	1.458	4.277	1.438
	0.15952	18	1.453	2.763	1.106
		20	1.453	2.757	1.105
	0.24904	18	1.484	2.454	0.957
		20	1.487	2.438	0.952
M4-G3-TB	0.07	18.5	2.598	0.981	0.493
		20	2.624	0.902	0.472
	0.15952	18.5	1.460	1.495	0.480
		20	1.461	1.489	0.479
	0.24904	18.5	1.491	2.456	0.803
		20	1.493	2.446	0.801

$t\,(u_\infty)_{in}/L_x = 20$ occurs towards the end of the domain ($x = 0.24904m$) for the deepest ripples (case M2-G3-TB), and does not exceed 0.2%. Compare this error with the effect of increasing the ripple depth from $k_g^* = 0.05$ (case M2-G2-TB) to $k_g^* = 0.15$ (case M2-G3-TB), for which the shape factor at the crest of $x = 0.24904m$ grows by more than 8%. For the pressure component C_p, the rate of temporal convergence falls with increasing ripple depth, however, even the deepest ripples of $k_g^* = 0.15$ showed similar convergence rates to the smooth wall surface. For a ripple of $k_g^* = 0.15$, the maximum variation in C_P between $tu_\infty/L_x = 18$ and tu_∞/L_x was 0.66% at $x = 0.24904m$, compared with a maximum of 0.52% for the coefficient of friction C_f, over a smooth surface at the same location. Finally, the viscous component C_v, did not shown any clear trend between ripple depth and temporal convergence. However, the largest

variation in C_v between $tu_\infty/L_x = 18$ $tu_\infty/L_x = 20$ occurred towards the end of the domain, with a variation of 0.45% at $x = 0.24904m$, which lies close to that seen for the smooth surface simulations. The weakest convergence occurs early on in case M4-G3-TB, where the value of C_p at $x = 0.07m$ varies by more than 8% between $t(u_\infty)_{in}/L_x = 18.5$ and $t(u_\infty)_{in}/L_x = 20$. It will be shown that at $x = 0.07m$ case M4-G3-TB remains in a state of laminar flow, and only enters a turbulent state over the ripple profiles. By $x = 0.15952m$, the boundary layer in case M4-G3-TB has reached a fully turbulent state and the flow demonstrates similar rates of convergence to the other cases, with the largest variation occurring in the value of C_p, which changes by $\approx -0.4\%$ between $t(u_\infty)_{in}/L_x = 18.5$ and $t(u_\infty)_{in}/L_x = 20$.

7.4 Transition and Boundary Layer Growth

In all three cases of $k_g^* = 0.025$, $k_g^* = 0.05$ and $k_g^* = 0.15$, for which $\Delta x^+ \approx 42.2$ prior to the ripple surface, the boundary layer exhibited laminar-turbulent transitional behaviour nearly identical to the reference smooth surface case. Figure 7.8 and Figure 7.9 display the wall-normal distribution of the streamwise velocity and spanwise velocity fluctuations at the first upstream crest of the textured region ($x = 2480\theta_{in}$), whilst the distribution of the streamwise velocity fluctuations, wall-normal velocity fluctuations and Reynolds shear stress are shown in Figure 7.10. When the boundary layer has entered the fully turbulent regime by this point, the downstream presence of the ripple with a depth of $k_g^* \leq 0.15$ exerts a negligible influence on the wall-normal and spanwise velocity fluctuations. When the ripple depth lies below the limit of $k_g^* \leq 0.05$, this negligible influence is extended to the streamwise mean velocity and streamwise velocity fluctuations. However, for a ripple of depth $k_g^* = 0.15$, the flow lying within

the inner region, excluding that within the viscous sub-layer, begins to accelerate as it approaches the ripple. Within this region the maximum streamwise component of turbulent stress and Reynolds turbulent stress are amplified.
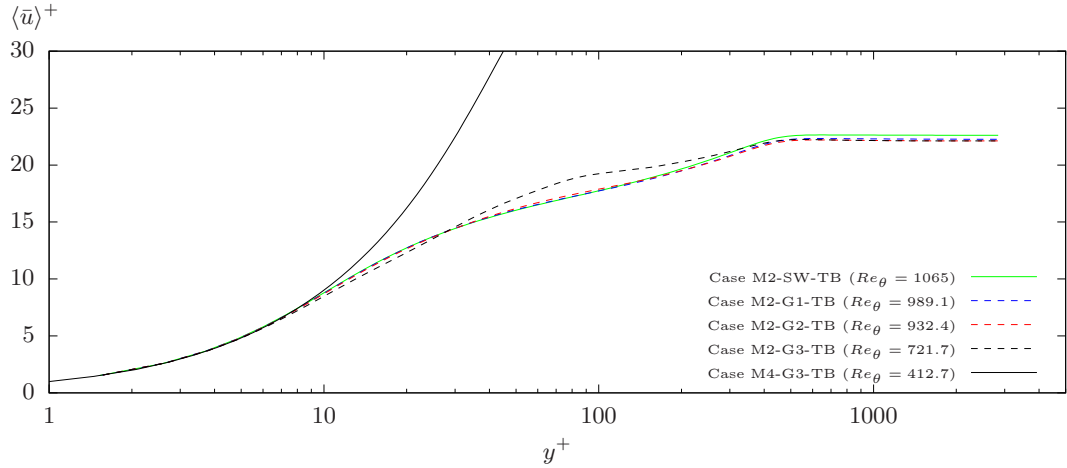
Figure 7.8: *Comparison of the distribution of the inner-scaled, time-averaged streamwise velocity at a streamwise location of $x = 0.07m$ for varying values of ripple depth and spatial resolution.*
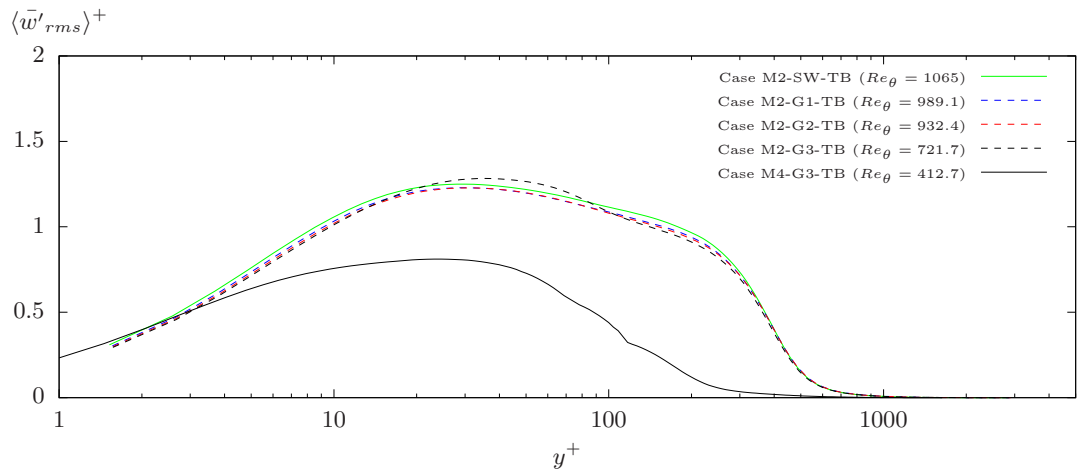
Figure 7.9: *Comparison of the distribution of the spanwise velocity fluctuations at a streamwise location of $x = 0.07m$ for varying values of ripple depth and spatial resolution.*

The split-hexahedral mesh in case M4-G3-TB displayed a diminished response to the trip. The boundary layer remained in a laminar state until it made contact with the first ripple geometry. Figure 7.11 displays the formation of coherent structures downstream of the trip in case M4-G3-TB. The structures are visualised by the second invariant of the velocity gradient tensor Q, for values of $Q > 5 \times 10^5$ $1/s$ (left)

(a) *RMS of streamwise velocity fluctuations*
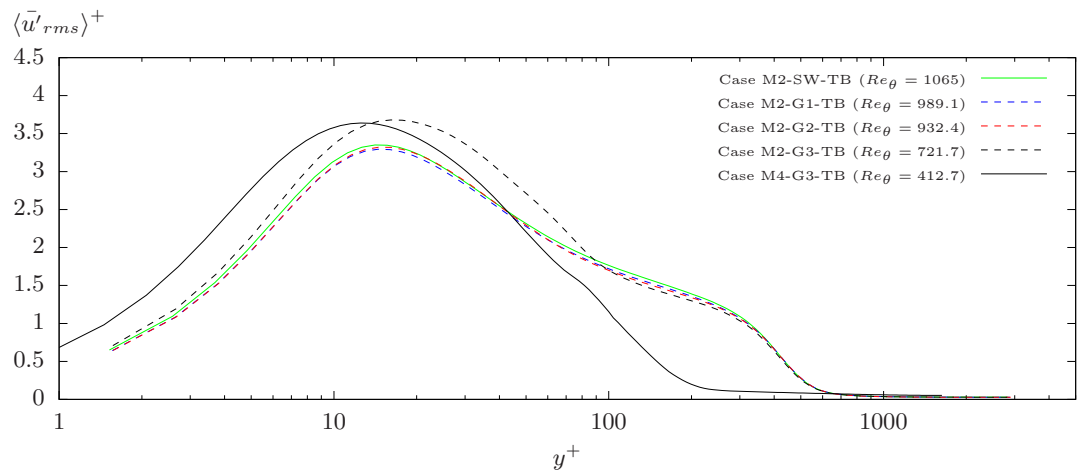
(b) *RMS of wall-normal velocity fluctuations*
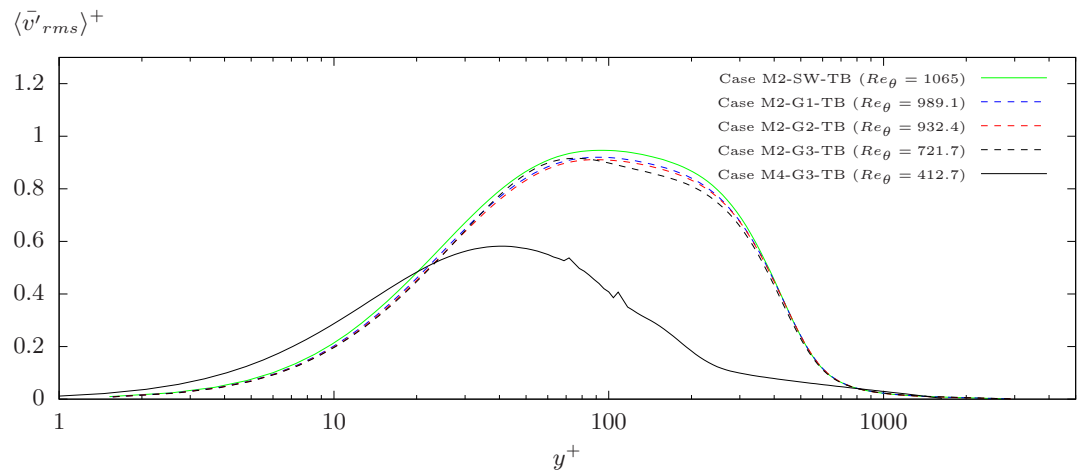
(c) *Reynolds shear stress*
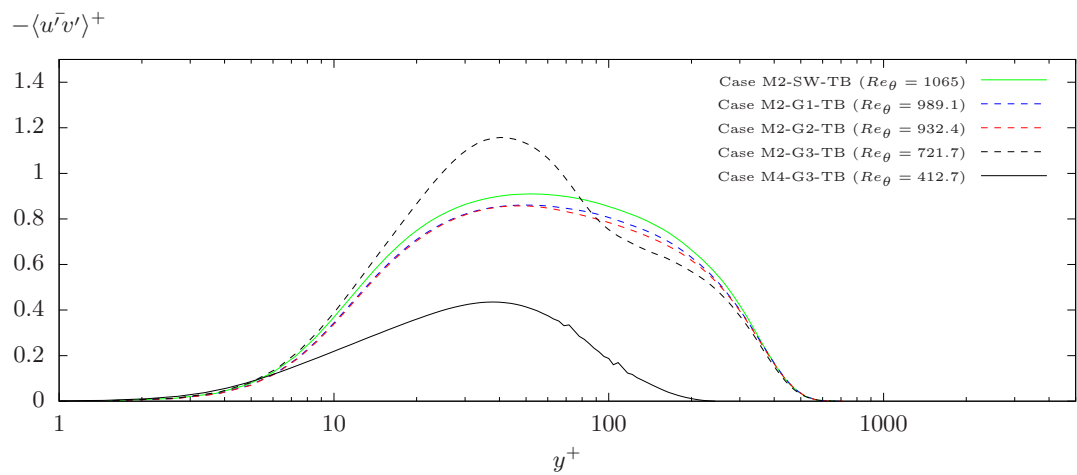
Figure 7.10: *Comparison of the distribution of the turbulent stress components at a streamwise location of $x = 0.07m$ for varying values of ripple depth and spatial resolution.*

and $Q > 5 \times 10^8$ $1/s$ (right). The visualised region covers the full length of the smooth wall and the first four ripples of the textured surface. In case M4-G3-TB, the initial response to the trip mimics that of the coarse streamwise spatial resolution of ≈ 42.2 viscous lengths when coupled with a 50% reduction in the strength of the trip $v^+_{ref} = 1.105 \rightarrow 0.551$, as applied in the reference smooth wall in case M2-T1-L1 (shown in Chapter 4), and observed in Figure 4.8. The trip induces large-scale disturbances which persist downstream, whilst smaller scale disturbances near to the wall dissipate immediately upon leaving the tripping plane. In case M4-G3-TB the boundary layer maintained stability beyond the point of transition in case M2-T1-L1 ($x/\theta_{in} = 1500$).

Along the remainder of the initial smooth wall region, the two-dimensional disturbances became increasingly distorted in the spanwise direction. Although the boundary layer lies within the laminar regime, as indicated by the streamwise velocity distribution in Figure 7.10, the increasing three-dimensionality of the disturbance correlates with the onset of turbulent motions in the near-wall region. Figure 7.10 illustrates the state of turbulent behaviour through the wall-normal distribution of the turbulent stress components at the starting point of the textured region ($x = 2480\theta_{in}$). By this point, streamwise velocity fluctuations, shown in Figure 7.10a, reach an overshoot throughout the region of a corresponding viscous sub-layer, whilst correlating closely with the form of the inner region turbulent profile. Figure 7.10b and Figure 7.9 show a growing strength in the wall-normal and spanwise velocity fluctuations, along with the Reynolds shear stress in Figure 7.10c, which, although weaker than the smooth reference case, already display a tenancy towards the general trend expected for a fully turbulent boundary layer.

By $Re_\theta \approx 2600$ the initially laminar boundary layer in case M4-G3-TB has transitioned into a fully developed turbulent state. Figure 7.12 and Figure 7.13 display the

(a) *Initial smooth wall*
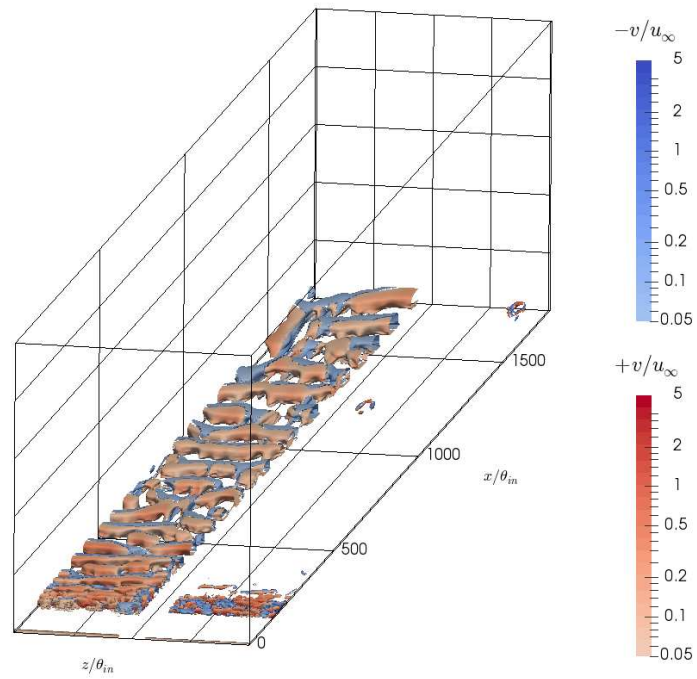
(b) *Transition to the ripple surface*
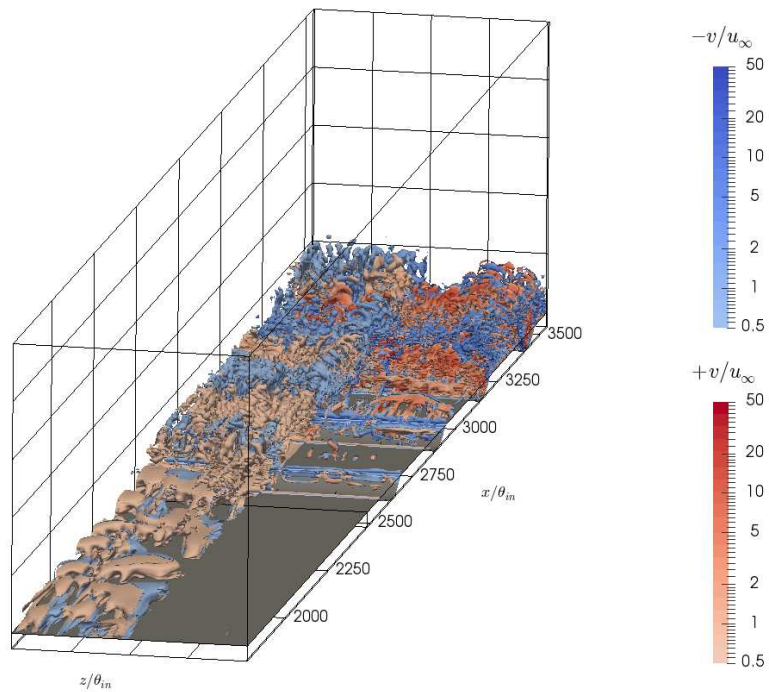
Figure 7.11: *Development of coherent turbulent structures in case M4-G3-TB. Contours are coloured by the instantaneous wall-normal velocity fluctuation as a percentage of the free-stream velocity at the inlet.*

wall-normal distribution of the streamwise velocity and spanwise velocity fluctuations at the first upstream crest of the textured region ($x = 2480\theta_{in}$), whilst the distribution of the streamwise velocity fluctuations, wall-normal velocity fluctuations and Reynolds shear stress are shown in Figure 7.14. The presence of shallow ripples, with depths of $k_g^* = 0.025$ and $k_g^* = 0.05$, has a negligible impact on the structure of the boundary layer in the inner region, in comparison to the reference smooth wall case. Ripples of $k_g^* = 0.05$ only produce mild changes in the outer region, with smaller increases in the the wall-normal and spanwise velocity fluctuations. However, at $Re_\theta \approx 2600$ the deeper ripples ($k_g^* = 0.15$) in case M2-G3-TB and case M4-G3-TB exert a strong influence on the boundary layer structure at the crest. Whilst there is good correlation with the reference smooth wall profile in the viscous sub-layer, the full velocity profile displays a large downward shift throughout the logarithmic region and the outer layer of the boundary layer, which is typically associated with increased drag forces at the wall. Both the wall-normal and spanwise velocity fluctuations show a strong increase through the inner and outer regions, including within the viscous sub-layer. The behaviour of each case becomes more inconsistent for the distribution of the streamwise velocity fluctuations, with the case M4-G3-TB predicting a decrease in the maximum value of $\langle \bar{u}'_{rms} \rangle^+$, and case M2-G3-TB predicting a significant increase in the value of $\langle \bar{u}'_{rms} \rangle^+$ throughout the whole of the viscous sub-layer, and at the point of maximum streamwise velocity fluctuations. Whilst both case M2-G3-TB and case M4-G3-TB predict an increase in the streamwise velocity fluctuations in the outer region, case M2-G3-TB displays a much smoother trend than case M4-G3-TB. The rugged nature of the distribution in case M4-G3-TB may be due to error that comes from the sudden shift in the streamwise spatial resolution between refinement regions. The location and impact of the boundary between refinement regions can clearly be seen in Figure 7.14c, where the refinement regions meet at the point where the Reynolds shear

stress reaches its maximum, and the proximity of the refinement region boundaries produce clear oscillations in the profile of $-\langle \overline{u'v'}\rangle^+$.
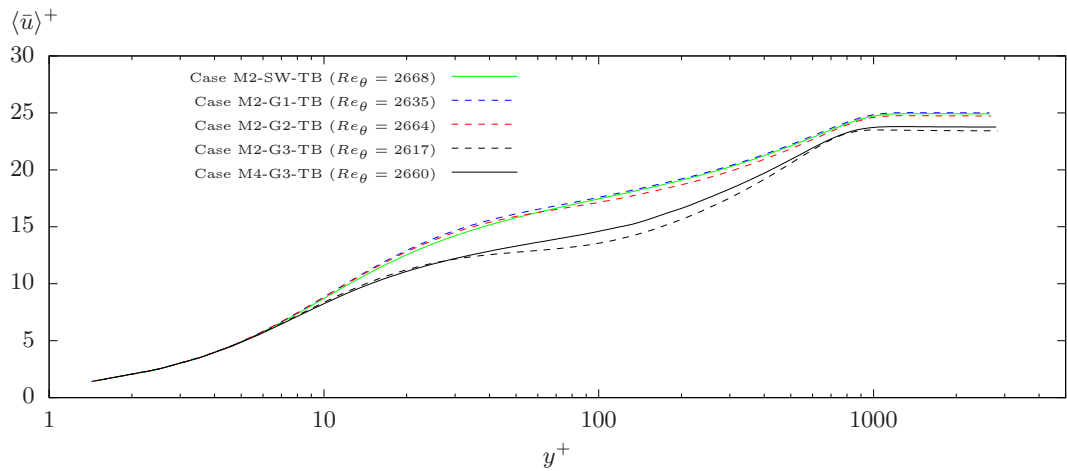

Figure 7.12: *Comparison of the distribution of the inner-scaled, time-averaged streamwise velocity at streamwise locations corresponding to $Re_\theta \approx 2600$ for varying values of ripple depth and spatial resolution.*
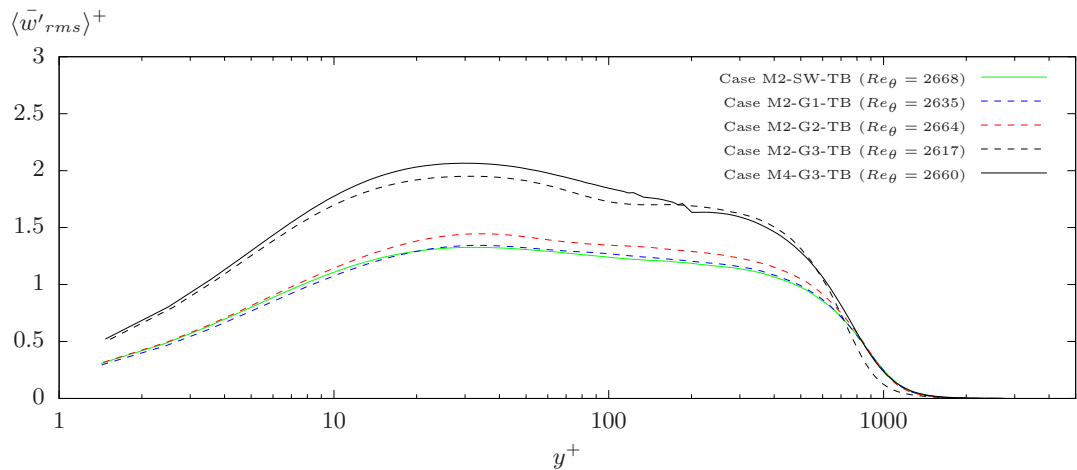
Figure 7.13: *Comparison of the distribution of the spanwise velocity fluctuations at streamwise locations corresponding to $Re_\theta \approx 2600$ for varying values of ripple depth and spatial resolution.*

Figure 7.15 displays the growth of the boundary layer along the streamwise length of the domain in terms of the momentum Reynolds number Re_θ, and the velocity thickness δ_{99}. Figure 7.16 displays the variation of shape factor H, and the Clauser pressure gradient parameter β, along the streamwise length of the domain. Equation (7.7) defines two methods used to approximate the streamwise pressure gradient which was used to determine β. Prior to the textured surface ($x/\theta_{min} \leq 2480$), the free-stream

(a) *RMS of streamwise velocity fluctuations*
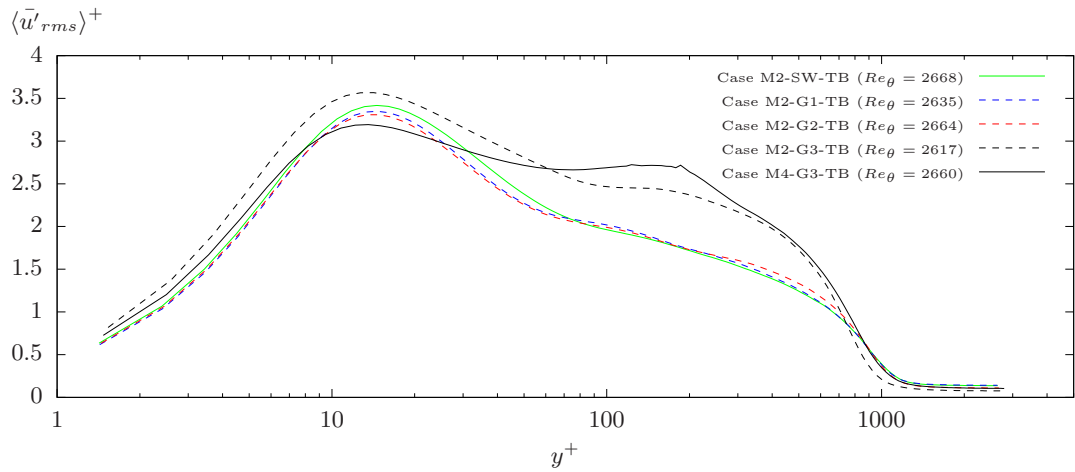
(b) *RMS of wall-normal velocity fluctuations*
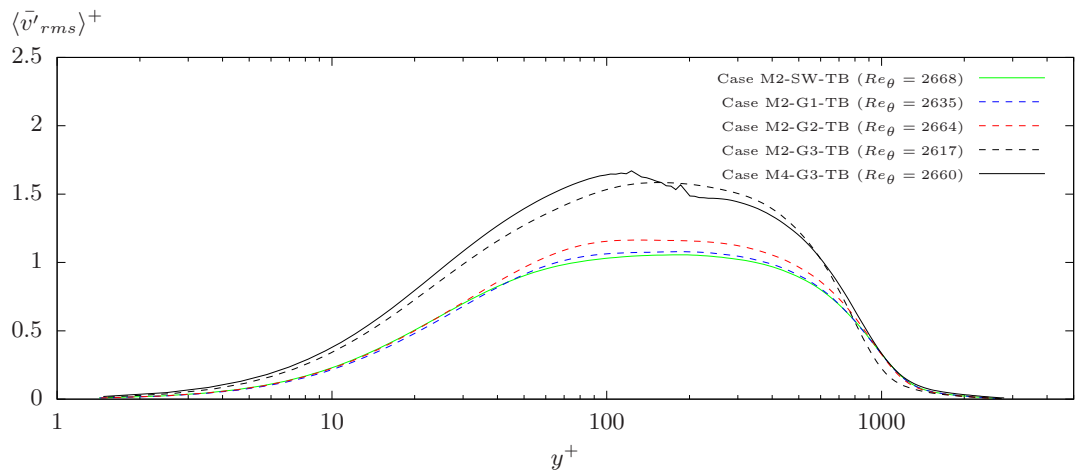
(c) *Reynolds shear stress*
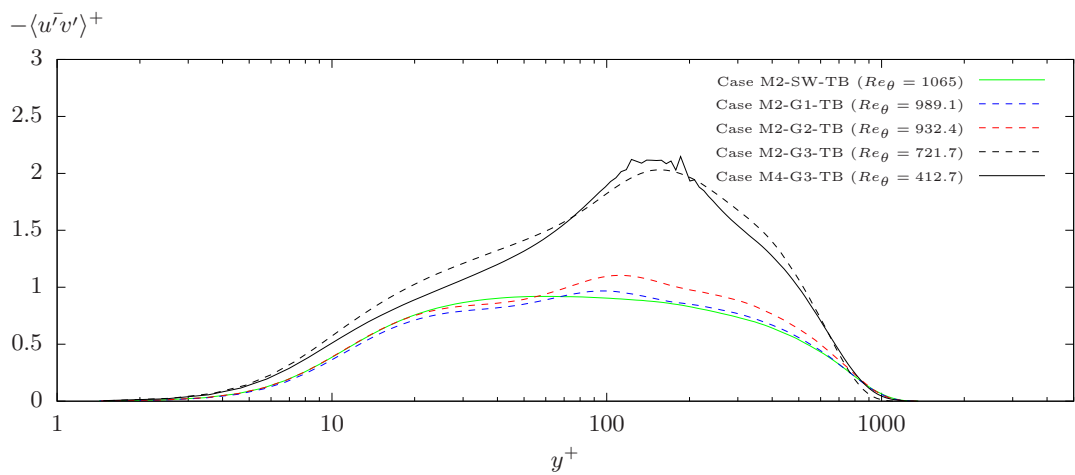
Figure 7.14: *Comparison of the distribution of the turbulent stress components at streamwise locations corresponding to $Re_\theta \approx 2600$ for varying values of ripple depth and spatial resolution.*

pressure gradient is obtained from upstream pressure variation. Along the length of the textured surface ($x/\theta_{in} > 2480$), the values of δ^* are taken directly from the crest profile, whilst the friction velocity and free-stream pressure gradient are determined from the ripple averaged values of the adjacent ripples in the upstream and downstream directions.

$$
\beta = \begin{cases}
\frac{\delta^*}{\bar{\tau}_0} \left(\frac{\langle \bar{p}_\infty (x - 177\theta_{in}) \rangle - \langle \bar{p}_\infty (x) \rangle}{117\theta_{in}} \right), & \text{for} \quad x \le 2480\theta_{min}, \\[2ex]
\frac{\delta^*}{\bar{\tau}_0} \left(\frac{\langle \bar{p}_\infty \rangle_n - \langle \bar{p}_\infty \rangle_{n+1}}{\lambda_x} \right), & \text{for} \quad x > 2480\theta_{min},
\end{cases}
\tag{7.7}
$$

In case M2-G1-TB and case M2-G2-TB, the inflowing laminar boundary layer maintains its strong response to the trip, and during the period of laminar-turbulent transition the growth of Re_θ and H, and the variation of β, strongly correlate to the reference smooth surface in case M2-SW-TB. A similar agreement in Re_θ is observed in case M2-G3-TB within $x/\theta_{in} < 2000$, but the boundary layer growth stalls as it approaches the first upstream crest of the deeper ripples ($k_g^* = 0.15$). Its shape factor profile maintains the expected form for the transitioning boundary layer and only differs by a uniform offset. Once the boundary layer has developed over $7-8$ ripples, the steady variation of H is distorted by periodic variations, characterised by sharp shifts, with a spatial period of 4 ripple wavelengths. Matching variations can be observed in both the local displacement and momentum thickness, and hence, in the pressure gradient parameter which depends on δ^*. Meanwhile, both the streamwise pressure gradient and ripple averaged friction velocity maintain a steady, smooth variation along the streamwise direction.

For ripples of $k_g^* = 0.15$ the growth rate of the boundary layer width, as defined by the velocity thickness δ_{99}, accelerates once the boundary layer has adapted to the

(a) *Momentum Reynolds number*
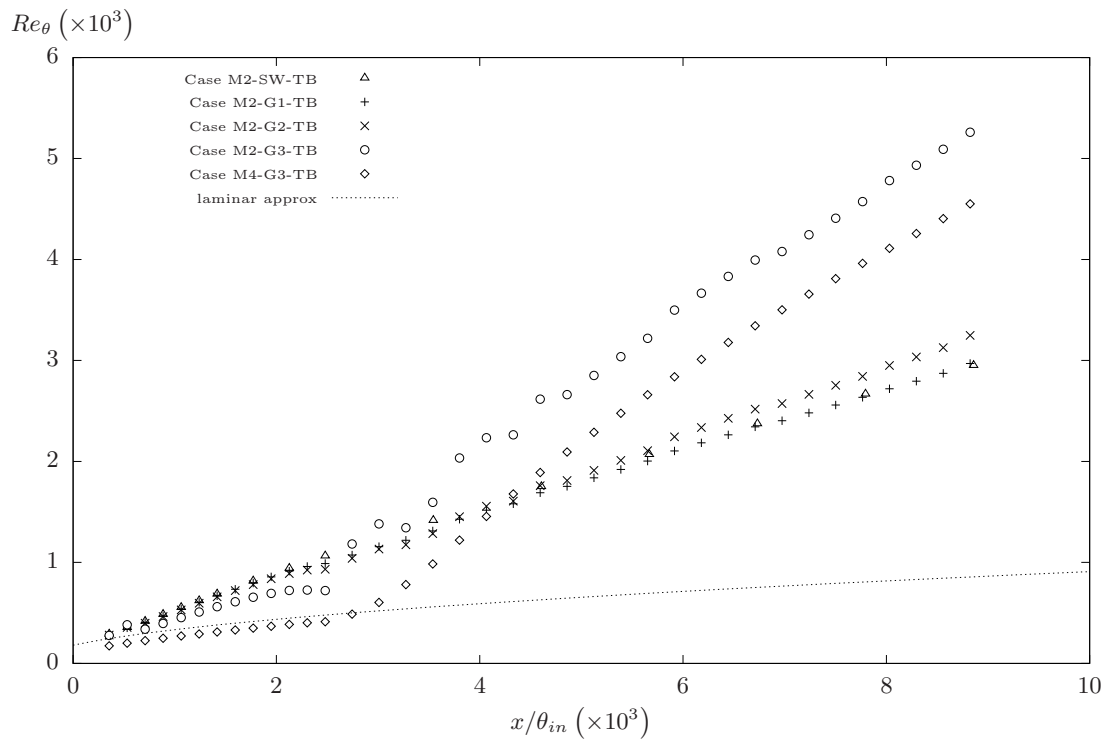
(b) *Velocity thickness*
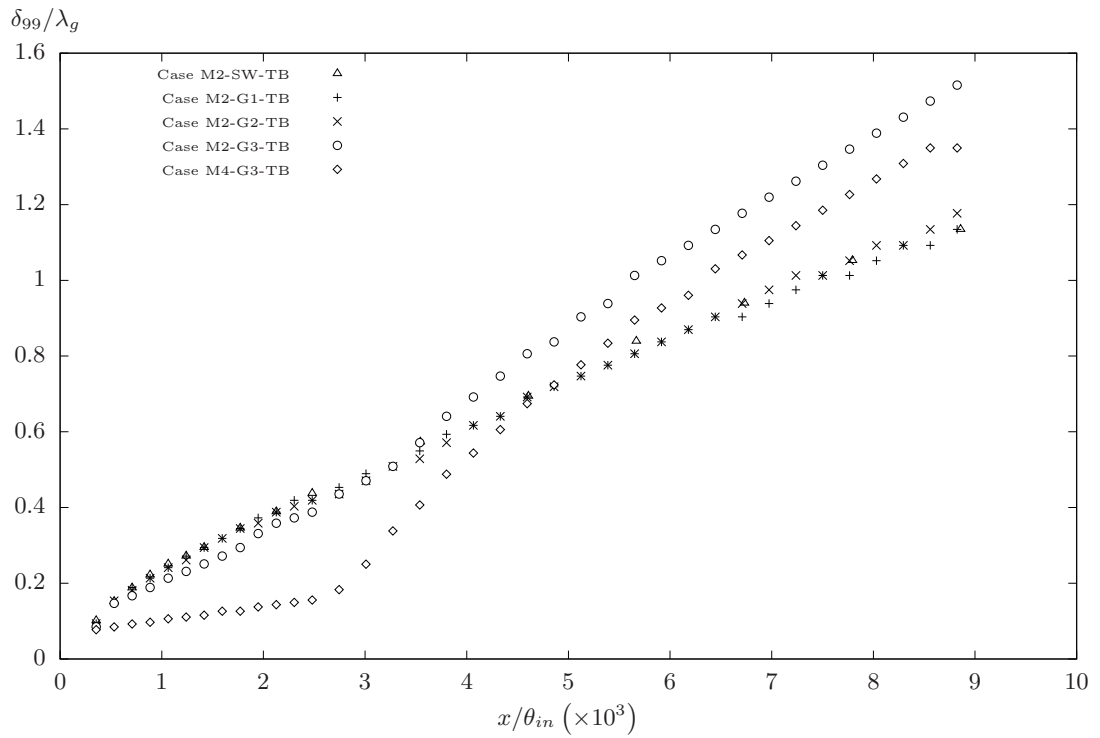
Figure 7.15: *Comparison of the growth of the momentum Reynolds number Re_θ, and velocity thickness δ_{99}, in a spatially developing turbulent boundary layer for varying values of ripple depth and spatial resolution.*

(a) *Shape factor*
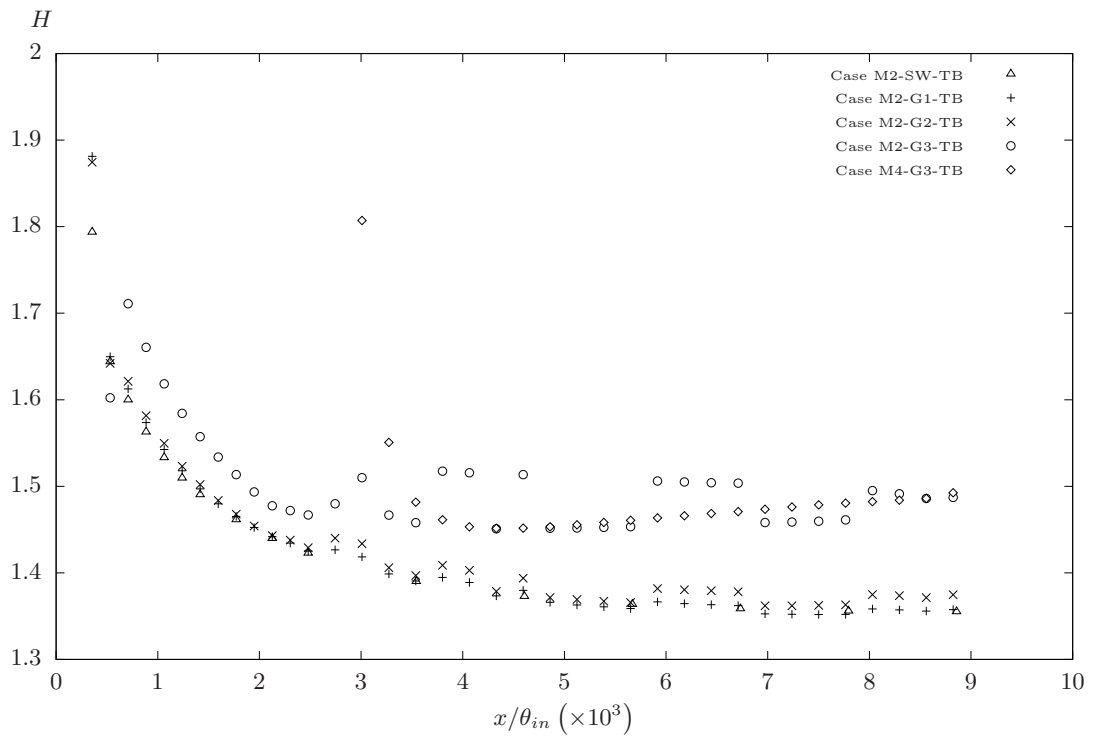
(b) *Pressure gradient parameter*
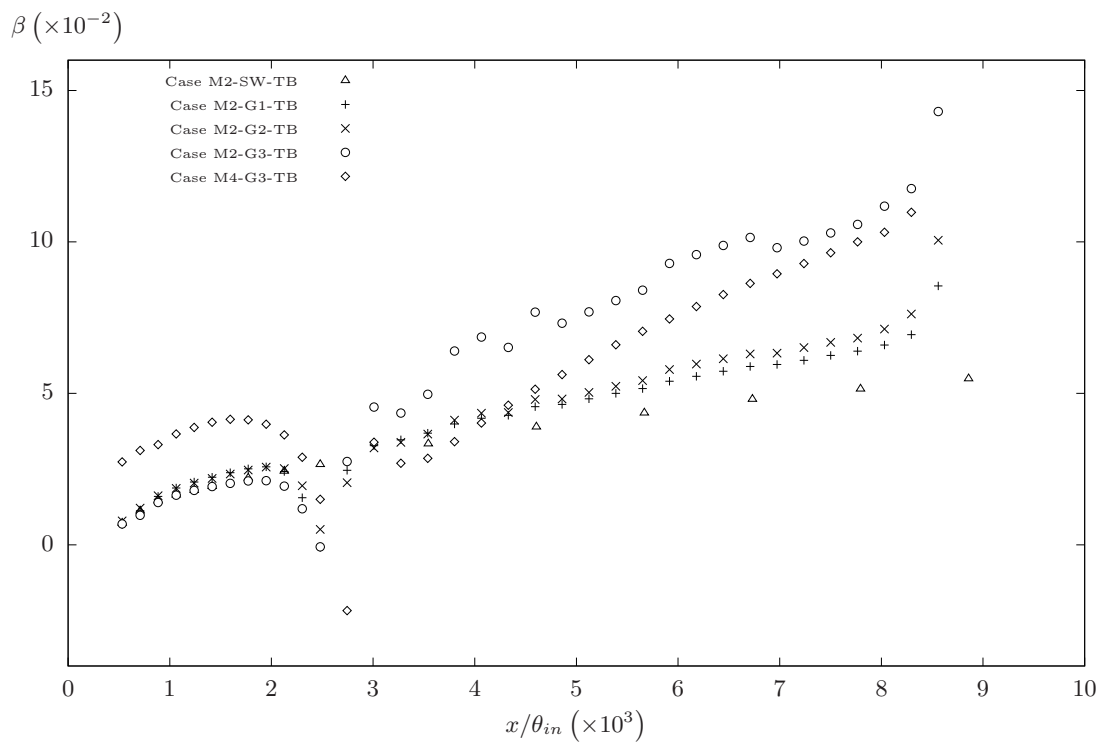
Figure 7.16: *Comparison of the growth of the shape factor H, and pressure gradient parameter β, in a spatially developing turbulent boundary layer for varying values of ripple depth and spatial resolution.*

presence of the textured surface and has achieved its new equilibrium. Since the growth rate of Re_θ accelerates at the same rate, the relationship between Re_θ and δ_{99}, which was observed for smooth wall boundary layer, is maintained at the higher values of Re_θ present in case M2-G3-TB. However, it should be noted that these values of δ_{99} take the origin at the ripple crest, and do not compensate for the origin shift throughout the ripple trough.

7.5 Flow Resistance

Figure 7.17 displays the variation of each individual component of flow resistance with the growth of Re_θ along the streamwise length of the domain. The coefficient of friction C_f, its individual viscous component C_v, and its individual pressure component C_p, are determined for each individual ripple ($n = 1, 2...24$) spanning a wavelength of λ_x. These ripple averaged values; $C_v \approx \langle \bar{C}_v \rangle_n$, $\langle \bar{C}_p \rangle_n$, and $\langle \bar{C}_f \rangle_n$, are defined in Equation (7.8) and Equation (7.9). Each component is determined from the spatially averaged drag forces, $\langle \bar{F}_v \rangle_n$ and $\langle \bar{F}_p \rangle_n$, produced post-run time from the time-averaged flow fields $\bar{u}$ and $\bar{p}$. The surface area and the reference velocity are taken as the reference smooth wall area $\lambda_x \times L_z$, and the ripple averaged free-stream velocity $\langle \bar{u}_\infty \rangle_n$ defined by Equation (7.2). In addition, Figure 7.18 provides the relationship between the momentum Reynolds number Re_θ and the ratio between the outer and inner length scales δ_{99}/l_v, (also referred to as the friction Reynolds number $Re_\tau = \delta_{99} u_\tau / \nu$).

$$\langle \bar{C}_v \rangle_n = \frac{\langle \bar{F}_v \rangle_n}{0.5 \rho \lambda_x L_z \langle \bar{u}_\infty \rangle_n}, \quad \langle \bar{C}_p \rangle_n = \frac{\langle \bar{F}_p \rangle_n}{0.5 \rho \lambda_x L_z \langle \bar{u}_\infty \rangle_n}, \tag{7.8}$$

$$\langle \bar{C}_f \rangle_n = \langle \bar{C}_v \rangle_n + \langle \bar{C}_p \rangle_n, \tag{7.9}$$

(a) *Coefficient of friction*
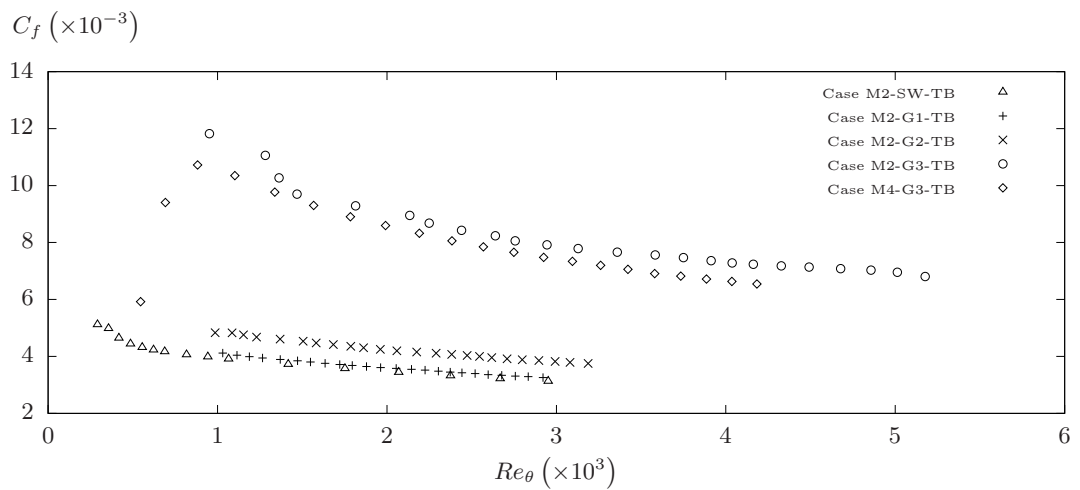
(b) *Viscous component of the coefficient of friction*
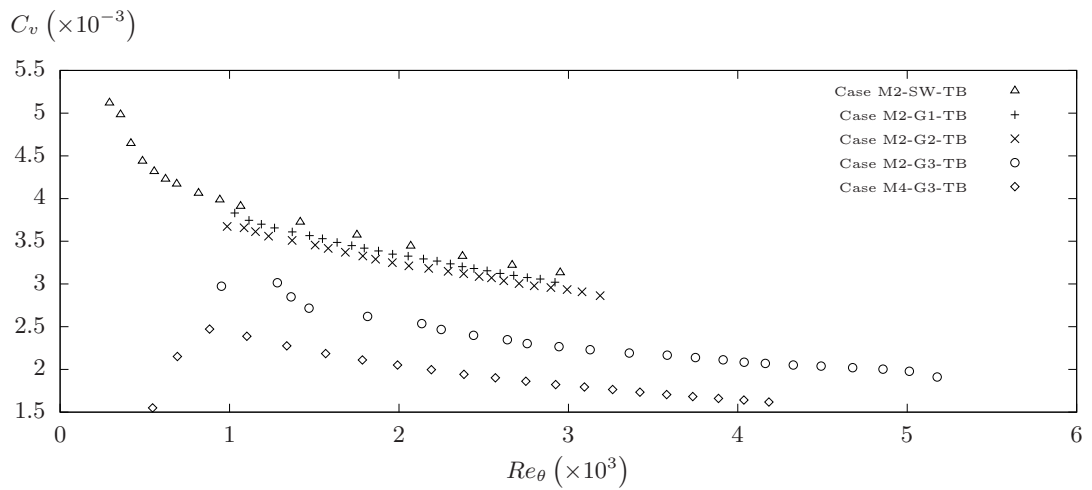
(c) *Pressure component of the coefficient of friction*
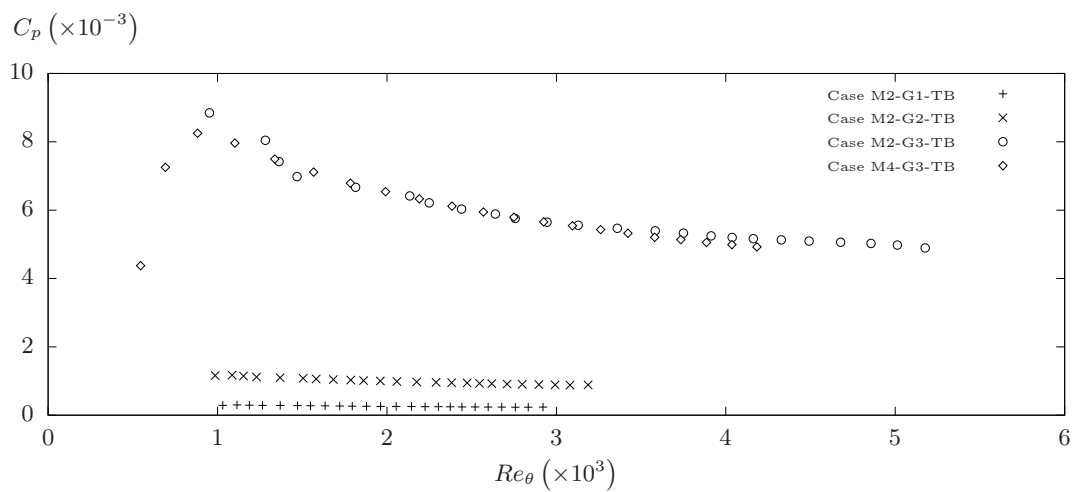
Figure 7.17: *Comparison of the growth of the ripple averaged coefficient of friction, and its individual pressure and viscous components, with momentum Reynolds number Re_θ, for varying values of ripple depth and spatial resolution.*
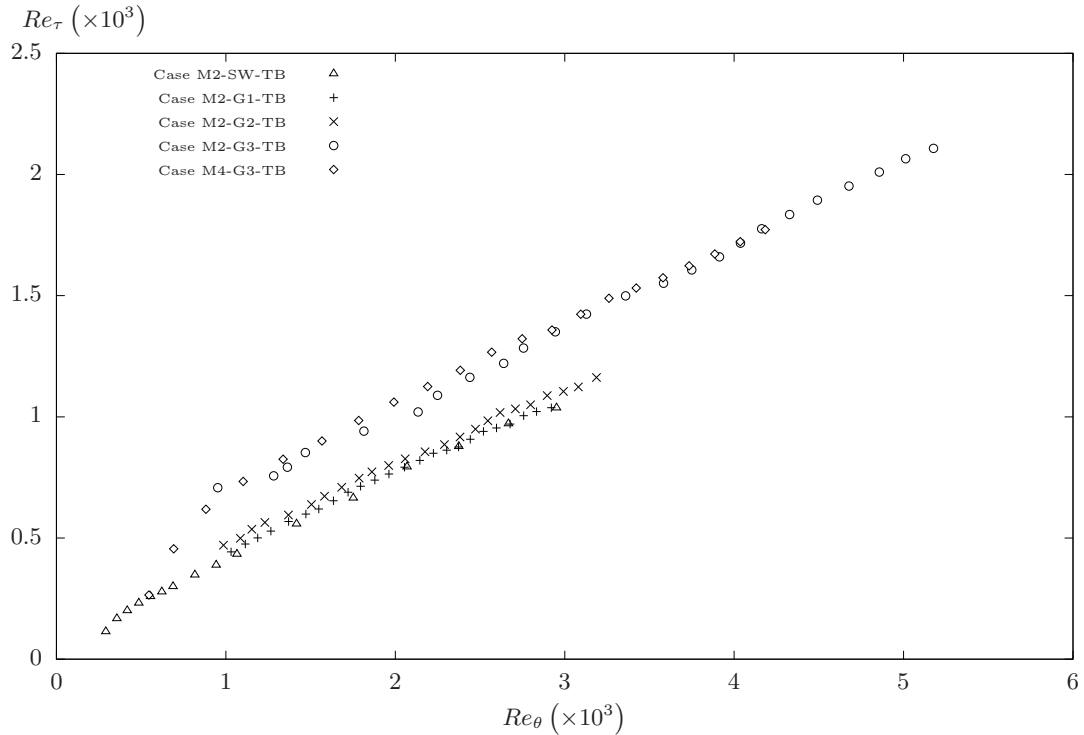
Figure 7.18: *Comparison of the growth of friction Reynolds number Re_τ, with momentum Reynolds number Re_θ, for varying values of ripple depth and spatial resolution.*

The solutions for $k_g^* = 0.15$ (case M2-G3-TB and case M4-G3-TB) predict a reduction in the viscous drag over all ripples which lie beyond the transitional regime. Moreover, each solution shows a consistent trend in the gradual decline of C_v with growing Re_θ. However, there is a considerable variation between the values of C_v, with case M4-G3-TB producing a further reduction of approximately -0.5 in C_v at equivalent values of Re_θ, compared to the lower spatial resolution in case M2-G3-TB. This behaviour could be attributed to either the large reduction in the streamwise spatial resolution, or a lingering effect of the upstream transitional regime. Analysis of the shear stress distribution in Section 7.6 shows that the finer spatial resolution in case M4-G3-TB enhances the strength of flow separation from the lee-side, and suppresses local shear stress spikes within the trough, all of which suggests a beneficial effect on the overall viscous drag reduction. Meanwhile, the near-wall spatial resolution shows a greatly diminished sensitivity on the ripple averaged pressure drag, relative to the absolute value of C_p. Since the pressure drag eclipses the viscous drag for a ripple of

depth of $k_g^* = 0.15$, the relative error in C_v is suppressed in influencing the relative error in the total flow resistance.

Overall, the relative contribution of the pressure drag grows with ripple depth. At $k_g^* - 0.15$ the pressure drag accountes for up to $\approx 71.5\%$ of the total drag over each individual ripple. This relative contribution is constant along the full streamwise length of the textured region, settling within the range of 71.3% and 71.6%. Case M4-G3-TB predicts that the relative pressure contribution gradually declines along the domain, from 76.5% after a distance of $5\lambda_x$, to 75.7% after a distance of $22\lambda_x$. For shallower ripples of $k_g^* = 0.025$ and $k_g^* = 0.05$, the relative pressure contribution is $\approx 7.1\%$ and $\approx 23.4\%$ respectively, and, similar to case M2-G3-TB, displays a negligible variation along the full streamwise length of the textured region.

Throughout all cases, the thickness of the fully turbulent boundary layer varies between 40% and 150% of the ripple spacing λ_g. Within this range, the streamwise length of the ripple in relation to the boundary layer thickness (i.e. the outer length scale) has a negligible impact on the pressure contribution ratio. Similarly, in an individual domain, where the ripple length is fixed whilst δ_{99}/k_g grew along the domain, the growth of δ_{99} in relation to k_g also displays a negligible influence on the relative pressure contribution. Whilst increasing the near-wall streamwise spatial resolution for the deepest ripple geometry (case M2-G3-TB) indicates a linear interaction between the relative pressure contribution and boundary layer growth; this interaction is negligible compared to the effect of increasing the ripple depth k_g^*, in relation to the ripple wavelength. On the other hand, increasing the ripple depth increases the size of the outer length scale in relation to the inner length scales, and this increase is consistent in the region spanning $Re_\theta \approx 1000$ and $Re_\theta \approx 3300$. For $Re_\theta > 1000$, the relations between Re_θ and Re_θ collapse onto a single linear relationship with good agreement

between the two mesh configurations. This suggests that the near-wall mesh configuration has not had a significant influence on the ratio between the largest and smallest length scales. In each case, the coefficient of friction continues to fall with Re_θ, with no significant interaction between the boundary layer thickness (in relation to ripple depth or ripple wavelength) and the flow resistance.

When the initially laminar boundary layer in case M4-G3-TB reaches the textured surface, it enters the transitional regime, characterised by the rapid accent in the coefficient of friction and its individual pressure and viscous components. Once the boundary layer has reached the 5th ripple geometry it has grown to $Re_\theta = 1000$ which typically lies just beyond the limit of the transitional regime. At this point, Figure 7.17 indicates that the streamwise growth of C_f, C_p and C_v closely conforms to case M2-G3-TB, where a fully turbulent regime exists prior to the ripples. Between $Re_\theta \approx 1000$ and $Re_\theta \approx 2000$ the coefficient of friction in case M4-G3-TB follows the expected smooth log-law relation, whilst case M4-G3-TB displays considerable scatter around a similar trend. This distance correlates to approximately $5\lambda_x \sim 6\lambda_x$, similar to the length of the transition regime in case M4-G3-TB. This suggests that, under current conditions, the deepest depth of $k_g^* = 0.15$ requires a length of at least $5\lambda_x$ to transition from a smooth wall boundary layer to the corresponding rough wall boundary layer. Furthermore, this transition can take place within either the fully turbulent regime or the transitional regime. Finally, the general structure of the boundary layer, at a given streamwise location of Re_θ downstream of the smooth-rough transition region, is independent of the state of the boundary layer during the smooth-rough transition. In the present analysis, it cannot be conclusively determined whether local discrepancies in the growth of the viscous flow resistance between case M2-G3-TB and case M4-G3-TB can be attributed to smooth-rough transition state or the near-wall spatial

resolution, cell quality and type.

7.6 Turbulent Stress Distribution

The current section focuses on the boundary layer structures and wall shear stress distribution within a fully turbulent boundary layer in the region of $Re_\theta \approx 2600$. At this point, the boundary layer may be assumed to have completed the smooth-rough wall transition based on the streamwise growth of flow resistance in Figure 7.17. The point of interest in each case is taken as the midpoint of the ripple crest at which the boundary layer development lies closest to $Re_\theta = 2600$. Table 7.5 provides the streamwise location, momentum Reynolds numbers and boundary layer thickness which correspond to the point of interest in each case. The wall-normal distributions of velocity and turbulent stress components are assessed locally at each point in Table 7.5, and are displayed in Figure 7.19.

Table 7.5: Properties of the boundary layer at a point corresponding to $Re_\theta \approx 2600$ in each case.

Case	x/θ_{in}	Re_θ	δ/λ_g
M2-SW-TB	7795	2668.3	1.053
M2-G1-TB	7766	2635.3	1.013
M2-G2-TB	7238	2663.9	1.013
M2-G3-TB	4595	2616.8	0.806
M4-G3-TB	5652	2660.4	0.895

The distribution of shear stress along the groove profile is assessed from the ripple which lies immediately upstream of the point of interest. Figure 7.19 displays the local distribution of shear stress, along a plane $z = 0m$, which is normalised using the local free-stream velocity $\langle \bar{u}_\infty \rangle$. Figure 7.20, Figure 7.21 and Figure 7.22 display the two-dimensional flow field in terms of the inner-scaled streamwise, wall-normal and spanwise turbulent stress components, in the near-wall region of the same ripple

profiles displayed in Figure 7.14. The inner length scale u_τ, for each flow field is taken from the local value at midpoint of the crest immediately downstream of the ripple (Table 7.5).

Firstly, consider the preservation of the viscous sub-layer as it moves into the ripple. For shallow ripples of $k_g^* = 0.025$ and $k_g^* = 0.05$, the viscous sub-layer remains in contact with the surface over the full length of the trough. As the boundary layer passes over the point connecting the crest to the lee-side, the sharp change in the surface tangent causes a sudden acceleration in the near-wall flow. This is characterised by a modest spike in the shear stress which grows with increasing ripple depth. A similar acceleration and shear stress spike occurs at the transition between the two segments of the lee-side. Upon leaving the crest, the viscous sub-layer expands along the first segment of the lee-side, which lowers the velocity gradient adjacent to the wall and produces a sharp drop in the wall shear stress. As it approaches the crest, it compresses to retain its previous width, bringing the shear stress to a similar magnitude as that observed at the crest. Immediately downstream of both points, the shear stress falls to a local minimum. When the viscous sub-layer maintains contact with the surface, as in case M2-G1-TB and case M2-G2-TB, the minimum shear stress occurs at two points along the lee-side, for which the local shear stress lies at approximately equal values, with each point lying immediately downstream of an instantaneous shift in the surface tangent. In case M2-G3-TB, the point of minimum shear stress correlates with two isolated vortices with the backwash creating a shear stress which acts in the direction of the flow.

The streamwise velocity fluctuations $\langle \bar{u}'_{rms} \rangle^+$, which reaches a maximum close to the wall at $y^+ \approx 15$, is enhanced as the viscous sub-layer moves along the lee-side. For $k_g^* \geq 0.05$, the region of high $\langle \bar{u}'_{rms} \rangle^+$ expands and the strength of the streamwise velocity fluctuations grow, as the viscous sub-layer moves into the ripple. By the time

(a) *Case M2-G1-TB (Re$_\theta$ ≈ 2600)*

(b) *Case M2-G2-TB (Re$_\theta$ ≈ 2600)*

(c) *Case M2-G3-TB (Re$_\theta$ ≈ 2600)*

(d) *Case M4-G3-TB (Re$_\theta$ ≈ 2600)*
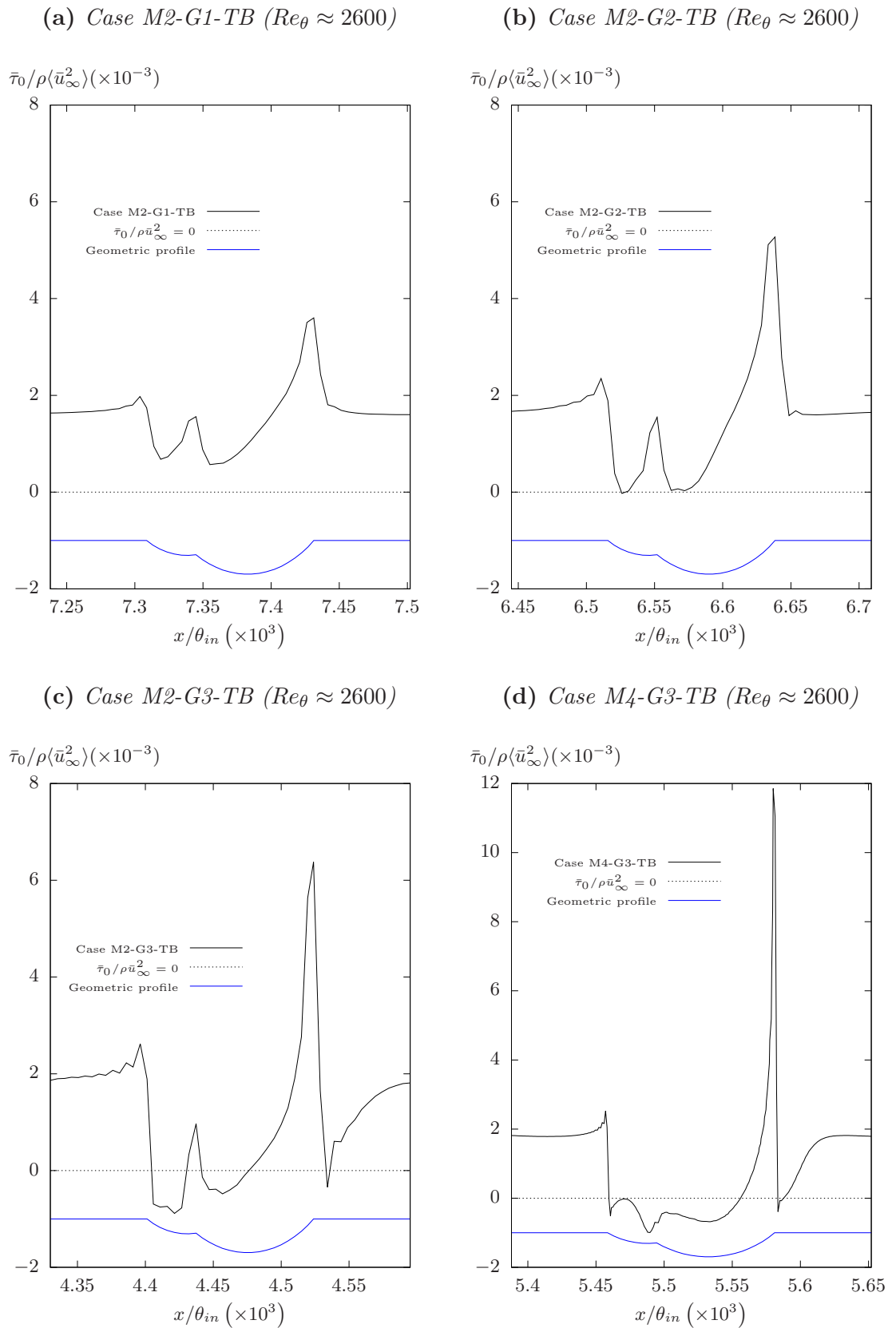
Figure 7.19: *Distribution of the local streamwise wall shear stress over the midline of two-dimensional ripple profiles at streamwise locations corresponding to Re$_\theta$ ≈ 2600 for varying values of ripple depth and spatial resolution.*

(a) $\bar{u'}^+_{rms}$ *(M2-G1-TB, n = 20)*

(b) $\bar{u'}^+_{rms}$ *(M2-G2-TB, n = 18)*
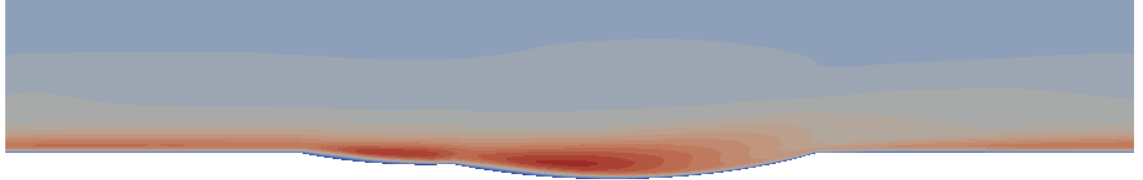
(c) $\bar{u'}^+_{rms}$ *(M2-G3-TB, n = 8)*
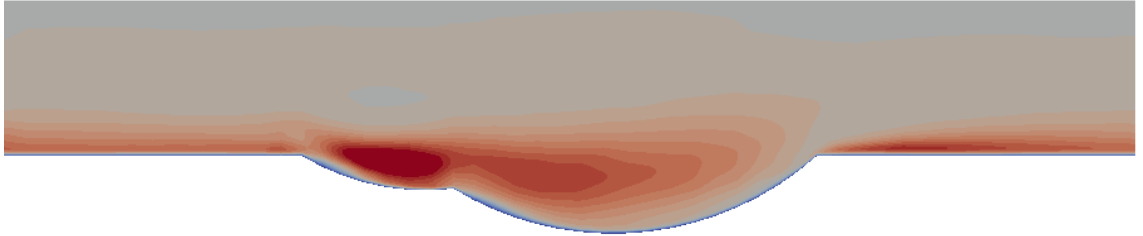
(d) $\bar{u'}^+_{rms}$ *(M4-G3-TB, n = 12)*
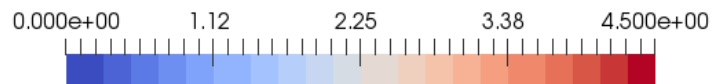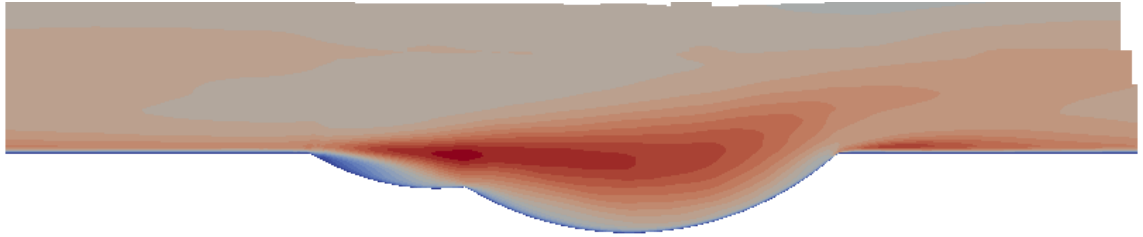
Figure 7.20: *Comparison of contour plots of the streamwise velocity fluctuations over ripple profiles at streamwise locations corresponding to $Re_\theta \approx 2600$. The inner-scale values are provided in Table 7.5.*

the flow reaches the following crest, the layer of high streamwise fluctuations which originates from the downstream crest has dissipated. Hence, a new region develops over the length of the crest. As shown in Figure 7.14b, by the midpoint of the crest, the streamwise velocity fluctuations have been replenished and their distribution collapses onto the smooth wall boundary layer profile from case M4-G3-TB.

(a) $\bar{v}'^{+}_{rms}$ *(M2-G1-TB, n = 20)*

(b) $\bar{v}'^{+}_{rms}$ *(M2-G2-TB, n = 18)*

(c) $\bar{v}'^{+}_{rms}$ *(M2-G3-TB, n = 8)*
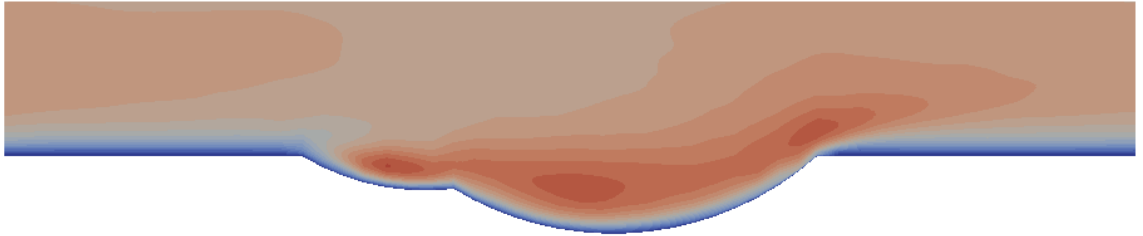
(d) $\bar{v}'^{+}_{rms}$ *(M4-G3-TB, n = 12)*
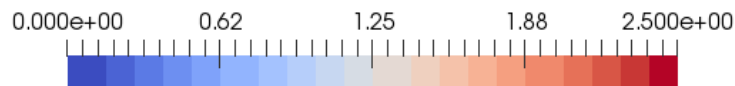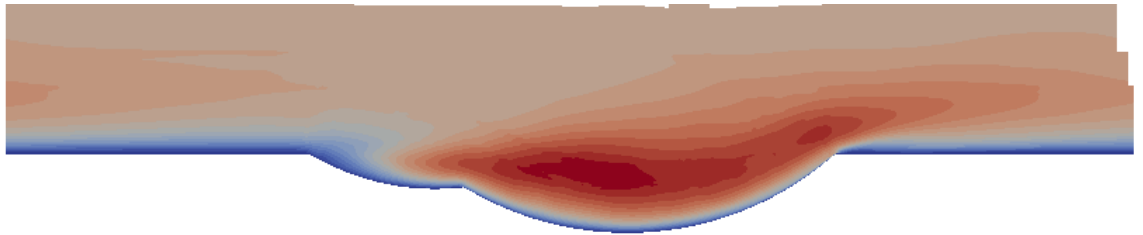
Figure 7.21: *Comparison of contour plots of the wall-normal velocity fluctuations over ripple profiles at streamwise locations corresponding to $Re_\theta \approx 2600$. The inner-scale values are provided in Table 7.5.*

When the boundary layer reaches the downstream end of a crest on a ripple of $k_g^* = 0.15$ the viscous sub-layer immediately detaches from the surface and forms a free-shear layer over the ripple trough. The near-wall spatial resolution exerts a clear influence not only on the length of the separation region, but also on the structures of the resulting vortices. With the coarser spatial resolution in case M2-G3-TB, the free shear layer regains contact with the lee-side immediately prior to the point connecting

(a) $\bar{w'}^+_{rms}$ *(M2-G1-TB, n = 20)*

(b) $\bar{w'}^+_{rms}$ *(M2-G2-TB, n = 18)*

(c) $\bar{w'}^+_{rms}$ *(M2-G3-TB, n = 8)*
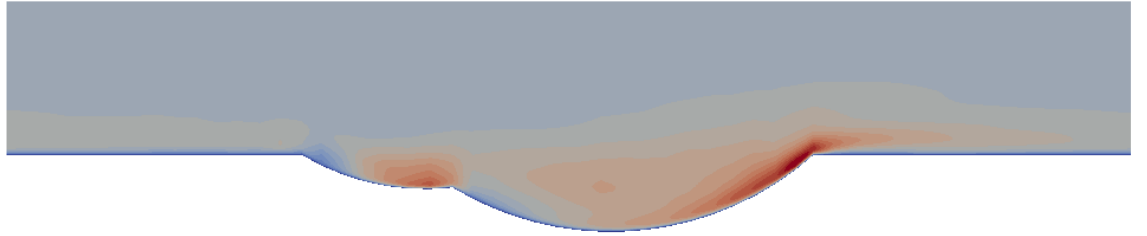
(d) $\bar{w'}^+_{rms}$ *(M4-G3-TB, n = 12)*
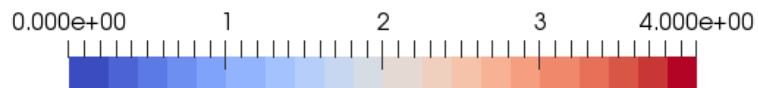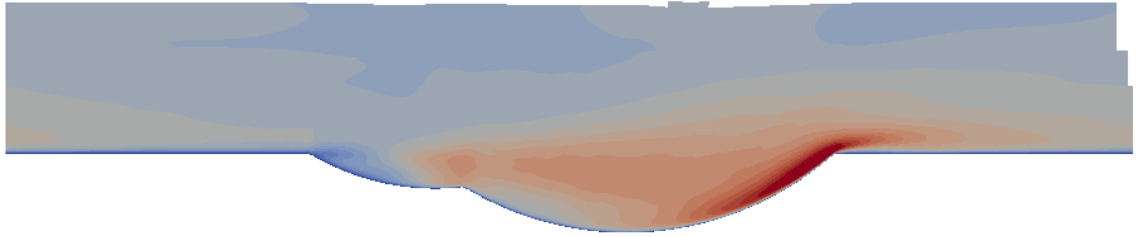
Figure 7.22: *Comparison of contour plots of the spanwise velocity fluctuations over ripple profiles at streamwise locations corresponding to $Re_\theta \approx 2600$. The inner-scale values are provided in Table 7.5.*

the two segments. Under the finer streamwise resolution in case M4-G3-TB the free-shear layer passes over the full length of the lee-side, only regaining contact with the surface once it reaches the stoss-side.

The resolution of the free-shear region exerts a significant influence on the preserva-tion of the streamwise velocity fluctuations throughout the trough. The detached shear

layer in case M2-G3-TB produced a greater amplification of the streamwise velocity fluctuations immediately downstream of the crest, compared to that in case M4-G3-TB. However, the streamwise fluctuations are rapidly suppressed above the point at which the detached shear layer rejoins the lee-side (Figure 7.20b). The strength of the weaker streamwise fluctuations in case M4-G3-TB is preserved as the free-shear layer maintains its elevation from the surface. As a result, the flow reaches the stoss-side with a greater strength of the streamwise velocity fluctuations when compared with case M2-G3-TB. This in turn suppresses the growth of the streamwise velocity fluctuations in the new inner region which grows along the flat crest, leading to a reduction in the strength of the streamwise velocity fluctuations at the midpoint of the crest, as seen in Figure 7.19b.

Similarly, increasing the steepness of the lee-side, and enhancing the strength of flow separation, exerts a strong influence on the amplification of wall-normal velocity fluctuations within the trough. For a depth of $k_g^* = 0.025$, the region of high $\langle \bar{v'}_{rms} \rangle^+$ which lies away from the wall, beyond $y^+ = 100$, maintains its structure over the full length of the ripple, with minimal variation in the strength of $\langle \bar{v'}_{rms} \rangle^+$. When the ripple depth is raised to $k_g^* = 0.05$, as in case M2-G2-TB, the previously unperturbed region of high $\langle \bar{v'}_{rms} \rangle^+$ begins to distort, particularly over the lee-side, however, turbulent spots containing concentrations of high $\langle \bar{v'}_{rms} \rangle^+$ are not yet observed. For $k_g^* = 0.15$, the wall-normal velocity fluctuations are amplified within the trough, with high concentrations focused around the regions of flow separation. These high concentrations of turbulent motion move out of the trough and propagate downstream, which amplifies the wall-normal velocity fluctuations over the crest throughout the inner region, including the viscous sub-layer, as seen in Figure 7.19c, Figure 7.21c and Figure 7.21d.

The maximum point of shear stress for each ripple occurs at the endpoint of the

stoss-side. As the flow accelerates over the stoss-side the wall shear stress rapidly increases until it spikes at the point where the stoss-side meets the crest. For a spatial resolution of $\Delta x^+ \approx 42.2$ in case M2-G3-TB, the maximum shear stress at the leading edge reached more than 300% of the reference smooth wall value. Increasing the streamwise spatial resolution to $\Delta x^+ \approx 10.6$ simultaneously amplified the shear stress spike to more than 600% of the reference smooth wall value. This rapid growth in the local shear stress is accompanied by a strong increase in the spanwise velocity fluctuations in a region immediately adjacent to the wall (Figure 7.22). The strength of high spanwise velocity fluctuations grow with the magnitude of the local shear stress spike, and hence, they grow with increasing ripple depth. As the viscous sub-layer grows along the ripple crest, the highly turbulent spot of large spanwise velocity fluctuations is forced away from the wall and gradually dissipates downstream. Although, by the mid-point of the crest, its presence still persists in the enhanced spanwise velocity fluctuations throughout the inner region, including the viscous sub-layer, as shown in Figure 7.19d. For a shallower depth of $k_g^* = 0.05$, the amplification of spanwise fluctuations on the lee-side is sufficiently weak (Figure 7.22b) to dissipate within a viscous sub-layer, resulting in only a marginal increase in the spanwise velocity fluctuations within the remainder of the inner region (Figure 7.19d).

Figure 7.23a and Figure 7.23b display the wall shear stress distribution in case M2-G3-TB and case M4-G3-TB, after further boundary layer development ($Re_\theta \approx 4550$). At this point, the outer length scale has grown from $\delta_{99}/\lambda_g \approx 0.8 \sim 0.9$ to $\delta_{99}/\lambda_g = 1.35$. However, the variation of shear stress, in relation to the reference smooth wall values at an equivalent value of Re_θ, shows minimal change across the full width of the ripple, compared to a boundary layer of $Re_\theta \approx 2600$.

(a) *Case M2-G3-TB (Re$_\theta$ ≈ 4500)*   **(b)** *Case M4-G3-TB (Re$_\theta$ ≈ 4500)*
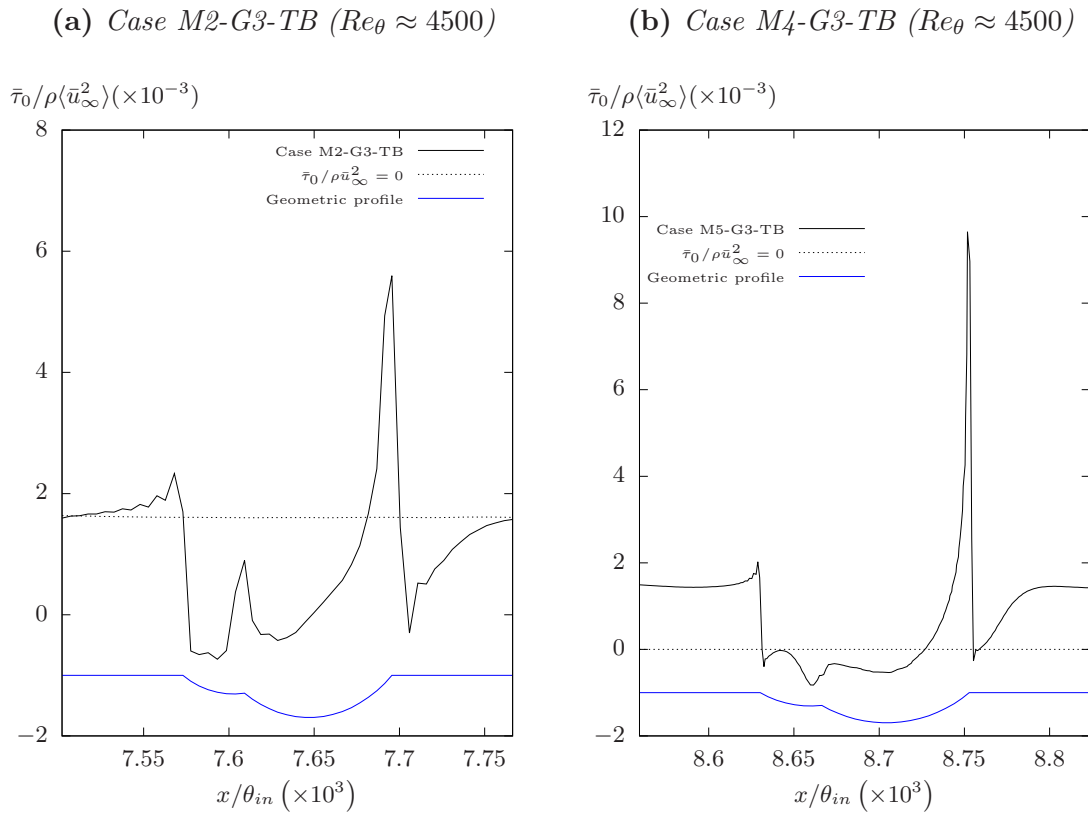
**Figure 7.23:** *Distribution of the local streamwise wall shear stress over the midline of ripple profiles at streamwise locations corresponding to Re$_\theta$ ≈ 4500 for a fixed value of ripple depth ($k_g^* = 0.15$) and varying values of spatial resolution.*

7.7 Channel Flow Validation

The present section compares the coarse hexahedral mesh M2, and the refined split-hexahedral mesh M4, with a high quality hexahedral mesh M5, with local refinement over the sharp angles of the ripple profile. The layout of all three meshes are given in Section 7.2.2. Due to the combination of high cell count and small time step which is associated with mesh M5 all three simulations for this comparison were performed in a simplified channel flow domain. Figure 7.24 displays the domain of the periodic channel simulations with periodic ripples on the lower wall and upper wall. The channel has a streamwise length of $L_x = 0.02238m$, covering three periodic ripple profiles on each wall, and a spanwise width of $L_z = 0.0081m$. The channel has height of $L_y = 2h_0 = 0.005968m$, where h_0 denotes the channel half-height as shown in Figure 7.24. This

value of h_0 was selected based on the results of case M2-G3-TB and case M4-G3-TB, in which a boundary layer width of $\delta_{99} \approx 0.003m$ corresponds a boundary layer of $Re_\theta \approx 2660$, when the surface consists of the ripple profile of depth $k_g^* - 0.15$. The flow is driven by a body force which produces a bulk flow velocity of $U_{av} = 92m/s$ (corresponding to $u_\infty \approx 105m/s$ in case M2-G3-TB) at the periodic inlet and outlet boundaries of the domain.
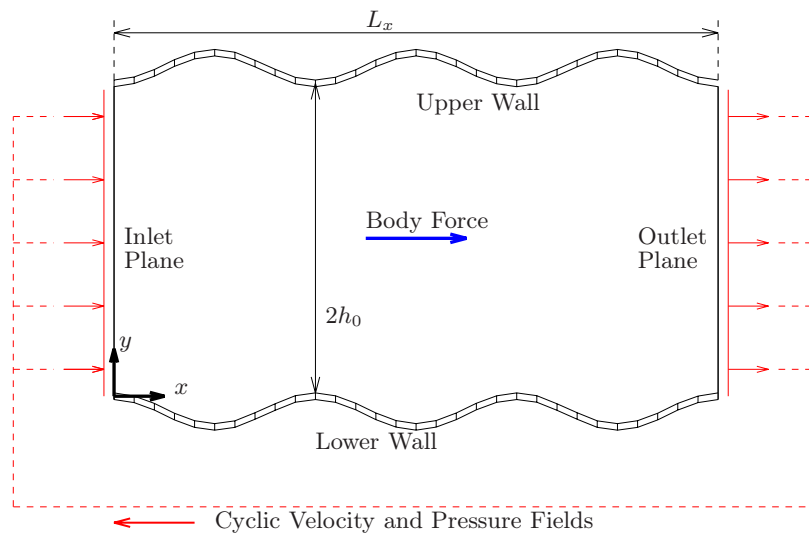
Figure 7.24: *Diagram of the flow domain and boundary conditions for a periodic turbulent channel flow with periodic ripples on the lower and upper walls.*

Table 7.6 outlines the three simulations which are used to compare three different mesh types in the channel domain. Each simulation involves a lower wall and upper wall consisting of periodic ripples with a depth of $k_g^* = 0.15$ (denoted by G3). Each simulation runs for a physical time of $t = 0.005s$, which corresponds to 20 passes through the domain $(20L_x/U_{av})$ based on the bulk flow velocity.

Figure 7.25 displays the temporal convergence of the drag forces in the channel, in terms of the dimensionless friction factor f, along with its pressure component f_p, and viscous component f_v, as defined in Section 5. The drag forces in the channel flow

Table 7.6: Setup for three simulation cases of a periodic turbulent channel flow over ripple profiles with the three types of mesh outlined in Table 7.3.

Case	k_g^*	Mesh	$\Delta t\,(s)$	$N_T\,(\times 10^6)$
M2-G2-CH	0.15	M2	1.6×10^{-7}	3.36
M4-G3-CH	0.15	M4	6×10^{-8}	9.69
M5-G3-CH	0.15	M5	2.8×10^{-8}	15.7

simulations display a similar rate of convergence to the boundary layer simulations. For all variables, the coarser hexahedral mesh M2, and the refined split-hexahedral mesh M4 produce significantly different effects on the error, in relation to mesh M5. Case M4-G3-CH consistently underpredicts the values of f, f_p and f_v by approximately $4.1\% \sim 4.9\%$ in comparison to mesh M5. The coarse hexahedral mesh in case M2-G3-CH produces similar magnitudes of error in C_p, although, instead producing an over-prediction of 4.3%, compared with mesh M5. However, the decreased streamwise resolution shows a more significant effect on the value of the viscous component of the friction factor f_v. Mesh M2 over-predicts the value of f_v by 14%, compared with Mesh M4, which under-predicts the value of C_v by only 4.7%.

The impact of the mesh structure and the spatial resolution on local viscous forces, and hence on f_v, is shown in Figure 7.26, which displays the distribution of time-averaged, streamwise shear stress over the centreline ($z = 0m$) of the lower wall of the channel. As for the spatially developing turbulent boundary layer, the coarsest resolution in mesh M2 fails to correctly capture the pattern of flow separation over the lee-side. Whilst mesh M2 underpredicts the maximum value of shear stress at the crest, the coarse streamwise resolution around the crests translate what should roughly be a single point of maximum shear stress, to an expansive area of high stress. On the other hand, whilst increasing the streamwise resolution raises the maximum shear stress at the crest, as in the case of mesh M4 and mesh M5, this high shear stress converges onto a single point maximum. This may have the effect of reducing the area

(a) *Friction factor*
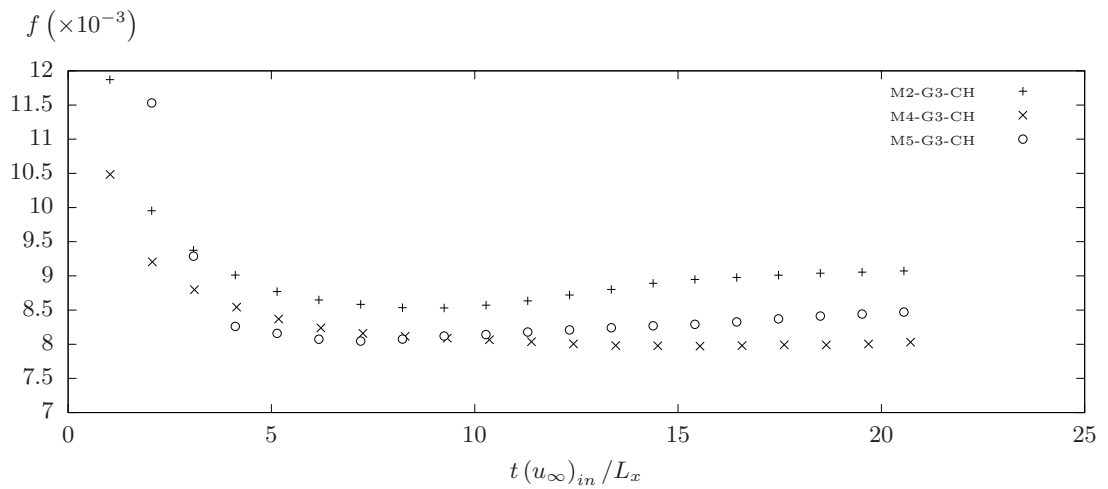
(b) *Pressure component of the friction factor*
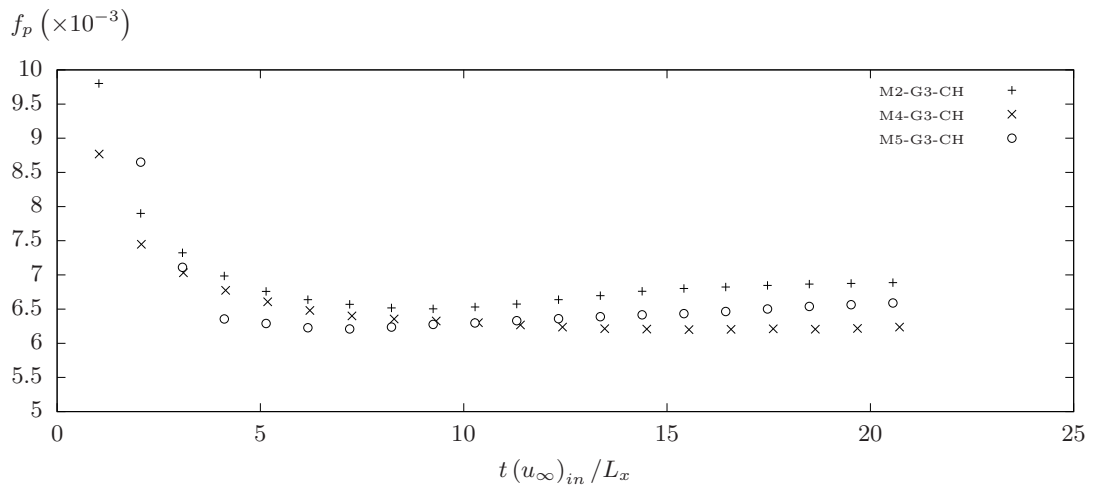
(c) *Viscous component of the friction factor*
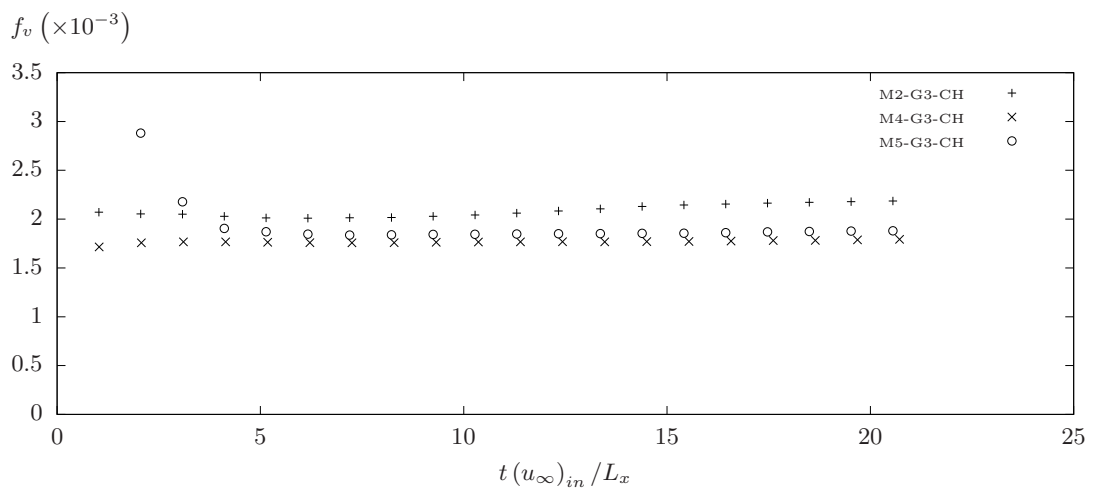
Figure 7.25: *Temporal convergence of the friction factor and its individual pressure and viscous components for turbulent channel flow over periodic ripples.*

of effect for high shear stress, under a similar principle to the drag reducing mechanism of streamwise riblets, although, in this case it acts to reduce the error in the resolved flow field. Along the remainder of the surface, mesh M4 and mesh M5 displays a strong correlation in the resolved shear stress distribution, particularly around the important region of separation from the lee-side.

The impact of the mesh structure and the spatial resolution on the boundary layer structure is displayed in Figure 7.27, Figure 7.28 and Figure 7.29, which show the profiles of streamwise velocity, velocity fluctuations and the Reynolds shear stress across one half of the channel width, over the midpoint of the ripple crest at $x = 2\lambda_x$. At the crest, mesh M4 and mesh M5 show strong agreement in the distribution of the streamwise velocity across the full half-height of the channel, whilst mesh M2 produces only minor divergence in the logarithmic region in the region around the centreline of the channel. A strong agreement between all three cases is present in the distribution of spanwise velocity fluctuations in Figure 7.28.

The most significant influence of the mesh can be seen in the streamwise and wall-normal velocity fluctuations in Figure 7.29. Mesh M2 produces a strong amplification in the value of $\langle \bar{u}'_{rms} \rangle^+$ throughout the inner region of the flow, in comparison to mesh M4 and mesh M5. The amplified values of $\langle \bar{u}'_{rms} \rangle^+$, in relation to the increased flow resistance of mesh M2, are consistent with previous findings on the relation between drag reducing/increasing effects (or drag variations due to error) and the streamwise velocity fluctuations in the inner region of the flow. The over-prediction in the maximum value of $\langle \bar{u}'_{rms} \rangle^+$ in mesh M2, compared with mesh M4, is consistent with the results from the inner region from the spatially developing boundary layer, as seen in Figure 7.14, when comparing mesh M2 and mesh M4 over a ripple of $k_g^* = 0.15$. Note that mesh M5 does not produce a similar over-prediction in $\langle \bar{u}'_{rms} \rangle^+$ to that seen

(a) *Case M2-G3-CH*   **(b)** *Case M4-G3-CH*

(c) *Case M5-G3-CH*
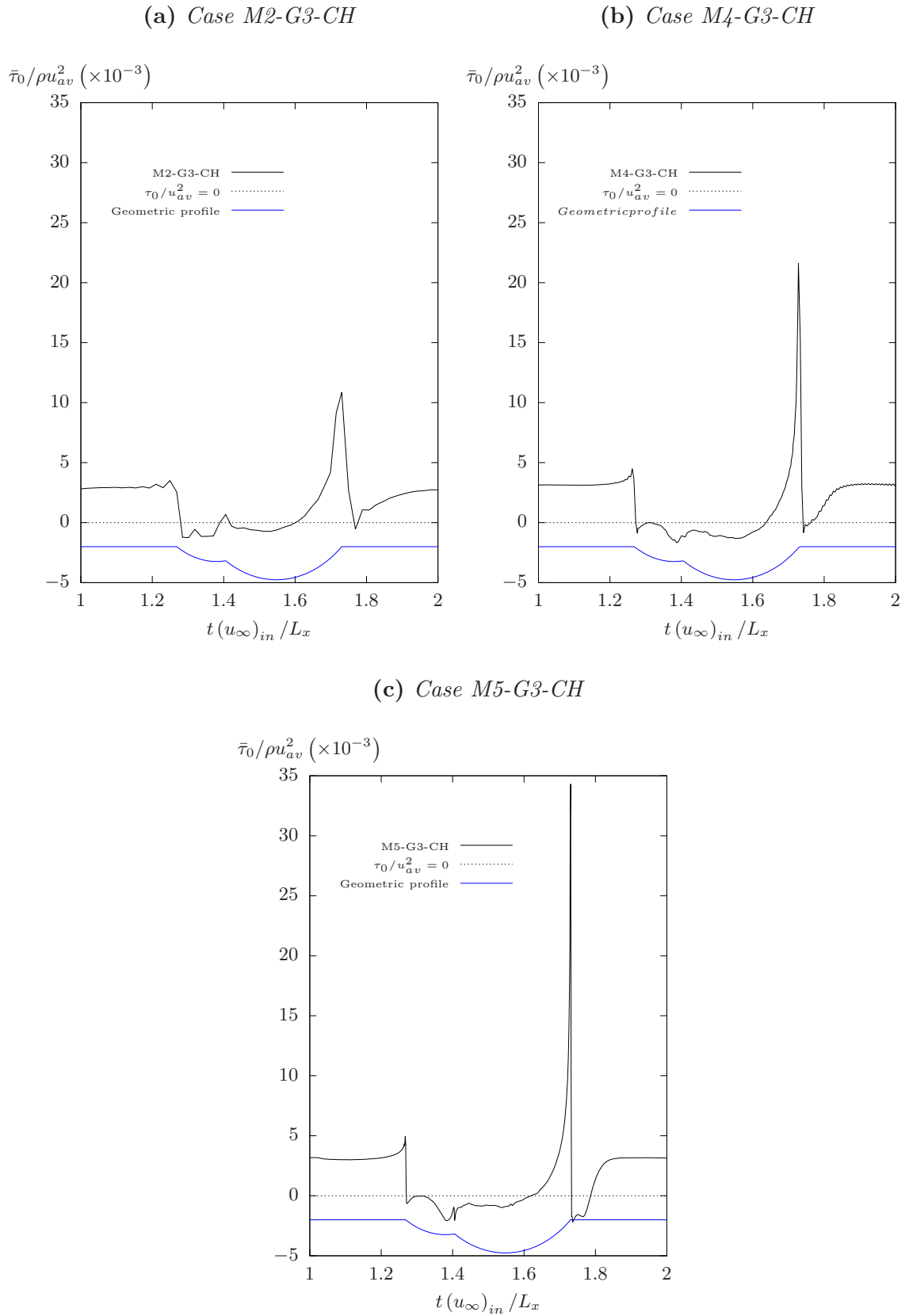
Figure 7.26: *Distribution of the local streamwise wall shear stress over the lower wall, along the centreline of the channel ($z = 0m$) between streamwise locations of $x/L_x = 1$ and $x/L_x = 2$.*
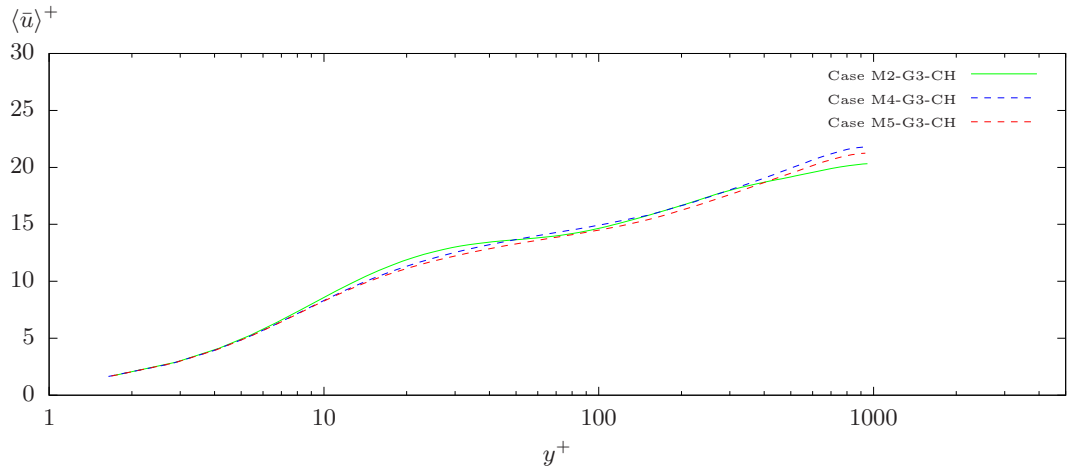
Figure 7.27: *Comparison of the distribution of the inner-scaled, time-averaged stream-wise velocity at a streamwise location of $x = 2\lambda_x$ in a periodic channel for varying values of spatial resolution.*
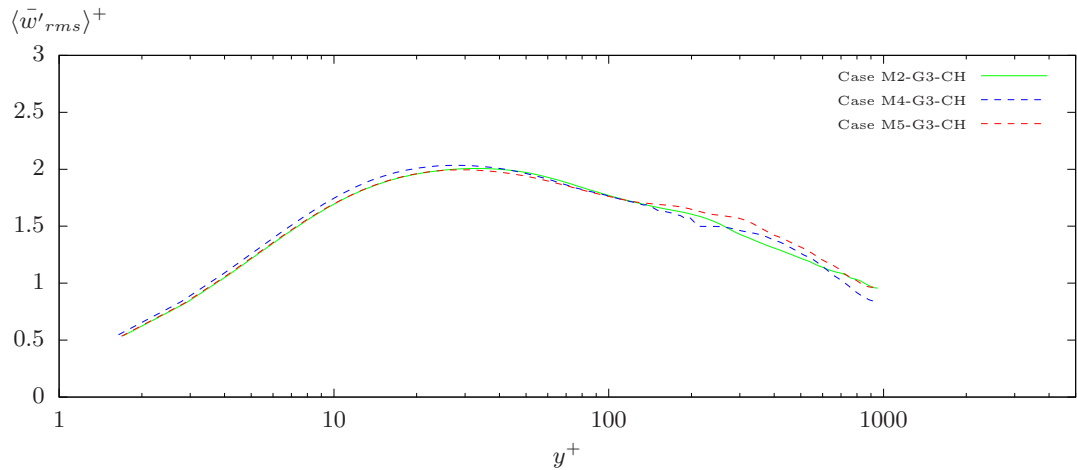
Figure 7.28: *Comparison of the distribution of the spanwise velocity fluctuations at a streamwise location of $x = 2\lambda_x$ in a periodic channel for varying values of spatial resolution.*

for mesh M2, despite mesh M2 and mesh M5 having an almost identical streamwise resolution around the midpoint of the crest. This would suggest that the amplified streamwise velocity fluctuations created by mesh M2, originate from within the trough and propagate downstream, as shown for the spatially developing turbulent boundary layer. As in the spatially developing boundary layer, mesh M4 produces an increase in the wall-normal velocity fluctuations as seen in the profile of $\langle \bar{v}'_{rms} \rangle^+$ in Figure 7.29b. The enhanced values of $\langle \bar{v}'_{rms} \rangle^+$ are not present in mesh M2 and mesh M5, and are only present in the near-wall region in mesh M4; specifically the regions in which the

(a) *RMS of streamwise velocity fluctuations*
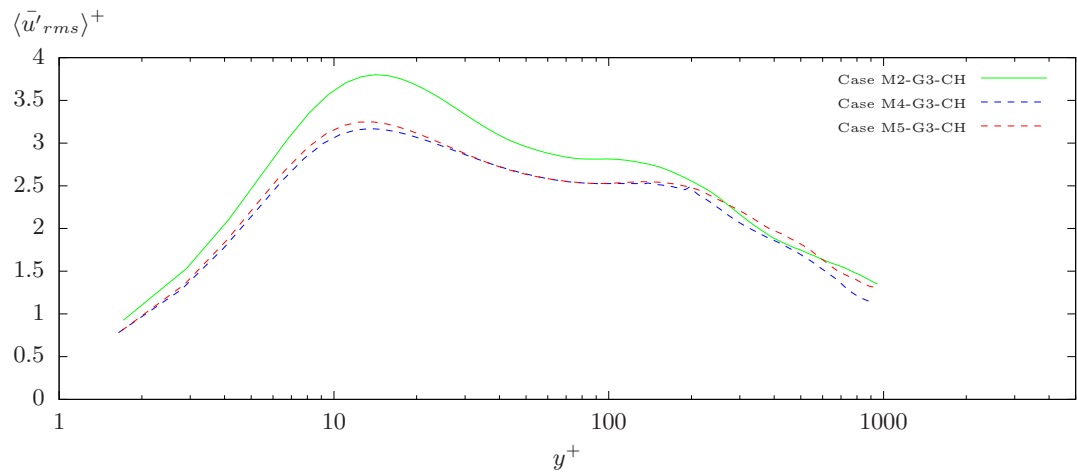
(b) *RMS of wall-normal velocity fluctuations*
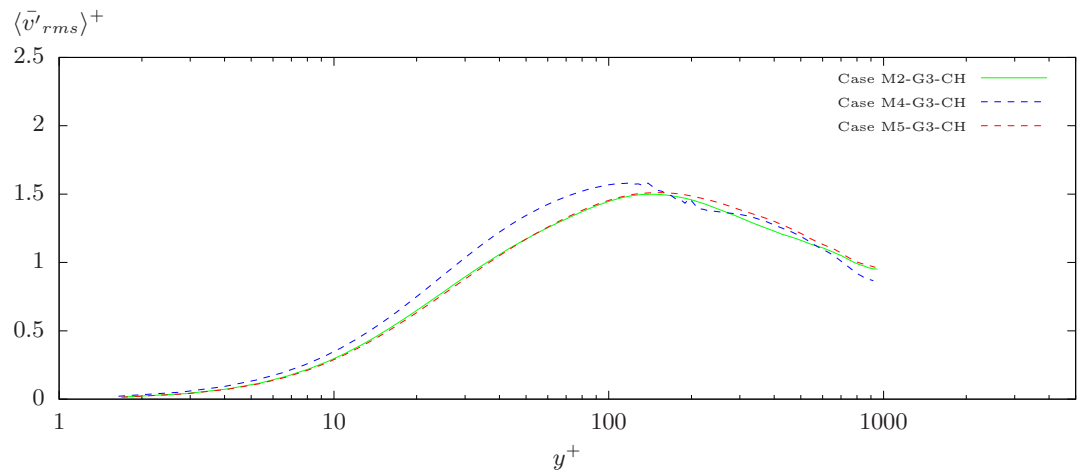
(c) *Reynolds shear stress*
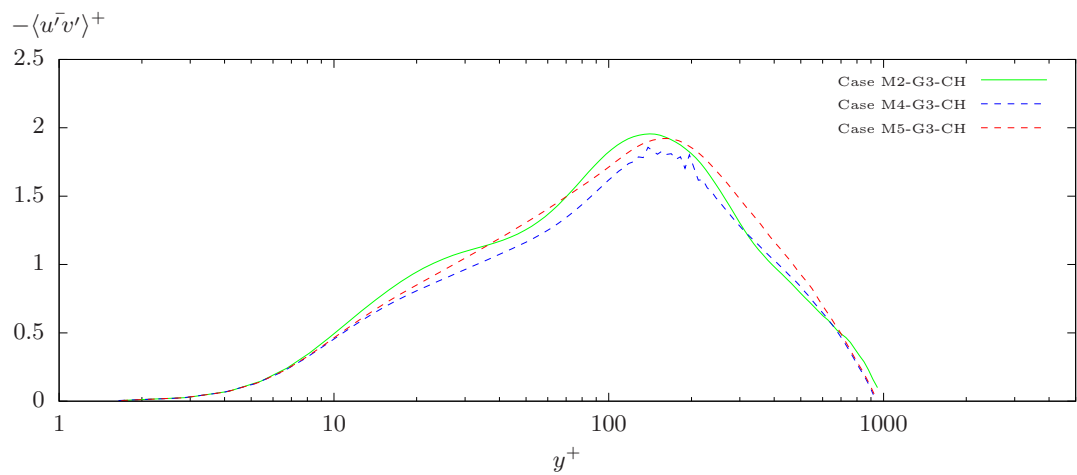
Figure 7.29: *Comparison of the distribution of the turbulent stress components at a streamwise location of $x = 2\lambda_x$ in a periodic channel for varying values of spatial resolution.*

streamwise resolution is increased through local octree refinement. The boundary of the refinement region in mesh M4 can be clearly identified by the presence of distortions in the profile of $-\langle \bar{u'v'} \rangle^+$ in Figure 7.29b. Hence, it can be concluded that, whilst the accuracy of $\langle \bar{u'}_{rms} \rangle^+$ is dependant on the streamwise resolution in the trough, the accuracy of $\langle \bar{v'}_{rms} \rangle^+$ is dependant on the streamwise resolution at the crest.

7.8   Summary

This section investigates the influence of simplified asymmetric ripple profiles on a spatially developing turbulent boundary layer. A selected ripple profile from Chapter 6 was substituted into the domain of the smooth wall boundary layer simulations developed in Chapter 4.

When the ripple depth lay within the limit of $k_g^* \leq 0.05$, the presence of ripples had minimal impact on the flow resistance and turbulent stress distribution within the boundary layer. For a depth of $k_g^* = 0.15$, the presence of the ripples created strong increases in the flow resistance throughout the domain, which were accompanied by strong amplification of the wall-normal and spanwise velocity fluctuations throughout the inner region of the boundary layer. The size of the outer length scale, i.e. the boundary layer thickness, in relation to the ripple depth and wavelength, did not display any significant influence on the flow resistance along the full streamwise length of the textured region. Similarly, the local distribution of wall shear stress within the ripple displayed no significant dependence on the outer length scale. Locations of high gradients in the wall shear stress are accompanied by large concentrations of highly turbulent spots containing amplified spanwise velocity fluctuations. This would be expected based upon the observation that suppression of spanwise motions within the

near-wall turbulent region are linked to drag reduction in drag reducing riblets.

To assess the quality of the meshing procedure, an automatically generated split-hexahedral mesh was compared against a refined hexahedral mesh in a periodic channel. By only refining the streamwise spatial resolution in the near-wall region, the split-hexahedral mesh was able to accurately replicate the distribution of shear stress at the wall, and the distribution of velocity and velocity fluctuations across the channel. It also showed a strong correlation with the results from refining a fully hexahedral mesh. In addition, by maintaining a coarser streamwise spatial resolution away form the wall, the split-hexhedral mesh could maintain stability with a time-step that was three times larger than the refined hexahedral mesh which projected the fine spatial resolution at the wall into the bulk of the channel. In exchange, the split-hexahedral mesh compromised on accuracy of the drag forces in the channel, which were under-predicted with an error of the order of 5%, relative to the solution from the refined hexahedral mesh.

CHAPTER 8

Conclusions and Future Work

8.1 Introduction

Whilst passive macroscale grooves have practical benefits in terms of manufacturability, previous investigations involving both laminar and turbulent flows have found such surfaces to produce either a detrimental or marginal effect on the flow resistance. Where these studies focused on simple geometric profiles, their findings allude to the potential for improved performance through geometric optimisation. This thesis has investigated the drag reducing potential of the geometric profiles of naturally occurring sand ripples, when applied as rigid periodic grooves in periodic laminar flow and spatially developing turbulent flow.

Even with current advances in computational power, the computational workload

of modelling physically realistic laminar-turbulent transition typically limits numerical investigations to periodic internal flows and simple textured geometries. This thesis has presented novel methodologies within the open source code OpenFOAM for combining automatically generated split-hexahedral meshing techniques with wall-resolved large-eddy simulations for modelling the laminar, transitional and fully turbulent regimes of a spatially developing turbulent boundary layer, along with with periodic macroscale grooves, within a single, continuous domain. In particular, these methods aim to reduce economic difficulties typically associated with geometric optimisation through increasing profile complexity, and the application of macroscale grooves to spatially developing turbulent flows.

8.2 Conclusions

8.2.1 Turbulent Boundary Layers in OpenFOAM

To achieve a controlled boundary layer transition in OpenFOAM, the methodology incorporates a novel tripping technique which destabilises a spatially developing laminar boundary layer, by imposing pseudo-random fluctuations onto the wall-normal velocity component of the flow adjacent to the solid wall. The trip produced a near instantaneous onset of transition when the velocity fluctuation imposed on the laminar boundary layer was of similar magnitude to the maximum velocity fluctuation in a turbulent boundary layer of equivalent thickness. A trip of half this strength could induce transition by inducing large-scale, two-dimensional disturbances in the flow which propagated downstream and rapidly destabilised, breaking up into smaller three-dimensional turbulent structures. It should be noted that the required strength of the trip was dependant on the near-wall spatial resolution. However, the current

results show that the aforementioned criteria for trip strength can be followed when the near-wall streamwise spatial resolution lies between 32.5 and 54.9 viscous lengths, and the spanwise and minimum wall-normal resolution lie on the order of $\approx 50\%$ and $\approx 2.5\%$ of the streamwise spatial resolution respectively.

The wall-adapting local eddy-viscosity model produced a significant overshoot in the maximum streamwise velocity fluctuations even at the finest resolution of $\Delta x^+ \approx 32.5$, in addition to an under prediction of the maximum wall-normal velocity fluctuations. Despite these discrepancies in turbulent stress, a coarsely resolved wall-adapting local eddy-viscosity model could still predict the fundamental properties of flow resistance and shape factor to a sufficient accuracy, even with near-wall cell dimensions that were more than 4.4 times greater than is required for a resolved direct numerical simulation approach. For streamwise and spanwise cell widths of 42.2 viscous units and 20 viscous units respectively, both data sets converged to within $\pm 3\%$ of the theoretical Coles-Fernholtz relation by $Re_\theta \approx 1000$. When the near-wall cell dimensions were increased by only 30% in each direction, the coefficient of friction failed to converge within a $\pm 5\%$ error bound across the full domain, suggesting that wall-resolved laminar-turbulent transition should begin with initial cell dimensions which are no more than 4.5 times those applied in direct numerical simulation. From this resolution, by reducing the cell width by 30% in each direction is sufficient to extend this accuracy to the transitional regime, where the coefficient of friction converges into the $\pm 3\%$ error bounds by $Re_\theta \approx 300$. The results show that great care must be taken when comparing the trends for shape factor between boundary layers. A new theoretical trend for the shape factor should be calculated in each case, to account for the influence of the streamwise variation in the free-stream velocity on the boundary layer growth.

8.2.2 Laminar Channel Flow: Arbitrary Geometry

Plaster casting was used to capture the profiles of asymmetric ripple bedforms which had formed naturally on a sand beach. These cases were reverse engineered and converted into digital surfaces which captured the detailed geometric features of the natural profiles whilst possessing an ideal streamwise and spanwise periodicity. Two distinct types of sand ripple geometries were identified. The first profile (denoted RN1) contained a unique stoss-side consisting of a pair of sinusoidal curves, as theoretically predicted for a ripple in an asymmetric laminar flow (Blondeaux *et al.* 2015). The second profile (denoted RN2) formed the classic 'vortex ripple' identified by a wide trough and a planar lee-side. These surfaces were investigated to determine their potential for reducing flow resistance in internal laminar flow.

The present analysis confirms that the 'snappyHexMesh' utility in OpenFOAM, and the discretisation of a domain through a split-hexahedral mesh, has great potential for reducing the economic impact of performing extensive parametric studies involving surfaces of arbitrary macroscale grooves, whilst still modelling flow resistance and flow separation to an acceptable accuracy. In addition to reducing pre-processing time, generating a split-hexahedral mesh has the potential to reduce the required CPU time by more than 80%, when compared to a fully structured hexahedral mesh, for investigating macroscale, two-dimensional transverse grooves. Notably, errors in the viscous drag are accompanied by errors of a similar magnitude of the additional pressure drag, leading to negligible errors in the overall flow resistance. The methodology was validated against a limited number of macroscale grooves with previously published solutions. These included; sinusoidal grooves to test the accuracy in predicting flow resistance, and periodic hills to test the accuracy in predicting flow separation. The automatically generated split-hexahedral meshes were able to produce the distribution

of wall shear stress, and predict the points of flow separation to a high accuracy, despite local distortions in the wall shear stress profile due to distorted unstructured cells at the wall.

Whilst snappyHexMesh was found to be highly effective in reducing the pre-processing time, the configurations of the domain and numerical solver were not fully independent of the surface geometry or flow properties. The stability of the channel flow was dependant on the Reynolds number of the flow. When the Reynolds number lay within the lower laminar regime ($Re_h << 500$), a solution could be converged using a steady-state solver. For Reynolds numbers lying above the theoretical limits of laminar-turbulent transition ($Re_h > 500$), the solution requires temporal terms in order to maintain stability, even though the final solution exhibited steady-state behaviour in all cases. In addition, three-dimensional ripple profiles in a flow of $Re_h > 500$ could not maintain stability with cyclic boundary conditions, even with a time-dependant numerical solver.

8.2.3   Natural Sand Ripples in Poisuille Flow

An extensive parametric study into the drag reducing potential of two-dimensional and three-dimensional sand ripples in laminar Poisuille flow was carried out. The Reynolds number range spanned the laminar and theoretically transitional regimes, whilst depth exceeded shallow groove depths studied previously and crossed the theoretical limit of flow separation for sand ripples. The investigation explored the impact of profile shape, Reynolds number, ripple depth and orientation on flow resistance, wall shear stress distribution and the velocity flow field. Whilst the current sand ripple profiles did not positively influence the flow resistance in purely, laminar flows, their features revealed the necessary criteria required for further optimisation of the surface geometry.

For two-dimensions ripple geometries in laminar channel flow, the investigation revealed a consistent correlation between the drop in the viscous component of the flow resistance and the rise in the total flow resistance. As such, whilst replacing a symmetrical sinusoidal groove profile with the naturally occurring asymmetric ripple profiles provided a greater overall reduction in the wall shear stress, they produced a detrimental effect on the overall flow resistance.

For two-dimensional ripples, whilst orientation could severely impact flow separation, it produced a negligible impact on flow resistance. This is contrary to the theories developed from previous investigations, most notably that of Mohammadi & Floryan (2013b) and Saha *et al.* (2015), which suggest a potential to achieve a drag reduction with spanwise oriented, two-dimensional grooves, through the geometric optimisation to reduce the pressure drag, whilst maintaining a region of shear layer detachment within the trough. The results identified that reversing the flow direction over an asymmetric ripple, and hence, changing the geometric forms of the lee-side and stoss-side, does not have any significant effect on the flow resistance until three key conditions are met. This applies even if this reversal suppresses or enhances the onset of flow separation. The first two conditions are that the ripple must have a geometry with three-dimensional spatial variation, and that the ripple depth, in relation to its periodic wavelength, must surpass a critical limit. The results suggest that limit this lies between the value of 7.5% and 15% of the groove wavelength. For the final condition, the inertial forces of the flow must be sufficient for the flow impact of the ripple on the flow field to extend beyond the near-wall region. In the current investigation, such a condition was found to exist when the Reynolds number lay close to the theoretical laminar-turbulent transitional regime for laminar channel flow. When these conditions are met, the viscous drag grows rapidly with an increasing amplitude of the spanwise

spatial variation, as the redistribution of flow diverts the high velocity fluid from the centre of the channel towards the crest of the lobe, and the details of the geometry of the lee-side and the stoss-side exert a non-negligible influence of the greatly amplified shear stress at this point. This influence is such that reversing the direction of the flow over an asymmetric ripple profile can have a greater impact on the flow resistance than would be achieved by replacing the entire ripple profile with a symmetrical sinusoidal profile.

8.2.4   Ripples in Spatially Developing Turbulent Flow

The present analysis applied a simplified two-dimensional ripple profile at three values of depth to wavelength ratio of $k_g^* = 0.025$, $k_g^* = 0.05$ and $k_g^* = 0.15$, into the numerical domain of the spatially developing turbulent boundary layer. Initially, the optimal resolution for a smooth wall boundary layer, where cell widths are equivalent to 4.5 times that required for a fully resolved direct numerical simulation, was applied for each depth. For the deepest ripple, an additional mesh was created using snappyHexMesh, in which the spatial resolution in the streamwise direction was increased using layers of local refinement in the near-wall region, without altering the wall-normal and spanwise cell width. Additionally, this new split-hexahedral mesh was against the initial 'smooth wall' hexhahedral mesh, and against a hexahedral mesh with a refined streamwise resolution across the full wall-normal height of the domain, for deep ripples in a periodic channel flow. The split-hexahedral mesh proved to be a suitable approach to improving the accuracy of shear stress profiles and turbulent stress distribution, whilst minimising the negative impact on computational efficiency, with regards to total cell count and required time step. In the present case, this amounted to a 75% reduction in the near-wall streamwise cell width, whilst producing only a 100% increase in the total cell

count and a 30% reduction in the required time-step.

The split-hexahedral mesh with a resolution of $\Delta x^+ \approx 10.6$ reduced the effectiveness of the trip. Whilst the trip succeeded in inducing large-scale, two-dimensional disturbances in the boundary layer, these disturbances failed to destabilise until they reached the first ripple profile. When a fully turbulent boundary layer reached the grooves with a depth of $k_g^* = 0.15$, the boundary layer required a further 4 groove wavelengths to reach a new equilibrium state. When the boundary layer remained laminar over the smooth wall, the first groove geometry triggered the onset of laminar-turbulent transition. The transitional regime extended for approximately 4 groove wavelengths, during which the boundary layer achieved its new equilibrium state. The main influence of transition downstream from this point took the form of a shift of the virtual flow origin, relative to the initial 'smooth wall' resolution. The late transition of the boundary layer due to increased spatial resolution produced no significant impact on the pressure flow resistance, and the ratio between Re_τ and Re_θ, for a given value of Re_θ. The sudden change in the streamwise spatial resolution between refinement layers had a negligible impact on the time-averaged wall-normal and spanwise turbulent motions throughout the inner and outer regions of the boundary layer.

Within the spatially developing turbulent boundary layer, all ripple profiles had a negative impact on flow resistance, in which the flow resistance grew with ripple depth, and comprised of a viscous drag reduction which was counteracted by a large pressure drag component. Notably, the distribution of shear stress in the groove was independent of Re_θ, as was the ratio between Re_τ and Re_θ, for a fixed value of ripples depth. This shows that the impact of the ripples on flow resistance was independent on the ratio between the outer length scale of the boundary layer and the length scale of the ripple.

8.3 Current Limitations of Study

- Whilst large-eddy simulation makes a single boundary layer simulation economically feasible, it does not enable extensive parametric studies, as is the case for periodic channel flow. Hence, the investigation in the present analysis was limited to two values of trip strength, which were tested for a fixed spatial resolution, prior to the mesh independence study. A more extensive investigation into the interactions between trip configuration and spatial resolution, will provide a more robust set of criteria for designing future simulations, particularly in cases of large-eddy simulation.

- Whilst the simulations of periodic groove in spatially developing boundary layers have been compared for different mesh types, and varying spatial resolution, they have not yet been compared with comparable experimental results. Whilst the smooth wall boundary layers have been validated against high resolution direct numerical simulation results, similar tripping configurations can produce a strong variation in the structure of the downstream flow, and hence any experiments must be initially configured and validated against these smooth surface results.

- Due to the large number of control factors in the parametric studies each configuration could only be tested at two values of orientation, both of which lay parallel to the streamwise direction. The observations regarding the relatively low influence of orientation on flow resistance are only applicable to surfaces which lie parallel to the streamwise axis. However, such a limitation was necessary at the present stage, as exploring a sufficient number of oblique orientation angles would not be practical alongside a multi-variant analysis of Reynolds number, groove depth and profile shape.

8.4 Recommendations For Future Work

Building on the findings of the present analysis, the following section discusses areas of further investigation into drag reducing surfaces in laminar and turbulent flow.

8.4.1 Oblique Grooves in Laminar Flow

- The parametric study of two-dimensional and three-dimensional ripples in laminar flow should be expanded to investigate the influence of surface orientation for oblique grooves which are not parallel to the streamwise axis.

- Further development and testing should aim to confirm the suitability of the methodology for incorporating oblique grooves in the domain. Particular attention should be directed to ensuring stability once the necessary periodic boundary conditions are applied to the spanwise direction. This includes the impact of circulation in the bulk flow with spanwise cyclic boundary conditions.

- The impact of cell refinement across the bulk of the channel should be investigated with regard to capturing the large scale rotating vortices induced by three-dimensional grooves in high Reynolds laminar flow.

- Within the laminar flow investigations, the number of discrete Reynolds numbers may be increased within the range of $100 < Re_h < 500$, whilst the number of discrete of groove depths values may be increased between $k_g^* = 0.075$ and $k_g^* = 0.15$, with particular attention around the point $k_g^* = 0.1$. This enhanced precision will provide clearer indications for the critical limits of i) the onset of vortex ripple behaviour, and ii) the onset of rotational motions throughout the bulk flow in three-dimensional ripple geometries.

8.4.2 Expansion of the Criteria for modelling Laminar-Turbulent Transition

- The modifications to a domain which are required to incorporate a given textured surface may impact the optimal configuration of upstream tripping conditions. Further optimisation of the pseudo-transient numerical trip is required to account for the influence of the spatial and temporal resolution on the response of the laminar boundary layer. A more extensive parametric study should be performed regarding the numerical trip, spatial resolution and turbulence model to assess the interaction.

- The impact of the downstream outlet conditions is unknown, pressure distortions cannot be identified and isolated from the results. The simulations may benefit from the addition of a damping region prior to the outlet boundary in order to eliminate reflections.

- The present analysis has focused the optimisation on pre-processing time and balancing spatial resolution and cell count. With the optimal methodologies now established, further optimisation should consider the impact of the configuration of the pressure-velocity coupling solver and the geometric matrix solver on the overall computational workload and calculation time.

- The wall-adapting local eddy-viscosity model was used to model the sub-grid scale turbulence in all simulations. Alternative sub-grid scale model should be tested to assess the interaction of the sub-grid scale model/modelling coefficient with spatial resolution and trip configuration.

8.4.3   Three-Dimensional Grooves in Turbulent Flow.

- The refined split-hexahedral mesh should be compared with a high resolution hexahedral mesh in a spatially developing turbulent boundary layer. The increased computational cost in the reduced time-step and increased cell count is too high to consider for the present analysis.

- To provide a more detailed understanding on the accuracy of the various meshing strategies, experimental investigations could be carried out using the LJMU high speed air blower facility, which can be directly compared with the numerical results. In preparation for future investigation, the high speed air blower facility governed the design of the numerical simulations for both the smooth and textured surface relations, and the ripple designs were simplified in part to improve their manufacturability.

- Simplification of the ripples removes some of the key geometric features in the naturally occurring sand ripple profiles. Since the present analysis has demonstrated the viability of the split-hexahedral mesh in modelling spatially developing turbulent flow, the present methodology can be expanded to incorporate increasingly complex geometric profiles. Further effectors to achieve a net drag reduction should consider utilising a split-hexahedral mesh to investigate either natural ripple profiles or applying three-dimensional geometries of shallow sand ripples ($k_g^* \leq 0.05$).

References

1. Ahn, J., Lee, J. H. & Sung, H. J. Statistics of the turbulent boundary layers over 3D cube-roughened walls. *International Journal of Heat and Fluid Flow* **44,** 394 –402 (2013).

2. Arolla, S. K. Inflow turbulence generation for eddy-resolving simulations of turbomachinery flows. *Journal of Fluids Engineering* **138,** 031201 (2016).

3. Arolla, S. K. & Durbin, P. A. LES of spatially developing turbulent boundary layer over a concave surface. *Journal of Turbulence* **16,** 81–99 (2015).

4. Asai, M. & Floryan, J. M. Experiments on the linear instability of flow in a wavy channel. *European Journal of Mechanics - B/Fluids* **25,** 971–986 (2006).

5. Bae, H. J., Lozano-Duran, A., Bose, S. T. & Moin, P. Turbulence intensities in large-eddy simulation of wall-bounded flows. *Physical Review Fluids* **3,** 014610 (2018).

6. Bagnold, R. A. Motions of waves in shallow water. *Proceedings of the Royal Society of London. Series A* **187** (1946).

7. Barthlott, W. & Neinhuis, C. Purity of the sacred lotus, or escape from contamination in biological surfaces. *Planta* **202,** 1–8 (1997).

8. Bartholdy, J. *et al.* On the formation of current ripples. *Scientific Reports* **5,** 11390 (2015).

9. Bechert, D. W. & Bartenwerfer, M. The viscous flow on surfaces with longitudional ribs. *Journal of Fluid Mechanics* **206,** 105–129 (1989).

10. Bechert, D. W., Bruse, M., Hage, W., Van Der Hoeven, J. G. T. & Hoppe, G. Experiments on drag-reducing surface and their optimization with an adjustable geometry. *Journal of Fluid Mechanics* **338,** 59–87 (1997).

11. Bechert, D. W., Bruse, M. & Hage, W. Experiments with three-dimensional riblets as an idealized model of shark skin. *Experiments in Fluids* **28,** 403–412 (2000).

12. Benschop, H. O. G. & Breugem, W. P. Drag reduction by herringbone riblet texture in direct numerical simulations of turbulent channel flow. *Journal of Turbulence* **18,** 717–759 (2017).

13. Best, J. The fluid dynamics of river dunes: A review and some future research. *Journal of Geophysical Research* **226,** 257–289 (2005).

14. Bhaganagar, K. & Hsu, T. Direct numerical simulations of flow over two-dimensional and three-dimensional ripples and implication to sediment transport: Steady flow. *Coastal Engineering* **56,** 320–331 (2009).

15. Blondeaux, P. Sand ripples under sea waves Part 1. Ripple formation. *Journal of Fluid Mechanics* **218,** 1–17 (1990).

16. Blondeaux, P., Foti, E. & Vittori, G. A theoretical model of asymmetric wave ripples. *Philosophical Transactions. Series A, Mathematical, Physical, and Engineering Sciences* **373,** 20140112 (2015).

17. Boomsma, A. & Sotiropoulos, F. Riblet drag reduction in mild adverse pressure gradients: A numerical investigation. *International Journal of Heat and Fluid Flow* **56,** 251–260 (2015).

18. Boomsma, A. & Sotiropoulus, F. Direct numerical simulation of sharkskin denticles in turbulent channel flow. *Phyiscs of Fluids* **28,** 035106 (2016).

19. Bose, S. T. & Park, G. I. Wall-modeled large-eddy simulation for complex turbulent flows. *Annual Review of Fluid Mechanics* **50,** 535–561 (2018).

20. Bradshaw, P. & Huang, G. P. The law of the wall in turbulent flow. *Proceedings: Mathematical and Physical Sciences* **451,** 165–188 (1995).

21. Breuer, M., Peller, N., Rapp, C. & Manhart, M. Flow over periodic hills - Numerical and experimental study in a wide range of Reynolds numbers. *Computers & Fluids* **38,** 433–457 (2009).

22. Canton, J. *et al.* On large-scale friction control in turbulent wall flow in low Reynolds number channels. *Flow Turbulence Combustion* **97,** 881–827 (2016).

23. Cao, Y. & Tamura, T. Large-eddy simulations of flow past a square cylinder using structured and unstructured grids. *Computers & Fluids* **80,** 36–54 (2016).

24. Charru, F. & Hinch, E. J. Ripple formation on a particle bed sheared by a viscous liquid. Part 1. Steady flow. *Journal of Fluid Mechanics* **550,** 111–121 (2006).

25. Charru, F., Andreotti, B. & Claudin, P. Sand ripples and dunes. *Annual Review of Fluid Mechanics* **45,** 469–493 (2013).

26. Chauhan, K. A., Monkewitz, P. A. & Nagib, H. M. Criteria for assessing experiments in zero pressure gradient boundary layers. *Fluid Dynamics Research* **41,** 021404 (2009).

27. Chen, H., Gao, Y., Stone, H. A. & Jiang, L. "Fluid bearing" effect of enclosed liquids in grooves on drag reduction in microchannels. *Physical Review Fluids* **1,** 083904 (2016).

28. Choi, H., Moin, P. & Kim, J. On the effects of riblets in fully developed laminar channel flows. *Physics of Fluids A: Fluid Dynamics* **3,** 1892–1896 (1991).

29. Choi H. Moin, P. & Kim, J. Direct numerical simulation of turbulent flow over riblet. *Journal of Fluid Mechanics* **250,** 1–42 (1993).

30. Chu, D. C. & Karniadakis, G. E. A direct numerical simulation of laminar and turbulent flow over riblet-mounted surfaces. *Journal of Fluid Mechanics* **250,** 1–42 (1993).

31. Clauser, F. Turbulent boundary layers in adverse pressure gradients. *Advances in Applied Mechanics* **4** (1956).

32. Coleman, S. E. & Eling, B. Sand wavelets in laminar open-channel flows. *Journal of Hydraulic Research* **38,** 331–338 (2000).

33. Coles, D. The law of the wake in the turbulent boundary layer. *Journal of Fluid Mechanics* **1,** 191–226 (1956).

34. Colombini, M. & Stocchino, A. Ripple and dune formation in rivers. *Journal of Fluid Mechanics* **673,** 121–131 (2011).

35. Davies, J., Maynes, D., Webb, B. W. & Woolford, B. Laminar flow in a microchannel using superhydrophobic walls exhibiting transverse ribs. *Physics of Fluids* **18,** 087110 (2006).

36. Devauchelle, O. *et al.* Rhomboid beach pattern: A laboratory investigation. *Journal of Geophysical Research: Earth Surface* **115,** F02017 (2010).

37. Devauchelle, O. *et al.* Stability of bedforms in laminar flows with free surface: from bars to ripples. *Journal of Fluid Mechanics* **642,** 329348 (2010).

38. Djenidi, L., Anselmet, F., Liandrat, J. & Fulachier, L. Laminar boundary layer over riblets. *Physics of Fluids* **6,** 2993–2999 (1994).

39. Du, Y., Symeonidis, V. & Karniadakis, G. E. Drag reduction in wall-bounded turbulence via a transverse travelling wave. *Journal of Fluid Mechanics* **457,** 1–34 (2002).

40. Durcos, F., Comte, P. & Lesieur, M. Large-eddy simulation of transition to turbulence in a boundary layer developing spatially over a flat plate. *Journal of Fluid Mechanics* **326,** 1–36 (1996).

41. Edelin, D., Josse, C., Castelain, C. & Fayolle, F. Experimental study of bedforms obtained with floating particles in a pipe flow. *Journal of Fluid Mechanics* **765,** 252–272 (2015).

42. Eitel-Amor, G., Örlü, R. & Schlatter, P. Simulation and validation of a spatially evolving turbulent boundary layer up to Re = 8300. *International Journal of Heat and Fluid Flow* **47,** 57–69 (2014).

43. El-Sammi, H., H., C. & Yoon, H. S. Drag reduction of turbulent flow over thin rectangular riblets. *International Journal of Engineering Science* **45,** 436–454 (2007).

44. Erm, L. P. & Joubert, P. N. Low-Reynolds-number turbulent boundary layers. *Journal of Fluid Mechanics* **230,** 144 (1991).

45. Floryan, J. M. Two-dimensional instability of flow in a rough channel. *Physics of Fluids* **17,** 044101 (2005).

46. Fredsoe, J., Andersen, K. H. & Sumer, B. M. Waves plus current over a ripple-covered bed. *Coastal Engineering* **38,** 117–21 (1999).

47. Garcia-Mayoral, R. & Jimenez, J. Drag reduction by riblets. *Philosophical Transaction Royal Society* **369,** 1412–1427 (2011).

48. Garcia-Mayoral, R. & Jimenez, J. Hydrodynamic stability and breakdown of the viscous regime over riblets. *Journal of Fluid Mechanics* **678,** 317–334 (2011).

49. Germano, M., Piomelli, U., Moin, P. & Cabot, W. H. A dynamic subgridscale eddy viscosity model. *Physics of Fluids A: Fluid Dynamics* **3,** 1760–1765 (1991).

50. Ghebali, S., Chernyshenko, S. I. & Leschziner, M. A. Can large-scale oblique undulations on a solid wall reduce the turbulence drag? *Physics of Fluids* **29,** 105102 (2017).

51. Goldstein, D. B. & Tuan, T. C. Secondary flow induced by riblets. *Journal of Fluid Mechanics* **363,** 115–151 (1998).

52. Greenshields, C. J. *OpenFOAM - The open source CFD toolbox: User's guide* Version 4.0.1 (2016).

53. Grigoriadis, D. G. E., Balaras, E. & Dimas, A. A. Large-eddy simulations of unidirectional water flow over dunes. *Journal of Geophysical Research* **114,** F02022 (2009).

54. Haddadi, B., Jordan, C. & Harasek, M. Cost efficient CFD simulations: Proper selection of domain partitioning strategies. *Computer Physics Communications* **219,** 121–134 (2017).

55. Henn, D. S. & Sykes, R. I. Large-eddy simulation of flow over wavy surfaces. *Journal of Fluid Mechanics* **383,** 751–779 (1999).

56. Howarth, L. On the solution of the laminar boundary layer equations. *Proceedings Royal Society London A* **164,** 547–579 (1938).

57. Hrvoje, J. *Error analysis and estimation for the finite volume method with application to fluid flows* PhD thesis (Imperial College of Science, Technology and Medicine, London, 1996).

58. Inoue, M. A. & Pullin, D. I. Large-eddy simulation of the zero-pressure-gradient turbulent boundary layer up to $Re = O(10^12)$. *Journal of Fluid Mechanics* **686,** 507–533 (2011).

59. Karniadakis, G. E. & Choi, K. S. Mechanisms on Transverse Motions in Turbulent Wall Flows. *Annual Reviews Fluids Mechanics* **35,** 45–62 (2003).

60. Khosronejad, A. & Sotiropoulos, F. Numerical simulation of sand waves in a turbulent open channel flow. *Journal of Fluid Mechanics* **753,** 150–216 (2015).

61. Kidanemariam, A. G. & Uhlmann, M. Formation of sediment patterns in channel flow minimal unstable systems and their temporal evolution. *Journal of Fluid Mechanics* **818,** 716–743 (2017).

62. Krieger, V., Peric, R., Jovanovic, J., Lienhart, H. & Delgado, A. Toward design of the antiturbulence surface exhibiting maximum drag reduction effect. *Journal of Fluid Mechanics* **850,** 262–303 (2018).

63. Langlois, V. & Valance, A. Three-dimensionality of sand ripples under steady laminar shear flow. *Journal of Geophysical Research* **110,** F04S09 (2005).

64. Lee, C., Choi, C. H. & Kim, C. J. Superhydrophobic drag reduction in laminar flows: A critical review. *Experiments in Fluids* **57,** 176 (2016).

65. Lee, J. H. & Sung, H. J. Direct numerical simulation of a turbulent boundary layer up to Re=2500. *International Journal of Heat and Fluid Flow* **32,** 1–10 (2011).

66. Lee, J. H., Seena, A., Lee, S.-h. & Sung, H. J. Turbulent boundary layers over rod- and cube-roughened walls. *Journal of Turbulence* **13,** N40 (2012).

67. Lee, S. J. & Lee, S. H. Flow field analysis of a turbulent boundary layer over a riblet surface. *Experiments in Fluids* **30,** 153–166 (2001).

68. Lefebvre, A., Paarlberg, A. J. & Winter, C. Characterising natural bedform morphology and its influence on flow. *Geo-Marine Letters* **36,** 379–393 (2016).

69. Lienhart, H., Breuer, M. & Koksoy, C. Drag reduction by dimples? - A complementary experimental/numerical investigation. *International Journal of Heat and Fluid Flow* **29,** 783–791 (2008).

70. Lilly, D. K. A proposed modification of the Germano subgrid-scale closure method. *Physics of Fluids A: Fluid Dynamics* **4,** 633–635 (1992).

71. Luchini, P., Manzo, F. & Pozzi, A. Resistance of groove surface to parallel flow and cross flow. *Journal of Fluid Mechanics* **228,** 87–109 (1991).

72. Lund, T. S., Wu, X. & Squires, K. D. Generation of turbulent inflow data for spatially-developing boundary layer simulations. *Journal of Computational Physics* **140,** 233 –258 (1998).

73. Lysenko, D. A., Ertesvag, I. S. & Rian, K. E. Modeling of turbulent separated flows using OpenFOAM. *Computers & Fluids* **80,** 408–422 (2013).

74. Mare, L., Klein, M., Jones, W. P. & Janicka, J. Synthetic turbulence inflow conditions for large-eddy simulation. *Physics of Fluids* **18,** 025107 (2006).

75. Martin, S. & Bhushan, B. Flow field analysis of a shark-inspired microstructure. *Journal of Fluid Mechanics* **756,** 5–29 (2014).

76. Martin, S. & Bhushan, B. Fluid flow analysis of continuous and segmented riblet structures. *RSC Advances* **6,** 10962–10978 (2016).

77. Marusic, I., Chauhan, K. A., Kulandaivelu, V. & Hutchins, N. Evolution of zero-pressure-gradient boundary layers from different tripping conditions. *Journal of Fluid Mechanics* **783,** 379411 (2015).

78. Matai, R. & Durbin, P. Large-eddy simulation of turbulent flow over a parametric set of bumps. *Journal of Fluid Mechanics* **866,** 503–525 (2019).

79. Maynes, D., Jeffs, K., Woolford, B. & Webb, B. W. Laminar flow in a microchannel with hydrophobic surface patterned microribs oriented parallel to the flow direction. *Physics of Fluids* **19,** 093603 (2007).

80. Meneveau, C. & Katz, J. Scale-invariance and turbulence models for large-eddy simulation. *Annual Review of Fluid Mechanics* **32,** 1–32 (2000).

81. Mohammadi, A. & Floryan, J. M. Groove optimization for drag reduction. *Physics of Fluids* **25,** 113601 (2013).

82. Mohammadi, A. & Floryan, J. M. Mechanism of drag generation by surface corrugation. *Physics of Fluids* **24,** 013602 (2012).

83. Mohammadi, A. & Floryan, J. M. Numerical analysis of laminar-drag-reducing grooves. *Journal of Fluids Engineering - Transactions of the ASME* **137,** 041201 (2015).

84. Mohammadi, A. & Floryan, J. M. Pressure losses in grooved channels. *Journal of Fluid Mechanics* **725,** 23–54 (2013).

85. Moradi, H. V., Budiman, A. C. & Floryan, J. M. Use of natural instabilities for generation of streamwise vorticies in a laminar channel flow. *Theoretical computational Fluid Dynamics* **31,** 233–250 (2017).

86. Moser, R. D., Kim, J. & Mansour, N. N. Direct numerical simulation of turbulent channel flow up to Re=590. *Physics of Fluids* **11,** 943–945 (1999).

87. Mukha, T. & Liefvendahl, M. The generation of turbulent inflow boundary conditions using precursor channel flow simulations. *Computers & Fluids* **156,** 21–33 (2017).

88. Mukha, T., Rezaeiravesh, S. & Liefvendahl, M. A library for wall-modelled large-eddy simulation based on OpenFOAM technology. *Computer Physics Communications* (2019).

89. Nadeem, M., Lee, J. H., Lee, J. & Sung, H. J. Turbulent boundary layers over sparsely-spaced rod-roughened walls. *International Journal of Heat and Fluid Flow* **56,** 16 –27 (2015).

90. Nesselrooij, M. V., Veldhuis, L. L. M., Oudheusden, B. W. & Schrijer, F. F. J. Drag reduction by means of dimpled surfaces in turbulent boundary layers. *Experiments in Fluids* **57,** 142 (2016).

91. Niavarani, A. & Priezjev, N. V. The effective slip length and vortex formation in laminar flow over a rough surface. *Physics of Fluids* **21,** 052105 (2009).

92. Nicoud, F. & Ducros, F. Subgrid-scale stress modelling based on the square of the velocity gradient tensor. *Flow, Turbulence and Combustion* **62,** 183–200 (1999).

93. Noriega, H., Guibault, F., Reggio, M. & Magnan, R. A case-study in open-source CFD code verification, Part 1: Convergence rate loss diagnosis. *Mathematics and Computers in Simulations* **147,** 152–171 (2018).

94. Noriega, H., Guibault, F., Reggio, M. & Magnan, R. A case-study in open-source CFD code verification, Part 2: Boundary condition non-orthogonal correction. *Mathematics and Computers in Simulations* **147,** 172–193 (2018).

95. Omidyeganeh, M. & Piomelli, U. Large-eddy simulation of three-dimensional dunes in a steady, unidirectional flow. Part 1. Turbulence statistics. *Journal of Fluid Mechanics* **721,** 454–483 (2013).

96. Omidyeganeh, M. & Piomelli, U. Large-eddy simulation of three-dimensional dunes in a steady, unidirectional flow. Part 2. Flow structures. *Journal of Fluid Mechanics* **734,** 509–534 (2013).

97. Omidyeganeh, M. & Piomelli, U. Large-eddy simulation of two-dimensional dune in a steady, unidirectional flow. *Journal of Turbulence* **12,** 1–31 (2011).

98. Orszag, S. A. & Kells, L. C. Transition to turbulence in plane Poiseuille and plane Couette flow. *Journal of Fluid Mechanics* **96,** 159–205 (1980).

99. Orszag, S. A. & Patera, A. T. Secondary instability of wall-bounded shear flows. *Journal of Fluid Mechanics* **128,** 347–385 (1983).

100. Osorio-Nesme, A. & Delgado, A. Flow characterization in periodic microchannels containing asymmetric grooves. *Fluid Dynamics Research* **49,** 055502 (2017).

101. Ou, J., Perot, B. & Rothstein, J. P. Laminar drag reduction in microchannels using ultrahydrophobic surfaces. *Physics of Fluids* **16,** 4635–4643 (2004).

102. Peric, M., Kessler, R. & Scheuerer, G. Comparison of finite-volume numerical methods with staggered and colocated grids. *Computers & Fluids* **16,** 389–403 (1988).

103. Quadrio, M. & Ricco, P. Critical assessment of turbulent drag reduction through spanwise wall oscillations. *Journal of Fluid Mechanics* **521,** 251–271 (2004).

104. Raayai-Ardakani, S. & McKinley, G. H. Drag reduction using wrinkled surfaces in high Reynolds number laminar boundary layer flows. *Physics of Fluids* **29,** 093605 (2017).

105. Rauen, W. B., Lin, B. & Falconer, R. A. Transition from wavelets to ripples in a laboratory flume with a diverging channel. *International Journal of Sediment Research* **23,** 1–12 (2008).

106. Rezaeiravesh, S. & Liefvendahl, M. Effect of grid resolution on large eddy simulation of wall-bounded turbulence. *Physics of Fluids* **30,** 055106 (2018).

107. Rhie, C. M. & Chow, W. L. Numerical study of the turbulent flow past an airfoil with trailing edge separation. *AIAA Journal* **21,** 1525–1532 (1983).

108. Robertson, E., Choudhury, V., Bhushan, S. & Walters, D. K. Validation of Open-FOAM numerical methods and turbulence models for incompressible bluff body flows. *Computers & Fluids* **123,** 122–145 (2015).

109. Roos, P. C. & Blondeaux, P. Sand ripples under sea waves. Part 4. Tile ripple formation. *Journal of Fluid Mechanics* **447,** 227–246 (2001).

110. Rothstein, J. P. Slip on superhydrophobic surfaces. *Annual Review of Fluid Mechanics* **42,** 89–109 (2010).

111. Saha, S., Klewicki, J. C., Ooi, A. & Blackburn, H. M. On scaling pipe flows with sinusoidal transversely corrugated walls: Analysis of data from the laminar to the low-Reynolds-number turbulent regime. *Journal of Fluid Mechanics* **779,** 245–274 (2015).

112. Sakib, N., Mohammadi, A. & Floryan, J. M. Spectrally-accurate immersed boundary conditions method for three-dimensional flows. *Computers and Mathematics with Applications* **73,** 2426–2453 (2017).

113. Sayadi, T. & Moin, P. Large eddy simulation of controlled transition to turbulence. *Physics of Fluids* **24,** 114103 (2012).

114. Schlatter, P. & Orlu, O. Assessment of direct numerical simulation data of turbulent boundary layers. *Journal of Fluid Mechanics* **659,** 116–126 (2010).

115. Schlatter, P. *et al.* Turbulent boundary layers up to Re=2500 studied through simulation and experiment. *Physics of Fluids* **21,** 051702 (2009).

116. Schlatter, P. & Orlu, R. Turbulent boundary layers at moderate Reynolds numbers: Inflow length and tripping effects. *Journal of Fluid Mechanics* **710,** 5–34 (2012).

117. Schlatter, P., Li, Q., Brethouwer, G., Johansson, A. V. & Henningson, D. S. Simulations of spatially evolving turbulent boundary layers up to Re=4300. *International Journal of Heat and Fluid Flow* **31,** 251–261 (2010).

118. Schlichting, H. *Boundary layer theory* 7th ed. (Springer, 1978).

119. Smagorinsky, J. General circulation experiments with the primitive equations. *Monthly Weather Review* **91,** 99–164 (1963).

120. Stroh, A., Hasegawa, Y., Schlatter, P. & Frohnapfel, B. Global effect of local skin friction drag reduction in spatially developing turbulent boundary layer. *Journal of Fluid Mechanics* **805,** 303–321 (2016).

121. Tay, C. M. J., Chew, Y. T., Khoo, B. C. & Zhao, J. B. Development of flow structures over dimples. *Experimental Thermal and Fluid Science* **52,** 278–287 (2014).

122. Tay, C. M. J., Khoo, B. C. & Chew, Y. T. Mechanics of drag reduction by shallow dimples in channel flow. *Physics of Fluids* **27,** 035109 (2015).

123. Tay, C. M. J., Khoo, B. C. & Chew, Y. T. Use of DES in mildly separated internal flow: Dimples in a turbulent channel. *Journal of Turbulence* **18,** 1180–1203 (2017).

124. Tay, J. & Lim, T. T. in *35th AIAA Applied Aerodynamics Conference* (2017). doi:10.2514/6.2017-3569. eprint: `https://arc.aiaa.org/doi/pdf/10.2514/6.2017-3569`. `https://arc.aiaa.org/doi/abs/10.2514/6.2017-3569`.

125. Teo, C. J. & Khoo, B. C. Flow past superhydrophobic surfaces containing longitudional grooves: Effects of interface curvature. *Microfluidics and Nanofluidics* **9,** 499–511 (2010).

126. Venditti, J. G. Turbulent flow and drag over fixed two- and three-dimensional dunes. *Journal of Geophysical Research* **112,** F04008 (2007).

127. Vittori, G. & Blondeaux, P. Sand ripples under sea waves Part 2. Finite-amplitude development. *Journal of Fluid Mechanics* **218,** 19–39 (1990).

128. Vittori, G. & Blondeaux, P. Sand ripples under sea waves Part 3. Brick-pattern ripple formation. *Journal of Fluid Mechanics* **239,** 23–45 (1992).

129. Walsh, M. J. Riblets as a viscous drag reduction technique. *AIAA Journal* **21,** 485–486 (1983).

130. Weller, H. G., Tabor, G., Jasak, H. & Fureby, C. A tensorial approach to computational continuum mechanics using object-oriented techniques. *Computers in Physics* **12,** 620–631 (1998).

131. Wharton, J. T. *Structural functional surface design and manufacture* PhD thesis (2017).

132. Wu, X. Inflow turbulence generation methods. *Annual Review of Fluid Mechanics* **49,** 23–49 (2017).

133. Wu, X. & Moin, P. Direct numerical simulation of turbulence in a nominally zero-pressure-gradient flat-plate boundary layer. *Journal of Fluid Mechanics* **630,** 5–41 (2009).

134. Xu, F., Zhong, S. & Zhang, S. Vortical structures and development of laminar flow over convergent-divergent riblets. *Physics of Fluids* **30,** 051901 (2018).

135. Xu, M., Lu, H., Gong, L., Chai, J. C. & Duan, X. Parametric numerical study of the flow and heat trasnfer in microchannel with dimples. *International Communications in Heat and Mass Transfer* **76,** 348–357 (2016).

Post-Processing Scripts

A.1 Boundary Layer Profile Extraction

surfaceTransformPoints -translate "(0.07 0 0)" setDicts/planeZero.stl setDicts/planeOne.stl
surfaceTransformPoints -translate "(0.16 0 0)" setDicts/planeZero.stl setDicts/planeTwo.stl
surfaceTransformPoints -translate "(0.25 0 0)" setDicts/planeZero.stl setDicts/planeThree.stl
topoSet

    cd timeFiles
declare -a files=(*)
cd ..
declare -i Length=6

    for i in $(seq 0 $Length) do

        filename="$files[$i]"
        cp -r timeFiles/$filename ./
        subsetMesh selectedCellsOne -resultTime 1

```
        subsetMesh selectedCellsTwo -resultTime 2
        subsetMesh selectedCellsThree -resultTime 3
        postChannel -time 1
        postChannel -time 2
        postChannel -time 3
        cd graphs
        cd 1
        declare -a profiles=( * )
        cd ..
        for j in $(seq 1 3)
        do

                cd $j
                for k in $(seq 0 7)
                do

                        pname="$profiles[$k]"
                        csvtool trim l $pname ¿¿ $pname

                done cd ..

        done

        mv 1 x-0.07
        mv 2 x-0.16
        mv 3 x-0.25
        cd ..

        mv graphs resultsPlots/$filename rm -r $filename

    done
```

A.2   Profile Collapsing

```
#!/bin/bash
rm streamwiseProperties
filename_1='x-0.01'
filename_2='x-0.04'
filename_3='x-0.07'
filename_4='x-0.10'
filename_5='x-0.13'
filename_6='x-0.16'
filename_7='x-0.19'
```

```
filename_8='x-0.22'
filename_9='x-0.25'


    declare -a files=($filename_1 $filename_2 $filename_3 $filename_4 $filename_5 $filename_6 $filename_7 $filename_8 $filename_9)


declare -i Length

declare -i i

    declare -i j

    echo "Location BoundaryLayerThickness DiscplaementThickness MomentumThickness ShapeFactor DisplacementReynoldsNumber MomentumReynoldsNumber FrictionReynoldsNumber FrictionVelocity SkinFrictionCoefficient Iww U99 P99" >> streamwiseProperties

    for j in $(seq 0 8);

    do

            time="${files[$j]}"
            filename=$time/Uf.xy
            U1=0
            U2=0
            Iw=0
            Dy=0
            y99=0


            Length=$(csvtool -t SPACE height $filename)
            u0=($(csvtool -t SPACE sub 1 2 $Length 1 $filename))
            y=($(csvtool -t SPACE sub 1 1 $Length 1 $filename))
            infty=$(csvtool -t SPACE sub $Length 2 1 1 $filename)
            infty99=`echo "0.99*$infty" — bc -l`
            length=`echo "$Length-1" — bc -l`
            p99=$(csvtool -t SPACE sub $Length 2 1 1 $time/pMean.xy)
            echo $Length
            TauOne=$(csvtool -t SPACE sub 1 1 1 1 $filename)
            TauTwo=$(csvtool -t SPACE sub 1 2 1 1 $filename)
            TauOne=`echo "$TauOne" — sed -e 's/[eE]+*/\\*10\\^/' — bc -l`
            's/[eE]+*/\\*10\\^/'`
            ut=`echo "sqrt(0.00001568*$TauTwo/$TauOne)" — bc -l`


            echo $ut

            Tau=`echo "$ut^2"— bc -l`

            cf=`echo "$Tau/(0.5*($infty^2))" — bc -l`
```

```
for i in $(seq 0 $length );

    do

    u=`echo "${u0[$i]}" — sed -e 's/[eE]+*/\\*10\\^/' — bc -l`


    if (( $(bc <<< "$u < $infty99") ))


    then


        y99=`echo "${y[$i]}" — sed -e 's/[eE]+*/\\*10\\^/' — bc -l`
    fi


    y2=`echo "${y[$i]}" — sed -e 's/[eE]+*/\\*10\\^/' — bc -l`
    if [ $i -eq 0 ]; then y3=`echo "${y[$i+1]}" — sed -e 's/[eE]+*/\\*10\\^/'
    — bc -l`
    Dy=`echo "$y2*2" — bc -l`
    elif [ $i -eq $length ];
    then
    y1=`echo "${y[$i-1]}" — sed -e 's/[eE]+*/\\*10\\^/' — bc -l`
    Dy=`echo "(0.01-$y2)*2" — bc -l`
    else
    y1=`echo "${y[$i-1]}" — sed -e 's/[eE]+*/\\*10\\^/' — bc -l`
    y3=`echo "${y[$i+1]}" — sed -e 's/[eE]+*/\\*10\\^/' — bc -l`
    cell=`echo "($y3-$y2)/($y2-$y1)" — bc -l`
    Dy=`echo "($y3-$y1)/2" — bc -l`
    fi


    u1=`echo "(1/$infty)*($infty-$u)*$Dy" — bc -l`
    U1=`echo "$U1+$u1" — bc -l`
    u2=`echo "(1/($infty^2))*$u*($infty-$u)*$Dy" — bc -l`
    U2=`echo "$U2+$u2" — bc -l`
    iw=`echo "((($infty/$ut)-($u/$ut))^2)*$Dy" — bc -l`
    Iw=`echo "$Iw+$iw" — bc -l`


done

H=`echo "$U1/$U2" — bc -l`
Re1=`echo "$U1*$infty/0.00001568" — bc -l`
Re2=`echo "$U2*$infty/0.00001568" — bc -l`
Re3=`echo "$y99*$ut/0.00001568" — bc -l`
Iww=`echo "$Iw/($U1*$infty/$ut)" — bc -l`
echo $H
echo "$time $y99 $U1 $U2 $H $Re1 $Re2 $Re3 $ut $cf $Iww $infty $p99"
>> streamwiseProperties

done
```

Turbulent Boundary Layer: Smooth Wall Profiles

(a) $x = 0.07m$
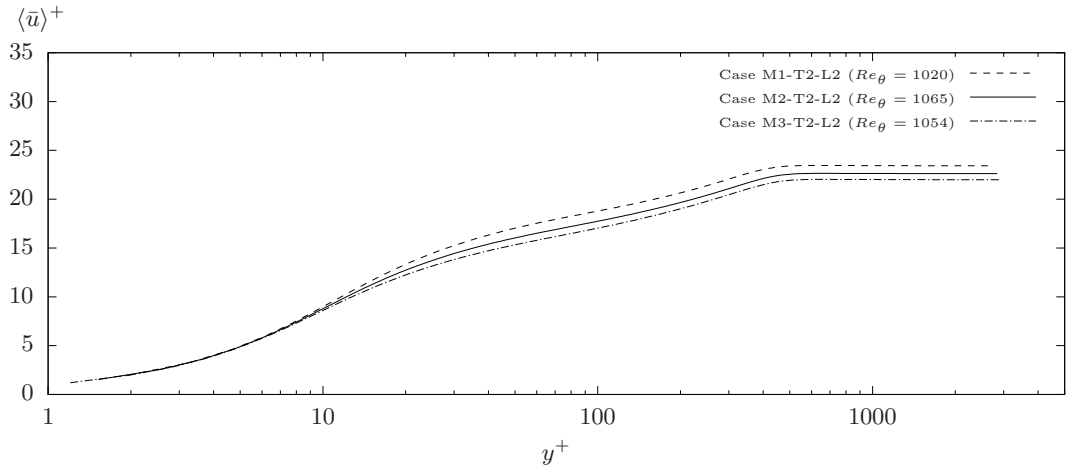
(b) $x = 0.16m$
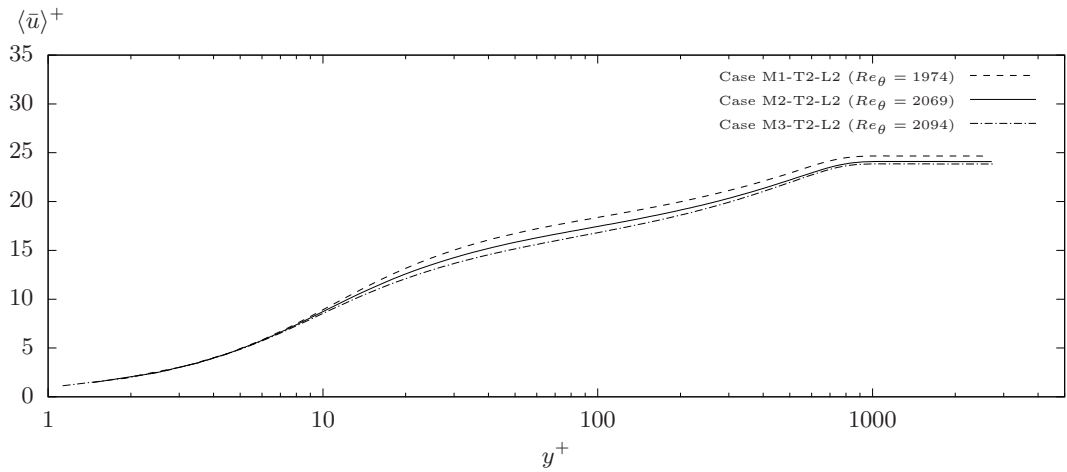
(c) $x = 0.25m$
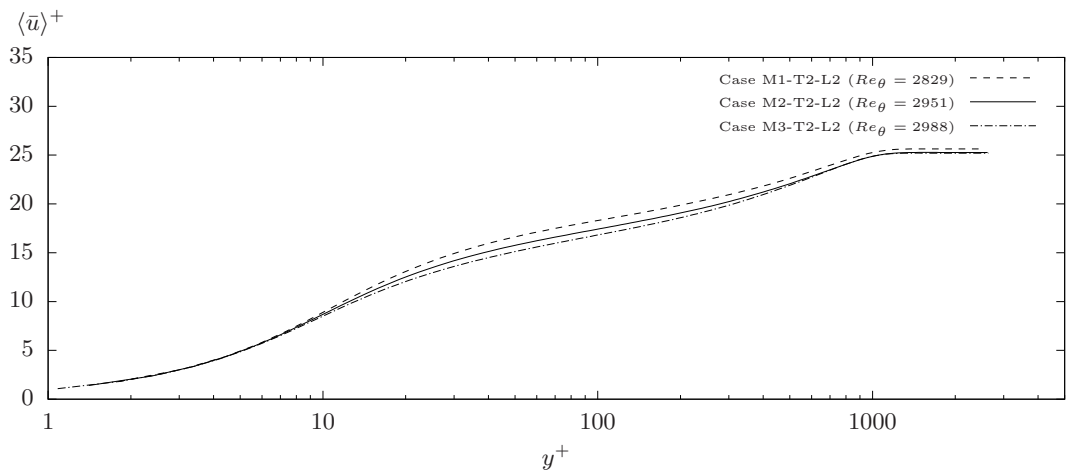
Figure B.1: *Distribution of inner-scaled, time-averaged streamwise velocity over a smooth wall, for varying levels of spatial resolution.*

(a) $x = 0.07m$
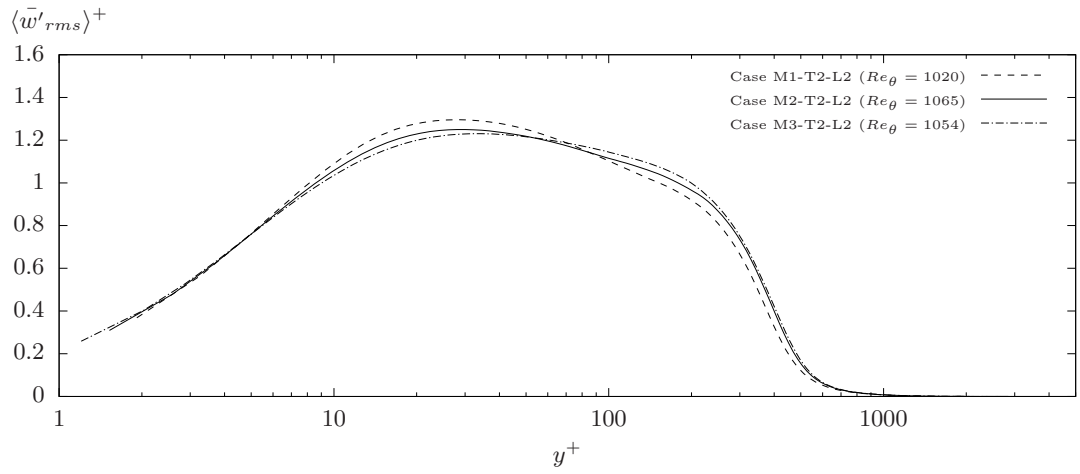
(b) $x = 0.16m$
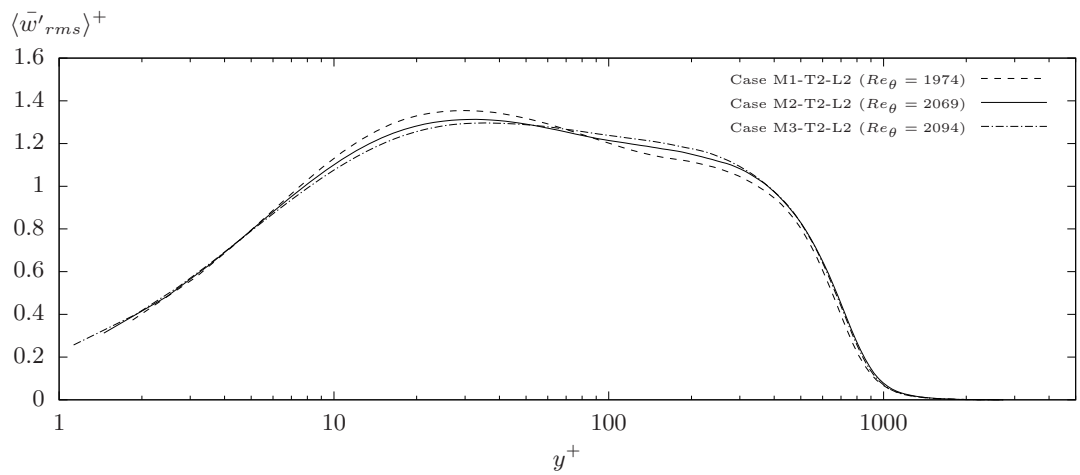
(c) $x = 0.25m$
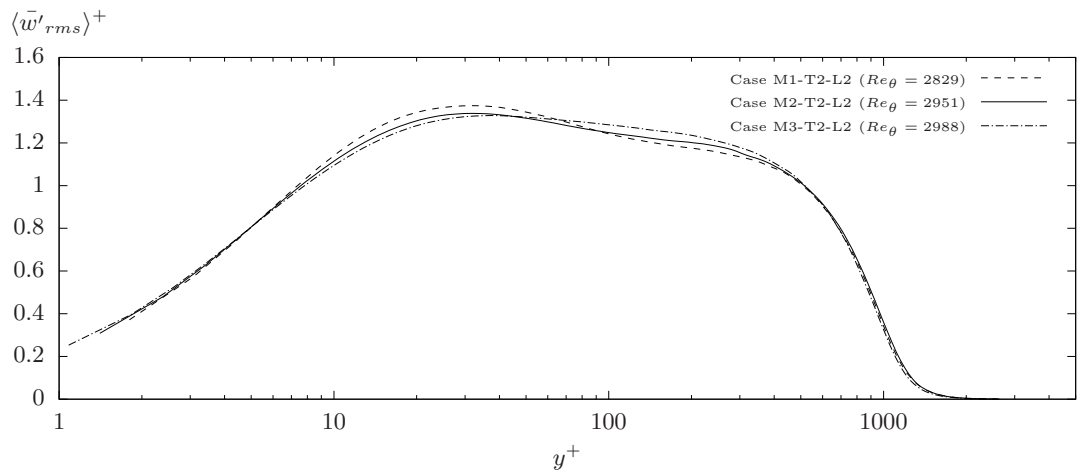
Figure B.2: *Comparison of the RMS of spanwise velocity fluctuations over a smooth wall, for varying levels of spatial resolution.*

Laminar Flow: Drag Results

Table C.1: Flow resistance components for all parametric simulations containing the two-dimensional profile of RN1.

Case	φ	Re_h	$Re_h f_p$	$Re_h f_{v1}$	$Re_h f_{v2}$
RN1-KG1-KZ0-F1	0°	50.8	0.194	2.845	3.014
	180°	50.8	0.200	2.845	3.014
RN1-KG1-KZ0-F2	0°	101.6	0.236	2.811	3.017
	180°	101.6	0.236	2.805	3.017
RN1-KG1-KZ0-F3	0°	507.8	0.420	2.641	3.024
	180°	507.8	0.420	2.64	3.024
RN1-KG1-KZ0-F4	0°	1015.6	0.567	2.501	3.032
	180°	1015.6	0.561	2.513	3.031
RN1-KG2-KZ0-F1	0°	51.2	0.386	2.702	3.039
	180°	51.2	0.386	2.702	3.039
RN1-KG2-KZ0-F2	0°	102.3	0.454	2.646	3.046
	180°	102.3	0.46	2.64	3.045
RN1-KG2-KZ0-F3	0°	511.5	0.773	2.357	3.056
	180°	511.5	0.773	2.356	3.055
RN1-KG2-KZ0-F4	0°	1023	1.000	2.149	3.066
	180°	1023	0.987	2.154	3.067
RN1-KG3-KZ0-F1	0°	51.6	0.630	2.532	3.074
	180°	51.6	0.642	2.519	3.074
RN1-KG3-KZ0-F2	0°	103.2	0.738	2.440	3.081
	180°	103.2	0.744	2.427	3.077
RN1-KG3-KZ0-F3	0°	515.8	1.176	2.049	3.105
	180°	515.8	1.175	2.047	3.101
RN1-KG3-KZ0-F4	0°	1031.5	1.437	1.805	3.114
	180°	1031.5	1.436	1.804	3.113

Table C.2: Flow resistance components for all parametric simulations containing the two-dimensional profile of RN2.

Case	φ	Re_h	$Re_h f_p$	$Re_h f_{v1}$	$Re_h f_{v2}$
RN2-KG1-KZ0-F1	0°	50.8	0.231	2.816	3.017
	180°	50.8	0.237	2.81	3.017
RN2-KG1-KZ0-F2	0°	101.7	0.28	2.778	3.021
	180°	101.7	0.286	2.771	3.021
RN2-KG1-KZ0-F3	0°	508.4	0.507	2.572	3.024
	180°	508.4	0.507	2.571	3.030
RN2-KG1-KZ0-F4	0°	1016.9	0.674	2.414	3.039
	180°	1016.9	0.668	2.42	3.038
RN2-KG2-KZ0-F1	0°	51.2	0.45	2.662	3.050
	180°	51.2	0.462	2.649	3.050
RN2-KG2-KZ0-F2	0°	102.5	0.531	2.588	3.057
	180°	102.5	0.543	2.575	3.057
RN2-KG2-KZ0-F3	0°	512.5	0.891	2.261	3.072
	180°	512.5	0.903	2.254	3.069
RN2-KG2-KZ0-F4	0°	1024.9	1.133	2.046	3.079
	180°	1024.9	1.132	2.044	3.079
RN2-KG3-KZ0-F1	0°	51.7	0.723	2.478	3.091
	180°	51.7	0.748	2.453	3.094
RN2-KG3-KZ0-F2	0°	103.4	0.84	2.373	3.099
	180°	103.4	0.871	2.347	3.098
RN2-KG3-KZ0-F3	0°	517.1	1.296	1.967	3.122
	180°	517.1	1.314	1.946	3.119
RN2-KG3-KZ0-F4	0°	1034.1	1.547	1.739	3.132
	180°	1034.1	1.551	1.725	3.131

Table C.3: Flow resistance components for all parametric simulations containing the two-dimensional profile of RS.

Case	φ	Re_h	$Re_h f_p$	$Re_h f_{v1}$	$Re_h f_{v2}$
RS-KG1-KZ0-F1	0°	50.7	0.171	2.866	3.013
RS-KG1-KZ0-F2	0°	101.5	0.209	2.833	3.015
RS-KG1-KZ0-F3	0°	507.3	0.385	2.673	3.023
RS-KG1-KZ0-F4	0°	1014.6	0.52	2.549	3.028
RS-KG2-KZ0-F1	0°	51.1	0.338	2.748	3.037
RS-KG2-KZ0-F2	0°	102.2	0.406	2.688	3.041
RS-KG2-KZ0-F3	0°	510.8	0.702	2.42	3.054
RS-KG2-KZ0-F4	0°	1021.6	0.904	2.234	3.062
RS-KG3-KZ0-F1	0°	51.5	0.559	2.596	3.070
RS-KG3-KZ0-F2	0°	103	0.659	2.508	3.076
RS-KG3-KZ0-F3	0°	514.8	1.058	2.15	3.096
RS-KG3-KZ0-F4	0°	1029.6	1.293	1.935	3.106

Table C.4: Flow resistance components for all parametric simulations containing the two-dimensional profiles of RN1 and RS.

Case	φ	Re_h	$Re_h f_p$	$Re_h f_{v1}$	$Re_h f_{v2}$
RN1-KG1-KZ1-F1	0°	50.8	0.185	2.853	3.013
	180°	50.8	0.185	2.853	3.013
RN1-KG1-KZ1-F3	0°	507.8	0.380	2.705	3.033
	180°	507.8	0.375	2.710	3.033
RN1-KG1-KZ2-F1	0°	50.8	0.159	2.879	3.013
	180°	50.8	0.159	2.879	3.013
RN1-KG1-KZ2-F3	0°	507.8	0.29	2.824	3.043
	180°	507.8	0.286	2.83	3.043
RN1-KG3-KZ1-F1	0°	51.6	0.585	2.573	3.073
	180°	51.6	0.591	2.569	3.073
RN1-KG3-KZ1-F3	0°	515.8	1.150	2.380	3.212
	180°	515.8	1.206	2.520	3.279
RN1-KG3-KZ2-F1	0°	51.6	0.483	2.676	3.072
	180°	51.6	0.483	2.676	3.072
RN1-KG3-KZ2-F3	0°	515.8	1.024	2.978	3.373
	180°	515.8	1.052	3.182	3.452
RS-KG1-KZ1-F1	0°	50.7	0.162	2.874	3.013
RS-KG1-KZ1-F3	0°	507.3	0.348	2.731	3.031
RS-KG1-KZ2-F1	0°	50.7	0.140	2.896	3.013
RS-KG1-KZ2-F3	0°	507.3	0.269	2.838	3.040
RS-KG3-KZ1-F1	0°	51.5	0.518	2.634	3.069
RS-KG3-KZ1-F3	0°	514.8	1.037	2.466	3.201
RS-KG3-KZ2-F1	0°	51.5	0.432	2.720	3.068
RS-KG3-KZ2-F3	0°	514.8	0.913	2.992	3.339

APPENDIX D

Laminar Flow: Shear Stress

(a) *RN1, $k_z^* = 0$, $Re_h \approx 50$, $\varphi = 0°$*   **(b)** *RN2, $k_z^* = 0$, $Re_h \approx 50$, $\varphi = 0°$*

(c) *RN1, $k_z^* = 0$, $Re_h \approx 50$, $\varphi = 180°$*   **(d)** *RN2, $k_z^* = 0$, $Re_h \approx 50$, $\varphi = 180°$*
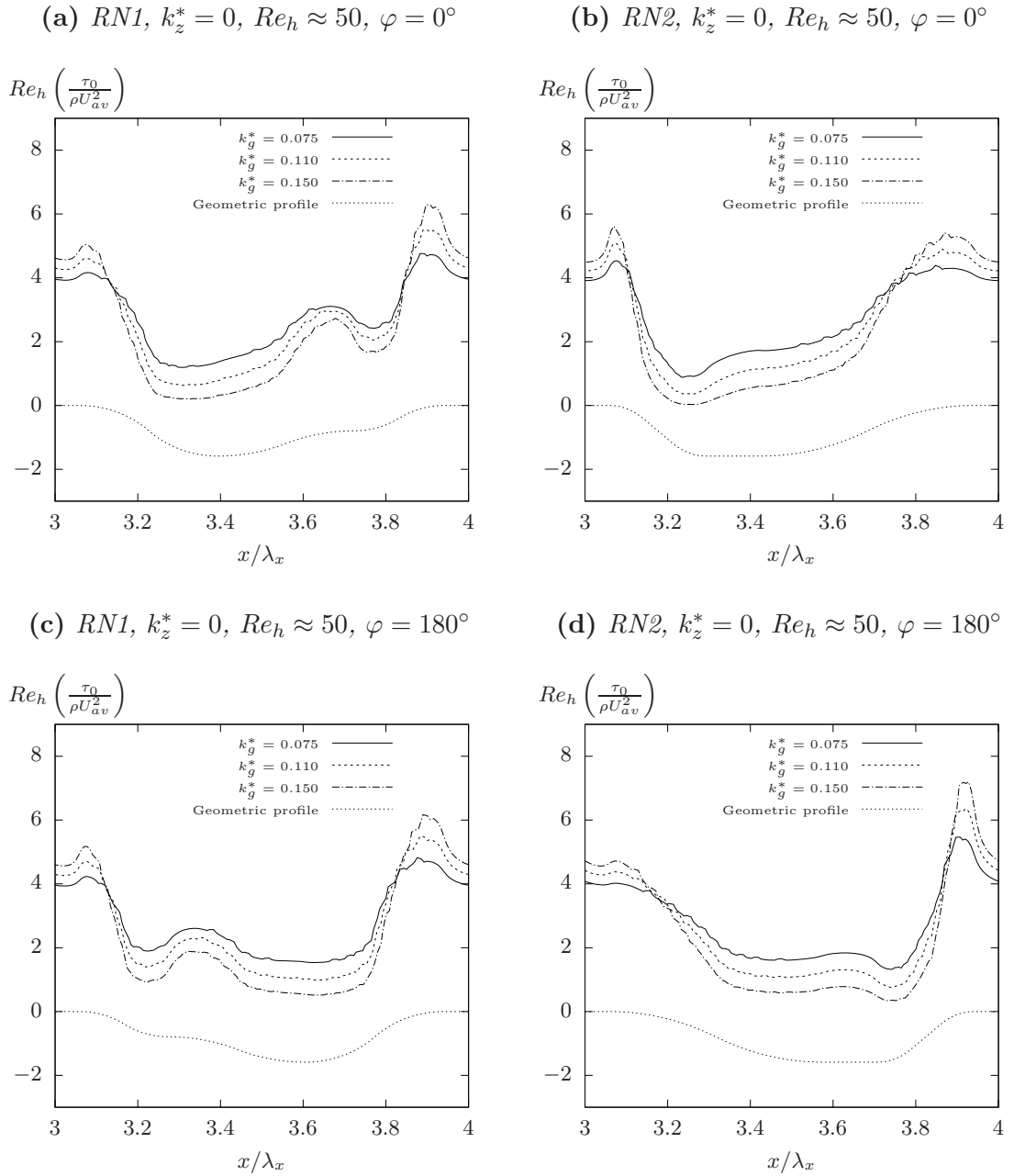
Figure D.1: *Distribution of the normalised streamwise shear stress over two-dimensional sand ripple profiles for a flow of $Re_h \approx 50$.*

(a) *RN1, $k_z^* = 0$, $Re_h \approx 100$, $\varphi = 0°$*

(b) *RN2, $k_z^* = 0$, $Re_h \approx 100$, $\varphi = 0°$*

(c) *RN1, $k_z^* = 0$, $Re_h \approx 100$, $\varphi = 180°$*

**(d)** *RN2, $k_z^* = 0$, $Re_h \approx 100$, $\varphi = 180°$*
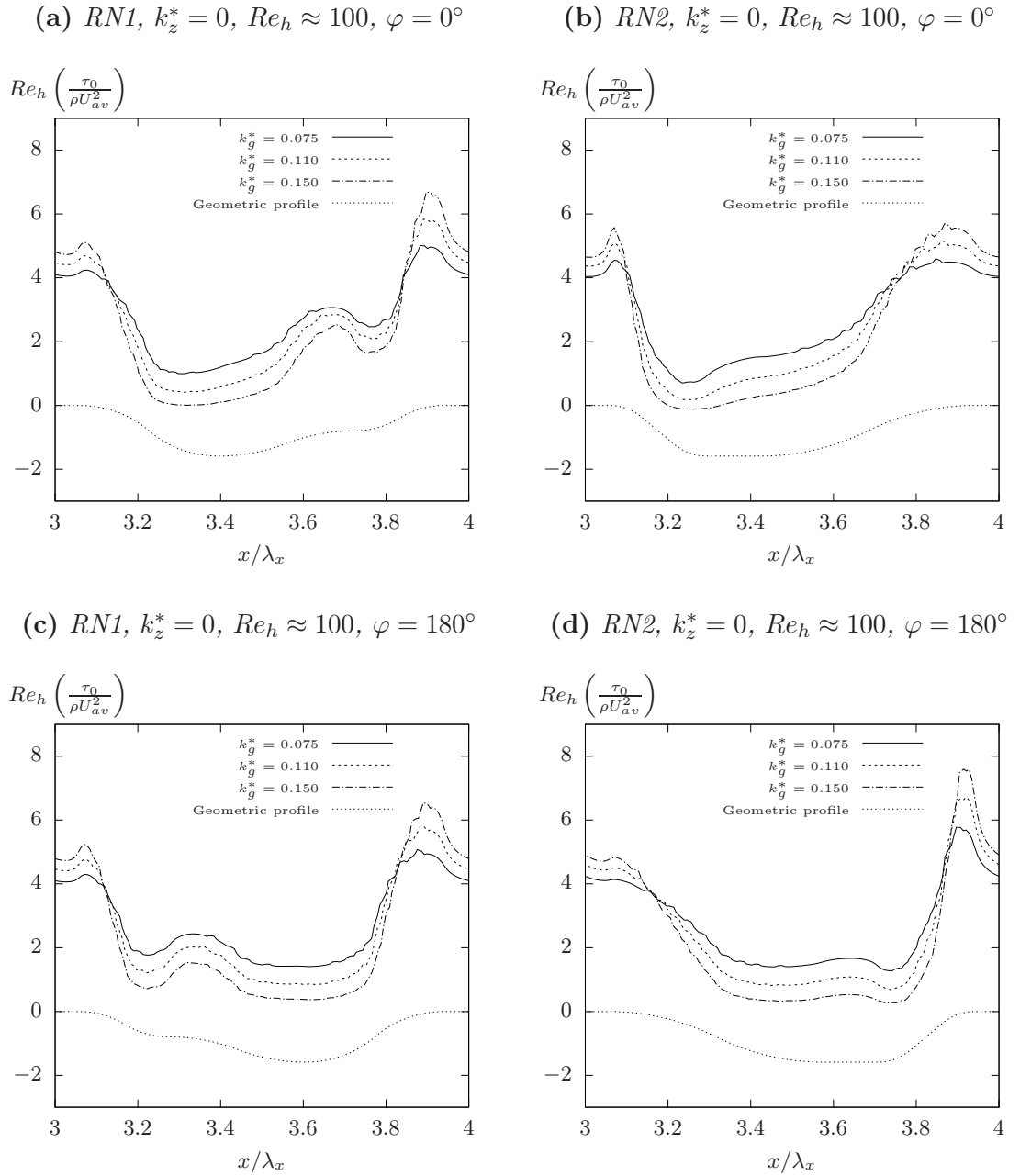
Figure D.2: *Distribution of the normalised streamwise shear stress over two-dimensional sand ripple profiles for a flow of $Re_h \approx 100$.*

(a) *RN1, $k_z^* = 0$, $Re_h \approx 500$, $\varphi = 0°$*

(b) *RN2, $k_z^* = 0$, $Re_h \approx 500$, $\varphi = 0°$*

(c) *RN1, $k_z^* = 0$, $Re_h \approx 500$, $\varphi = 180°$*

**(d)** *RN2, $k_z^* = 0$, $Re_h \approx 500$, $\varphi = 180°$*
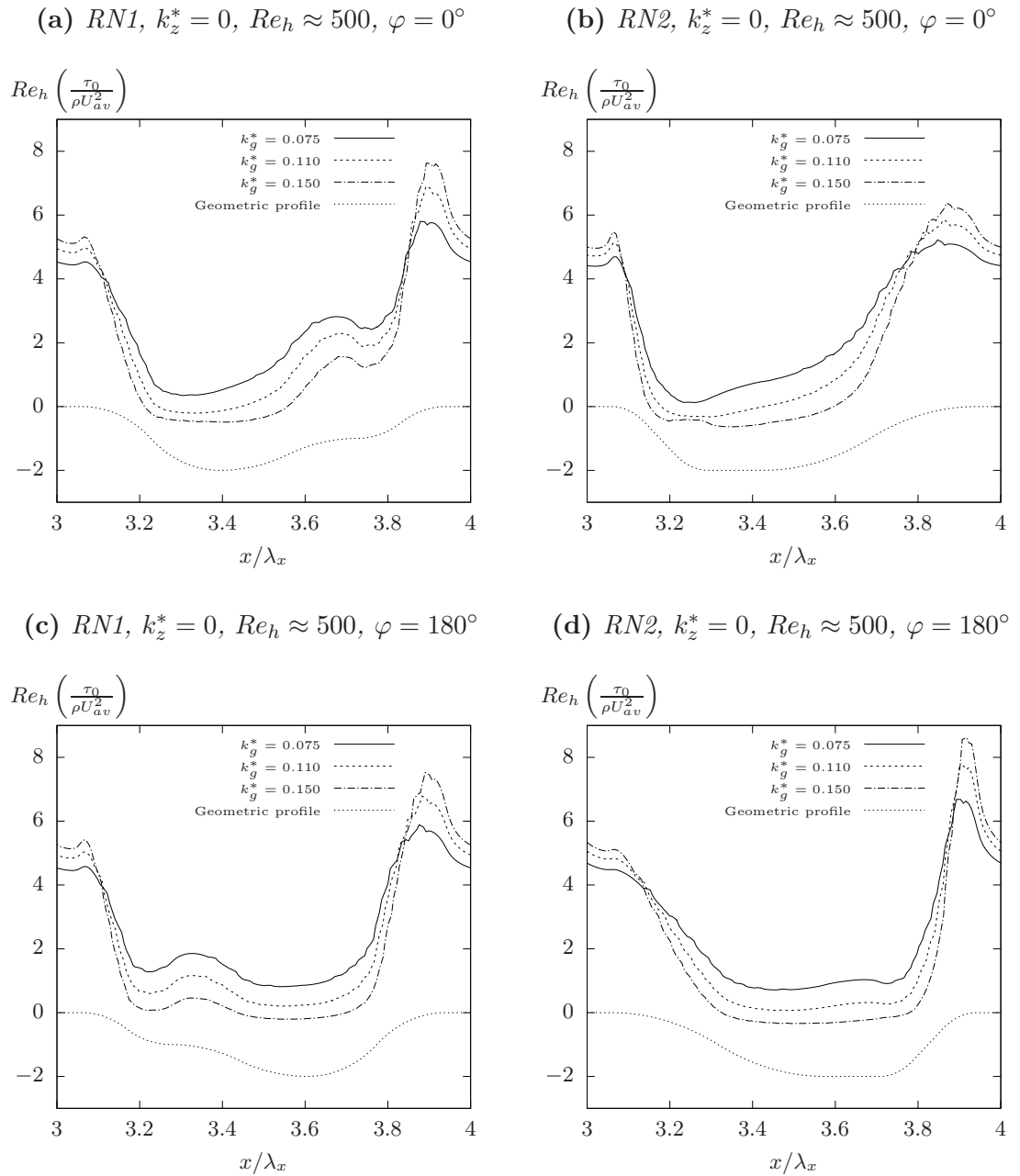
Figure D.3: *Distribution of the normalised streamwise shear stress over two-dimensional sand ripple profiles for a flow of $Re_h \approx 500$.*

(a) *RN1,* $k_z^* = 0,$ *Re$_h$* $\approx 1000,$ $\varphi = 0°$

(b) *RN2,* $k_z^* = 0,$ *Re$_h$* $\approx 1000,$ $\varphi = 0°$

(c) *RN1,* $k_z^* = 0,$ *Re$_h$* $\approx 1000,$ $\varphi = 180°$

**(d)** *RN2,* $k_z^* = 0,$ *Re$_h$* $\approx 1000,$ $\varphi = 180°$
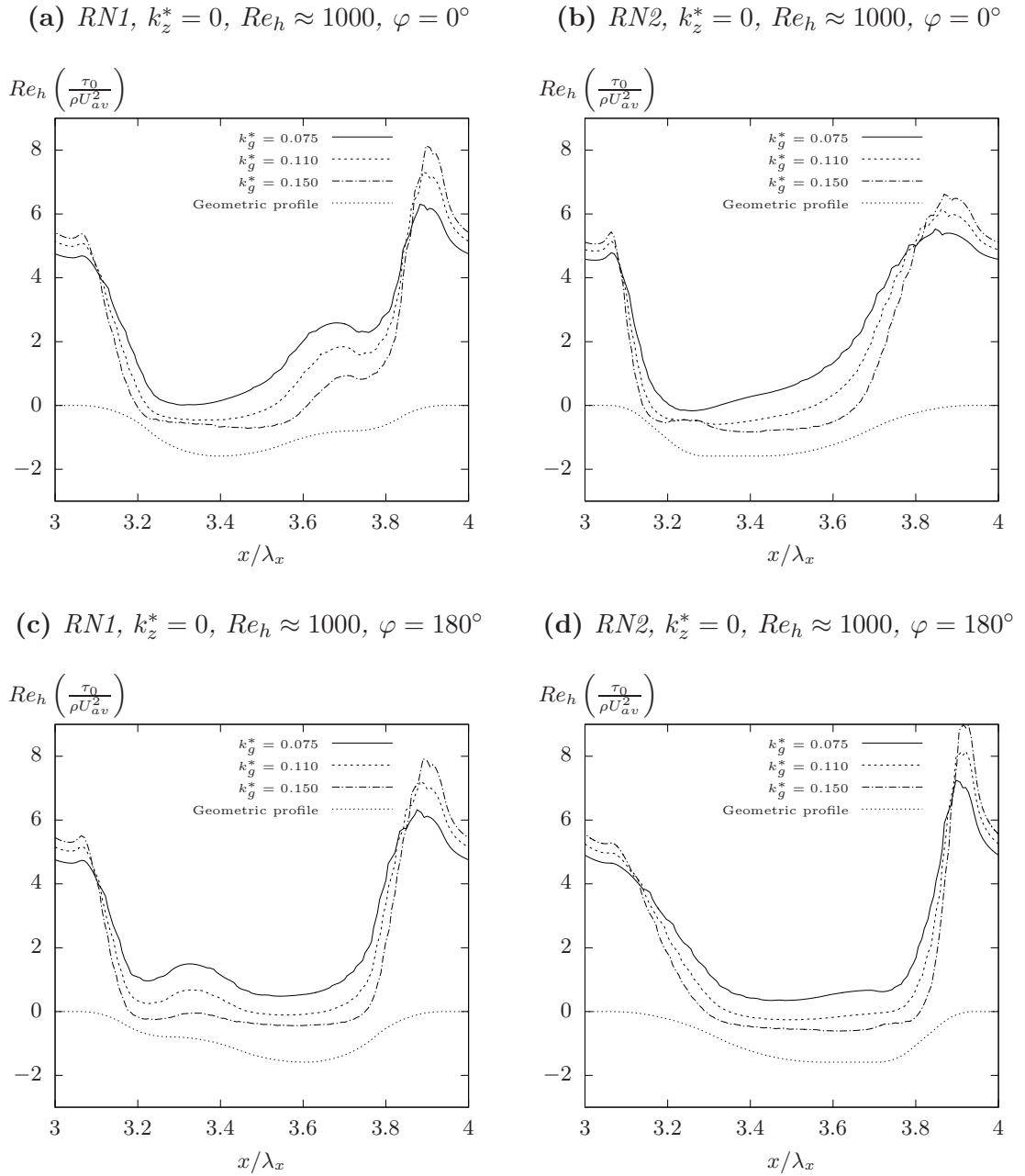
Figure D.4: *Distribution of the normalised streamwise shear stress over two-dimensional sand ripple profiles for a flow of Re$_h$ ≈ 1000.*

(a) *RS, $k_z^* = 0$, $Re_h \approx 50$, $\varphi = 0°$*

(b) *RS, $k_z^* = 0$, $Re_h \approx 100$, $\varphi = 0°$*

(c) *RS, $k_z^* = 0$, $Re_h \approx 500$, $\varphi = 0°$*

(d) *RS, $k_z^* = 0$, $Re_h \approx 1000$, $\varphi = 0°$*
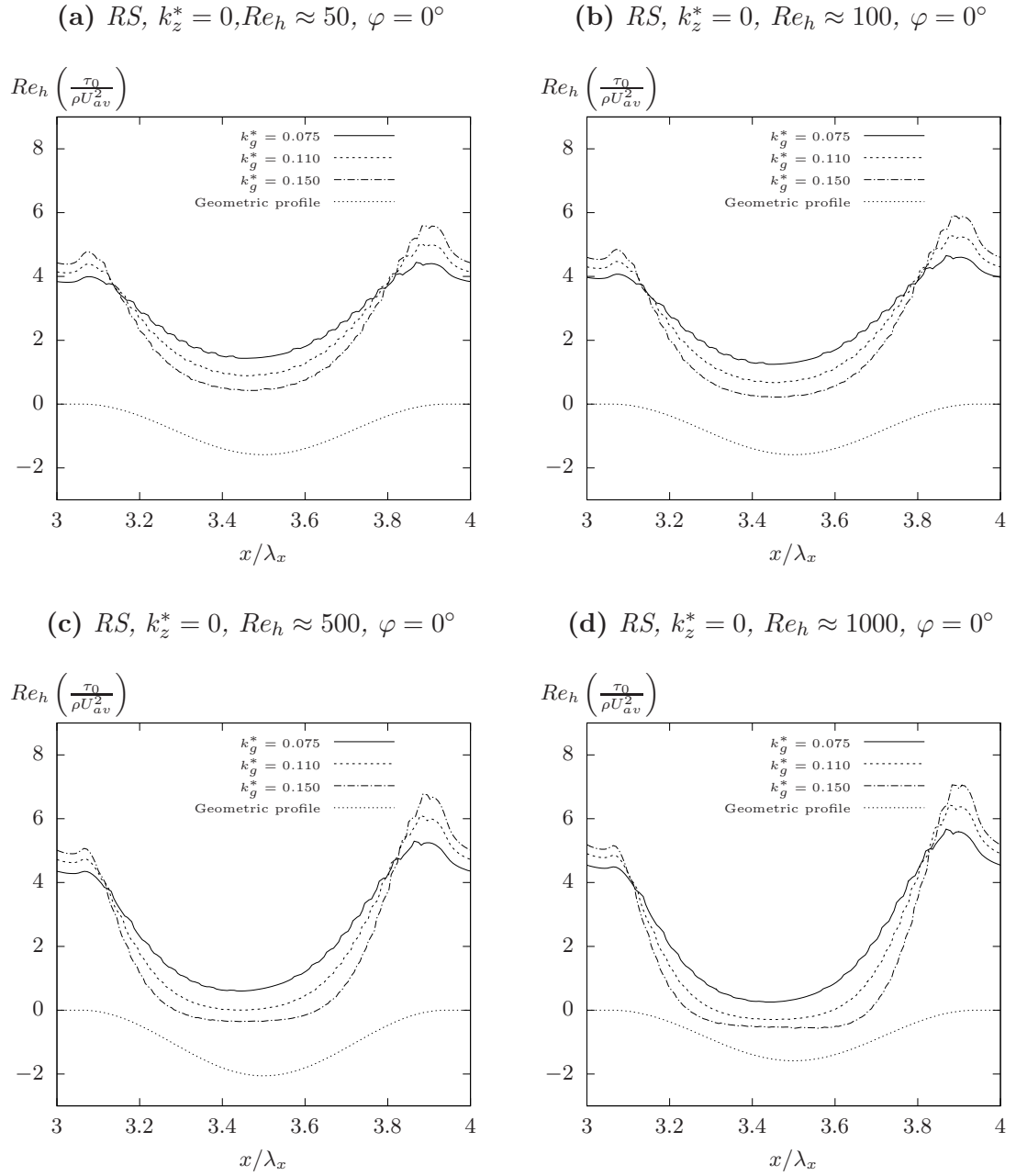

Figure D.5: *Distribution of the normalised streamwise shear stress over two-dimensional sinusoidal profiles for flows of $Re_h \approx 50$, $Re_h \approx 100$, $Re_h \approx 500$ and $Re_h \approx 1000$.*

(a) *RN1, $k_g^* = 0.15$, $Re_h \approx 50$, $\left(z/L_z = 0\right)$*   **(b)** *RN1, $k_g^* = 0.15$, $Re_h \approx 50$ $\left(z/L_z = 0.5\right)$*
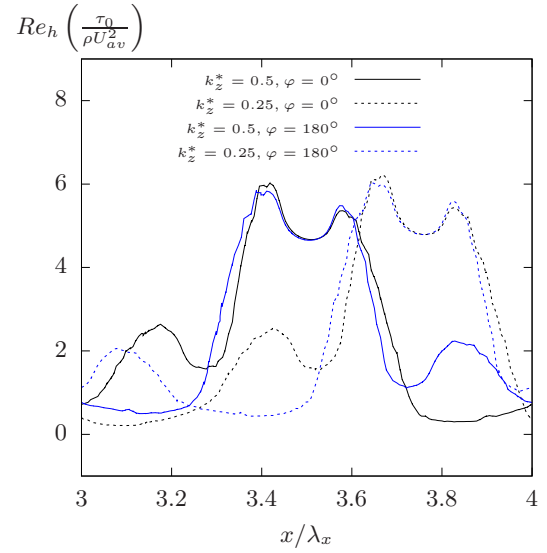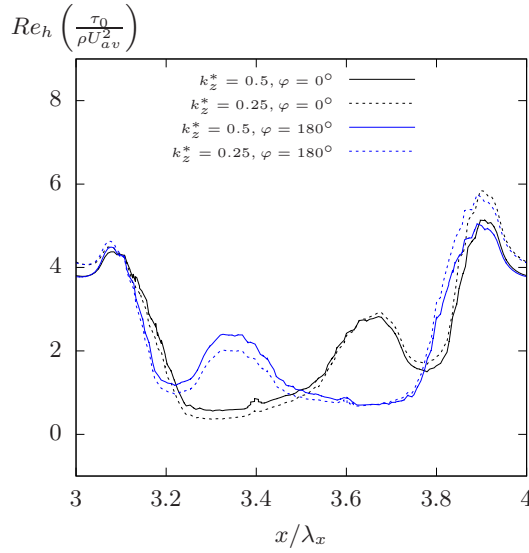
(c) *RN1, $k_g^* = 0.075$, $Re_h \approx 50$ $\left(z/L_z = 0\right)$*   **(d)** *RN1, $k_g^* = 0.075$, $Re_h \approx 50$ $\left(z/L_z = 0.5\right)$*
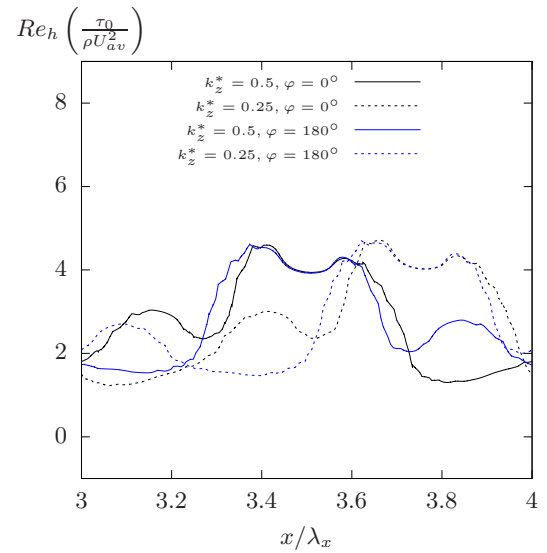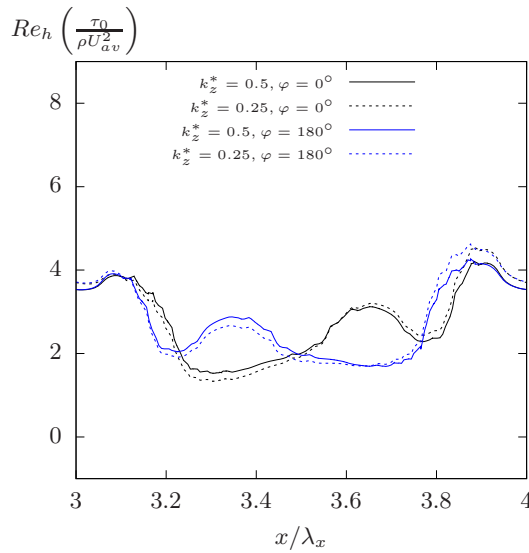
Figure D.6: *Distribution of the normalised streamwise shear stress over three-dimensional sand ripple profiles for a flow of $Re_h \approx 50$.*

(a) *RN1, $k_g^* = 0.15$, $Re_h \approx 500$ $(z/L_z = 0)$*

(b) *RN1, $k_g^* = 0.15$, $Re_h \approx 500$ $(z/L_z = 0.5)$*
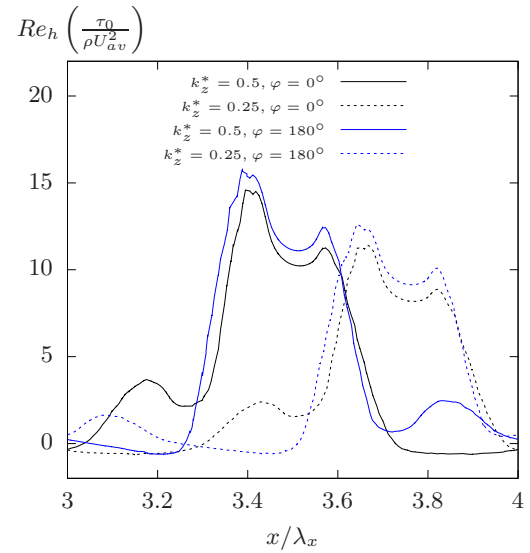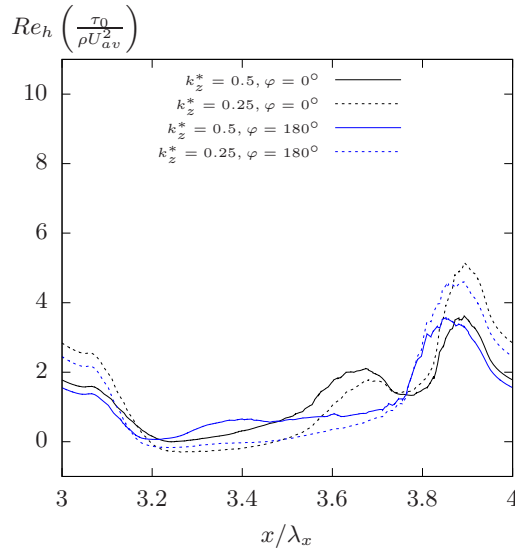
(c) *RN1, $k_g^* = 0.075$, $Re_h \approx 500$ $(z/L_z = 0)$*

(d) *RN1, $k_g^* = 0.075$, $Re_h \approx 500$ $(z/L_z = 0.5)$*
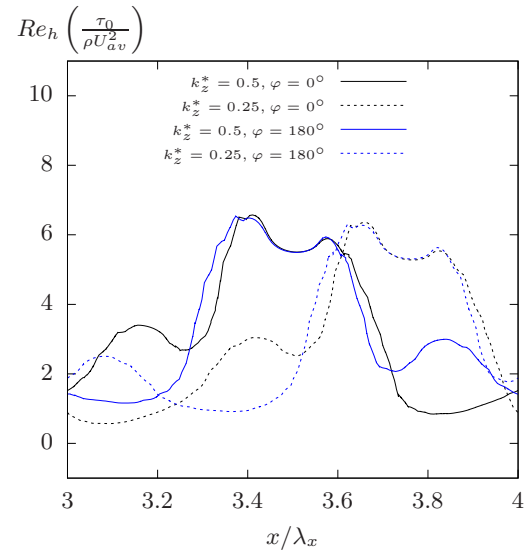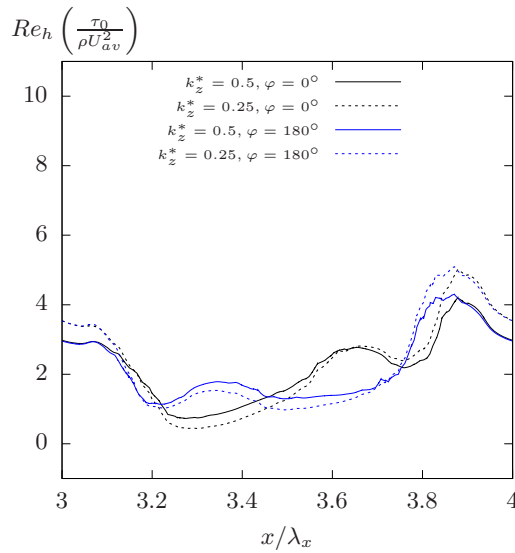
Figure D.7: *Distribution of the normalised streamwise shear stress over three-dimensional sand ripple profiles for a flow of $Re_h \approx 500$.*

(a) *RS, $k_g^* = 0.15$, $Re_h \approx 50$ $\left(z/L_z = 0\right)$*   **(b)** *RS, $k_g^* = 0.15$, $Re_h \approx 50$ $\left(z/L_z = 0.5\right)$*

(c) *RS, $k_g^* = 0.075$, $Re_h \approx 50$ $\left(z/L_z = 0\right)$*   **(d)** *RS, $k_g^* = 0.075$, $Re_h \approx 50$ $\left(z/L_z = 0.5\right)$*
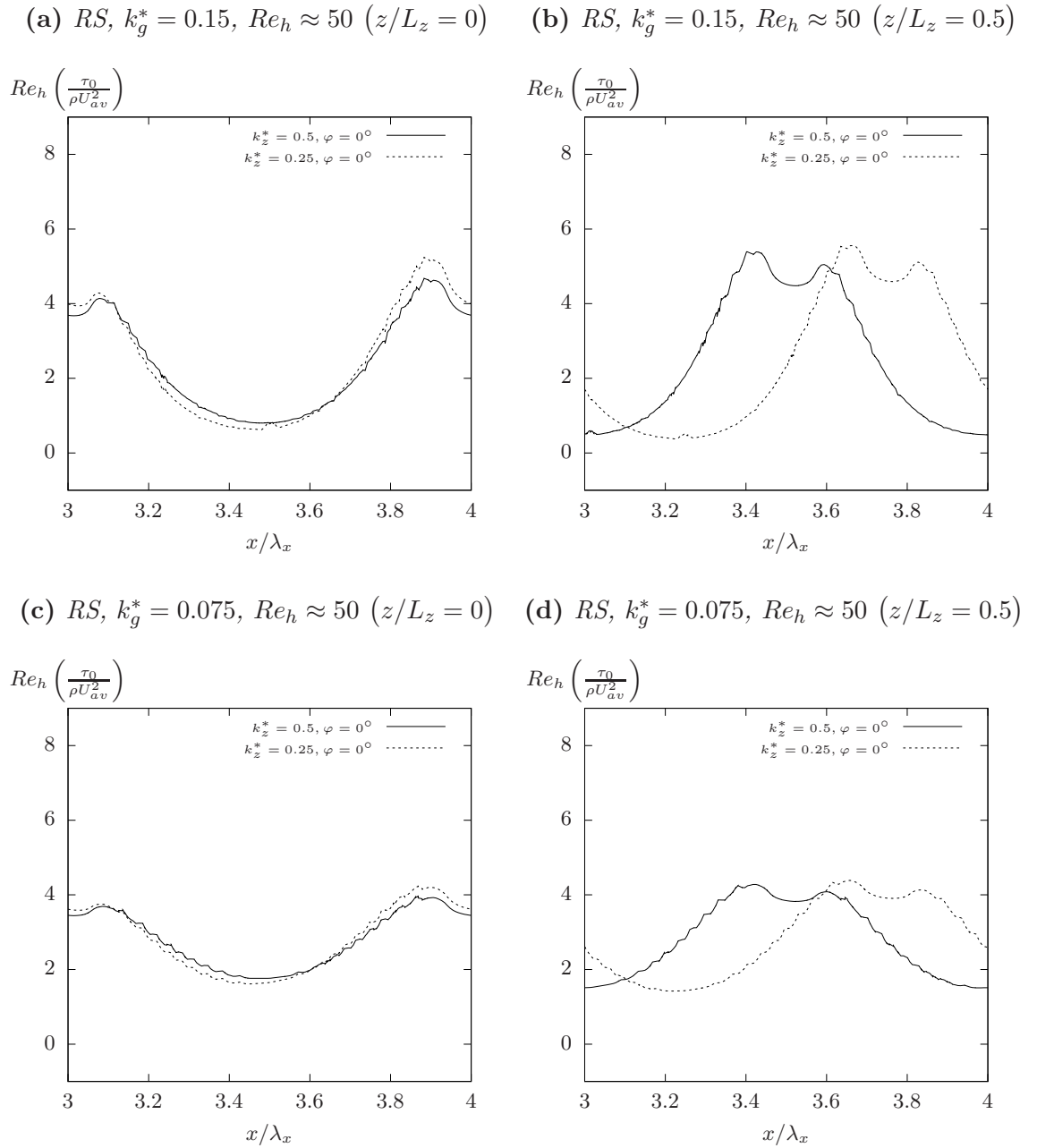
Figure D.8: *Distribution of the normalised streamwise shear stress over three-dimensional sinusoidal profiles for a flow of $Re_h \approx 50$.*

(a) *RS,* $k_g^* = 0.15$, $Re_h \approx 500$ $\left(z/L_z = 0\right)$ **(b)** *RS,* $k_g^* = 0.15$, $Re_h \approx 500$ $\left(z/L_z = 0.5\right)$
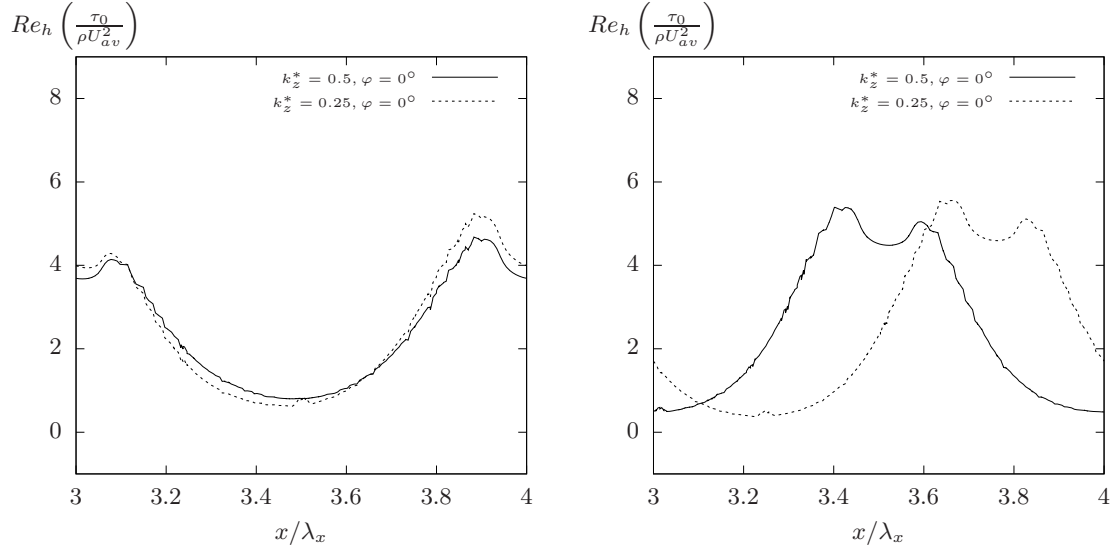
(c) *RS,* $k_g^* = 0.075$, $Re_h \approx 500$ $\left(z/L_z = 0\right)$ **(d)** *RS,* $k_g^* = 0.075$, $Re_h \approx 500$ $\left(z/L_z = 0.5\right)$
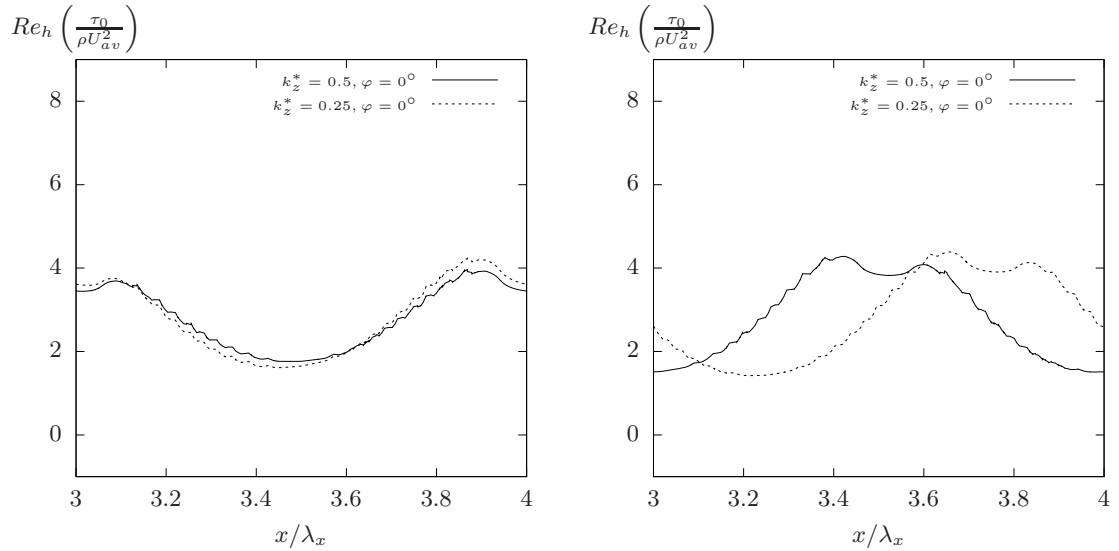

Figure D.9: *Distribution of the normalised streamwise shear stress over three-dimensional sinusoidal profiles for a flow of* $Re_h \approx 500$.